UNIVERSITY OF CALIFORNIA,
IRVINE

# Controlling the Speciation and Uniformity of Supported Catalysts Using Flame Spray Pyrolysis

DISSERTATION

submitted in partial satisfaction of the requirements
for the degree of

DOCTOR OF PHILOSOPHY

in Chemical and Biomolecular Engineering

by

Musa O. Najimu

Dissertation Committee:
Assistant Professor Erdem Sasmaz, Chair
Professor Plamen Atanassov
Assistant Professor Bihter Padak

2022

# DEDICATION

To my late mum,
...the only mum on earth who faithfully loved and sacrificed all she had for her only surviving child.
...who passed away few weeks to my dissertation defense, while waiting for me.

# TABLE OF CONTENTS

# LIST OF FIGURES

# LIST OF TABLES

# ACKNOWLEDGMENTS

First and foremost, I thank Allah, the Almighty God for sparing my life and for granting me the perseverance to keep pushing to the end of the PhD journey.

I would like to acknowledge and thank my advisor Professor Erdem Sasmaz for his guidance and support on the various research undertakings I have engaged in. His guidance always got me back on track when needed, and I am grateful for the opportunities for the quality of research and the training as independent researcher. I am also grateful to my two other committee members, Professor Bihter Padak and Professor Plamen Atanassov, for their insightful discussions, comments and support.

I aknowledge the opportunities to use Irvine Material Research Institute (IMRI) facilities at UC Irvine. I also acknowledge Professor Vincent Mcdonell, Associate Director of the Advanced Power and Energy program and the Director of the University of California Irvine Combustion Laboratory for the opportunity for interesting collaboration.

I thank all the faculty and staff of Chemical and Biomolecular Engineering department and the Henry Samueli School of Engineering at UC Irvine for their support during my PhD study at UC Irvine. I am grateful for the opportunities to work as a grader for Thermodynamic course and as a teaching assistant for the senior classes- Chemical Engineering Laboratory and Chemical Engineering Design Courses. It did give me the opportunities to meet and interact with a lot of smart students of various backgrounds, and to impart as much as I can. The instructors, personnel and colleagues I worked with were also amazing. I would also like to thank UCI for being family friendly - the support from the FRESH Basic Needs Hub was very helpful.

I would like to thank the department of Chemical Engineering at the University of South Carolina for initially accepting me to their PhD program (before transferring to UC Irvine), and Professor Jochen Lauterbach for serving as my Coadvisor during my one year stay at the University of South Carolina. The courses taken at the University of South Carolina have been very helpful. I would like to appreciate all lab members in the Sasmaz group – the old members at the University of South Carolina where I started my PhD journey and the current members of the Samsaz group here at the University of California Irvine. Everyone's comments and questions have been very beneficial to my research. I would also thank all the amazing undergraduate students I have had the opportunity to mentor and work with, both at the University of South Carolina and University of California Irvine, who are currently doing well at their various undertakings.

I would like to extend my appreciations to my mentors and friends, both local and remote, for their support in the PhD journey. I thank my immediate family - the kids for their patience whenever I was busy working on research, and their mum for her support and for taking care of the kids. Finally, I would like to thank my mum (late) and dad for their supports, patience, and sacrifice while I was embarking on this educational pursuit. The passing away of my mum on July 16, 2022, few weeks before my dissertation defense was

indeed a great loss to me. I pray Allah reward her for her selfless sacrifice, grant her Jannah and overlook her shortcomings.

# VITA

## Musa O. Najimu

### EDUCATION

**Doctor of Philosophy in Chemical and Biomolecular Engineering** **2022**
University of California, Irvine *Irvine, CA*

**Masters of Science in Chemical Engineering** **2017**
King Fahd University of Petroleum and Minerals *Dhahran, Saudi Arabia*

**Bachelor of Science in Chemical Engineering** **2013**
Obafemi Awolowo University *Ile-Ife, Nigeria*

### RESEARCH EXPERIENCE

**Graduate Research Assistant** **2019–2022**
University of California, Irvine *Irvine, CA*

### TEACHING EXPERIENCE

**Teaching Assistant, CBE 150 B** **Spring 2022**
University of California Irvine *Irvine, CA*

**Teaching Assistant, CBE 140 B** **Winter 2022**
University of California Irvine *Irvine, CA*

**Teaching Assistant, CBE 140 A** **Fall 2021**
University of California Irvine *Irvine, CA*

**Teaching Assistant, CBE 40 C** **Spring 2021**
University of California Irvine *Irvine, CA*

**Teaching Assistant, CBE 140 A** **Fall 2020**
University of California Irvine *Irvine, CA*

## REFEREED JOURNAL PUBLICATIONS

**Incorporation of Film Theory in Single Droplet Combustion Model for Prediction of Precursor Release in Flame Spray Pyrolysis** **2022**
Proceedings of the Combustion Institute, under review

**Evaluation of Single Site Catalysts in the Path of Commercialization** **2022**
To be submitted

**Control of Pd Species on $CeO_2$ using Flame Spray Pyrolysis** **2022**
To be submitted

**Evaluation of Methane Oxidation Reaction over Atomically Dispersed Pd** **2022**
To be submitted

## REFEREED CONFERENCE PUBLICATIONS

**Atomically Dispersed Pd in Flame Synthesized $Pd/CeO_2$ Catalyst for Methane Oxidation Reaction** **May 2022**
North America Catalysis Meeting

## CONFERENCE PRESENTATIONS

**Incorporation of Film Theory in Single Droplet Combustion Model for Prediction of Precursor Release in Flame Spray Pyrolysis** **2022**
39th International Symposium on Combustion

**Single Droplet Combustion Modelling for Catalyst Synthesis with Flame Spray Pyrolysis** **Nov 2021**
AIChE Annual Conference

**Enhanced Metal-Support Interaction of Flame Synthesized $Pd/CeO_2$ Catalysts for Methane Oxidation** **Nov 2021**
AIChE Annual Conference

# ABSTRACT OF THE DISSERTATION

Controlling the Speciation and Uniformity of Supported Catalysts Using Flame Spray Pyrolysis

By

Musa O. Najimu

Doctor of Philosophy in Chemical and Biomolecular Engineering

University of California, Irvine, 2022

Assistant Professor Erdem Sasmaz, Chair

Catalytic oxidation of methane to less potent gases has been the current technology for controlling methane emissions from natural gas-powered vehicles. Pd is commonly used as an active metal for methane oxidation, but its amount is desired to be minimized due to its high cost. The stability and activity of Pd species at wide operating temperatures depend on the Pd dispersion and local structure on the $CeO_2$ surface. Here, we adopt flame spray pyrolysis (FSP), a high-temperature synthesis, to stabilize Pd on $CeO_2$. The $Pd/CeO_2$ catalyst synthesized in the oxidizing environment generates highly active Pd species, while the reducing environment has less active Pd species for methane oxidation. Decreasing Pd loading on $CeO_2$ can enhance the reaction rate due to better dispersion. Detailed structural characterizations of catalysts synthesized at different loading and synthesis conditions using CO diffuse reflectance infrared Fourier transform spectroscopy (DRIFTS) experiments identify the highly active sites as atomically dispersed Pd and the less active sites as the combination of highly dispersed $Pd^{n+}$ , $Pd^0$ , and $Pd^0$ cluster. These results indicate that the control of Pd structures is a function of its loading and the FSP synthesis condition. Evaluation of the methane oxidation reaction over these structures reveals that the enhanced methane oxidation activity by the atomically dispersed Pd is due to the facilitation of the conversion from $CH_2$ to carbonates during the methane oxidation reaction. This study demonstrates

that FSP can be used to control Pd structures for synthesizing atomically dispersed Pd for enhanced methane oxidation activity.

In addition to controlling the chemical property of catalysts by FSP, the uniformity of catalyst particles can be governed by the release rate of precursors in FSP. However, there is a lack of experimental techniques for the direct measurement of the precursor release, and its quantification through the single droplet combustion (SDC) modeling has been based on the immediate release of the precursor from the droplet. Here, a single droplet combustion model that includes film theory has been developed, and the thickness of the mass boundary layer that limits the release of precursor to the combustion zone is coupled with the droplet temperature for a more accurate prediction of the temporal precursor release during synthesis. The model reveals that the mass boundary layer can influence nanomaterial formation and its coupling with droplet temperature allows a more accurate comparison of precursor release rate. We also developed design rules that can guide experiments on the choice of solvent composition and nozzle operating parameters to improve homogeneity. Quantifying the precursor release through thermodynamic phase relation and diffusion model with two moving boundary conditions is further developed to investigate precursor concentration on catalysts homogeneity and more precise prediction. This new methodology for accurate prediction of precursor release is the first application of film theory for the understanding and design of flame-synthesized homogeneous catalysts.

# Chapter 1

# Introduction

Heterogeneous catalysis is the bedrock of industrial catalysis and is primarily based on supported metal nanoparticle catalysts. Several of these supported nanoparticle-based structures face the challenges of irregular morphology and broad size distribution of nanoparticles leading to a multiplicity of active sites and hence reduced catalytic performance [1]. Downsizing the nanoparticles to sub-nanoclusters minimizes some of these challenges, while downsizing further up to the extreme limit of single atoms or single atom alloy can enhance catalytic performance through maximizing surface free energy and specific activity [2, 3], while also minimizing the utilization of precious metals. However, some reactions are not favored by single atom catalysts, requiring some optimal sizes of the supported metal catalysts [4, 5], while several other valuable reactions are yet to be assessed. For most applications, these metal species - single atom or nanoparticle/clusters - are typically anchored on supports such as metal oxide, carbon and others. In addition to the supported metal species, the anchoring supports can also play significant roles in the performance of the catalysts [6]. They can directly participate in the reaction or induce some effects on the supported metal species. Certain properties of the supports influencing some of their roles in catalytic performance can be related to the particle size of the support [7, 8, 9]. Hence, having control

over the speciation of the supported metal and the uniformity of the support particle on which the atoms are anchored can be important in achieving high catalytic performance for valuable reactions. Of equal importance is having a nanomaterial synthesis method that can allow easy control of both the speciation and the homogeneity of the catalysts.

## 1.1 Single Sites Catalyst

Single-site catalysts (SSCs) comprising single-atom catalysts (SAC) and single-atom alloy catalysts (SAA) are currently fast advancing beyond mere scientific interest to practical viability and emerging to replace the state-of-the-art metal nanoparticle-based heterogeneous catalysis. SAAs are composed of catalytically active elements that are atomically dispersed and alloyed in the surface layer of a less active and more inert metal host. In contrast, SACs are composed of atomically dispersed metal on an oxide or carbon support [10].

Basset and coworkers in the late 1990s were among the earlier researchers to report works on the low-temperature hydrogenolysis of alkanes with atomic Zr on hydrogenated silica [11] and dehydrogenation of isobutane by silica-supported tin-isolated Pt catalysts [12], which highlighted the significance of "site isolation effect" over "ensemble effect". Later, Flytzani-Stephanopoulos and co-workers [13] discovered ceria-supported isolated Au species as a source of activity in the water-gas shift reaction in 2003, after which Zhang and his coworkers [14] eight years later explicitly coined the term 'single atom' in their discovery of high activity and stability of FeOx supported Pt single atoms for CO oxidation. Since then, the curiosity of academic scientists aroused by the scientific fascination of the subject matter led to the increasing number of publications on SSCs. The significant development of this research, aided by the advancement of characterization techniques and computational chemistry, as researchers solve the challenges one after the other amidst much debate, is today bridging the transition from mere scientific interest to practical viability.

Scientific interest in SSCs arose from their benefits over conventional heterogeneous catalysts. Its first source of attraction was the atom economy/utilization efficiency advantage of the SSCs, where a minimal quantity of precious and expensive metals is needed to achieve similar and better catalytic performance compared to the large metal used in nanoparticle-based catalysts. In addition, SSCs overcome the inhomogeneity of supported metal nanoparticle catalysts by sharing the homogeneity property in homogeneous catalysis, where the same identity and uniqueness of active sites are guaranteed. This homogeneity of active sites in SSCs resulting from the similar spatial and electronic properties with substrates prevent side reactions commonly encountered in heterogeneous catalysis and therefore stands as its source of higher selectivity, thus reducing the separation cost due to product purification [15]. In addition, due to the knowledge and understanding of the local environment of the single sites obtained by advanced characterization techniques and the uniformity of their atoms' environment, further understanding and better insights into reactions mechanisms are fortified by deploying concepts from molecular chemistry such as coordination, organic and organometallic chemistry. This, in turn, simplifies the rational design of catalysts for several reactions.

Although SSCs have a wide range of applicability, their commercialization is yet to be reported. SSCs are expected to meet specific general criteria such as excellent mechanical properties, the ability to enable transport of chemical species via the active surface, and the chemical activity of the surface during pretreatment and catalysis, similar to industrial solid heterogeneous [16]. As previously detailed, most SACs have better activity than their NP counterpart, as illustrated in the earlier sections. However, their overall catalytic performance needs to be improved to be industrially relevant. Also, they are more prone to sintering than their nanoparticle counterparts due to the isolated nature of metal atoms in SSCs; hence, industrially relevant SSCs need to be prepared to be thermally stable under both reaction and pretreatment conditions. Reported solutions to most of the SSCs problems described here are related to their synthesis, loading, and site uniformity. This section

highlights some of the efforts currently exerted to solve these problems.

### 1.1.1 Synthetic methods of enhancing stability

Several synthesis methods have been employed for anchoring single atom species and general preparation of SACs. These methods include coprecipitation, incipient wetness co-and sequential impregnation, atomic layer decomposition [17], among others, and details of these synthesis methods and procedures have been documented in a recent review paper [3]. These methods have availed different strategies such as defect deployment, confinement strategy, electrochemical deposition, and chemical etching, efficiently synthesizing stable and active SSCs. Additionally, many other recently revealed strategies, mostly from high-temperature synthesis methods for stabilizing SSCs. Right from the early development of SSCs, Flytzani-Stephanopoulos [13] identified the importance of the high-temperature effect in synthesizing Au and Pt SACs that are active and stable for WGSR. Today, high-temperature synthesis is re-emerging as a method recently reported for stabilization of single atoms of metals on a variety of supports [3], and it is continuously being explored for efficient anchoring of stable and active single atom species. Although there is no consensus in the literature on the cut-off temperature above which a synthesis method qualifies as a high-temperature method – some have reported high-temperature synthesis at greater than 1000 $^{o}$C [18], a high-temperature synthesis can therefore be one in which the temperature is high enough to perform certain special functions that are beyond remediation of surface impurities like in other synthesis methods that also require thermal energy. These functions are described in the next couple of paragraphs.

Most of these high temperature stabilization strategies are top-down synthesis approaches where the metals first exist as a NC or NP on the support before being transformed to single atoms by applying consequential thermal energy in a certain way. There is little

concern about initial particle growth due to surface migration or Ostwald ripening from high temperatures. The high temperature synthesis enables paths through which the single atoms are consequently formed. These paths can generally apply to certain groups of supported metal and support or can be specific to a particular support/metal combination. Still, a wide variety of support, including reducible oxide, non-reducible oxides and non-oxide supports are applicable. Several of these high-temperature synthesis methods open possible SACs manufacturing routes that ordinarily are conventionally challenging [19]. However, generally, the high temperature enables the effective cleaning of the support surface from any adsorbed species and poisons such as hydroxyls and carbonates for sufficient interaction and consequently strong binding of the adatom with the support [20]. Also, the survival of single atoms during high temperature synthesis indicates their strong binding to the support and consequently their thermal stability.

Beyond the cleaning effect of the support surface, high temperature plays some critical specific roles in the formation process of the SACs, and these roles can be dependent on the synthesis method and the formation process. High temperature can cause surface migration and diffusion of atoms from their nanoparticles to sites at which they are bonded by lowering the activation barrier for these processes. Following wet incipient impregnation and coprecipitation methods of synthesizing $Pt/CeO_2$ and $Au/CeO_2$, respectively, Flytzani-Stephanopoulos [13, 21] identified the additional use of air calcination (a process before the final step of leaching) at 400 $^oC$ for 10 h as an essential step in producing active and stable single atoms of these metals for WGSR. Formation and stabilization of the single Au species were unambiguously induced by the heating step of the catalyst's preparation procedure through lattice substitution as evidenced by the simultaneous identification of Au ions together with an increased amount of surface oxygen species observed using X-Ray Photoelectron Spectroscopy and temperature-programmed reduction technique. Omitting the heating step in the overall synthesis procedure resulted in the leaching of the Au atoms on the $CeO_2$ surface and consequently led to inactivity of the synthesized catalysts, confirming

the importance of the heating step. Due to the high temperature, Au atoms migrate to and fill the surface vacant Ce sites to form a stable structure. Consequently, the electron charges distribution between the Au ion and ceria weakens the Ce-O bond, increasing the ceria support's reducibility and surface oxygen species. In addition, the temperature has a favorable interaction with the surface defects by reducing the number of anchoring sites provided by the ceria, thereby preventing agglomeration.

In some top-down approaches to synthesizing and stabilizing SACs using high temperature synthesis methods, high temperature can cause the transfer of single atom species from their NP to binding sites on support. The transfer can be in the form of surface migration or gas phase mobility, depending on the energetics of each process. Using a high temperature aging protocol, Jones et al. [20] reported thermally stabilized single atoms of Pt on ceria by aging the catalysts at 800 °C for 10 hr in flowing air. Here, high thermal energy was employed to initiate the transfer of Pt under ambient conditions to step sites of $CeO_2$ , where they are bonded and stabilized as single atoms. This is because oxidized Pt clusters are more favorably formed on the $CeO_2$ (111) terraces than metallic Pt clusters due to the latter instability and ease of fast oxidation under the synthesis condition. $PtO_2$ moiety, by its small adsorption energy on the parent oxidized cluster, is released facile at high temperature and prefers to migrate via gas phase rather than by surface migration due to the higher diffusion barrier associated with the latter. The oxidized Pt clusters consequently choose to be stabilized on the step site of the $CeO_2$ (111) due to the higher adsorption energy of $PtO_2$ on the step site than on the terrace [20, 22]. The method of Pt deposition and the initial location of Pt does not seem to matter as this strategy of thermally induced Pt transfer demonstratively worked to stabilize single Pt atoms in both cases when a physically mixed Pt/La-$Al_2O_3$ catalysts with $CeO_2$ and a Pt nanoparticle on $CeO_2$ prepared by conventional incipient wetness impregnation are subjected to this same synthesis conditions. Even though applying the thermal energy for a longer time improves the formation of a stable single Pt atom, the impact of the thermal energy on the $CeO_2$ support does not influence its atom

trapping feature, which is intrinsic and only dependent on the $CeO_2$ nanostructure with $CeO_2$ polyhedral superiorly dispersing single atoms than $CeO_2$ cube and nanorod structures. Apart from the use high temperature aging for metal dispersion, $Pt^{2+}$ single ions can be dispersed and stabilized at the monolayer of high $CeO_2$ step edges [23] through catalyst annealing at 700 K under ultra-high vacuum (UHV) without any formation of 2 or 3-dimensional PtOx clusters, as illustrated by the STM images of $Pt/CeO_2$ having an extremely low monolayer of Pt on the highly step-decorated $CeO_2$ . The stabilization of $Pt^{2+}$ ions from the deposited Pt is promoted exclusively by the step edges and not by the surface oxygen defects. However, the high-temperature annealing stabilizes the Pt by enabling its segregation on the step edges and promoting its oxidation by external oxygen rather than by $Pt^0/Ce^{4+}$ redox couple mechanism, as shown by the non-commensurate reduction of $CeO_2$ . Based on the energetics of the process, the Pt adatom undergoes segregation preferentially at the $CeO_2$ (111) step edge having excess oxygen – a location where it has the highest binding energy than the binding energy at the stoichiometric step edge, stoichiometric or defective (111) terraces, and the cohesive energy of the bulk metallic Pt. This nonstoichiometric step edge anchors the $PtO^4$ moieties having $Pt^{2+}$ from the ionic Pt-O bond based on computed electronic structure and density of state of the units as evidence of oxidation. Consequently, engineering the step density on $CeO_2$ could maximize stabilized Pt loading and avoid nucleation of metallic Pt as the amount of stabilized Pt is first limited by the amount of step density available for occupancy and oxidation (up to 80 % of the step density), followed by the amount of Pt deposited.

The use of high-temperature synthesis to stabilize metal single atoms is not limited to $CeO_2$ support due to its defects; metals can also be stabilized using non-defect properties of supports. Lang et al. [24] demonstrated the use of high-temperature calcination to cause the transfer of Pt to $Fe_2O_3$ support, which utilizes its reducibility to anchor isolated Pt rather than through defects such as the $CeO_2$ supports [20, 23] discussed above. Based on the study, Pt can only be dispersed and stabilized through a strong covalent metal-support interaction

(CMSI) on the $Fe_2O_3$ support by calcining at 800 °C in air. The CMSI does not occur at 800 °C in argon or 600 °C in an air environment. In comparison to the high-temperature synthesis by Jones et al. [20] and Dvorak et al. [23], this implies that irrespective of the anchoring manner of Pt on the support, the transfer of Pt through high temperature is similar, and both the high temperature and the environment are critical to the Pt transfer process.

In another top-down approach, high temperature can be employed in transforming metal nanoparticles into single atoms through direct atomization. This method requires that sintering, a counter effect of the atomization, be avoided. Driving the effect of pyrolysis of metal nanoparticles (NP) beyond sintering by which Pd, Pt, and Au nanoparticles can be downsized to and stably anchored as their respective single atoms on nitrogen-doped carbon (CN) has been reported [18]. In the pyrolysis of Pd NP on CN, sintering creates large and sintered Pd NPs by binary collision and coalescence of the smaller Pd-NPs (particle migration and coalescence mechanisms) rather than by emission and subsequent capturing of Pd atoms by the larger Pd nanoparticles (Ostwald ripening) [25, 26] as indicated by the in situ environmental TEM experiments. However, during more intense pyrolysis, such as at above 900 °C, direct atomization by Pd atom emission and capturing of CN defects are suppressed due to the decreased vapor pressure of the large sintered Pd NPs. Yet, their thermal motions and intensive collisions with the CN in the neighborhood of the N defects enable thermodynamically stable coordination of the surface Pd with the defects, which consequently facilitates a decrease of particle size to the point at which atomization by emission and capture of Pd atoms on the N defects is favorable. This implies that the formation and stabilization of Pd SA from their nanoparticle, though still contingent on the availability of N defects which are created by the thermal effect on the support, indeed requires driving the pyrolysis process to the atomization-dominant stage by using high temperature (or high thermal energy which is a function of temperature and time) to overcome the energy barrier associated with both the decomposition of the Pd clusters/nanoparticle and subsequent formation of single Pd atoms on $N_4$ defect which initiate and hence drive direct atomization.

High temperature synthesis methods can also be applied for the synthesis of stable monometal single atoms on support from bimetallic catalysts such as bimetallic supported on MOFs (BMOFs). Here, the high temperature acts as an agent of disassembly to generate the stable SSCs from the bimetallic catalysts. The homogeneous distribution of bimetals on MOF [27] allows the stabilization of the single atom of the metals on the support when the difference in the thermal response of the two metal atoms is exploited. Li et al. [28] used a pyrolysis technique to stabilize Co single atoms on N-doped porous carbon by selectively boiling off Zn at (temperature over the 902 °C boiling point of Zn) over 800 °C (between 800 and 900 °C) from a pre-synthesized bimetallic Zn/Co supported on metal-organic frameworks ($Zn_1Co_1$-BMOF ). The high-temperature pyrolysis caused carbonization of the N-containing organic linker leading to the reduction of Co nodes and the formation of N heteroatom/ N-doped porous carbon support, which anchors the metals [29]. Also, the Zn atoms that create spatial intervals between Co atoms evaporate by the thermal effect leaving behind some free N sites, which further help stabilize the Co single atoms. However, the pyrolyzing temperature is very critical as this determines the amount of Co-N (800 and 900 °C for Co-$N_4$ and Co-$N_2$ , respectively), and it, therefore, needs to be modulated to less than 1000 °C to avoid breakage of all Co-N bonds and hence the formation of Co nanoparticle. A high Zn/Co ratio may be desirable to provide enough binding N sites for stabilizing the Co single atom when pyrolyzing at high temperatures. Formation of Co NP when Co supported on MOF with no Zn is subjected to similar conditions implies that the working strategy is combining high temperature, nature of the support, and the thermal response difference of the supported bimetallic species.

### 1.1.2 Effort to increase loading

Since the activity of SSCs is enhanced beyond that of NP counterparts, increasing the concentration of these active isolated species is essential to improve the overall performance of

the catalysts. Therefore, only SSCs with sufficiently high metal loading might be realized for the commercialization [30]. For instance, highly loaded atomically dispersed transition metal in SSZ-13 that achieves unprecedented 100 % adsorption efficiency has been recommended for immediate industrial application [31]. However, increasing loading is still widely accepted as one of the current key challenges in the SACs [24]. This is because, in most cases, it is accompanied by one or any combination of loss of catalytic activity, selectivity decline and inefficient use of the supported metals, leading to partial or total loss of the benefit of the SACs. With respect to this, increasing loading is typically associated with either of these two problems or the combination of both.

Several attempts to increase the loading of single atoms are sometimes associated with total loss of the single atoms through transformation to NCs and NPs [32]. The transformation of a single atom to NCs/NPs is associated with the thermodynamic particle formation process related to the increased metal concentration. Another identified synthesis-related key challenge is the coexistence of single atoms with NCs/NPs on a support at high loading [33], with the density of NCs/NPs increasing with increased loading [24]. This challenge is encountered by many synthesis methods. For instance, Fujiwara and Pratsinis [34, 35] were able to use the flame synthesis approach to achieve a synthesis of an exclusive single atom of Pd on $TiO_2$ at very low loading ( less than 0.05 wt%); however, catalysts at the optimum loading of 0.1wt% for NO reduction containing the active single Pd atoms additionally has spectator sub nanoclusters leading to inefficient use of the expensive noble metals. In another study, a coprecipitation synthesis of 1 wt% $Pt/CeO_2$ catalysts followed by calcination results in the coexistence of both single Pt atom as well as PtOx clusters in the distorted $CeO_2$ interface comprising both $Pt^{2+}$ and $Pt^{4+}$ to a different degree depending on the calcination temperature. When calcined at 600 °C, the ensuing catalyst contains both the surface-stable $Pt^{2+}$ in the square planar-coordinated structure and the $Pt^{4+}$ in the subsurface, while calcination at 800 °C results predominantly in surface $Pt^{2+}$ [32]. Although the coexistence of the $PtO_x$ with the single Pt atoms was identified to be beneficial for the effective redox properties of

the catalysts, the inability of this synthesis protocol to exclusively produce a single atom of Pt on the support is still clearly indicated. It is important to note that the coexistence problem can be general and sometimes independent of the supports or metals involved. Different one wt % $Pt/SiO_2$ , $Pt/Al_2O_3$, $Pt/ZrO_2$ , and $Pt/TiO_2$ catalysts prepared by incipient wetness impregnation and calcined at 400 $^oC$ in the air all suffer from the problem of coexistence of Pt single atom with nanoparticle on the corresponding support based on infrared spectroscopy characterization, even though the single atom, in this case, was identified as a spectator for both CO oxidation and water gas shift reaction [36]. Many others have reported the formation of NCs or NPs at one wt %, for instance, $Pt/CeO_2$ prepared by impregnation plus calcination [33]. Other than atom inefficiency and deterioration of catalytic activity, the coexistence of SA and NP on support uniquely makes the understanding and isolation of active sites difficult except for the use of additional characterization protocols where applicable. More importantly, improving catalytic performance through rational design of these catalysts can pose a challenge.

Some synthesis techniques and strategies are emerging by which exclusive formation of single atoms on supports can be achieved at high loading, and several of these high-loading SACs have been reported. One strategy to exclusively obtain isolated single atoms is to maintain the optimal surface concentration of the metal atom on the support. Using XPS, Low energy ion scattering (LEIS), X-ray absorption spectroscopy (XAS), electron microscopy, and density functional theory, it has been found that $CeO_2$ can support Pt single atom as high as three wt % corresponding to a surface concentration of 1 atom $Pt/nm^2$ without formation of any clusters or 3D aggregates [22]. This has been achieved by the atom tapping synthesis method described above. Another essential strategy is to first identify the stabilization sites on support and then increase them for maximal loading of the SA on the support. Rather than the surface oxygen vacancy of $CeO_2$ , step edge density was identified to promote the stabilization of ionic Pt species selectively, and engineering this step edge density to as high as 0.18 ML, which led to the atomic stabilization of deposited Pt of loading as high as 0.18

ML, following a simple supply-and-demand phenomenon [23]. However, surface edges are not necessarily required to stabilize SACs. A 1 wt % Pt was dispersed and stabilized on $Fe_2O_3$ support through a strong covalent metal-support interaction from the $Fe_2O_3$ reducibility [24]. Additionally, high loading can be stabilized by external binding agents. UV-generated ethylene glycolate radicals on $TiO_2$ nanosheet facilitated atomic dispersion and stabilization of up to 1.5 wt % Pt [37]. A 2.16 wt % Pt/FeOx was also further stabilized with Na in a coprecipitation method through the formation of $NaFeO_2$ surface layer, which promotes Pt dispersion via Pt–O–Na–O–Fe-species [38].

For isolated single atoms on zeolite, a general-purpose strategy of in situ separating and confining of the metal precursor into the cages of zeolite can achieve up to atomic metal dispersion of 0.65 wt % (M-ISAS@Y, M = Pt, Pd, Ru, Rh, Co, Ni, Cu), higher than the conventional wet incipient technique [39]. High metal loading on zeolite can also be atomically dispersed by adopting a modified ion exchange technique where species that compete against the metal atoms for the zeolite binding sites are avoided [31, 40]. While the incipient wet impregnation method could not also disperse one wt % of Pd using the H-form of zeolite (SSZ-13, ZSM-5, and Beta), the modified-ion exchange strategy could disperse up to 2 wt % of Pd by using Pd nitrate precursor with the $NH_4$-form of the zeolite forming an $NH_4NO_3$ intermediate, which can quickly decompose to gaseous product [31].

On carbon-based supports, dispersion of high metal loading could be achieved through doping with certain functionalities that can enhance the stabilization of dispersed metal atoms. Nitrogen binding sites on graphene created by high-temperature nitrogen doping and reduction of graphene oxide facilitated the dispersion of 1.7 wt % Ru [3]. High loading of Pt up to 5 wt % atomically dispersed on S-doped zeolite-templated carbon (ZTC) via a simple wet-impregnation technique was stabilized by the abundant S-functionalities and flexibility-induced local geometrical optimization of the carbon framework [41]. A $Na_2CO_3$ salt-assisted method was also used to disperse and stabilize isolated Pt atoms up to 5.3 wt

% on a nitrogen-doped graphene [42]. Also, a reduced graphene aerogel, by its high surface area and high electron donor character, stabilizes and disperses a remarkably high loading of 14.8 wt % of isolated Ir species [30].

### 1.1.3 Ensuring uniformity of single atom catalysts

SACs share the benefits of homogeneous catalysts whose atoms are isolated and readily accessible to reactant species while acting as the active sites [15]. This bridging between heterogeneous and homogeneous catalysis SACs has been proven by their application in traditional homogeneous catalysis such as Rh/ZnO and CoO-nanosheet-supported Rh SAC for the hydroformylation of olefin [43, 44] $Pt/Al_2O_3$ SAC for hydrosilylation [45], Fe-N-C SACs for selective oxidation of C–H bonds in water [46], Pt atomically dispersed on alpha-molybdenum carbide for low-temperature hydrogen production from methanol and water [47], leading to heterogenization of homogeneous catalysts [15]. As heterogeneous catalysts, their improved catalytic performance over nanoparticle-based catalysts owes its credit to the resulting electronic structure and unsaturated coordination environments of their isolated active sites [14, 48]. Despite all of these and moving forward on understanding the exact structures and active sites of SACs, the actual uniformity of SACs is being questioned.

While active sites of homogeneous and heterogeneous catalysts are considered 'uniform' and 'non-uniform' respectively, the active sites of SACs have been described as 'relatively uniform' [15]. This implies that in the true sense of it, despite their excellent catalytic performance, most SACs are not perfectly uniform and are therefore structurally non-uniform [49, 50]. However, several experimental and theoretical studies have shown the importance of their structures to their chemical properties and applications. Their local electronic structure and coordination environment can dictate their charge state and all of these define the degree of adsorption of reactants which consequently dictates the catalytic performance

[51, 52, 50, 53, 54]. In addition, the lack of information on the uniformity of SAs obscures the understanding of their catalytic properties through a limited mapping of exact structure-property relationships [55, 56]. Detailed structural determination including the incisive characterization of metal-support bonds and the location of the isolated species requires that the isolated metal atoms are uniform like in a molecular structure [57]. Of equal importance, uniformity of the supported species facilitates the precise determination of their structures under ambient conditions and during catalysis [52, 58], which can eventually improve catalytic selectivity [50]. Thus, controlled synthesis of structures of SACs active sites and exploration of their uniformity are of high significance and have therefore been suggested as one of the moving-forward ways in the field of metal-oxide supported SACs [51, 58]. To this effect, several research groups [48, 52, 56, 49, 50, 58, 59] have been focusing on, as an extension of their previous works [60], exploring the uniformity of SACs most especially on metal-oxides with respect to their synthesis and characterization of their unique features.

Most reported SACs in the literature had been described as structurally non-uniform with metal atoms occupying various coordination environments [56], a key reason for the mismatch between DFT models and experimental findings. To a large degree of consensus, the real cause has been attributed to the heterogeneous nature of supports concerning the distribution of surface sites. Expectedly, atomically dispersed metals on the sites result in different structures and geometry causing their nonuniformity. Consequently, the degree of uniformity of SACs highly relies on the choice of supports utilized in anchoring them. It is generally known that well-made zeolites have uniform surface and adsorption sites that are structurally equivalent and therefore easily generate uniform SACs [57, 61, 62]. However, for metal-oxide supports which are intrinsically less uniform and most of which anchor metal atoms by their defects, many of the reported SACs supported on them are nonuniform due to their inherent surface heterogeneity. Yet, some uniform metal-oxide supported SACs afforded through synthetic and population-based strategies have recently been reported.

Creating a well-defined metal-oxide surface is one way to generate the surface uniformity required of uniform SACs. In a combination of surface science and DFT studies, Pt has been atomically and uniformly dispersed on a well-defined $Cu_2O(111)$ [55]. Additionally, improving support crystallinity is a strategy that can ensure homogeneity of surface sites of the support for uniformity of SAs. As depicted, high temperature pretreatment of MgO at 1273 K increases its crystallinity, facilitating the formation of uniform surface bonding sites for Ir/MgO SACs [49]. Using a low metal loading through some synthetic synthesis approaches is another strategy that has been used to ensure uniformity. Since supports' surfaces are inherently heterogenous, the effect of such heterogeneity on catalysts' uniformity can be managed by populating only the most thermodynamically favorable binding sites which could be achieved by using low loading. Unlike MgO particles that anchor atomically dispersed Ir at various sites by two or three surface O atoms, the uniform Ir/MgO SACs [49] achieved by the 1273 K calcined support that preferentially anchors Ir at edges and corners by three surface O atoms could only be performed at a low loading of 0.01 % [59]. A synthetic approach involving strong electrostatic adsorption (SEA) promotes uniformity of the local coordination environment of isolated Pt species on a support such as $CeO_2$ and $TiO_2$ at loading not higher than 0.05wt % [48, 52, 56].

### 1.1.4 Control of activity of single atom catalyst

Earlier studies reported the activity of the SACs for various applications with more focus on SACs' superiority over their nanoparticle-based counterparts. However, research attention is shifting towards improving the intrinsic chemical activity of SACs. The activity of SACs is dictated by the nature of their active sites which is determined partly by their structure and coordination. CO oxidation reactivity and behavior under reaction conditions of $Pt/TiO_2$ SACs were tuned by controlling the structures of the atomically dispersed catalysts [52]. The CO oxidation reaction on three structurally different Pt catalysts, i.e. $Pt^{2+}$, $Pt^{4+}$ and Pt on

steps and terraces, proceeds by the same Mars-van Krevelen reaction mechanism, however, the apparent activation energy for the reaction as well as the evolution of the oxidation state and local coordination of the Pt catalyst under CO oxidation reaction are different. The structures were controlled by subjecting Pt SAC synthesized by strong electrostatic adsorption to various environmental (pretreatment) conditions. Oxidation of the SACs at 300 oC leads to Pt species substituting in six-fold coordinated Ti ($Ti_{6c}$) with an oxidation state of 4+. Mild reduction leads to Pt species being pulled out of the Ti lattice with an oxidation state of 2+, while harsh reduction leads to the formation of mobile Pt species on the steps and terrace of $TiO_2$ with a close-to neutral oxidation state of 1+. Among all the three structurally different SACs, the structure with near neutral oxidation state exhibited two- to fivefold enhanced activity with respect to the other SACs depending on the temperature. Also, Jiang et al [63] showed that $Pd/CeO_2$ SACs synthesized by the atom trapping method with 800 oC calcination and incipient wet impregnation (IWI) method with 350 °C calcination are structurally different. These catalysts have the same oxidation state of Pd, but the atom-trapped system predominantly had coordination-unsaturated $Pd^{2+}$ cations. It was claimed that decreased Pd-O coordination (which corresponds to the higher Pd-O coordination of non-lattice oxygen) was caused by the cleavage of the Pd-O bonds in $Pd_1O_4$ under an oxygen environment at the high temperature of the atom trapping method. The cationic $Pd^{2+}$ with lower coordination concerning the lattice oxygen from the support enhances CO-Pd binding, which led to the 90 % CO oxidation conversion at 93 °C, a temperature much lower than the fully saturated coordination $Pd^{2+}$. However, the catalysts with the undercoordinated $Pd^{2+}$ showed a reduced activity after being subjected to CO reduction, which was claimed to be due to its transformation to probably small $PdO_x$ clusters, as suggested by the authors.

## 1.2 $Pd/CeO_2$ systems for emissions control applications

$Pd/CeO_2$ catalyst system is essential for energy production and environmental remediation [64, 65] applications, especially for CO and methane oxidation reactions. Different structures have proven to be active for both reactions [65, 66]. Ye et al. [66] controlled the quantitative ratio of exposed Pd atoms to interacted Pd atoms in a $Pd@CeO_2$ core-shell nanotube through the $CeO_2$ shells of various thicknesses. While internal atoms are functional as anchoring sites of nanoparticles on the support [67], it was shown that the exposed Pd atoms provided the sites for CO adsorption and reaction. In contrast, the interacted Pd atoms were critical to activating the interfacial lattice oxygen, thereby promoting oxygen adsorption. However, an optimal distribution of Pd species between the exposed and interacted ones was responsible for the enhanced catalytic performance of the core-shell nanotube for the CO oxidation [66]. Cargnello [68] reported the enhanced metal-support interactions of Pd in a core-shell structure deposited as single units on hydrophobic $Al_2O_3$ forming supramolecular catalysts. Although the IWI $Pd/CeO_2$ catalyst has more exposed Pd than the core-shell $Pd@CeO_2$ structure, the close contact of the Pd with the $CeO_2$ in the core-shell structure enables the maximized transformation of metallic Pd into PdOx, which was considered as the active site. The maximized metal-support interaction and the oxygen release capacity of ceria favored the sustained oxidation of catalysts during the catalytic reaction. The $Pd@CeO_2$ /hydrophobic-$Al_2O_3$ showed complete $CH_4$ conversion below 400 $^oC$ and demonstrated a $CH_4$ oxidation reaction rate that is 40 times and 200 times higher than the $Pd/CeO_2$ -IWI and $Pd/CeO_2$ /$Al_2O_3$ catalysts, respectively. The nature of active sites of the catalysts is similar to those of ceria-supported counterparts based on the similarity of the apparent activation energy. Still, the enhanced reactivity of the core-shell (supramolecular) catalyst was due to its increased number of active sites resulting from the maximized interaction. The strong interaction was also responsible for the high thermal stability of the supramolecular

catalysts up to 850 °C for 12 h. In addition, a DFT study [69] has indicated that the active sites for methane activation are located at the interface of the $Pd/CeO_2$ catalysts. It was shown that Pd atoms at the interface migrate from the cluster to assume higher oxygen coordination offered by the defect sites in the $CeO_2$ lattice, resulting in a $PdO_2$ octahedral unit that is very reactive for methane oxidation due to the over coordination. The partially embedded PdOx oxidized clusters with stabilized $Pd^{4+}$ states in the ceria lattice at the interface were responsible for the exceptionally high methane activation. Jiang et al. [63] showed that increased coordination-unsaturated $Pd^{2+}$ induced by increased oxygen vacancy was more active (90 % CO conversion at 93 °C) than the coordination-saturated $Pd^{2+}$, $Pd^{2+}$-derived $PdO_x$ cluster, Pd/PdO NPs and $Pd/CeO_2$ solid solution. This is because the cationic $Pd^{2+}$ that is saturation-uncoordinated concerning the lattice oxygen of ceria support enhances CO-Pd binding due to increased back donation of the electron, contributing to the enhanced oxidation reaction. It is also reported that the $Pd/CeO_2$ catalysts synthesized by the solution combustion method had three- or five-times higher reaction rates per gram of Pd and showed a complete CO conversion at 100 K lower than the wet incipient catalysts [70]. Both catalysts contain PdO particles that undergo dynamic and reversible PdO-Pd-PdO transformation during heating and cooling; however, the solution combustion catalysts had more portion of initial PdO that did not participate in the transformation. The superior activity of the solution combustion catalysts for methane oxidation was attributed to these stable Pd-O active sites that do not involve the transformation. Also, atomically dispersed Pd-O species stabilized as PdO and $PdO_2$ on ceria are highly active in low-temperature CO oxidation [71]. However, the atomically dispersed $PdO_2$ structure has a much stronger binding to the support.

Based on this review, it is evident that Pd species can be stabilized differently on the ceria surface, and the nature of their stabilization can influence both the stability and activity of the $Pd/CeO_2$ catalysts for both CO and methane oxidations reactions. Undercoordinated atomically dispersed Pd species are more active for the low-temperature CO oxidation re-

action than highly coordinated Pd species due to enhanced CO-Pd binding, but they lack stability under the reaction condition. However, over coordinated, highly cationic Pd atom at the interface of $PdO_x/CeO_2$ catalysts is very active for the methane oxidation reaction. To meet the more stringent environmental regulations and continue to lower the temperature at 50 % conversion ($T_{50}$) of methane should be less than 400 °C in lean exhaust conditions. During a cold start, further control of the Pd structure is needed to achieve a more active one for relevant emissions control reactions while minimizing the utilization of the precious metal. In several Pd structures, the enhanced metal support interaction has been identified as critical for enhanced methane activation. Atomically dispersed Pd can benefit the methane oxidation reaction due to the improved metal-support interaction. Because atomically dispersed metals are generally susceptible to sintering during synthesis and under reaction conditions due to their isolation nature, the atomically dispersed Pd should be additionally stable for the methane oxidation reaction. The challenge remains to find a suitable synthesis method that allows the synthesis of the atomically dispersed Pd to achieve such activity and stability.

## 1.3 Homogeneity of catalyst support particles

Much emphases have been placed on the importance of the particle size of supported metal species. The particle size of the support on which metal species are deposited can also dictate the activity of supported catalyst by influencing certain structural property such as the reducibility of the catalyst. It has been shown that smaller ceria nanoparticles exhibit higher oxygen storage, making them more active for ethanol oxidation reaction when Au is deposited on them [7]. The concentration of the oxygen vacancy can be enhanced by increasing the ceria crystal size [8] and the concentration of $Ce^{3+}$ and the lattice parameter of the ceria can also be influenced by the particle size [9]. The particle size can induce lattice

relaxation in the ceria nanoparticle. In fact, the physical effect of the ceria particle size on $Ce^{3+}$ concentration and lattice parameter of ceria can be stronger than the chemical effect of hydrogen reduction [72]. In several cases, the sizes of catalyst particles are usually not uniform. They are sometimes typically considered as unimodal distribution but they can be more complex. The distribution of the particle size can be skewed or even be bimodal. Having the ability to predict such complexity in the particle size distribution can be very beneficial in the design of high performing supported metal catalysts.

## 1.4 Flame spray pyrolysis as a viable synthesis method

The synthesis method of interest should be able to control the structures to allow the synthesis of atomically dispersed Pd. It should additionally ensure the stability of the synthesized atomically dispersed Pd. For stability, high-temperature synthesis methods are generally noted to enhance the stability of synthesized systems, partially evidenced by the ability of the atoms to survive high temperatures. They have demonstrated a promising approach for synthesizing atomically dispersed metal on a support. They perform a critical role in ensuring the stability of the atomically dispersed metals under extreme thermal environments and reaction conditions by specifically enabling bond breakage and bond formation using the associated high thermal energy, which is not obtainable via other synthesis methods. Flame spray pyrolysis (FSP) becomes a suitable synthesis method for $Pd/CeO_2$ as it satisfies the condition of high temperature that allows the stability of the synthesized system and is also supported by the high stability of flame synthesized materials. In addition, it is a fast synthesis process and does not require additional post-treatment of synthesized materials like the wet impregnation synthesis protocol. For the control of $Pd/CeO_2$ structures, special anchoring and defect sites such as peroxide and oxygen vacancy that can serve as trapping sites [73] can be created on support during the FSP synthesis. The nucleating species can

also be controlled in terms of size and speciation in the FSP process. All of these emphasize the possibility of controlling the $Pd/CeO_2$ structures for synthesizing atomically dispersed Pd using flame spray pyrolysis.

In addition to being able to control the environment, FSP has defined process steps that can be engineered to control nanomaterial properties. As the particle size can be controlled in the nucleation stage using the precursor concentration, the particles in the agglomeration stage can be quenched to control their sizes. The control of the particle size distribution can therefore be achieved by controlling the release rate of precursor during the synthesis. There is a lack of experimental techniques to monitor the release rate of precursor and it is hence determined by studying the droplets combustion where precursor release occur, using the modeling approach.

## 1.5 Aims and objectives

This research aims to control the speciation and homogeneity of supported metal catalysts.

Hence the objectives of this thesis are to

(1) control the structures of the Pd on ceria support to synthesize atomically dispersed Pd using the FSP approach.

(2) compare the activities of atomically dispersed Pd with other structures for the methane oxidation reaction.

(3) evaluate the combustion of precursor droplets through physics-based modeling to understand and control the homogeneity of the nanomaterial in FSP.

As a proof of concept, an outlook on the application of machine learning in flame spray

pyrolysis for material discovery is also developed.

## 1.6 Outline of the thesis

This thesis begins with a general introduction as Chapter 1 (this chapter).

Chapter 2 discusses the control of Pd structures and compares their activities for the methane oxidation reaction.

Chapter 3 discusses using operando DRIFTS experiments to evaluate low-temperature methane oxidation reaction over atomically dispersed Pd to elucidate the essential steps and determine the kinetic parameters.

Chapter 4 introduces the development of a novel model-based methodology to predict the homogeneity of flame synthesized catalyst, using single droplet combustion modelling.

Chapter 5 discusses the extension of the model to be more robust by relaxing the assumptions and the quantification of precursor release for its application to rationalize FSP-synthesized materials.

Chapter 6 provides an outlook on machine learning applications to guide nanomaterial synthesis in flame spray pyrolysis.

The details in the main chapters are documented in the appendices. Appendix A provides the supplementary information for the control of the speciation of Pd in chapter 2. Appendix B discusses the design and optimization of the reactor system employed for catalytic performance evaluation. Appendix C provides detailed MATLAB source code for the single droplet combustion modelling. Appendix D details the python code developed on the outlook of the application of machine learning in FSP. Appendix C details the MATLAB code

developed for solving the equations in the single droplet combustion model.

# Chapter 2

# Control of Pd Species on $CeO_2$ using Flame Spray Pyrolysis

## 2.1 Introduction

$Pd/CeO_2$ is an essential catalyst for emissions control application, and several structures of Pd have been investigated for these reactions. For the benefits of enhancing the activity of the precious metal while minimizing its utilization, atomically dispersed Pd can be considered for relevant reactions in the emissions control industry.

Ye et al [66] controlled the quantitative ratio of exposed Pd atoms to interacted Pd atoms in a $Pd@CeO_2$ core-shell nanotube through the $CeO_2$ shells of various thicknesses. While internal atoms are functional as anchoring sites of nanoparticles on the support [67], it was shown that the exposed Pd atoms provided the sites for CO adsorption and reaction while the interacted Pd atoms were critical to activating the interfacial lattice oxygen, thereby promoting the adsorption oxygen. However, an optimal distribution of Pd species between the exposed and interacted ones was responsible for the enhanced catalytic performance of

the core-shell nanotube for CO oxidation [66]. Cargnello [68] reported the enhanced metal-support interactions of Pd in a core-shell structure deposited as single units on hydrophobic $Al_2O_3$ forming supramolecular catalysts. Although the IWI $Pd/CeO_2$ catalyst has more exposed Pd than the core-shell $Pd@CeO_2$ structure, the close contact of the Pd with the ceria in the core shell structure enables the maximized transformation of metallic Pd into $PdO_x$ which was considered as the active site. The maximized metal-support interaction and the oxygen release capacity of $CeO_2$ favored the sustained oxidation of catalysts during the catalytic reaction. The $Pd@CeO_2$ /hydrophobic-$Al_2O_3$ showed complete $CH_4$ conversion below 400 °C and demonstrated a $CH_4$ oxidation reaction rate that is 40 times and 200 times higher than the $Pd/CeO_2$ -IWI and $Pd/CeO_2$ /$Al_2O_3$ catalysts, respectively. The nature of active sites of the catalysts are similar to those of $CeO_2$-supported counterparts based on the similarity of the apparent activation energy, but the enhanced reactivity of the core-shell (supramolecular) catalyst was due to its increased number of active sites resulting from the maximized interaction. The strong interaction was also responsible for the high thermal stability of the supramolecular catalysts up to 850 °C for 12 hours. In addition to Cargnello's work, some DFT studies have demonstrated that the active Pd at the interface of a partially embedded PdOx on ceria has shown exceptionally high methane activation. However, instead of this, the metal support interaction can be enhanced further by considering atomically dispersed Pd in which the atoms are just interacting with the ceria support to enhance of methane oxidation activity. The ability to control these structures and sizes – either in combination or isolation – can allow direct assessment and comparison concerning atomically dispersed Pd for emissions control applications.

FSP is a high temperature synthesis method that can control structures and enhance stability. It is a very fast and highly scalable process with little or no need for post synthesis treatment. During FSP synthesis of supported catalysts, the support is thermodynamically nucleated first due to its high concentration while the metals or metal oxide can nucleate on the support in the form of clusters or isolated species depending on concentration and

synthesis conditions. Special anchoring and defect sites such as peroxide and oxygen vacancy that can serve as trapping sites [73] can also be created on support during the FSP synthesis. The high combustion temperature during the synthesis provides sufficient thermal energy to disperse the metals, placing their atoms onto the most stable sites on the support [74], at which the binding energy of the dispersed atoms is the highest [75]. At the same time, the fast quenching prevents the recombination and vaporization of the dispersed atoms and the heterogeneously nucleated isolated atoms, ensuring the maintenance of the dispersed metals on the support during synthesis.

Here, we synthesized different Pd structures, including atomically dispersed Pd, by controlling the chemical environment of the flame synthesis technique. This was achieved by controlling the equivalence ratio, which dictates the solvent combustion gas products, in which the equivalence ratio greater than one represent oxidizing environment and less than one represent the reducing environment. Due to its relevance to emission controls especially in natural gas vehicles, the methane oxidation reaction is employed as a probe reaction to investigate and compare the activity of these structures. Considering these catalysts for practical methane oxidation reaction application, the lean condition at 5000 ppm of methane has been adopted for the methane oxidation reaction. The DRIFTS is adopted for detailed characterization of the catalysts.

## 2.2 Materials and Methods

### 2.2.1 Synthesis of catalysts

Flame synthesis of catalysts was carried out with a custom-built flame spray pyrolysis set-up (shown in figure 2.1) that was made up of a McKenna Burner (Holthius and Associates); air-assisted external mixing nozzle (Schlick Atomizing technologies, Germany); a flow system

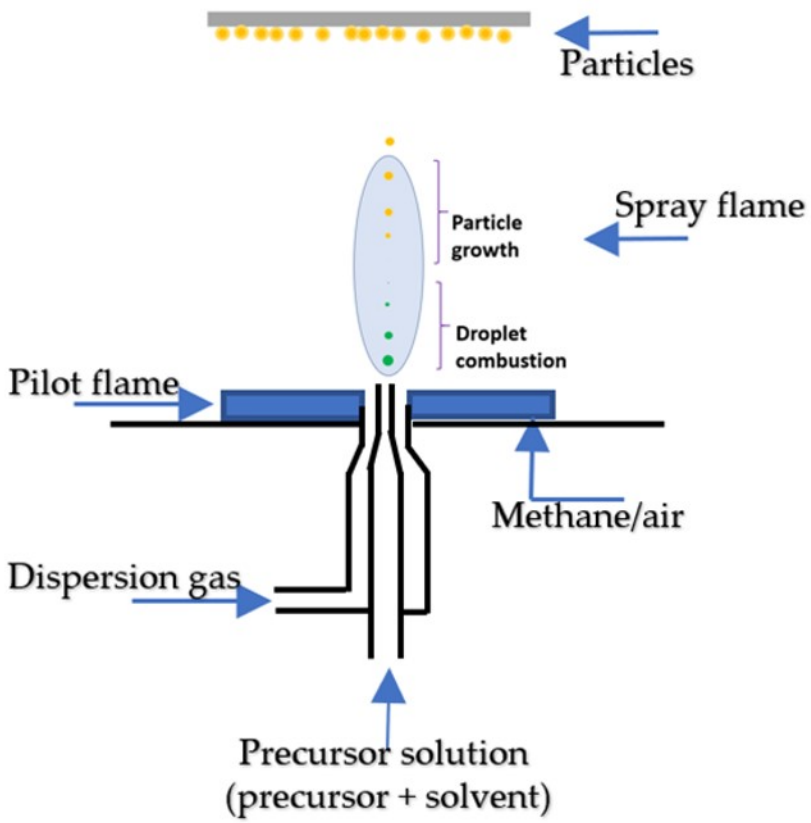


Figure 2.1: Flame Spray Pyrolysis set-up

consisting of mass flow controllers (Brooks), power supply controller box and rotameter (Cole Parmer); and a filter paper particle collection system. Precursor solutions were made from ceria precursors such as cerium acetylacetonate and cerium 2-ethylhexanoate (Alfa Aesar, 49 percent in 2-ethylhexanoic acid) and palladium acetylacetonate (Sigma Aldrich) in a mixture of solvents. Solvents considered include ethyl hexanoic acid (EHA), toluene, acetonitrile, acetic acid and 1-butanol. Following preparation, precursor solution was injected into the flame environment through a nozzle tip of 0.5 mm at a predetermined pressure drop and flow rate ranging from 2-3 ml/min using a syringe pump (NE-4000, New Era Pump Systems Inc). The atomized precursor spray was consequently ignited by a stable and temperature-uniform premixed pilot flame made from 1 L/min of methane and 10 L/min of air. Ensuing particles from the flame were deposited on a filter paper (Whatman GF/D 257mm glass microfiber filters) mounted in a water-cooled particle collection system and consequently

removed through scraping after synthesis. The flame equivalence ratio of the spray flame has been adjusted between 0.8 and 1.5 by controlling the flow rates of the liquid precursor and the oxygen dispersion gases using the equation 2.1

$$Equiv.ratio(ER) = \frac{\left(\frac{F}{O}\right)_{actual}}{\left(\frac{F}{O}\right)_{stoichiometry}} \tag{2.1}$$

where F is the flow rate of the fuel which is the solvent mixture of EHA and toluene and O is the flow rate of the oxygen dispersion gas.

### 2.2.2 Characterization

The freshly synthesized catalysts were characterized for the catalyst oxidation states, phase information, and catalyst activity. X-ray diffraction (XRD) of the samples was carried out on a Rigaku SmartLab X-ray Diffractometer that has a 2.2 KW Cu-K $\alpha$ X-ray source. Measurements were taken with scanning between 20 to 80 deg $2\theta$ with a scan speed of 2 deg/min.

The total elemental concentration of Pd metal in the $Pd/CeO_2$ catalysts was measured by Atomic Absorption Spectroscopy (AAS) using the PerkinElmer A Analyst 400 spectrometer. Prior to this, the samples were digested in aqua regia (3:1 of HCl to $HNO_3$ ). X-ray Photoelectron Spectroscopy (XPS) experiments were conducted using a Kratos AXIS Ultra DLD XPS system equipped with a hemispherical energy analyzer and a monochromatic Al K$\alpha$ source operating at 15 keV and 150 W. Before analysis, samples were exposed to vacuum to remove physisorbed species.

Xray Absorption spectroscopy (XAS) experiments were conducted at the 10-BM beamline of the Advanced Photon Source (APS), Argonne National Laboratory. Pd K edge measurements were carried out in the fluorescence yield mode using the four-element Vortex detector

for all synthesized samples while the data for PdO was collected in transmission mode. Pd metal foil was used as reference during experiment and the reference of PdO data was used as a standard for alignment of all data to a common energy axis during data processing. All data processing was carried out in Athena and Artemis software.

Diffuse reflectance infrared Fourier transform spectroscopy (DRIFTS) experiments were conducted in Harrick praying mantis equipment coupled with an Invenio R Bruker spectrometer equipped with a multi-detector unit containing liquid nitrogen mercury cadmium telluride (LNMCT) and RT-DLaTGS detectors. The sample holder is enriched in the sample compartment which has a KBr window for transmission of IR light to and from the sample. The LNMCT detector was specifically used for experiments, and it was usually cooled with liquid nitrogen before the start of any experiment. The optics of the spectrometer, as well as the sample compartment of the Harrick praying mantis equipment, are purged with $N_2$ gas at 3 L/min and 1 L/min respectively, to reduce the atmospheric $CO_2$ and water vapor in the two compartments. For all the in-situ CO adsorption DRIFTS experiments, 10 ccm of total gas flow containing (0.1 percent) 1000 ppm CO: $N_2$ was flown over the samples in the DRIFTS cell. Before any measurements, the DRIFTS cell was loaded with samples, purged with dry $N_2$ for 30 min at 200 $^{o}$C to remove any physisorbed species on the samples. Spectra were recorded initially every 1 min for the first 10 min followed by every 5 min until a total experimental time of 30 min was reached. Measurements were taken with 64 scans for both sample and background at 4 $cm^{-1}$ resolution. The sample temperature was adjusted by using the WATLOW temperature controller on the Harrick heater connected to the sample holder in the DRIFTS cell. Temperature is maintained for at least 15 mins to ensure a steady state is reached before the start of spectra measurement at that temperature. All measurements and data analysis were conducted using the OPUS software version 8.5 designed for the spectrometer.

### 2.2.3 Methane oxidation light-off activity

The activity test was performed in a fixed-bed reactor housed in a furnace, with the catalysts placed in between quartz wool inside the reactor. Gases were injected through the reactor via mass flow controllers and the effluent gases were analyzed by a gas chromatograph (GC) equipped with both a thermal conductivity detector (TCD) and flame ionization detector (FID). Methane oxidation reactions were carried out between room temperature and 800 $^{o}$C at the gas hourly space velocity (GHSV) of 48,000 ml/g/h using inlet gas feed containing 0.5% $CH_4$, 4% $O_2$ and $N_2$ as balance. Prior to reactor temperature ramping, gases were passed over catalysts bed for 1 hr to ensure steady flow over catalysts bed.

## 2.3 Result

### 2.3.1 Catalyst characterization using XRD, XPS and STEM

The ER 0.8 condition containing 20 % of $O_2$ with $CO_2$ and $H_2O$ and the ER 0.98 1.0 condition also containing some $O_2$ constitute the oxidizing environment conditions while the ER 1.2 and 1.5 not containing $O_2$ make up the reducing environment synthesis conditions (detailed combustion gas compositions at all the synthesis conditions are shown in figure A.1). The XRD patterns of the 1 wt.% $Pd/CeO_2$ synthesized at both oxidizing and reducing environment conditions exhibit only the crystallographic planes of fluorite cubic structure of $CeO_2$ with crystallite size ranging from 9-13 nm (figure 2.2). The lattice constant of the ceria support remains at 0.542 nm [76], with neither lattice expansion nor contraction of the ceria support at both synthesis conditions class. ICPMS confirms the presence of Pd indicating that Pd is not lost during the synthesis at all the synthesis conditions, and also suggesting that the absence of crystallographic planes of Pd can be attributed to high

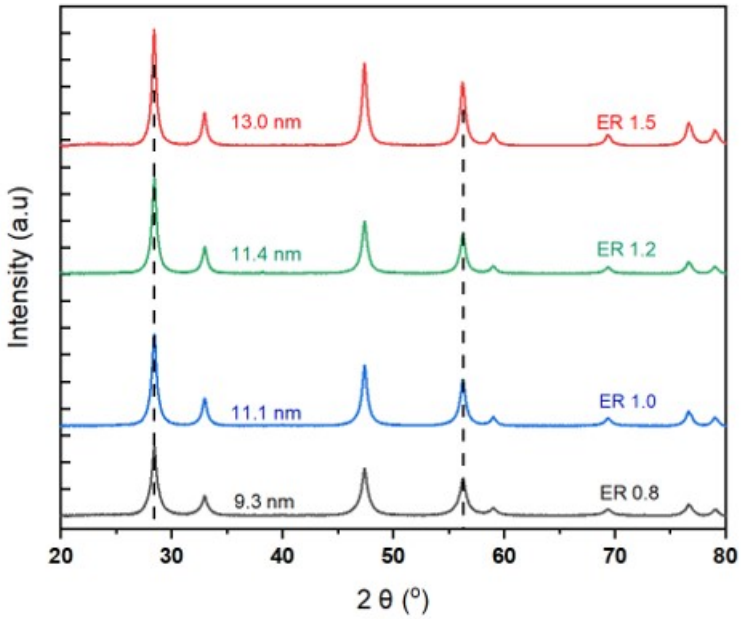


Figure 2.2: XRD patterns of 1 wt% $Pd/CeO_2$ synthesized at different conditions

Pd dispersion at both reducing and oxidizing environment conditions. Pd 3d core-level XP spectra confirm the high dispersion , shown in Figure 1b, as the same binding energy at 338 eV of the Pd 3d core-level electrons of catalysts synthesized at both reducing and oxidizing environment conditions can be attributed to highly dispersed $Pd^{2+}$ and Pd-O-Ce species [77, 78, 79, 80]; no Pd metal phase at 335 eV or large cluster PdO at 336.5eV are formed. The high binding energy of Pd 3d core-level electrons also suggests strong Pd interaction with the $CeO_2$ support.

The STEM images of the $Pd/CeO_2$ catalyst synthesized at reducing environment show only lattice fringes of $CeO_2$ on the 1 wt.% $Pd/CeO_2$ and 0.25 wt.% $Pd/CeO_2$ samples, and Pd is not observed due to the similar Z-contrast for Pd and Ce [13]. The $CeO_2$ support has a predominant exposure of 110 and 111 surfaces. The $CeO_2$ support has a particle size of about 10 nm, consistent with the calculated crystallite size from XRD. However, the EDX data indicates some clusters of Pd species while the EDX is not very sensitive in assigning atomically dispersed Pd in the image h in figure 2.4.

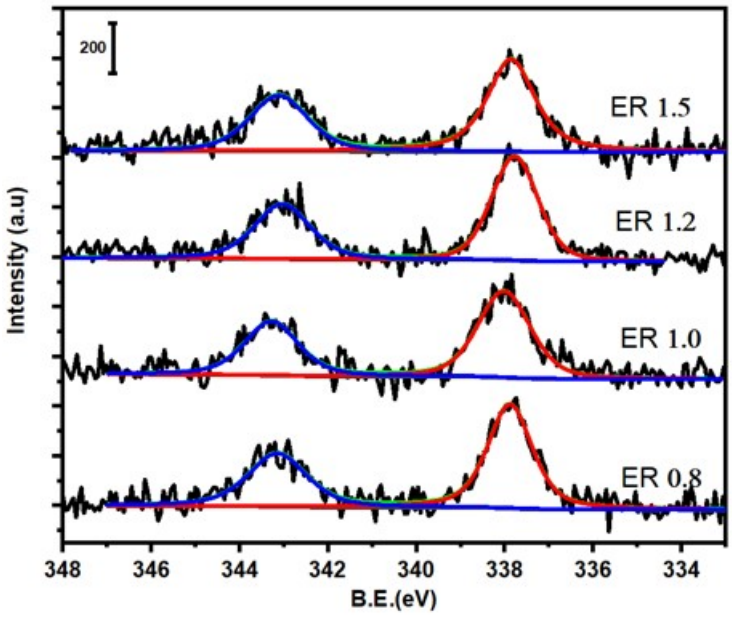


Figure 2.3: XPS of 1 wt% $Pd/CeO_2$ synthesized at different conditions

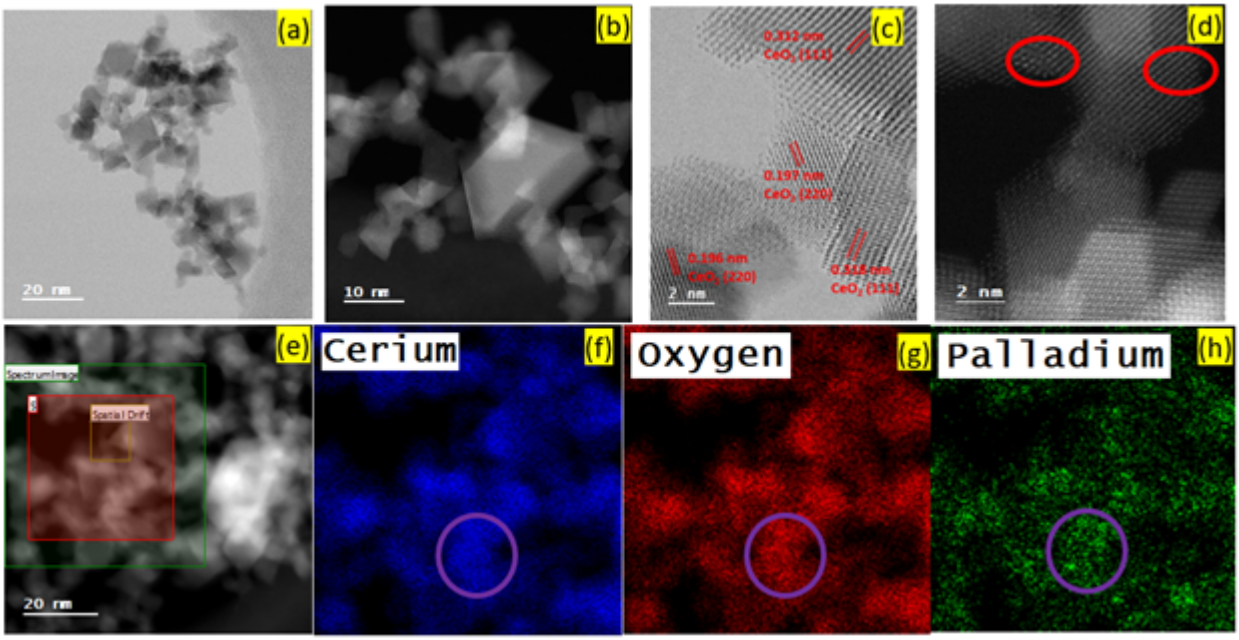


Figure 2.4: STEM images and EDS images 1 wt.% $Pd/CeO_2$ catalyst synthesized at ER 1.5 Comparing areas of purple circles across Ce, O and Pd, EDS shows the less dispersed bright dots of Pd

### 2.3.2 Methane oxidation activity

Methane oxidation reaction in a fixed bed reactor is used to investigate the activity of the catalysts synthesized at both oxidizing and reducing conditions. The performance evaluation was carried out in a reactor with no micro channeling (as described in B.3.2), with enhanced residence time (as described in B.3.3) and optimized gas hourly space velocity (as described in B.3.4). As shown in figure 2.5, 1 wt.% $Pd/CeO_2$ catalysts synthesized at all the synthesis conditions are active evidenced by the increasing exponential growth of the conversion with temperature in consistence with the Arrhenius relation. However, the 1 wt.% catalyst synthesized in an oxidizing environment consistently demonstrates a higher methane conversion at all temperatures, exhibiting $T_{50\%}$ of 381 °C which is about 100 °C lower than the $T_{50\%}$ of 1 wt.% catalyst synthesized in a reducing environment. They also demonstrate a higher exponential growth rate of the light off curve than the catalysts synthesized at the reducing environment, indicating that they contain a more active site for methane oxidation reaction or an additional site that is more active than the sites on the reducing environment catalysts. To further understand the more exceptionally active site for the methane oxidation reaction, 0.5 and 0.25 wt.% $Pd/CeO_2$ catalysts were synthesized in the oxidizing environment, and their rates of methane oxidative conversion per gram of Pd are compared with the 1 wt.% Pd catalyst synthesized in the oxidizing environment condition, as shown in figure 2.6. The 0.5 wt.% has similar active sites as the 1 wt.% catalyst due to the similar exponential growth rate, but has an increased number of the more active site due to its higher methane conversion rate. However, the higher exponential growth rate of the 0.25 wt.% sample compared to that of the 0.5 and 1 wt.% samples indicates that the 0.25 wt.% exclusively contains the more active sites which are also more in number compared to the 0.5 and 1 wt.% samples due to its higher methane conversion rate. This implies an increased dispersion as with decreasing loading which is consistent with the reducing particle size of Pd species observed in XRD patterns at different loading a s shown in figure A.2. To further

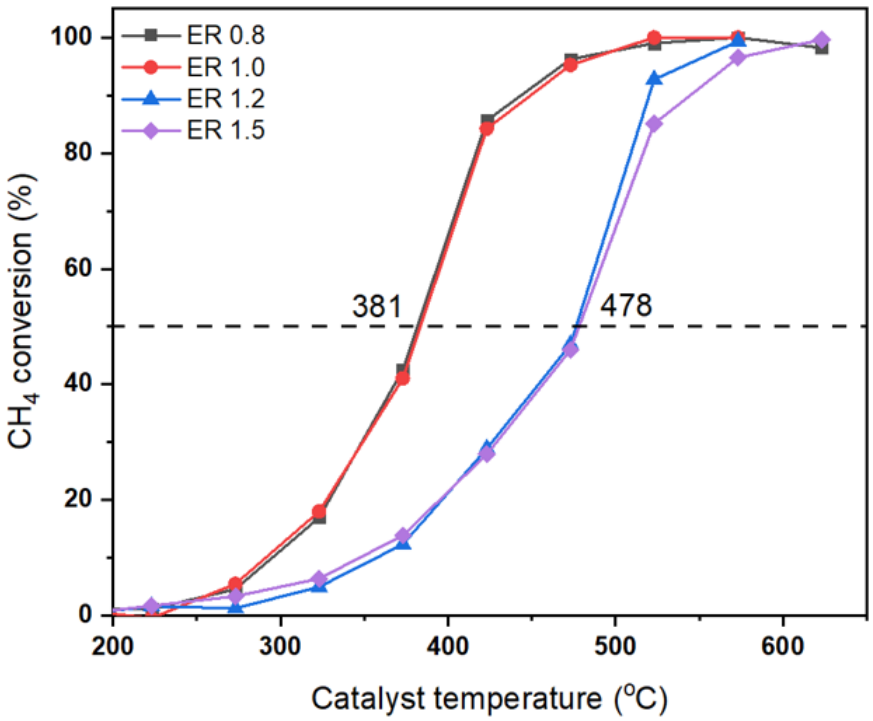


Figure 2.5: Methane oxidation activity over 1 wt% $Pd/CeO_2$ synthesized at 0.8, 1.0, 1.2 and 1.5 equivalence ratio

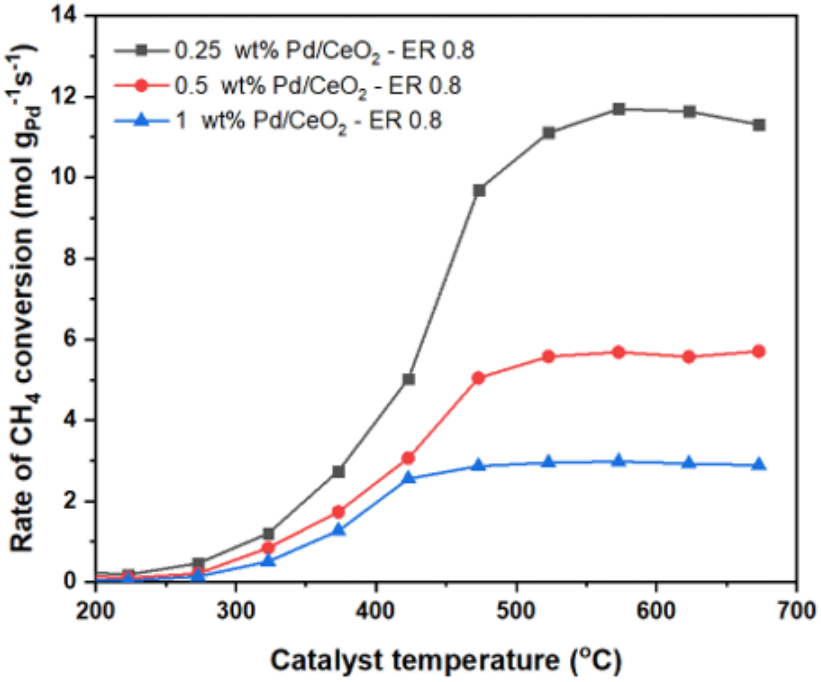


Figure 2.6: Rate of methane oxidation conversion obtained at different loading of $Pd/CeO_2$ catalysts

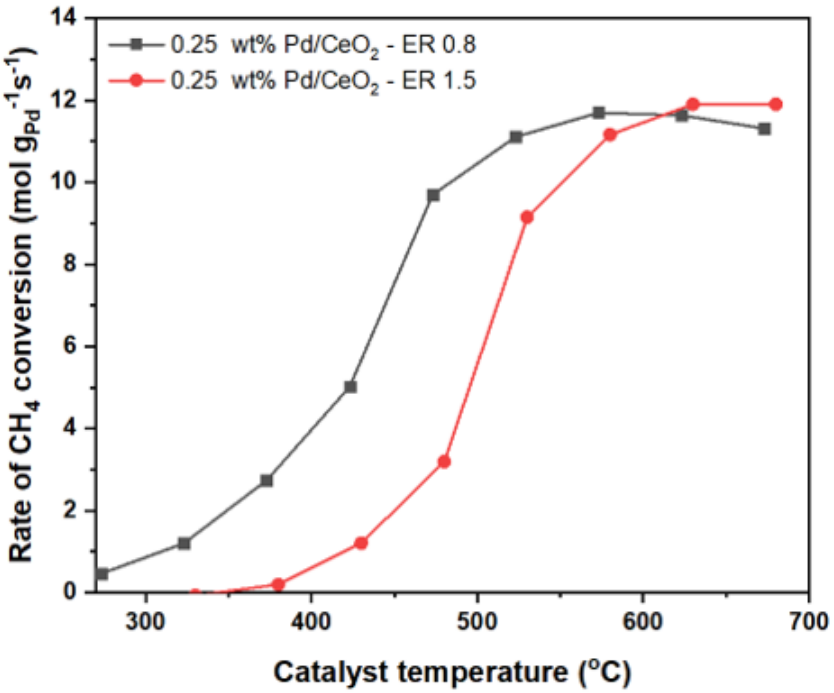


Figure 2.7: Rate of methane oxidation activity over 0.25 wt% $Pd/CeO_2$ catalysts synthesized at equivalence ratios of 0.8 and 1.5

understand the active site at the reducing environment, a 0.25 wt.% sample is synthesized at the reducing environment and compared with the 0.25 wt.% sample synthesized at the oxidizing environment, as shown in figure 2.7. The similarity of the exponential growth in the rate of methane conversion of the 0.25 wt.% catalyst synthesized in both oxidizing and reducing environments indicates they share the more active sites but the 0.25 wt.% catalyst synthesized in the reducing environment has some additional sites that are less active due to the lower methane oxidation rates at all temperatures. It summarizes that the reducing environment exclusively creates a less active site on the 1 wt.% sample but in combination with a more active site at 0.25 wt.% loading. On the other hand, the more active site is created exclusively on a 0.25 wt.% sample while in combination with the less active sites at 1 wt.% loading. We hypothesize that the differences in the nature of the active sites are due to the differences in the structures of the Pd species created on $CeO_2$ at both synthesis conditions as well as the behaviors of these structures.

### 2.3.3 Identification of the Pd species structures

Pd structures synthesized in both reducing and oxidizing environments are investigated through extensive CO adsorption experiments under DRIFTS. For 1 wt.% $Pd/CeO_2$ samples synthesized in a reducing environment, three Pd structures are observed on $Pd/CeO_2$ as shown in figure 2.8. Highly dispersed $Pd^{n+}$ and $Pd^0$ due to linearly adsorbed CO at 2110 $cm^{-1}$ and 2090 $cm^{-1}$ respectively are observed while $Pd^0$ clusters are also observed due to linearly adsorbed CO at 2049 $cm^{-1}$ and the bridge sites between 1800 -2000 $cm^{-1}$. The highly dispersed $Pd^{n+}$ initially adsorbs CO faster than the other structures within the first 20 mins. However, CO adsorption becomes more dominant on the highly dispersed $Pd^0$ after 20 mins due to the increasing intensity and full width at half maximum (FWHM) of its band. In both adsorption regimes, adsorption continues growing on the bridge sites. At 60 mins, CO adsorption on all the structures reaches equilibrium as indicated by the same intensity and FWHM of the peaks on two other spectra taken every 5 mins afterward. Similar to the ER 1.5 catalyst, the same highly dispersed $Pd^{n+}$, $Pd^0$, and $Pd^0$ clusters at the same vibrational frequencies are also observed on the ER 0.8 catalyst (figure 2.9). The structures also demonstrate similar dynamic behaviors in terms of initial fast adsorption on highly dispersed $Pd^{n+}$ and predominant adsorption peak is observed on the highly dispersed $Pd^0$ at a later stage. However, an additional peak at 2134 $cm^{-1}$ constitutes Pd species assigned to atomically dispersed $Pd^{2+}$ [63, 36]. The observed peak at 2166 $cm^{-1}$ is the CO gas-phase peak since the linearly adsorbed CO peak cannot be greater than 2150 $cm^{-1}$. However, the 2134 $cm^{-1}$ is between the R-branch and the Q-branch of the CO gas-phase peak at 2115 $cm^{-1}$ (as shown in figure A.3), causing the increased intensity over the R-branch peak. The partial overlapping of the 2134 $cm^{-1}$ peak with the 2115 $cm^{-1}$ peak of the CO gas-phase causes the increased intensity observed on the first CO gas phase peak.

Pd structure on the low loading catalyst is also investigated to further understand the structures created by both reducing synthesis and oxidizing conditions, as shown in figures 2.14

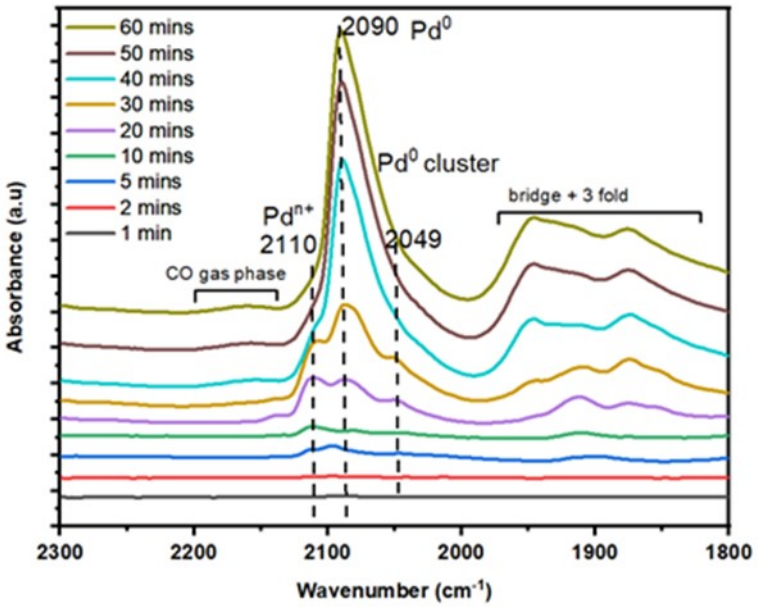


Figure 2.8: Room temperature CO adsorption DRIFTS on ER 1.5 1 wt% $Pd/CeO_2$

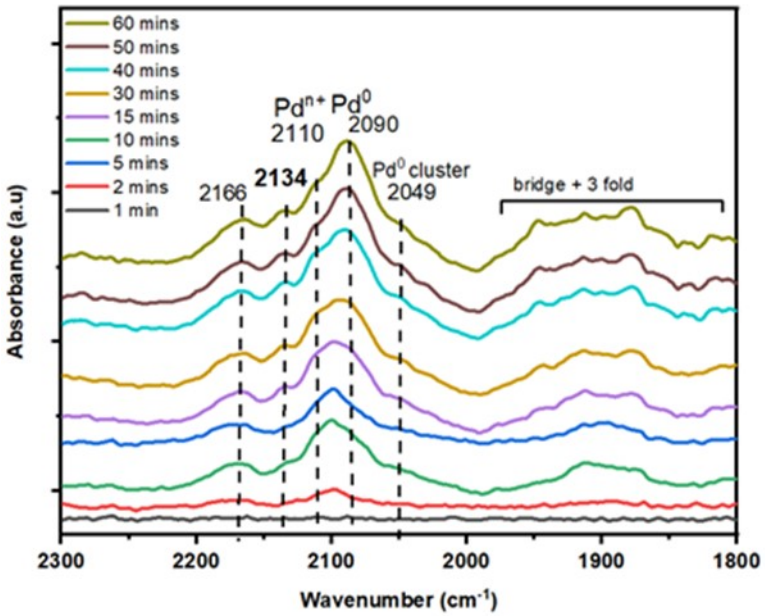


Figure 2.9: Room temperature CO adsorption DRIFTS on ER 0.8 1 wt% $Pd/CeO_2$

and 2.15, respectively. The 0.25 wt.% $Pd/CeO_2$ catalyst synthesized at the reducing environment contains highly dispersed highly dispersed $Pd^{n+}$, $Pd^0$, and $Pd^0$ and atomically dispersed $Pd^{2+}$ is additionally observed at 2134 $cm^{-1}$ similar to the species on the structures contained in the 1 wt.% $Pd/CeO_2$ synthesized in the oxidizing environment. However, linearly adsorbed CO is observed at 2134 $cm^{-1}$ for atomically dispersed $Pd^{2+}$ without any bridge site and signatures of linearly adsorbed CO below 2100 $cm^{-1}$ indicating only the presence of atomically dispersed Pd on the oxidizing environment for 0.25 wt%.is created by the oxidizing environment for 0.25 wt.% $Pd/CeO_2$ .

### 2.3.4 Analogy for the stabilization of different Pd structures

An analogy for the formation of different Pd structures on $CeO_2$ in the flame can be generated. The $CeO_2$ synthesized by FSP generally have trapping sites such as oxygen vacancy and peroxides which can be used to anchor Pd species [73]. When $Pd(acac)_2$ and CeEH in dissolved EHA and toluene solvents are injected into the flame, the vapors of the precursors undergo reactions including thermal decomposition and direct oxidation, according to the reactions below. The cerium ethyl hexanoate undergoes thermal decomposition into $CeO_2$ between 400 °C and 500 °C [81] while the $Pd(acac)_2$ can undergo gaseous decomposition to Pd between 180 to 305 °C [82] either in the inert environment or oxidizing environment. The oxidizing environment can further oxidize the Pd to oxidized Pd species while the PdO can decompose back to Pd at a temperature greater than 900 °C. Hence, metallic Pd and PdO are available for nucleation in the oxidizing environment while the Pd is availbale in the reducing environment.

$CeEH \rightarrow CeO_2, CO_2, H_2O$

$Pd(acac)_2 \rightarrow Pd, L \rightarrow Pd, CO_2, H_2O$

$2Pd + O_2 \rightarrow 2PdO$

$PdO \rightarrow Pd$

The thermal decomposition temperatures of the two precursors are close to each other when the flame temperature of 2500 °C is considered. However, the $CeO_2$ support is thermodynamically nucleated first due to its high concentration [83], prior to Pd. The Pd species can exist as a metal or metal oxide nucleating on the $CeO_2$ support in form of clusters or isolated species, depending on the synthesis conditions and loading. At reducing environment, the high Pd vapor concentration at high loading such as 1 wt % facilitates the formation of clusters by homogeneous nucleation, which can be of various sizes. These different sizes of Pd clusters can then nucleate heterogeneously on the support. At low loading, the low Pd vapor concentration thermodynamically limit the homogeneous nucleation resulting in coexistence of isolated of Pd species and clusters of different sizes, which both nucleate on the $CeO_2$ support forming the atomically dispersed Pd and Pd clusters. At extremely low concentration, isolated species are expected to be dominant resulting only atomically dispersed Pd after nucleation. However, at oxidizing environment, some of the Pd vapors can be oxidized depending on the available oxygen in the system while the remaining Pd vapors can form clusters or combination of clusters and isolated species. The vaporize cluster sizes can nucleate similar to the reducing environment while the oxidized Pd species preferentially nucleate heterogeneously on ceria to form the atomically dispersed Pd. At low loading, all the Pd vapor can be oxidized for formation of oxidized species, leading to the exclusive formation of atomically dispersed Pd.

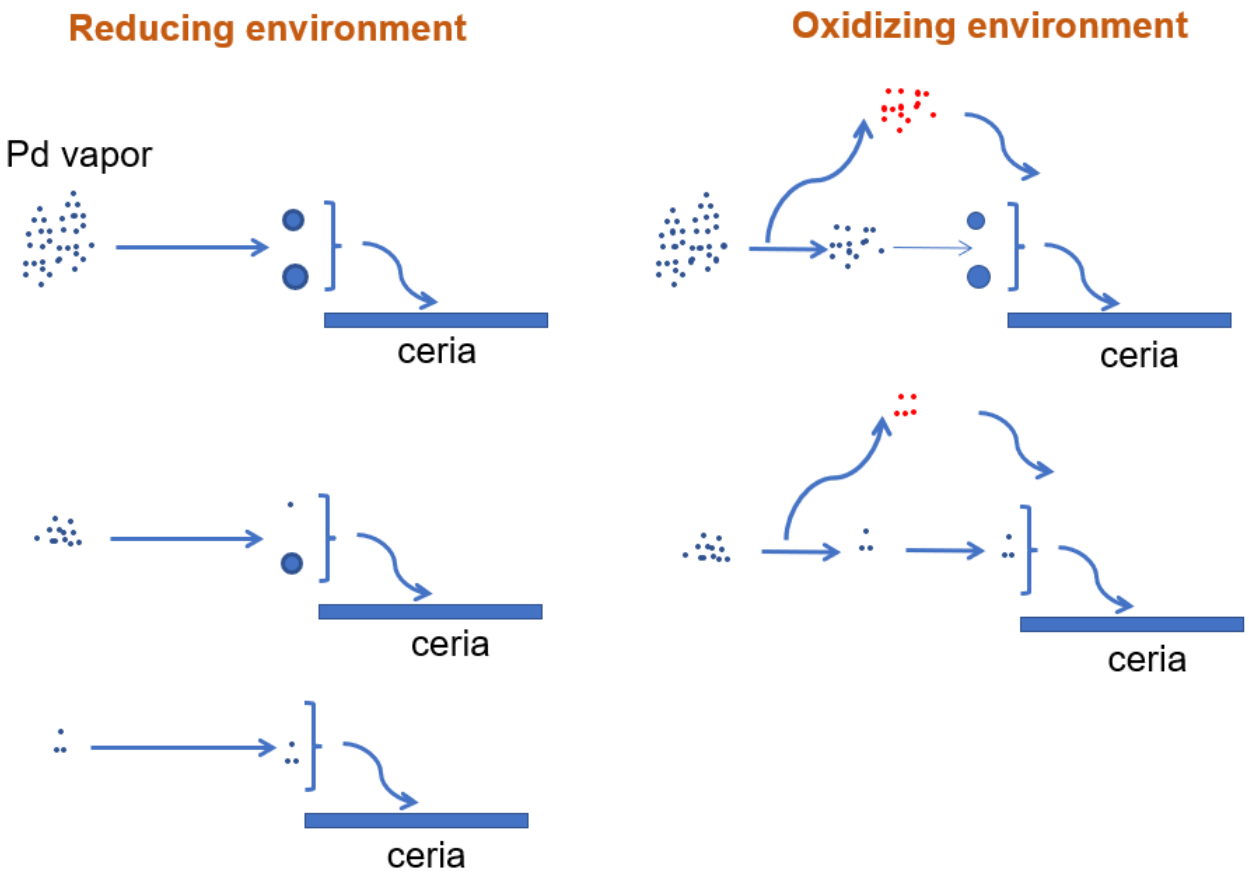


Figure 2.10: Analogy for the synthesis of different structures of Pd on $CeO_2$ in flame spray pyrolysis.

### 2.3.5 Dispersion of Pd at different loading using X-ray Absorption Spectroscopy

The x-ray absorption spectroscopy is adopted to characterize the local coordination of the Pd structures for the samples. Figure 2.11 shows EXAFS data of Pd foil fitted to the first and second shell of Pd, with the fitting parameters in the table. The amplitude factor of 0.79 is obtained from this fitting and used for the fitting of the EXAFS data of PdO in figure 2.12 and the EXAFS data of other samples. As shown in table 2.1 and consistent with the fitting in figure 2.13, the 0.5 wt.% $Pd/CeO_2$ EXAFS data has a Pd-O scattering with a coordination number of 2.34 and the bond length indicated by R of 1.97 A. This bond length of 1.97 A is shorter than the bond length with R= 2.01 A in PdO nanoparticle [84, 85, 86] and the coordination number of 2.34 in the 0.5 wt.% is lower than that of the PdO nanoparticle of 4.0 [84, 85, 86], indicating a tiny PdO cluster. However, the EXAFS data cannot be additionally fitted to the Pd-Pd interactions in PdO while it has a good fit when the Pd-Pd first shell path in Pd foil is included for modeling as shown figure 2.13. In addition, the Pd-Pd bond of the metallic character in the 0.5 wt.% data has the same bond distance as Pd-Pd in metallic Pd, however, the coordination number is far less by about 6, indicating there could be a Pd cluster. As the loading is increased from 0.5 wt.% to 1 wt.%, the Pd-O coordination number becomes increased to 2.8 but it is still less than the coordination number of 4 of Pd-O bond in PdO nanoparticle. In addition, the bond distance for the 1 wt.% sample is the same as that of the Pd-O in the 0.5 wt.%. These indicate a bigger PdO cluster for the 1 wt.%. In addition, the Pd-Pd coordination number also increased to 6.1 indicating a possibility of the Pd cluster. At 2 wt.%, the Pd cluster is increased due to the increased Pd-Pd coordination number.

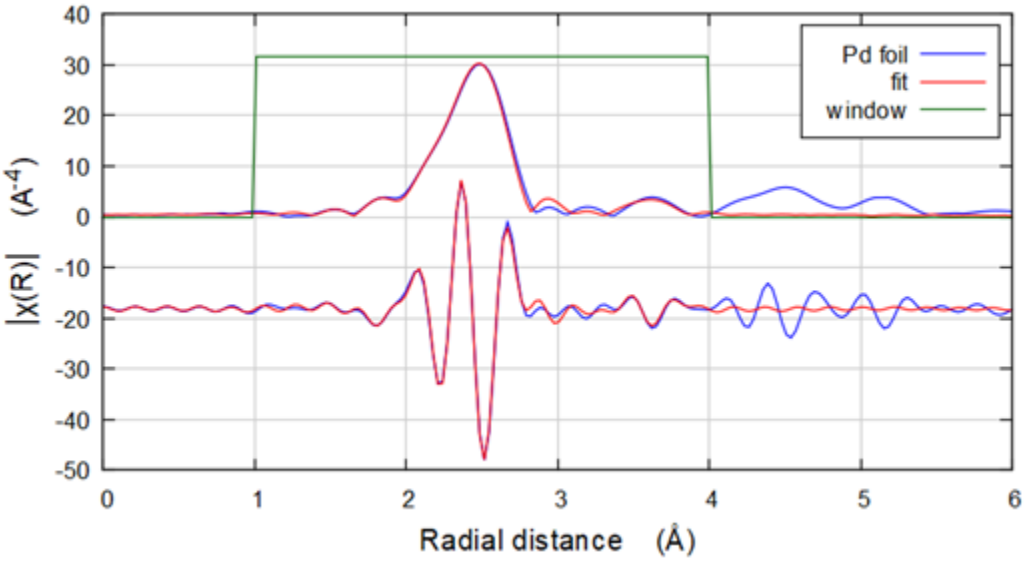


Figure 2.11: Fourier transforms of EXAFS spectra at the Pd K-edge for Pd foil. The fitting data are displayed as red lines.

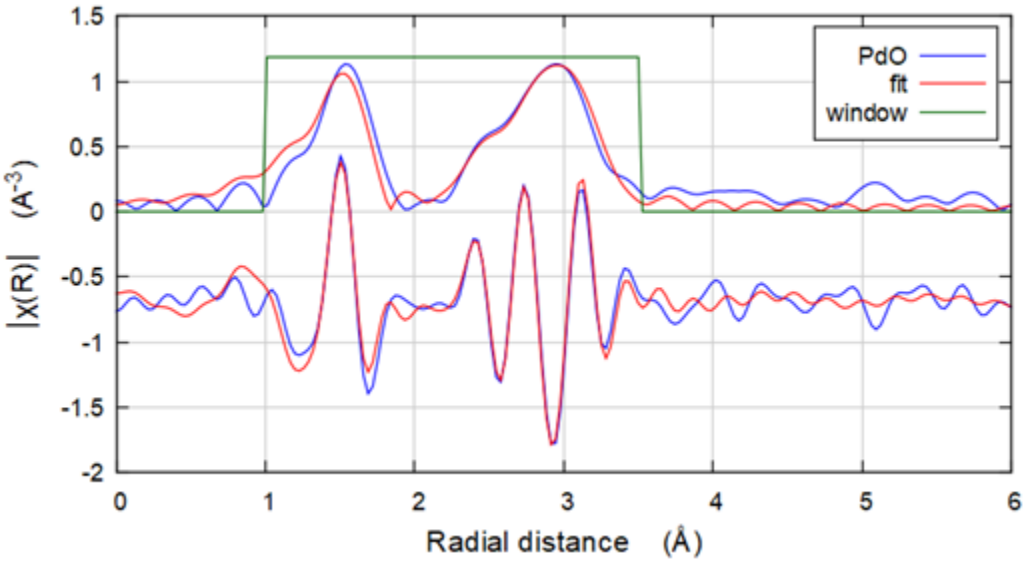


Figure 2.12: Fourier transforms of EXAFS spectra at the Pd K-edge for PdO. The fitting data are displayed as red lines.

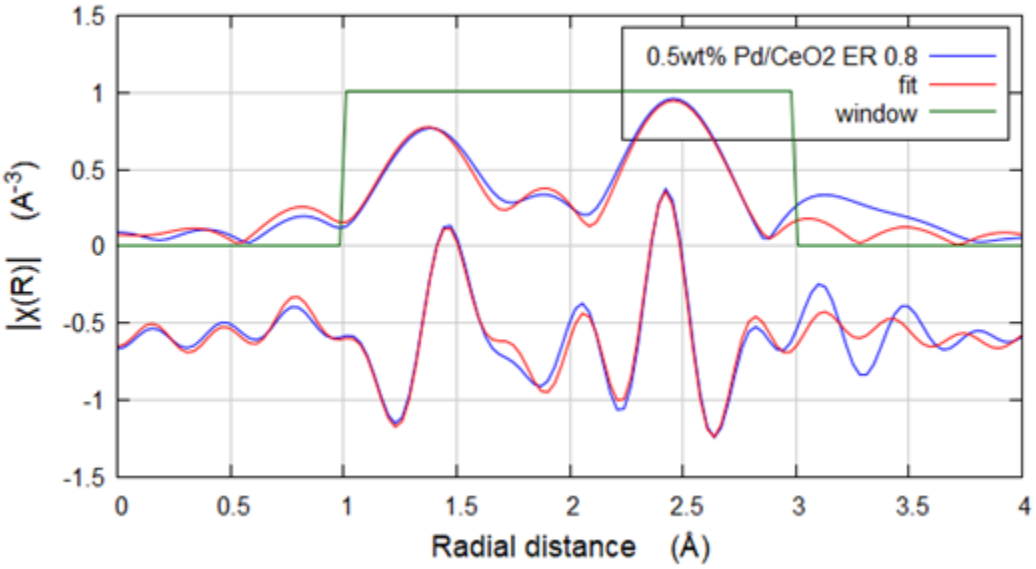


Figure 2.13: Fourier transforms of EXAFS spectra at the Pd K-edge for 0.5 wt.% $Pd/CeO_2$ . The fitting data are displayed as red lines.

Table 2.1: EXAS fitting parameters for catalysts synthesized in the oxidizing environment

| Sample | Path | CN | R (A) | $\sigma^2$ | Red. Chi-sq |
|---|---|---|---|---|---|
| Pd foil | Pd-Pd | 12 | 2.74 | 0.00549 ± 0.00024 | 95 |
| | Pd-Pd | 6 | 3.85 | 0.00948 ± 0.0014 | |
| PdO | Pd-O | 4.00 | 2.01 | 0.00225 ± 0.0009 | 216.6 |
| | Pd-Pd | 4.00 | 3.05 | 0.00446 ± 0.00089 | |
| | Pd-Pd | 8.00 | 3.44 | 0.00668 ± 0.00094 | |
| 0.5 wt. % $Pd/CeO_2$-ER 0.8 | Pd-O | 2.34 ± 1.34 | 1.97 | 0.00144 ± 0.0057 | 25.65 |
| | Pd-Pd | 5.52 ±2.19 | 2.75 | 0.00714 ± 0.0032 | |
| 1 wt. % $Pd/CeO_2$-ER 0.8 | Pd-O | 2.8 ± 1.2 | 1.96 | 0.00144 ± 0.0046 | 56.2 |
| | Pd-Pd | 6.1 ± 4.4 | 2.77 | 0.01588 ± 0.0086 | |
| 2 wt. % $Pd/CeO_2$-ER 0.8 | Pd-O | 2.1 ± 0.8 | 1.96 | 0.00065 ± 0.00395 | 55.9 |
| | Pd-Pd | 7.56 ± 2.5 | 2.77 | 0.01367 ± 0.00363 | |

### 2.3.6 Dynamic behavior of the atomically dispersed Pd under temperature

The dynamic behavior of the structures under temperature is investigated to identify the differences in their activities. Figures 2.14 and 2.15 show the temperature-dependent DRIFTS spectra of 1 wt.% $Pd/CeO_2$ synthesized at the reducing and oxidizing environments, respectively. With increasing temperature, the linearly adsorbed CO on the highly dispersed $Pd^{n+}$, $Pd^0$, and $Pd^0$ clusters together with the bride-adsorbed CO on both ER 0.8 and ER 1.5 catalysts reduce in intensities until they completely disappear around 300 °C. Simultaneously, the vibrational frequency of the adsorbed CO associated with the three Pd structures for both catalysts red shift progressively, with a similar shifting rate on both catalysts, as indicated by the same grouped peak shifting shown in figure A.4. On top of having similar vibrational frequency on both catalysts, the similarity of the shifting rate confirms their chemical identity. On the other hand, the linearly adsorbed CO peak on the atomically dispersed $Pd^{2+}$ on the oxidizing environment catalyst becomes more intense and broadened while also undergoing a redshift in the band without disappearing even up to 500 °C. The increasing intensity is certainly not due to the transformation of any or all of the three structures to the atomically $Pd^{2+}$ since no similar transformation occurs on the reducing environment catalyst. The decreasing intensity of the linearly adsorbed CO on top and bridge sites is rather due to the temperature-enhanced oxidation by the lattice oxygen of ceria, which is supported by the redshift of the wavenumbers associated with the structures due to reduced dipole-dipole coupling. To however investigate whether the atomically dispersed Pd is a spectator species in which the adsorbed CO is not oxidized at increasing temperature, $O_2$ is additionally introduced after flowing in CO at 400 °C. As shown in figure A.5, the linearly adsorbed CO peak associated with the atomically dispersed Pd immediately disappeared with a simultaneous enhancement in $CO_2$ production indicating the oxidation of the adsorbed CO. This indicates that the simultaneous red shift and increasing intensity of the linearly adsorbed

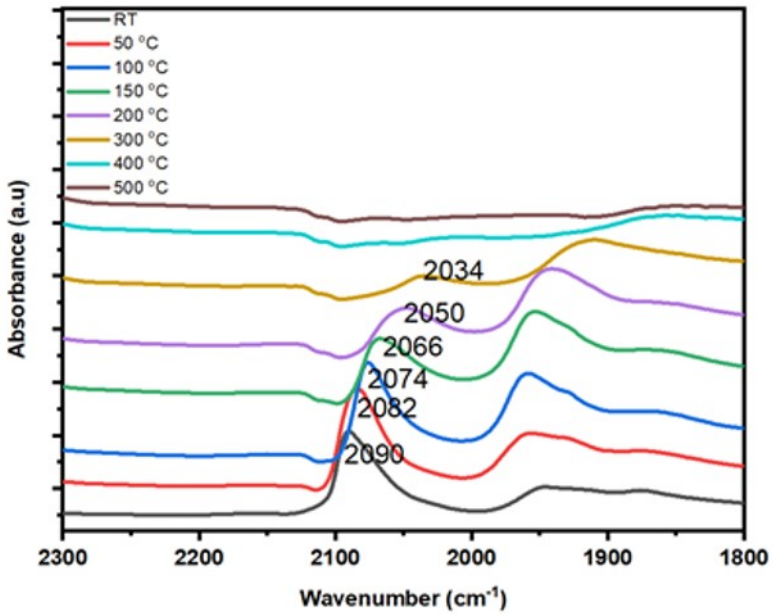


Figure 2.14: Temperature dependent CO adsorption DRIFTS on ER 1.5 1 wt% $Pd/CeO_2$

CO associated with the atomically dispersed Pd is only related to a structural change that is associated with the atomically dispersed species, which is surface reconstruction. In consistence with this, a simultaneous broadening and redshift of linearly adsorbed CO on $TiO_2$ supported atomically dispersed Pt species was also demonstrated using a combination of insitu XANES, FTIR and TEM to be due to the structural changes occurring as a result of some changes in the environmental treatment condition of the atomically dispersed Pd [52].

The Pd structures on the 0.25 wt.% loading catalyst is also investigated under temperature. As shown for the 0.25 wt% catalyst synthesized at reducing environment, the adsorbed CO on the highly dispersed structures also undergo lattice-enhanced oxidation due to the simultaneous redshit and the decreasing intensity during temperature ramping, while there is a simultaneous redshift and increasing intensity of linearly adsorbed CO on the atomically dispersed Pd, also indicative of the surface reconstruction. For the 0.25 wt % synthesized at the oxidizing environment, the exclusive atomically dispersed Pd also undergoes surface reconstruction due to the observed simultaneous redshift and increased intensity. The absence of bridge sites during the temperature ramping confirms the absence of sintering of

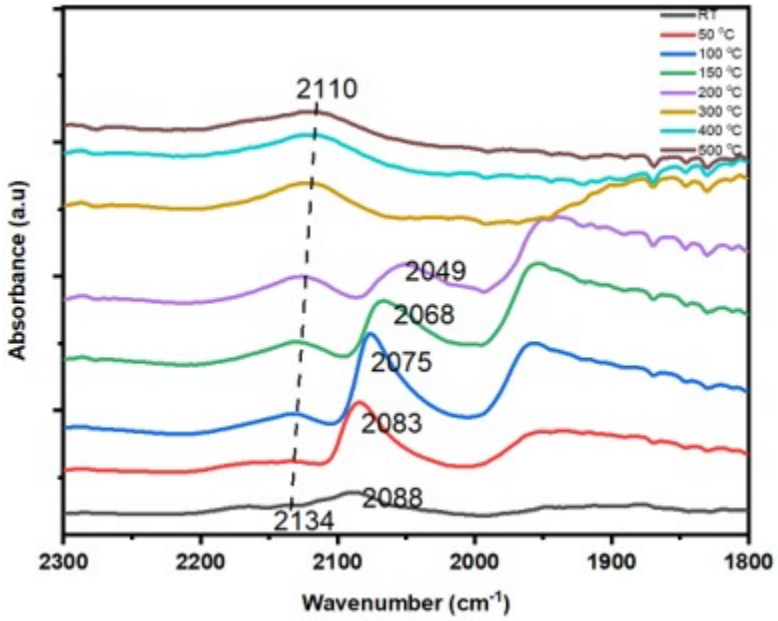


Figure 2.15: Temperature dependent CO adsorption DRIFTS on ER 0.8 1 wt% $Pd/CeO_2$

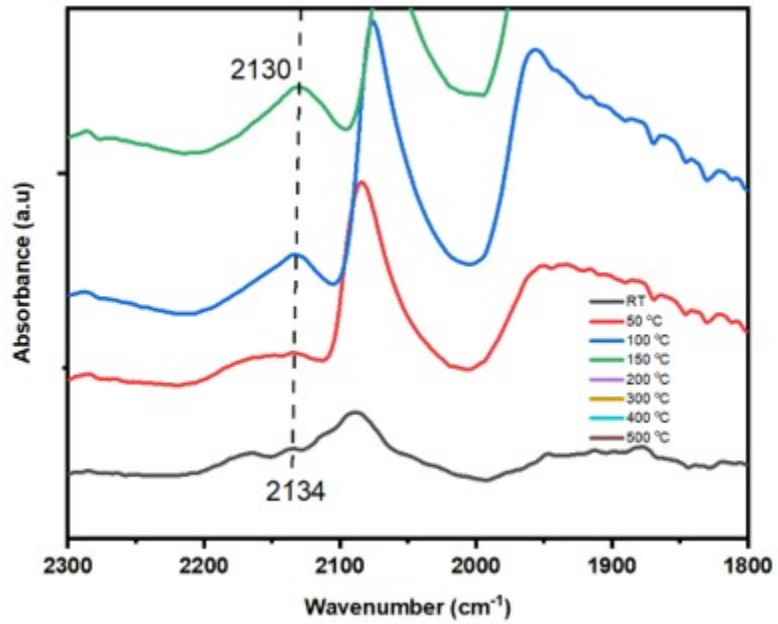


Figure 2.16: Temperature dependent CO adsorption DRIFTS on ER 0.8 1 wt% $Pd/CeO_2$ - zoomed

the atomically dispersed Pd and consequently its stability.

Structural changes that occur during reaction can dictate the reactivity of the structures. Pd system can undergo structural changes under thermal condition and reaction conditions. Phase transformation occurs between Pd and PdO in the operating ranges of methane combustion which influences the activity of the Pd-based catalyst [87]. In addition, there are also direct evidences that surface reconstruction can occur for $Pd/CeO_2$ system. Pd-O-Ce structure can be formed insitu from Pd metal and PdOx when temperature is increased, which was shown to facilitate CO oxidation reaction. It is possible that Pd-O-Ce structure or some other structures are formed when the atomically dispersed Pd is subjected to temperature. The presence of the atomically dispersed Pd can provide a more enhanced methane oxidation activity due to its higher metal support interaction compared to the highly dispersed $Pd^{n+}$, $Pd^0$ and $Pd^0$ clusters. However, the additional structures of the atomically dispersed Pd created insitu can also contribute to the enhanced methane oxidation activity.

### 2.3.7 Stability of the atomically dispersed Pd

The stability of the atomically dispersed Pd is investigated using the DRIFTS. The oxidizing environment-synthesized 1 wt % $Pd/CeO_2$ catalyst cooled down in $N_2$ after temperature ramping upto 500 $^oC$ is investigated. As shown in figure 2.17, the highly dispersed $Pd^{n+}$, $Pd^0$ and $Pd^0$ clusters are observed at their respective vibrational frequencies. The atomically dispersed Pd is also re-observed at the 2134 $cm^{-1}$, which overlaps with the R-branch of the gas phase CO peak. A second temperature ramping of the catalysts under DRIFTS showing surface reconstruction of the atomically dispersed Pd further confirms its presence after the first temperature ramping. However, the enhanced bridge site after temperature ramping in figure 2.17 can be associated with the sintering of the clusters due to the temperature. Figure 2.18 shows the CO DRIFTS of spent 1 wt % $Pd/CeO_2$ synthesized at the oxidizing

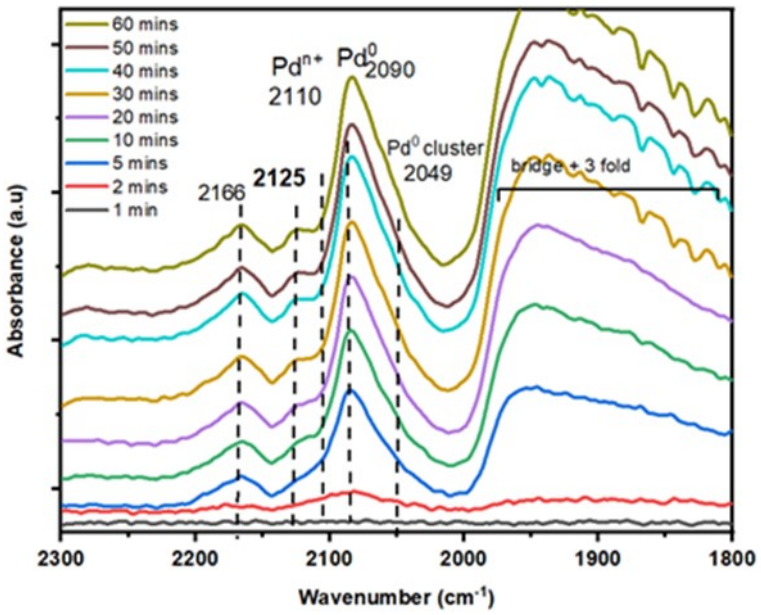


Figure 2.17: Room temperature CO adsorption DRIFTS on ER 0.8 1 wt% $Pd/CeO_2$ after 500 °C temperature

environment (ER 0.8) after methane oxidation reaction up to 800 °C. Linearly adsorbed CO at 2134 $cm^{-1}$ is also observed indicative of the stability of the atomically dispersed Pd after the methane oxidation reaction. However, the 2049 $cm^{-1}$ peak for the Pd cluster becomes more distinctive and intense indicative of the growth of the Pd clusters due to the methane oxidation reaction.

With the atomically dispersed Pd demonstrating surface reconstruction under temperature, the re-observance of the atomically dispersed Pd after temperature ramping is a strong indication of the reversibility of the surface reconstruction of the atomically dispersed Pd. This also connotes that the atomically dispersed Pd remains stable as isolated species and does not sinter to form nanoparticles during and after the temperature ramping even though it undergoes reconstruction under temperature. Similarly, the re-observance of the atomically dispersed Pd after methane oxidation reaction is indicative of its stability after the reaction, although there is no direct evidence of surface reconstruction under methane oxidation reaction. In addition, an 8 hr stability test for the 1 wt.% $Pd/CeO_2$ catalyst synthesized at the

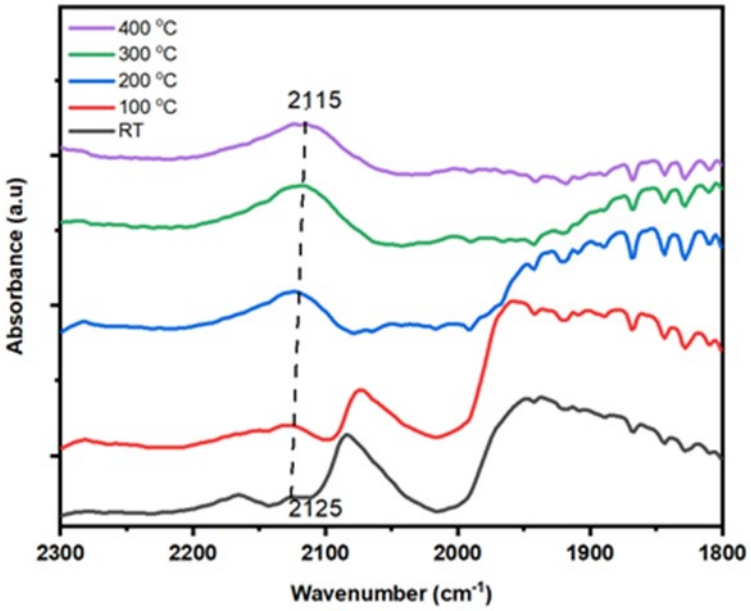


Figure 2.18: CO adsorption DRIFTS on ER 0.8 1 wt% $Pd/CeO_2$ for second temperature increase

oxidizing environment shows relatively constant full conversion at 800 °C as shown in figure A.6.

Phase transformation of Pd systems in the operating range of the methane oxidation reaction is a common phenomenon causing hysteresis in methane combustion rate and consequently playing a role in the reaction [88, 87]. The PdO to Pd transformation occurs during heating at around 900 °C while the reverse does not occur until it is cooled in the oxidizing environment below 600 °C due to the strongly bound oxygen on the Pd surface that inhibits bulk oxidation [89]. The transformation during the heating can be in two steps corresponding to the decomposition of the PdOx/Pd and the crystalline PdO in the range 750 to 800 °C and 800 to 850 °C respectively [90]. However, the use of rare earth metal promoters and adoption of support such as $CeO_2$ and $TiO_2$ can facilitate the re-oxidation of the Pd[91, 92, 93]. The stabilization of the $Pd^{n+}$ on the $CeO_2$ and $CeO_2$-$MnO_2$ during CO oxidation reaction has also been reported [84]. Other studies have identified the source of the transformation from PdO as the breaking down of the Pd-O-Ce interfacial bonding. The Pd-O-Ce interaction at the $PdO/CeO_2$ interface can breakdown from 800 °C to induce fragmentation into metallic

Pd particles [85]. This indicates that atomically dispersed Pd developed here exhibits a high stability of the Pd-O-Ce bond up to 800 °C due to the high temperature synthesis method.

### 2.3.8 Relative activity of the Pd structures using DRIFTS

The relative activities of the highly dispersed $Pd^{n+}$, $Pd^0$ and $Pd^0$ clusters and atomically dispersed Pd are directly investigated under DRIFTS. In situ DRIFTS experimentation was carried out on the 1 wt.% $Pd/CeO_2$ catalyst synthesized at oxidizing environment to investigate the relative activities of the Pd structures. Oxygen gas is introduced after the catalyst synthesized at the oxidizing environment is saturated with CO at 400 °C (after the second temperature ramping), which is the temperature at which the linearly adsorbed CO on the atomically dispersed $Pd^{2+}$ is more dominant. As shown in figure 2.19a, there is a blue shift of the wavenumber of the atomically dispersed $Pd^{2+}$ by 4 $cm^{-1}$ with a slight decrease in intensity after 1 min of oxidation. In addition, the linearly adsorbed CO on both the atomically dispersed $Pd^{2+}$ completely vanishes and the small hump for the other three Pd structures also vanish completely after 2 minutes of $O_2$ introduction. When $O_2$ is stopped, the linearly adsorbed CO on the atomically dispersed $Pd^{2+}$ does not reappear after 20 mins (as shown in figure **??**), due to continuous oxidation at this high temperature and within this time interval, as evidenced by the sustained $CO_2$ gas phase peak. However, by consequently reducing the temperature to room temperature and purging with $N_2$, CO adsorption experiment shows reappearance of the linearly adsorbed CO on all the three structures (figure **??**) and the atomically dispersed structures, indicating the stability of these structures after the CO oxidation.

Adsorbing CO at 100 °C which is the temperature at which the intensity of the linearly adsorbed CO on the other structures is dominant, and introducing $O_2$, oxidation begins evidenced by $CO_2$ production and the linearly adsorbed CO on the atomically dispersed

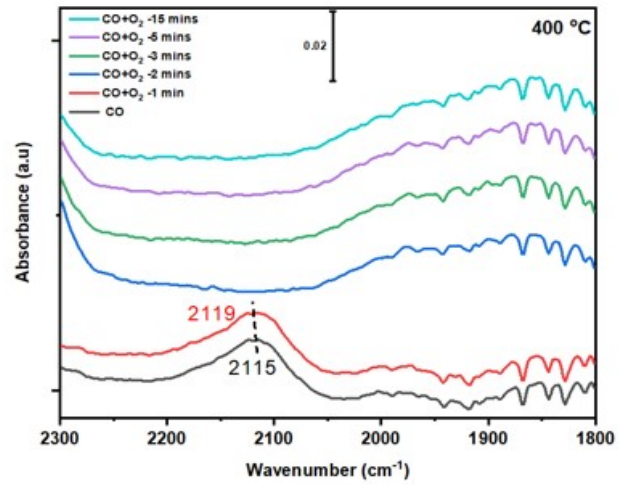


(a) CO oxidation-400 °C

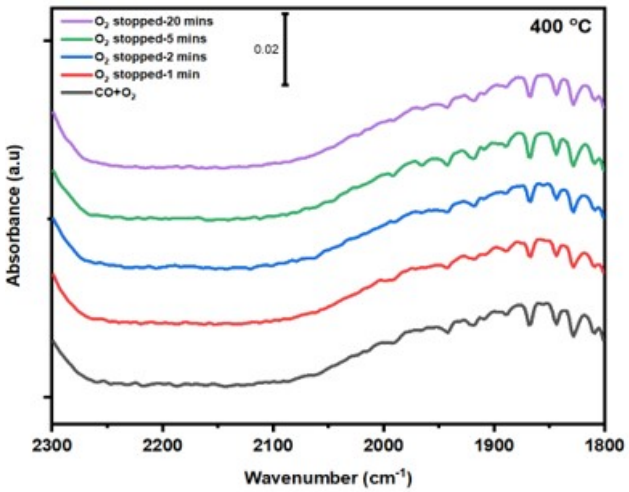


(b) CO oxidation at 400 °C-stopped $O_2$

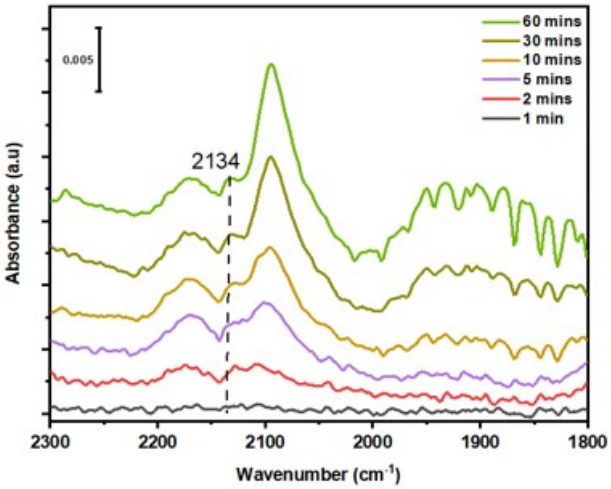


(c) CO DRIFTS after CO oxidation-400 °C

Figure 2.19: CO oxidation DRIFTS at 400 °C on ER 0.8 1 wt% $Pd/CeO_2$

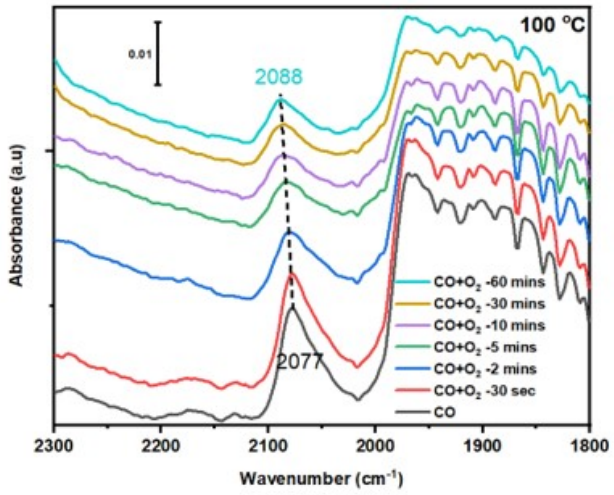


(a) CO oxidation-100 °C

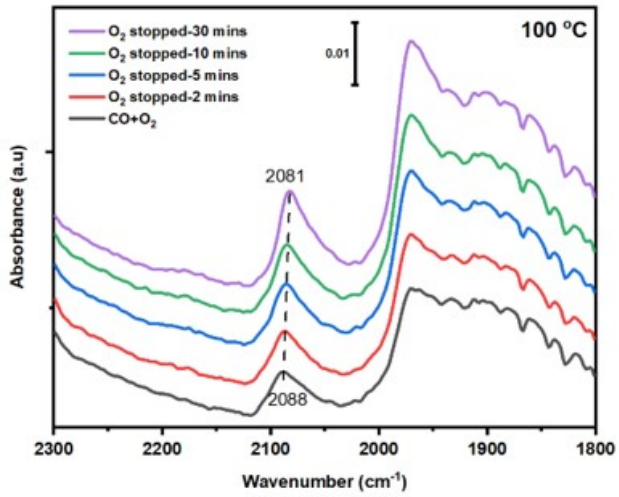


(b) CO oxidation at 100 °C-stopped $O_2$

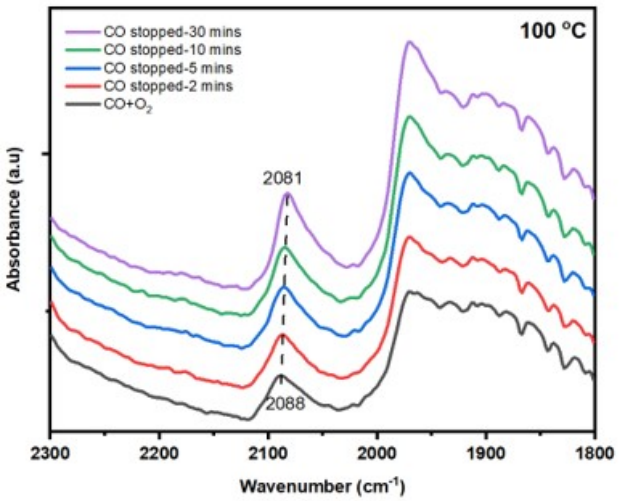


(c) CO DRIFTS after CO oxidation-100 °C

Figure 2.20: CO oxidation DRIFTS at 100 °C on ER 0.8 1 wt% $Pd/CeO_2$

$Pd^{2+}$ completely vanishes at 2 mins. In contrast, the intensity of the linearly adsorbed CO on the other structures reduces, and blue shifts from 2077 $cm^{-1}$ to 2088 $cm^{-1}$, remaining stable after 60 mins (figure 2.20a). However, when the $O_2$ is stopped, there is a decrease in $CO_2$ production indicative of slowed-down oxidation and an increase in the intensity of the linearly adsorbed CO on the three structures while their vibrational frequencies shift to lower wavenumber from 2088 to 2081 $cm^{-1}$ after 30 mins (figure 2.20b). The stopped oxidation of the adsorbed CO consequently allows for the increased CO adsorption which causes the reduction of the Pd species leading to the redshift of the associated adsorbed CO band. It is also possible that the increased coverage due to the adsorption can cause a blue shift in the adsorbed CO band due to dipole-dipole coupling, in which case, the reduction of the species (red shift) could be dominating over the dipole-dipole interaction (blue shift) leading to the resultant red shift. As revealed by the two *in situ* oxidation experiments, oxidation of the atomically dispersed Pd species and the other structures is associated with a blue shift in their respective bands, but the wavenumber of the initial band is maintained after the oxidation. This indicates that the atomically dispersed $Pd^{2+}$ and the other Pd structures undergo increased oxidation states during the CO oxidation reaction and that their oxidation states are likely restored after the oxidation reaction. In other words, the Pd species become more oxidized during the CO oxidation reaction relative to their initial oxidation states. However, the degree of oxidation by these Pd species differs based on the magnitude of the blue shift during the *in situ* reaction and the rate of reduction of the intensity of linearly adsorbed CO. The linearly adsorbed CO on the atomically dispersed $Pd^{2+}$ has a blue shifting rate of 4 $cm^{-1}$/min which is greater than the 0.18 $cm^{-1}$/min shifting rate on the other structures, indicating faster oxidation on the former. In addition, the intensity of the linearly adsorbed CO on the $Pd^{2+}$ reduces faster than that on the other structures. Although the two temperatures allow isolation of the structures for activity investigation, it is, however, possible that the low reaction temperature at 100 °C causes a lower oxidation rate such that the CO adsorption rate during the *in situ* reaction could be

significant, resulting in an underestimation of the oxidation rate of these structures at 100 $^{o}$C.

To directly compare the activity of these two groups of structures eliminating the temperature effect, in situ oxidation was conducted on a fresh 1 wt.% $Pd/CeO_2$ sample synthesized at the oxidizing environment, at 215 $^{o}$C which is an optimal temperature at which the adsorbed peak intensity is roughly the same for both atomically dispersed $Pd^{2+}$ and other structures as determined by extrapolation from the temperature-ramped experiments. The different rate of CO adsorption during the oxidation is avoided by stopping CO flow after reaching equilibrium prior to introducing $O_2$. Upon $O_2$ introduction, there is a positive $CO_2$ production rate and the linearly adsorbed CO on all the structures experience a slight blue shift after 1 min. In addition, both the linearly adsorbed CO on all the structures and the bridge site-adsorbed CO completely disappear within two minutes, in which, the rate of disappearance on the atomically dispersed $Pd^{2+}$ is similar to that on all the other structures combined, indicating the superior oxidation rate by the atomically dispersed $Pd^{2+}$ over that of the other individual structures. The confirmed superior activity of the atomically dispersed $Pd^{2+}$ demonstrated using *in situ* DRIFTs experiments further confirmed the assignment of both structural identification and methane activity.

## 2.4 Discussion

Different Pd structures have been created on ceria using the flame spray pyrolysis technique. The dispersion of the Pd species on ceria can be achieved by controlling the Pd vapor concentration in the flame, and oxidizing the Pd vapor. Irrespective of the synthesis conditions, at high concentration of Pd vapor, formation of clusters of different sizes is favorable due to the high concentration of Pd vapor, which nucleate heterogeneously on the trapping sites of the ceria support. Consequently, lowering the Pd vapor facilitates the isolation of nucleating Pd

species resulting in the formation of atomically dispersed Pd. However, oxidized Pd species formed in the oxidizing environment has a higher tendency to nucleate as isolated Pd species, further facilitating the formation of atomically dispersed Pd. Hence, highly dispersed $Pd^{n+}$, $Pd^0$ and $Pd^0$ clusters can be created at high loading at all synthesis conditions but the atomically dispersed Pd can be additionally created in the oxidizing environment. Consequently, the oxidizing environment has a higher tendency to exclusively form atomically dispersed Pd as the loading is reduced.

The behavior of atomically dispersed Pd can be considered as metastable under temperature as it undergoes surface reconstruction under temperature and yet, it remains isolated. The atomically dispersed Pd also remains isolated after methane oxidation reaction up to 600 $^oC$ while it also demonstrate a 8 hr stability under methane oxidation at 800 $^oC$. We claim that the surface construction observed under temperature also occurs during the temperature ramping methane oxidation activity test since the chemical environment during the methane oxidation reaction is less likely to counteract the thermally-induced surface reconstruction.

The catalysts containing the atomically dispersed Pd demonstrates higher methane oxidation activity than the highly dispersed $Pd^{n+}$, $Pd^0$ and $Pd^0$ clusters. It is also evident that the surface reconstruction of the atomically dispersed Pd is not detrimental to the methane oxidation reaction. While the higher metal support interaction in atomically dispersed Pd can facilitate the enhanced methane oxidation activity over the highly dispersed $Pd^{n+}$, $Pd^0$ and $Pd^0$ clusters, the surface construction could be contributing to the enhanced methane oxidation reactivity.

## 2.5 Conclusion and Recommendation

The FSP synthesis technique has created dispersed Pd species on ceria with different degrees of dispersity depending on the FSP condition and the loading. The speciation of nucleating Pd species during synthesis depends on the available oxygen during the flame synthesis process, in which the oxidizing environment promotes the formation of oxidized Pd species for nucleation during synthesis. The extent of the number of oxidizable species is dependent on the relative amount of vaporizing Pd species in the flame. Hence, lowering the amount of Pd promotes the high dispersion of species and increases the percentage of the oxidizing species which leads to the exclusive formation of atomically dispersed Pd. The synthesized atomically dispersed Pd remains isolated while undergoing surface reconstruction under temperature. In addition to enhancement of methane oxidation reaction by the atomically dispersed Pd due to its higher support interaction, the surface reconstruction could also be contributing to the higher methane performance of the atomically dispersed Pd.

Based on this work, the following work is hereby proposed for investigation. While there is an indication of surface reconstruction related to the atomically dispersed Pd under a thermal environment as well as the stability of the atomically dispersed $Pd^{2+}$ after methane oxidation reaction, the dynamic behavior of the atomically dispersed Pd is yet to be established and evaluation of the structures under methane oxidation reaction can be considered to further support our claim of no counter-effect of the thermally-induced surface reconstruction by the chemical environment during the methane oxidation reaction. The path of reversibility of the surface reconstruction under temperature and reaction conditions can also be investigated. Further enhancement of loading for exclusive stabilization of Pd in FSP using the oxidizing environment will also be beneficial for the catalytic reactions.

# Chapter 3

# Evaluation of Methane Oxidation Reaction over Atomically Dispersed Pd using Operando Diffuse Reflectance Infrared Fourier Transform Spectroscopy

## 3.1 Introduction

It is known that methane oxidation proceeds on PdO via the redox Mars-van Krevelen mechanism in which the first C-H bond activation is the rate-determining step [87]. The reaction is controlled over metallic Pd by the competitive adsorption of methane and oxygen via the Langmuir-Hinshelwood mechanism [87]. It is, however, unknown what reaction mechanism is supported by the atomically dispersed Pd. To develop the appropriate mechanism, the

individual intermediate species involved in the reaction need to be identified to guide the development of elementary steps for the reaction and to have insight regarding the rate limiting step.

Our previous work has controlled the structure of Pd on ceria using FSP and also demonstrated that the atomically dispersed $Pd^{2+}$ is more active for methane oxidation than other structures. Here, we evaluated methane oxidation reaction over synthesized structures including atomically dispersed Pd using *in situ* DRIFTS to identify possible intermediates species that facilitate the enhanced methane oxidation activity over the atomically dispersed Pd.

## 3.2 Method

### 3.2.1 In-situ DRIFTS characterization of the methane oxidation reaction

*In situ* evaluation of methane oxidation was carried out using *in situ* DRIFTS experiments conducted in Harrick praying mantis equipment coupled with an Invenio R Bruker spectrometer equipped with a multi detector unit containing liquid nitrogen mercury cadmium telluride (LNMCT) and RT-DLaTGS detectors. The sample holder is enriched in the sample compartment which has KBr windows for transmission of IR light to and from the sample. The LNMCT detector specifically used for experiments was cooled with liquid nitrogen before the start of any experiment. The optics of the spectrometer as well as the sample compartment of the Harrick praying mantis equipment are purged with $N_2$ gas at 3 L/min and 1 L/min respectively to reduce the atmospheric $CO_2$ and water vapor in the two compartments. For all the in-situ $CH_4$ oxidation reaction experiments, 40 ccm of total gas flow containing (0.1 %) 1000 ppm $CH_4$: $N_2$ was flown over the samples in the DRIFTS cell for 30

mins before introducing oxygen. Measurements were taken with 64 scans for both sample and background at 4 $cm^{-1}$ resolution. The sample temperature was adjusted by using the WATLOW temperature controller on the Harrick heater connected to the sample holder in the DRIFTS cell. All measurements and data analysis were conducted using the OPUS software version 8.5 designed for the spectrometer.

## 3.3 Results

The methane oxidation reaction at 400 °C over the combination of highly dispersed $Pd^{n+}$, $Pd^0$, $Pd^0$ cluster and atomically dispersed structures is evaluated *in situ* using the DRIFTS. Figure 3.3 shows the result from the *in situ* DRIFTS evaluation of methane oxidation reacton over 1 wt% $Pd/CeO_2$ synthesized at ER of 0.8. The sample is first purged with $N_2$ for 30 mins before injecting $CH_4$. Under $CH_4$ adsorption, the gas phase $CH_4$ at 3013 $cm^{-1}$ is observed while carbonates species at 1273 $cm^{-1}$ and 1540 $cm^{-1}$, formates species at 1353 $cm^{-1}$ and C-H methyl species at 2966 $cm^{-1}$ are formed and their intensities increase during $CH_4$ adsorption. A peak at 1475 $cm^{-1}$ is also found to emerge during methane adsorption. As oxygen is injected after 3 minutes of methane adsorption, the $CH_4$ gas phase peak intensity is maintained due to the high $CH_4/O_2$ ratio while there is an enhanced intensity of $CO_2$ doublet peaks at 2400 $cm^{-1}$ due to the methane oxidation reaction. Simultaneously, the intensities of formate and carbonate peaks continue to grow while the peak at 1475 $cm^{-1}$ begins to decrease in intensities. Although the 1475 $cm^{-1}$ peak has been previously assigned to the symmetric and asymmetric $CH_3$ bending, it cannot be assigned to the vibration of $CH_2$ in the methyl group in this case since the 1475 $cm^{-1}$ peak decreases while the adsorbed $CH_3$ as assigned due to the 2966 $cm^{-1}$ increases. It can be therefore appropriately assigned to the $-CH_2-$ scissor vibration due to adsorbed $CH_2$. This implies that the conversion of adsorbed $CH_2$ and forming formates and carbonates can be essential elementary steps during

the low temperature methane oxidation over the atomically dispersed $Pd^{2+}$.

When the methane is adsorbed for 20 min (compared to 3 min), as shown in figure **??**, an adsorbed CO species is observed at 2093 $cm^{-1}$. The formation of adsorbed CO species has been facilitated by the partial oxidation of the adsorbed $CH_4$ by the lattice oxygen of the ceria due to the longer adsorption at 400 °C. Upon introducing $O_2$, the adsorbed CO vanishes immediately due to its oxidation. Hence, the following elementary steps are proposed to be part of the reaction mechanism for the low methane oxidation reaction over the atomically dispersed $Pd^{2+}$.

$$CH_4 + * \leftrightarrow CH_4^*$$
$$CH_4^* \leftrightarrow CH_3^* + H^*$$
$$CH_3^* \leftrightarrow CH_2^* + H^*$$
$$O_2 + H^* \leftrightarrow OH^* + O^*$$
$$CO^* + OH^* \leftrightarrow COOH^*$$
$$COOH^* \leftrightarrow CO_2 + H*$$

To further clarify the essential step that facilitates the methane oxidation reaction, the reaction is evaluated over highly dispersed $Pd^{n+}$, $Pd^0$ and $Pd^0$ clusters, excluding the atomically dispersed $Pd^{2+}$. Similar to the 1 wt. % ER 0.8 catalyst, adsorption of methane results in methane dissociation, and formation of formates and carbonates. During methane oxidation, both $CH_3$ and $CH_2$ peak intensities increase while the carbonates intensity decreases but the carbonate/$CH_2$ peak intensity remains less than 1, indicating that the essential step lies in the conversion of $CH_2$ to carbonates rather than $CH_3$ to $CH_2$. Comparing the operando results of the methane oxidation over all the structures with and without atomically dispersed $Pd^{2+}$ indicates that the conversion of $CH_2$ to carbonates is being facilitated by the additional atomically dispersed $Pd^{2+}$ since the 1 wt.% oxidizing environment catalyst is more active than the reducing environment catalyst.

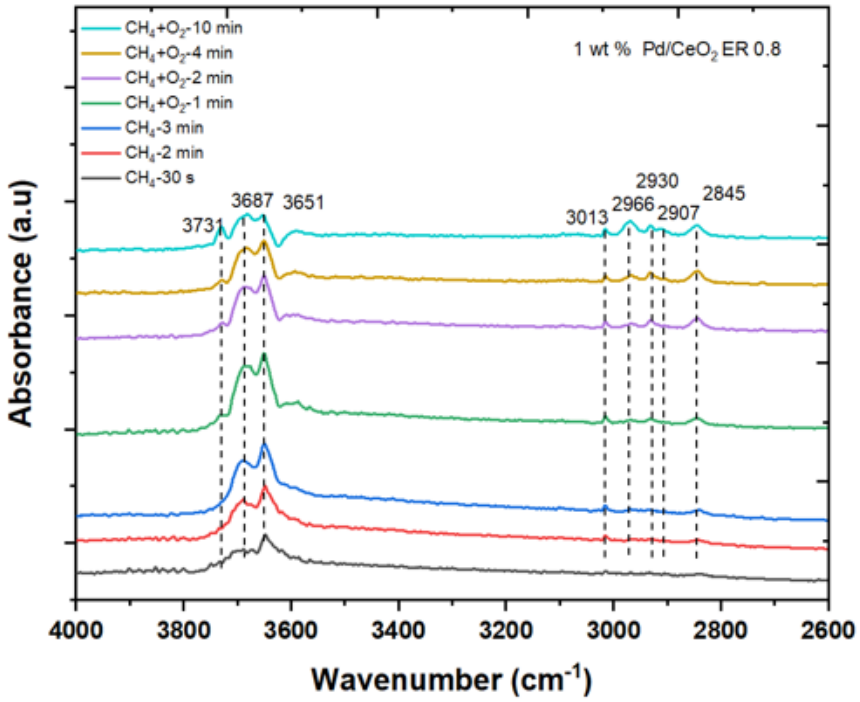


(a) The range between 4000 to 2600 $cm^{-1}$

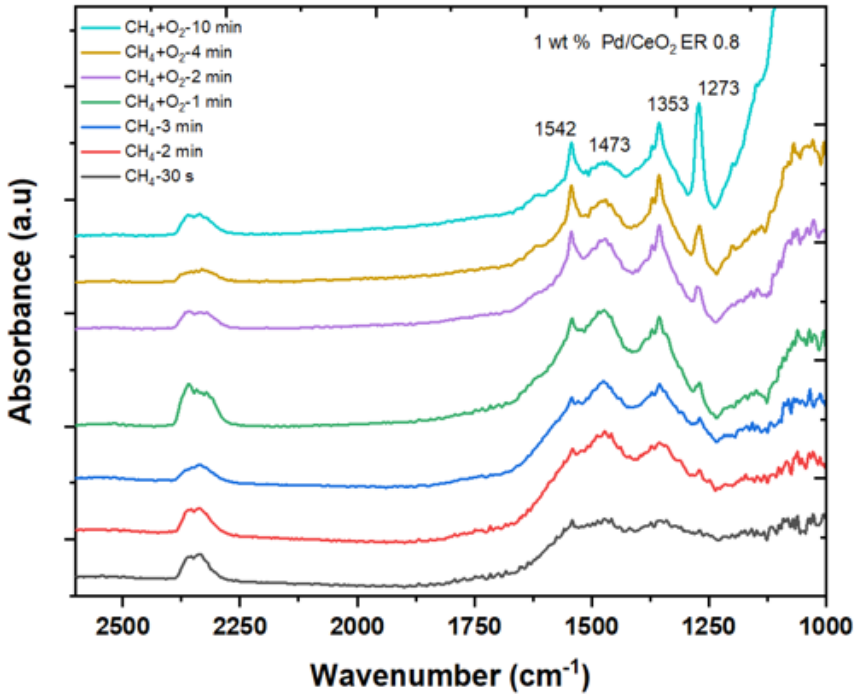


(b) The range between 2600 to 1000 $cm^{-1}$

Figure 3.1: Insitu-DRIFTS evaluation of methane oxidation reactions at 400 °C over 1 wt% $Pd/CeO_2$ synthesized at oxidizing environment (22 cc of $CH_4/N_2$ and 5 cc of $O_2$).

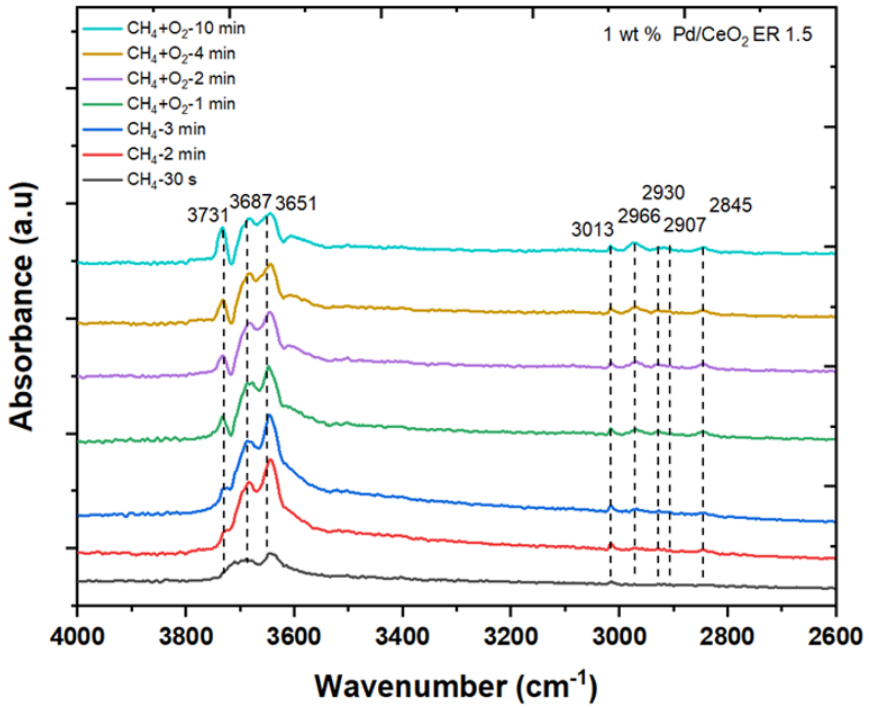


(a) The range between 4000 to 2600 $cm^{-1}$

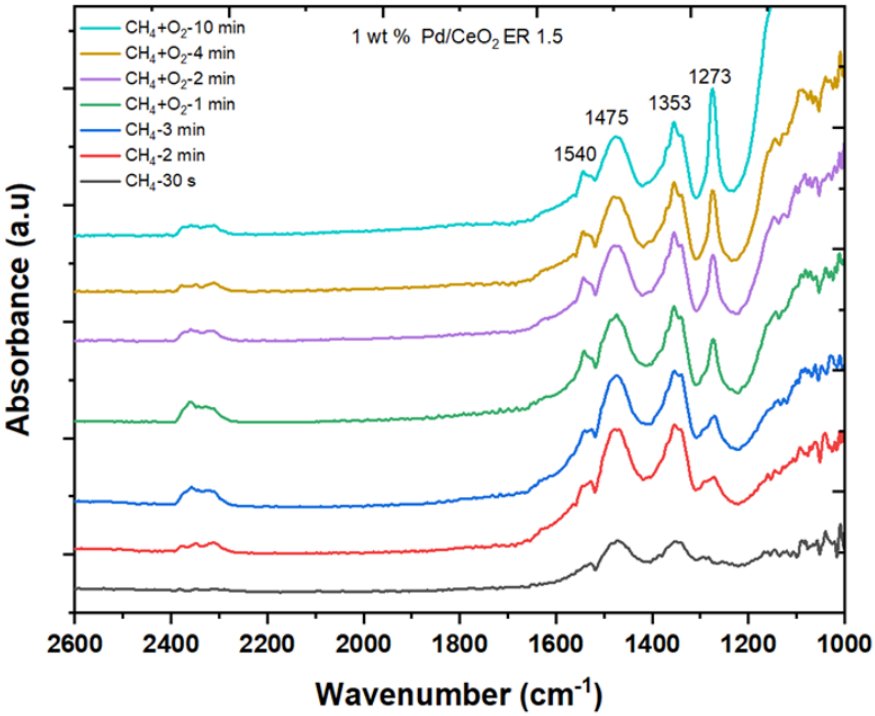


(b) The range between 2600 to 1000 $cm^{-1}$

Figure 3.2: Insitu-DRIFTS evaluation of methane oxidation reactions at 400 °C over 1 wt% $Pd/CeO_2$ synthesized at reducing environment (22 cc of $CH_4/N_2$ and 5 cc of $O_2$).

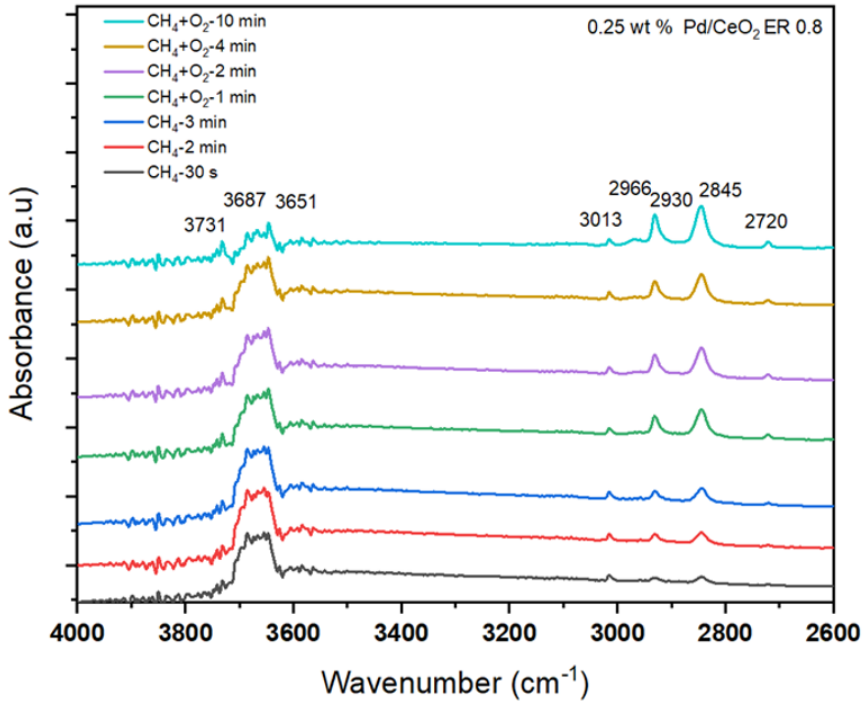


(a) The range between 4000 to 2600 $cm^{-1}$

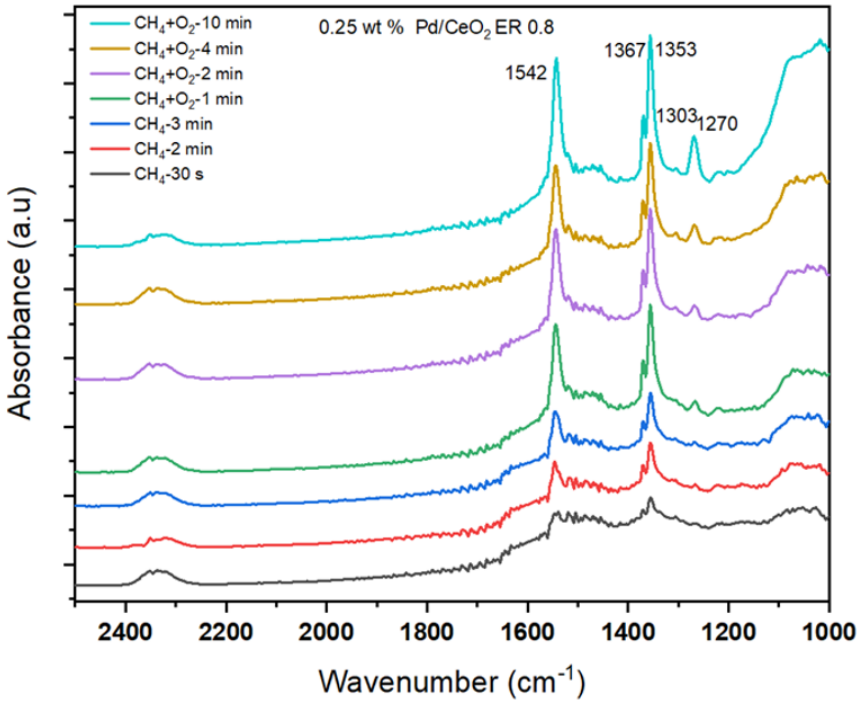


(b) The range between 2600 to 1000 $cm^{-1}$

Figure 3.3: Insitu-DRIFTS evaluation of methane oxidation reactions at 400 °C over 0.25 wt% $Pd/CeO_2$ synthesized at oxidizing environment (22 cc of $CH_4/N_2$ and 5 cc of $O_2$).

To confirm the facilitation of the conversion of $CH_2$ to carbonate by the atomically dispersed $Pd^{2+}$, methane oxidation is evaluated on the 0.25 wt.% catalyst containing only the atomically dispersed $Pd^{2+}$. Like the 1 wt.% samples synthesized at oxidizing and reducing environments, methane adsorption leads to dissociation of $CH_3$ and forming of carbonates and formates due to reaction with surface oxygen. However, the $CH_2$ peak is barely observed. With oxygen introduction, the peak intensity of carbonates is greatly enhanced and has a high carbonate/$CH_2$ intensity ratio, which is higher than the carbonates to $CH_2$ ratio formed during oxidation when the atomically dispersed $Pd^{2+}$ coexists with other structures. The similarity in the high carbonate/$CH_2$ ratio ( greater than 1) for the only atomically dispersed $Pd^{2+}$ and $Pd^{2+}$ in combination with others while the carbonate/$CH_2$ is less than 1 for the structures without atomically dispersed $Pd^{2+}$ is indicative that the atomically dispersed $Pd^{2+}$ facilitate the conversion of $CH_2$ towards carbonates. The higher ratio for only the exclusive atomically dispersed further confirms this assertion.

## 3.4 Conclusion and proposed work

The methane oxidation reaction is evaluated using operando DRIFTS experiments for different structures including atomically dispersed Pd. Similar intermediates were identified during methane oxidation reaction over the other structures. The results of the operando DRIFTS experiments on the structures indicate that the essential step for the methane oxidation reaction lies in the conversion of adsorbed $CH_2$ to carbonate, and its facilitation can be responsible for the exceptional activity of the atomically dispersed Pd. Kinetic modeling can be developed to investigate the reaction mechanism and determine the kinetic parameters. The Langmuir-Hinshelwood and Mars Van Krevelen mechanisms can be investigated.

# Chapter 4

# Incorporation of Film Theory in Single Droplet Combustion Model for Prediction of Precursor Release in Flame Spray Pyrolysis

## 4.1 Introduction

Flame spray pyrolysis (FSP) is a synthesis technique that produces a variety of materials such as titania, silica, supported catalysts, and solid solutions via the combustion of precursors and solvents. The process proceeds by atomization of liquid precursors and solvents, spray combustion, and subsequent formation of particles via either or both droplet-to-particle and gas-to-particle routes in the flame [94]. The intermediate step of spray combustion entailing the evaporation and combustion of droplets in the flame can be critical to the formation of particles, and its understanding is essential for elucidating nanoparticle formation and the

rational design of nanomaterials synthesized by FSP. Although spray droplet combustion is complicated due to the heterogeneity of the atomization process [95], the complexity is typically simplified by considering spray monodispersity [96] and the isolation of a single droplet for combustion investigation.

Several single droplet combustion studies have been conducted to understand particle formation in flame synthesis. Abram et al. [97] have reported the influence of synthesis temperature on particle formation route of sub-micron precursor droplets, particle size control via the droplet-to-particle mechanism, and on the robustness of submicron droplets for formation of Eu-doped $Y_2O_3$ nanophosphors particles. Experiments carried out with laser-induced breakdown spectroscopy (LIBS) and phase Doppler anemometry and SDC studies have shown that the solvent composition of the droplet can modulate particle formation's route and, consequently, the morphology of the formed particle [98]. In addition to the experimental studies, single multi-component droplet combustion and population balance models have been applied to evaluate particle formation by focusing on the detailed conversion routes of different solvent and precursor ratios, resulting in a particle formation map, which depends on precursor and droplet behaviors [99]. Meierhofer et al. [100] have also demonstrated the similarity of the particle products formed in single droplet combustion and flame spray combustion. Through visualization and spectroscopy studies , they have shown how micro-explosion in droplets was used to screen precursor/solvent formulation for the synthesis of homogeneous $Li_4Ti_5O_{12}$ materials. Because the SDC model can provide a wide variety of information during droplet vaporization process, it can be further explored to better understand and design nanomaterials synthesized by FSP.

Most droplet vaporization models deployed for the understanding and design of flame synthesized nanomaterials fall into the $D^2$-law and the infinite liquid conductivity model classes [97], [98]. The $D^2$-law is a simple vaporization model that assumes constant droplet temperature during vaporization and has been applied to evaluate droplet lifetime to infer diffusion

barrier during precursor precipitation [98]. Although the law has been a classical approach for assessing droplet evaporation, its non-validity in several situations, such as dilute conditions [101] and the presence of solute [98], has been highlighted. In addition, recent modifications to the $D^2$-law do not free it from its assumption of constant droplet temperature both in space and time during vaporization [102]. On the other hand, the infinite-liquid conductivity model considers and captures the droplet temperature transient behavior that occur during droplet vaporization, and it has been applied to quantify precursor release during FSP [103]. However, this model does not capture some other phenomena occurring during synthesis. For example, apart from the drag effect caused on droplets by the gas through momentum transfer, the convective effect of the relative motion between the gas and the droplet during synthesis can cause diffusional and thermal films around droplets based on film theory, which can create resistance to mass and heat transfers, respectively [104, 105]. In addition, the Stefan flow due to radial diffusion of vaporizing solvent away from spherical droplet can reduce the free stream gas velocity, which consequently influences the boundary layer [106]. Since the precursor is typically much less volatile than the solvents, the gaseous precursor molecules must diffuse into the mixing and reaction zones through the mass boundary layer already created around the droplet. Although the SDC model without the film theory was applied to understand the particle size distribution of simulated $ZrO_2$ nanoparticles [103], it is possible that the model is not generalizable to other materials or FSP synthesis conditions due to the non-consideration of the film theory phenomenon that can influence the precursor vaporization.

As precursor release has been demonstrated for the understanding of particle size distribution [103], this work aims to combine the SDC model with film theory for the characterization of precursor release in FSP. The SDC model with film theory is first developed for a single solvent droplet and then extended to a solvent mixture droplet. The mass boundary layer and the droplet temperature are identified as relevant parameters to precursor release rate and coupled for its characterization. The effect of initial droplet conditions and solvent

compositions are then evaluated on precursor release rate. Nozzle operating conditions were also assessed using the model and the droplet information obtained from phase Doppler anemometry, allowing the ranking of synthesis conditions in the order of precursor release. This study is the first application of film theory for the understanding and design of flame synthesized nanomaterials.

## 4.2 Materials and Methods

Precursor droplet combustion was investigated by combining single droplet combustion modelling and spray atomization experiments. The spray and combustion diagnostics were carried out to determine the initial conditions of the spray, which subsequently undergoes combustion.

### 4.2.1 Model Development

Single droplet combustion was modeled as an evaporating droplet moving in a hot environment based on the conservation of mass, energy and momentum, and thermodynamic relationships similar to the modeling approach employed in previous droplet vaporization spray combustion models [104, 103]. A momentum balance was added to account for the effect of droplet motion. Also, accounting for convective transport effect due to relative movement between the droplet and the gas, film theory was adopted where heat and mass transfer resistance between the gas and the droplet surface reflects thermal and diffusional films around the droplet. For a non-vaporizing droplet, the thickness of the thermal and diffusional films depends on the Nusselt number and Sherwood number, respectively [104]. For a vaporizing droplet, both diffusional and thermal film thicknesses are modified by correction factors $F_M$ and $F_T$, respectively, representing the relative film thickness change because

of the Stefan flow [104]. This is an infinite liquid conductivity model in which the temperature within the droplet is spatially uniform but time-varying - this is more accurate than the simplified constant droplet temperature model ($d^2$-law) which is both spatial- and time-invariant. The following assumptions and considerations are relevant to the model: (1) Droplets are assumed to be spherical and noninteracting. (2) The gas-phase heat and mass transfer are quasi-steady, and radiative transfer is negligible. (3) No chemical reaction is occurring in the droplet boundary layer. (4) Clausius-Clapeyron equation is used to indicate the nonlinear relationship between fuel vapor pressure and surface temperature, accounting for the phase equilibrium between vaporized species and liquid-phase species. (5) The liquid droplet properties are constant at the average temperature between the liquid solvent's initial temperature and boiling point. (6) Chemical reactions do not occur in the gas film [103]; the gas film consists of fuel vapors and the oxidizing gas, and their properties are dependent on gas film averaged temperature, and fuel vapor concentration, which are based on the 1/3 rule recommended for thermophysical properties averaging [107]. (7) In the case of precursor droplets (droplet containing precursor and solvents), the heat of vaporization of the precursor (or heat of precursor decomposition) can be considered negligible compared to the heat of vaporization of solvents due to the negligible precursor concentration relative to the solvent [108].

**Details of the model**

The droplet combustion in the flame synthesis environment has been modeled as the simultaneous motion and vaporization of precursor droplet in the high temperature gas environment of the flame. Heat transferred from the bulk of the flame (flame temperature) to the droplet causes the vaporization of the droplet and the vaporized solvent diffuses radially away from the spherical droplet satisfying the continuity equation, while also creating a boundary layer around the droplet due to the relative motion between the droplet and the gas, based on

film theory.

Taking energy balance at the droplet-gas interface, the heat transferred from the bulk of the flame to the droplet is used to heat up the droplet by:

$$\frac{dT_d}{dt} = \frac{\dot{Q}_d}{C_{pF} m_d} \tag{4.1}$$

where $m_d$ is the mass of the droplet and $\dot{Q}_d$ is the heat energy rate at which the droplet is directly heated up after droplet vaporization, which is defined as:

$$\dot{Q}_d = \dot{m} \left[ \frac{\bar{C}_{pF} \left( T_\infty - T_d \right)}{B_T} - \triangle H_v \right] \tag{4.2}$$

Due to the heat transferred, the vapor diffuses radially from the droplet at a vaporization rate $\dot{m}$ which is defined in equation (4.3), obtained by solving the continuity equation with the appropriate boundary conditions

$$\dot{m} = \pi \bar{\rho}_g \bar{D}_g d_d Sh^* ln \left( 1 + B_M \right) \tag{4.3}$$

where the $\bar{D}_g$ is the diffusivity of the component in the gas mixtures, and $B_M$ is the Spalding mass transfer number which is defined below in equation (4.4)

$$B_M = \frac{y_{Fs} - y_{F\infty}}{1 - y_{Fs}} \tag{4.4}$$

$B_T$ is the corresponding Spalding heat transfer number as defined in equation (4.5). It is a non-dimensional thermodynamic parameter which is the ratio of drive toward vaporization through the heat of combustion (along with the sensible enthalpy difference between the ambient environment and the droplet surface), divided by the resistance to vaporization

through the heat of vaporization:

$$B_T = (1 + B_M)^{\Phi} - 1 \tag{4.5}$$

where $\Phi$ is defined as:

$$\Phi = \left(\frac{\bar{C}_{pF}}{\bar{C}_{pg}}\right)\left(\frac{Sh^*}{Nu^*}\right)\frac{1}{Le} \tag{4.6}$$

in which $Le$ is the Lewis number defined as the ratio of thermal diffusivity to mass diffusivity. The non-dimensional parameters $Sh^*$ and $Nu^*$ are given by these parameters

$$Sh^* = 2 + \frac{(Sh_0 - 2)}{F_M}; \tag{4.7}$$

$$Nu^* = 2 + \frac{(Nu_0 - 2)}{F_T} \tag{4.8}$$

where $Sh_0$ and $Nu_0$ are the non-dimensional parameters for non-vaporizing droplet, approximated by the Frossling correlations in equation (4.9)

$$Sh_0 = 2 + 0.552Re^{1/2}Sc^{1/3}; \qquad Nu_0 = 2 + 0.552Re^{1/2}Pr^{1/3} \tag{4.9}$$

where the $Sc$ and $Pr$ are the Schmidt number and Prandtl number defined as the ratio of momentum diffusivity to mass diffusivity and the ratio of momentum diffusivity to thermal diffusivity, respectively. $F_M$ and $F_T$ are the correction factors due to Stefan flow in an evaporating droplet, which is given by

$$F(B) = (1 + B)^{0.7}\frac{\ln(1 + B)}{B} \tag{4.10}$$

Based on mass balance at the droplet interface, the droplet vaporization is accompanied by a decrease in the droplet mass and droplet size as described by equation (4.11) and equation

(4.12), respectively.

$$\frac{dm_d}{dt} = -\dot{m} \tag{4.11}$$

$$\frac{dd_d}{dt} = -\frac{2\dot{m}}{\pi\rho_d d_d^2} - \frac{d_d}{3\rho_d}\frac{d\rho_d}{dT_d}\frac{dT_d}{dt} \tag{4.12}$$

For the sake of simiplicity, the liquid density is considered not changing with temperature. For multicomponent mixture such as for EHA/toluene solvent mixture, the multicomponent mass balance described by equation (4.13) is adopted.

$$\frac{dm_{d,i}}{dt} = -x_{i,s}\dot{m_{tot}} \tag{4.13}$$

and the corresponding $\frac{dd_d}{dt}$ is derived from equation (4.14)

$$d_d = \left(\frac{6}{\pi}\sum\frac{m_{d,i}}{\rho_{d,i}}\right)^{1/3} \tag{4.14}$$

For the precursor droplet motion, the drag force exerted by the dispersion gas on the droplet causes its upward movement with the velocity $u_d$. Based on momentum balance, the rate of change of $u_d$ is given by equation (4.15) when the effect of gravity is neglected due to the high dispersion gas velocity from the nozzle.

$$\frac{du_d}{dt} = \frac{3}{4}\frac{C_D}{d_d}\frac{\rho_{g,\infty}}{\rho_d}\left|u_{g,\infty} - u_d\right|\left(u_{g,\infty} - u_d\right) \tag{4.15}$$

The drag coefficient of the evaporating droplet is obtained using the correlation in equation

(4.16).

$$C_D = \frac{24}{Re}\left[1 + \frac{Re^{2/3}}{6}\right] \tag{4.16}$$

in which $Re$ is the Reynold's number defined as in equation (4.14)

$$Re = \frac{2\rho_\infty \left|u_\infty - u_d\right| r_d}{\bar{\mu}_g} \tag{4.17}$$

in which the $\rho_\infty$ is the free-stream density, and the $\bar{\mu_g}$ is the average viscosity of vapor mixture. The vertical distance travelled by the droplet during the vaporization process can be obtained from $u_d$ using equation (4.18) from equation of motion.

$$\frac{dz}{dt} = u_d \tag{4.18}$$

In addition to the drag effect caused through the momentum transfer between the gas and droplet, the relative motion of the droplet with respect to the gas also causes some convective transport which is considered using the film theory. According to film theory, there is resistance to mass and heat transfer between the droplet surface and the gas flow which are modelled as gas film of thicknesses given by equations (4.19) and (4.20), respectively.

$$\sigma_M = F_M \sigma_{M0} \tag{4.19}$$

$$\sigma_T = F_T \sigma_{T0} \tag{4.20}$$

where $\sigma_{M0}$ and $\sigma_{T0}$ are the thicknesses of the diffusional and thermal films respectively for non-vaporizing droplets, defined as:

$$\sigma_{M0} = \frac{2r_d}{Sh_0 - 2} \qquad\qquad \sigma_{T0} = \frac{2r_d}{Nu_0 - 2} \tag{4.21}$$

and $F_M$ and $F_T$ are the correction factors to the diffusional and thermal film thicknesses

Table 4.1: Liquid properties of EHA and toluene solvents

| S/N | Properties | EHA | Toluene |
|---|---|---|---|
| 1 | Liquid density (Kg/m3) | 843 | 821.5 |
| 2 | Boiling point (K) | 498 | 383.6 |
| 3 | Heat of vaporization (KJ/mol) | 66.6 | 38 |
| 4 | Specific heat capacity (J/Kg/K) | 1560.9 | 1811.4 |

of non-vaporizing droplet respectively, to account for the Stefan flow occurring due to the vaporization process.

**Liquid phase properties**

Liquid phase properties of the fuel are constant and evaluated at $T = 0.5(T_0 + T_{bp})$. It is assumed that the liquid phase properties are relatively constant with temperature. The overall liquid property is obtained by the mass-weighted mixing rules as in equation ((4.22)) for the heat capacity and density.

$$\bar{C}_{p,g} = \sum_{1}^{n}(Y_i C_{p,i}); \qquad \bar{\rho}_g = \sum_{1}^{n}\left(\frac{Y_i}{\rho_{v,i}}\right) \tag{4.22}$$

The liquid phase properties used are detailed in table 4.1

**Gas phase properties**

The gas phase contains the mixture of solvent vapor and dispersion gas. With the assumption of ideal mixing (ignoring the effect of the difference in molar volume) in the liquid phase and the assumption of ideal gas behavior in the vapor phase, the molar concentration of individual species in the vapor phase $x_i$ is determined from the corresponding mole fraction in the liquid phase and the pure component vapour pressure by Raoult's law, as described

in equation (4.23). :

$$x_i = \frac{x_{l,i} P_{vp,i}}{P_{atm}} \tag{4.23}$$

The vapor pressure $P_{vp,i}$ is obtained using Clausius Clapeyron equation in (4.24) while the mole fraction is obtained from the solvent mass fraction using equation (4.25).

$$\ln\left(\frac{P_{vp,i}}{P_{atm}}\right) = -\frac{\triangle H_v}{R}\left(\frac{1}{T_d} - \frac{1}{T_{bp,i}}\right) \tag{4.24}$$

$$molfrac_i = \frac{\frac{massfrac_i}{MW_i}}{\sum_i^n \frac{massfrac_i}{MW_i}} \tag{4.25}$$

The corresponding mass fraction $Y_i$ is given by

$$Y_{Fs} = \frac{X_{Fs} MW_i}{\sum_1^n X_i MW_i} \tag{4.26}$$

The fuel vapors mix with the oxidant. The individual components properties are evaluated at T while their composition is obtained as $\bar{Y}_{Fs}$

$$\bar{T} = T_s + Ar\,(T_\infty - T_s)\,; \qquad \bar{Y}_{Fs} = Y_{Fs} + Ar\,(Y_{F\infty} - Y_{Fs}) \tag{4.27}$$

Using the 1/3 rule, the $Ar = 3$; $Y_{F\infty}$=0 (there is full combustion of the fuel). The vapor phase specific heat capacity $C_p$ and density are weight-averaged using the expression

$$\bar{C}_{p,g} = \sum_1^n (Y_i C_{p,i}); \qquad \bar{\rho}_g = \sum_1^n \left(\frac{Y_i}{\rho_{v,i}}\right) \tag{4.28}$$

while the Wilke mixing rule is applied to the thermal conductivity and viscosity of the vapor

Table 4.2: Physical properties of flame oxidant

| S/N | Properties | Values |
|---|---|---|
| 1 | Tinf (K) | 2500 |
| 2 | Y | 0 |
| 3 | u | gas velocity |
| 4 | Density ($Kg/m^3$) | 1.429 |
| 5 | Molecular weight MW ($Kg/mol$) | 16e-3 |
| 6 | ($W/m/K$) | 0.02658 |
| 7 | Viscosity ($Pa.S$) | 4.47e-5 |
| 8 | D ($m^2/s$) | 1.76e-5 |

phase mixture, as shown in equations (4.29) and (4.30), respectively.

$$k_{mix} = \sum_{i=1}^{n} \frac{y_i k_i}{\sum_{j=1}^{n} y_j \phi_{ij}} \tag{4.29}$$

and

$$\mu_{mix} = \sum_{i=1}^{n} \frac{y_i \mu_i}{\sum_{j=1}^{n} y_j \phi_{ij}} \tag{4.30}$$

where

$$\phi_{ij} = \frac{\left[1 + \left(\frac{\mu_i}{\mu_i}\right)^{0.5} \left(\frac{MW_j}{MW_i}\right)^{0.25}\right]^2}{\sqrt{8}\left[1 + \left(\frac{MW_i}{MW_j}\right)\right]^{0.5}} \tag{4.31}$$

$\phi_{ij} = 1$ and $y_i$ = mole fraction of the $ith$ component; n=3, and i=fuel 1, fuel 2, oxidant.

The solvent vapor properties and oxidant properties are highlighted in table 4.3 and table 4.2, respectively. Vapor phase viscosity and binary diffusion coefficient of n-decane were used for EHA due to non-availability of the EHA properties. Actual values of the boiling point and heat of vaporization of EHA at 498 K and 66.6 KJ/mol (76.3 KJ/mol), respectively, have been used for EHA in the model.

Table 4.3: Physical properties of EHA and toluene solvent vapor

| S/N | Physical properties | EHA | Toluene |
|---|---|---|---|
| 1 | Binary diffusion coefficient ($m^2/s$) | 3.97e-6 at 300 K | 1.04e-5 |
| 2 | Dynamic viscosity $kg/m/s$ | 7.5e-6 at 450 K | 9.45e-6 |
| 3 | Thermal conductivity ($W/m/k$) | 0.02756 | 0.0132 |
| 4 | Density ($Kg/m3$) | 3.9 at 393K | 2.519 |
| 5 | Specific heat capacity ($J/Kg/K$) at 400K | 1550.5 | 1518 (139.9 KJ/mol) |
| 6 | Molar volume (mL/mol) | 159.7 | 106.3 |

**Precursor consideration**

We have considered dilute precursor concentration in EHA/toluene solvent mixture such that solvent properties approximate precursor solution properties, heat of precursor vaporization is negligible, the change in precursor concentration during vaporization is negligible, and the precursor solution could be considered ideal mixture. The precursor of choice is volatile and does not chemically interact with EHA to avoid micro-explosion. In addition, there is no chemical interaction between EHA and Toluene solvents.

**Numerical method of solution**

The developed precursor droplet combustion model consists of five ordinary differential equations for single component droplet or six ordinary differential equations for multicomponent droplet . These constitute an initial value problem that is suitably solved by an iterative procedure using the explicit Euler method executed in MATLAB, with the initial conditions described in table 4.4. The iterations in the Euler numerical method are terminated based on the simultaneous satisfaction of two conditions: if the droplet size reduces to $< 1$ and if the change in temperature between consecutive iterations $T_i - T_{i-1}$ is $< 0.1K$. The model provides the droplet surface temperature profile, droplet lifetime before complete vaporization, droplet velocity profile, droplet size evolution, and heating rate. It requires physical and thermodynamic properties of the solvent fuels, dispersion/oxidant gas properties, flame tem-

Table 4.4: Initial conditions for the model

| S/N | Properties | Values |
|---|---|---|
| 1 | Vertical distance, $z_0$ (m) | 0 |
| 2 | Droplet velocity, $u_0$ (m/s) | Defined or as measured by PDI |
| 3 | Temperature, $T_0$ (K) | 298 |
| 4 | Droplet size, $d_{d0}$ (m) | Defined or as measured by PDI |
| 5 | Droplet mass, $m_{d0}$, (Kg) | $\rho * (4/3) * \pi * (d_{d0}/2)^3$ |
| 6 | Mass of individual solvent components | $m_{1d,0} = x1 * m_{d0}; m_{2,d0} = x2 * m_{d0}$ |

perature, dispersion gas velocity and droplet initial conditions. Solvents considered include ethyl hexanoic acid (EHA), toluene, and ethanol. Due to the unavailability of some EHA properties, n-decane properties were used for EHA due to the similarities of their molecular weights.

Vapor phase viscosity and binary diffusion coefficient of n-decane were used for EHA due to non-availability of the EHA properties. Actual values of the boiling point and heat of vaporization of EHA at 498 K and 66.6 KJ/mol (76.3 KJ/mol), respectively, have been used for EHA in the model. Values of other EHA properties used in the model are highlighted in Table 1

### 4.2.2 Spray Atomization

The spray characteristics were obtained by optical spray measurements using Phase Doppler Interferometry (PDI). PDI is a non-intrusive method that simultaneously measures spray droplet size distribution and the velocity distribution. The technique measures droplet size and velocity based on the difference in fringe spacing and the difference in the velocity of the moving fringe patterns respectively with and without the droplet passing through the beam interference zone. The spray diagnostic tests were carried out using the PDI system at the University of California Irvine Combustion Laboratory (UCICL) [109]. The PDI system consists of a two-component transmitter that emits the four laser beams, and a receiver that

collects the refracted light at an angle of $30^o$ angle with respect to the transmitter centreline. The nozzle was set in between the transmitter and receiver. Data were collected for 30 seconds or until 10,000 valid measurements were obtained. Measurements were collected 5 mm downstream of the nozzle tip. Measurements were obtained every 1mm radially away from the spray plume centre until the number of valid measurements dropped to about 10 counts. Since the measurements were being taken close to the nozzle tip (5 mm axially away from the tip), an extra validation check was enabled to reject any erroneous measurements. After all measurements were analyzed to remove any negative velocity for further validation of measurements, at least 26,000 valid measurements were analyzed for droplet size and velocity distribution from which the Sauter mean diameter (SMD) and the average velocity of the droplets were obtained using equation (4.32) and equation (4.33) respectively. The gas velocity was estimated from the maximum velocity obtained in the velocity distribution measurements (equation (4.34)), which corresponds to the velocity of the finest droplets, which are rapidly accelerated by the atomizing air.

$$\text{SMD }, D_{32} = \frac{\sum_i^n d_i^3}{\sum_i^n d_i^2} \tag{4.32}$$

$$\text{droplet vel, } u_0 = \frac{\sum_i^n v_i}{n} \tag{4.33}$$

$$\text{gas vel, } u_g = max(v_i) \tag{4.34}$$

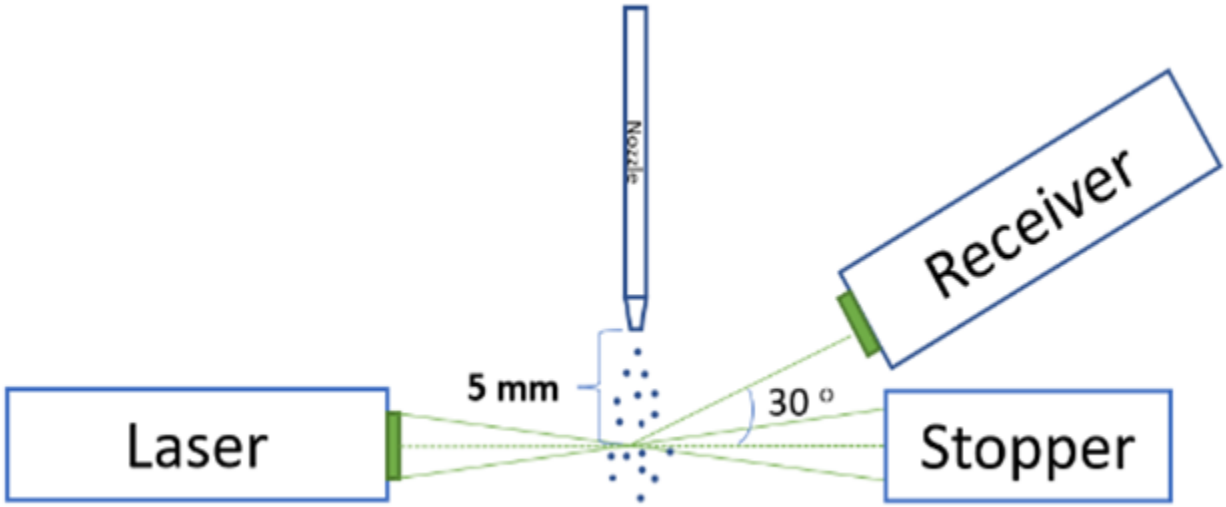


Figure 4.1: Phase Doppler Interferometry (PDI) experimental set-up

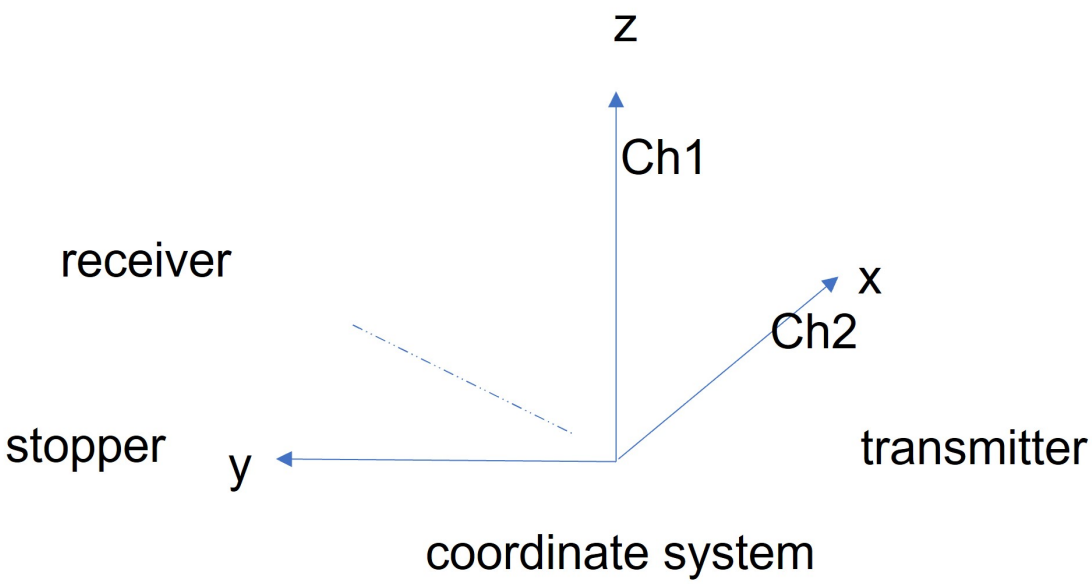


Figure 4.2: PDI coordinate system

## 4.3 Results and Discussions

### 4.3.1 Modelling result

The SDC model reveals the detailed process of solvents' vaporization immediately following their injection into the flame. As shown in figure 4.3a and figure 4.3b, the model depicts that solvent droplet vaporization begins with an initially high overall heat transfer rate ($> 0.015$ J/s) which decreases rapidly in 0.16 ms. This causes an immediate increase in droplet temperature and solvent vaporization rate, followed by a constant temperature zone where the solvent vaporization reduces. The decreasing heat transfer rate is due to the decreasing temperature gradient from increasing droplet temperature since the flame temperature remains constant. The solvent vaporization rate decreases to 1.18 ms after reaching the maximum constant droplet temperature because the overall heat transfer influences the phase change. This phenomenon of solvent vaporization proceeds simultaneously inside the flame with increasing velocity of the droplet, up to the velocity of the moving gas, due to the momentum transfer, as shown in figure 4.3c. Also, during this process, vaporized solvent builds up near the droplet surface resulting in growth of a mass transfer boundary layer (figure 4.4a). Similarly, a thermal boundary layer grows near the droplet surface (figure 4.4b). Based on this depiction, a two-stage droplet vaporization process is evident. First, there is a region of increasing vaporization rate, corresponding to the decreased heat transfer rate (increased temperature). Second, a region of decreasing vaporization rate exists corresponding to a constant droplet temperature. In the first region of droplet vaporization, the rapidly reducing heat transfer is due to increasing droplet temperature while the thermal boundary layer remains relatively constant. The heat transfer reduces more slowly in the second region of droplet vaporization until it reaches zero due to the decreasing vaporized solvent rate. Similarly, the vaporization rate increases in the first region while the mass boundary layer remains relatively constant, decreasing in the second region. In contrast, the mass bound-

ary layer begins to increase at a later stage. In the first region, the vaporization rate is heat transfer controlled since the direct vaporization rate keeps increasing with the droplet temperature. This might be because the vaporization rate is expected to be constant at a particular temperature irrespective of droplet size or decrease if the amount of vaporizable solvents limits it. Therefore, the solvent vaporization rate in the second stage is limited by the instantaneous droplet size (amount of vaporizable solvents) during vaporization, which may be related to the surface area of the droplet.

The precursor vaporization in the droplet is evaluated since it proceeds much more slowly than the solvent vaporization due to the solvent's lower ratio of vaporization temperature to boiling point. Irrespective of the precursor's boiling point and concentration, the heat transfer rate from the flame bulk influences precursor vaporization in the droplet. The increasing droplet temperature in the first region of solvent vaporization can cause an increase in precursor vaporization. On the other hand, in the area of constant droplet temperature, precursor concentration will influence the direct vaporization of the precursor from the droplet, whether or not the droplet temperature is above the boiling point of the precursor. The differential diffusion of the precursor within the droplet is considered negligible due to the low concentration of the precursor in the solvent and short diffusion time compared to droplet evaporation [103]. Since the precursor and solvent are initially homogeneously distributed in the droplet and diffusion time is short, we assume precursor concentration on the droplet surface does not increase. Hence, the droplet temperature and the mass transfer boundary layer remain critical parameters for characterizing the precursor droplet vaporization in addition to the droplet lifetime. This is because the droplet temperature will determine the intrinsic rate of precursor vaporization without resistance [110] and possibly thermal decomposition. At the same time, the mass transfer boundary layer thickness (MBLT) caused by the flowing gas and the solvent vapor creates resistance to the transport of the released precursor vapors [18], thereby controlling the net release rate of the precursor. Although the droplet temperature and MBLT do not directly quantify the precursor release

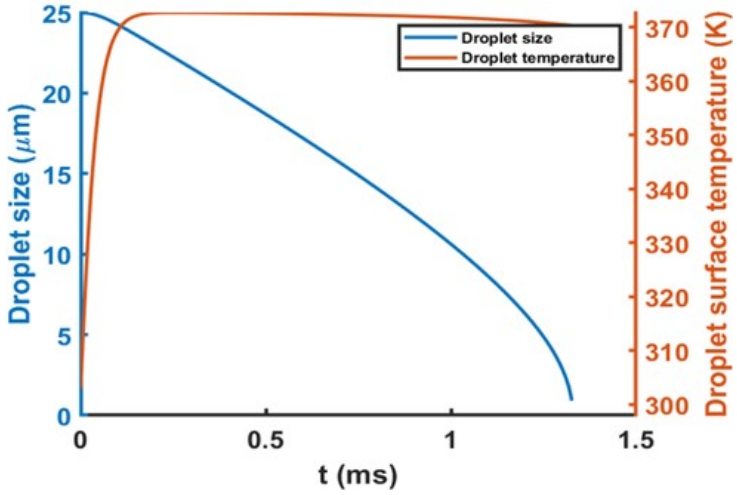


(a) Droplet size and temperature

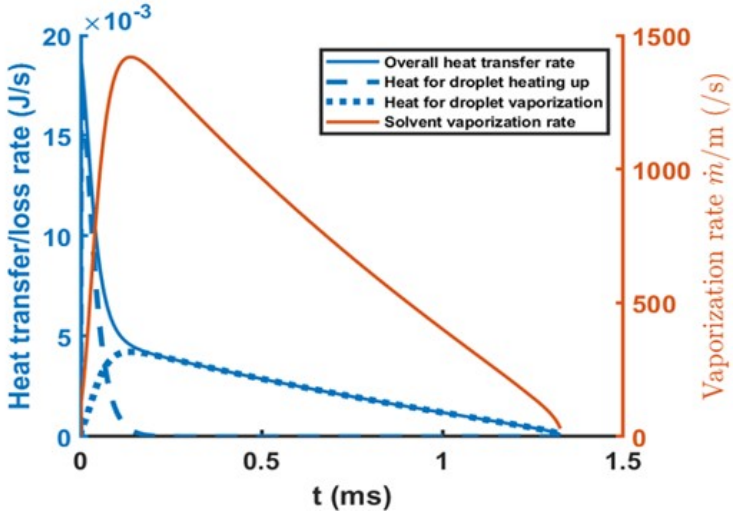


(b) Vaporization rate and heat transfer

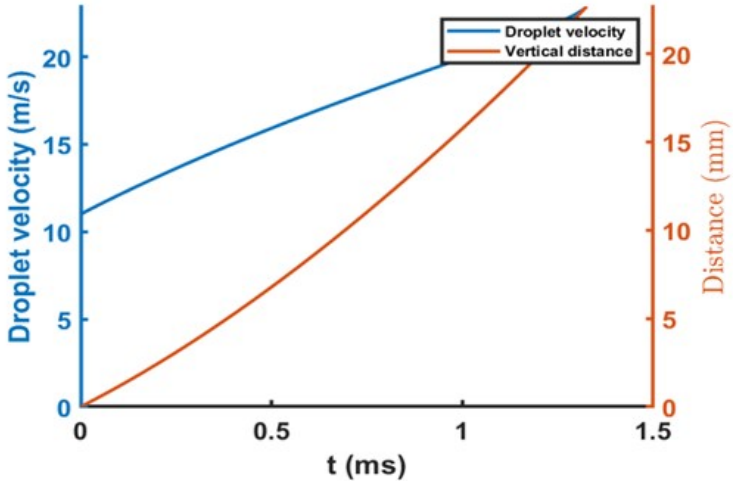


(c) Droplet velocity and penetration

Figure 4.3: Droplet vaporization phenomenon: droplet size, velocity and solvent vaporization

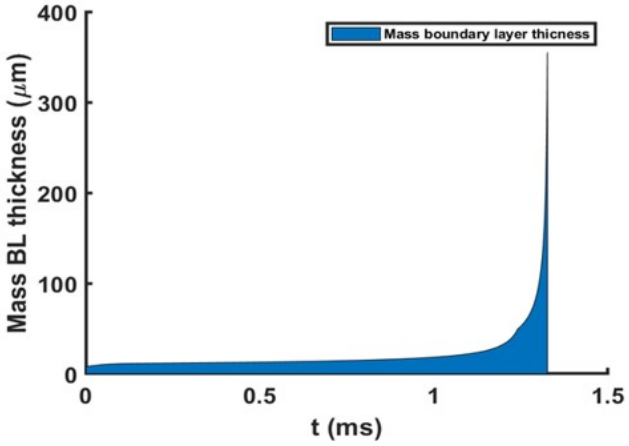


(a) Mass boundary layer thickness

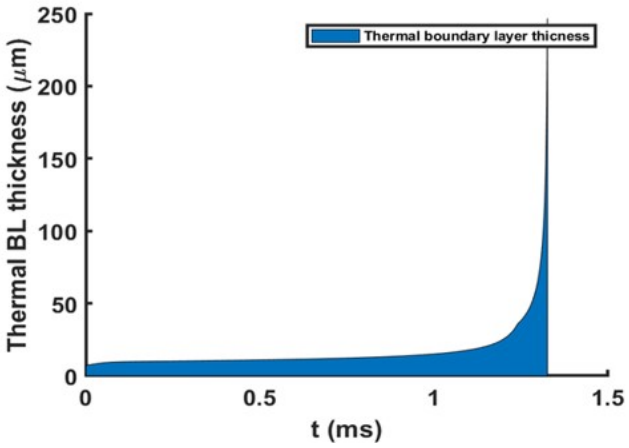


(b) Thermal boundary layer thickness

Figure 4.4: Droplet vaporization phenomenon: mass and thermal boundary layer thicknesses

rate, they are the driving force for the precursor release and the resistance to their release to the combustion zones, which can be considered for the qualitative and relative prediction of the precursor release. Since the intrinsic precursor vaporization from its droplet is dependent on the precursor volatility and the droplet temperature, qualitative characterization of precursor release based on the coupling of the droplet temperature and MBLT is accurate when the precursor is excluded in the model for cases having the same precursor type and liquid phase concentration. This is because, based on the combination of Clausius Clapeyron relation and Raoult's law describing the phase change thermodynamics, the concentration of the precursor vapor at the immediate surface of the droplet is only dependent on the droplet temperature, the precursor concentration in the liquid phase, the precursor boiling point and latent heat of vaporization. Despite this, the qualitative prediction may be limited to cases of dilute precursor concentration in solvents. It is important to note that a small precursor release rate will lead to the enhancement of number of small primary particle size during synthesis [103].

The model is explored to understand the effects of solvent composition and initial droplet size on the precursor vaporization process. The supplementary information of 2D video simulations of 25- and 10-micron droplets visually shows how they vaporize at different times in the same flame environment, validating the model. As shown in Figure 4.5a, droplet lifetime depends on the initial droplet size; as expected, a smaller droplet has a smaller droplet lifetime than a larger droplet but in a nonlinear dependence. Also, a small droplet has a small MBLT due to the size effect; however, the final droplet temperature remains constant irrespective of the initial droplet size due to the overwhelming impact of the same solvent composition on droplet temperature. Hence, a smaller precursor-solvent droplet will maximize precursor vaporization due to its rapid heating up and small MBLT, leading to larger sizes of primary particle. Conversely, a larger droplet size will result in smaller primary particles, which is consistent with the experimental observation of Heine and Pratsinis [103] for their flame-synthesized $ZrO_2$ nanoparticles.

Furthermore, the model also reveals that the solvent choice and composition can control the precursor vaporization process. As shown in figure 4.6a, the droplet with higher EHA content experiences a higher rapid heating rate and attains a higher final temperature leading to faster solvent and precursor evaporation. Since the effective increase in droplet temperature due to the excess energy required for solvent vaporization is influenced by the specific heat capacity, the lower specific heat capacity of the EHA causes more increase in droplet temperature. Although the same flame temperature has been assumed in this work, the high enthalpy of combustion of EHA could have also increased the flame temperature and, consequently, the droplet temperature. In addition, the mass boundary layer is slightly influenced by the solvent ratio.

While the MBLT becomes relatively the same up to 10 mm above the nozzle, increasing the EHA content lowers the MBLT beyond 10 mm, as shown in figure 4.6b, which may not be significant. Hence, a precursor droplet containing a higher EHA concentration will experience enhanced precursor vaporization due to the more rapid heating and higher final droplet temperature arising from its low specific heat capacity and. Hence, the number of larger primary particles can be increased by increasing EHA composition.

The generated scheme shown in figure 4.7 depicts that the model requires solvent thermodynamic properties (both liquid and vapor), dispersion gas properties, and flame properties such as flame temperature and the velocity of moving gas as direct input into the model. In addition, physical properties of the droplets, such as droplet size and velocity, are required as initial conditions for the model. Our FSP experimental set-up consists of an air-assisted nozzle that can be operated under certain conditions. Droplet information can be obtained to apply the SDC model for the FSP synthesis of nanomaterials. With any constant precursor concentration/loading, precursor release can be directly related to nozzle operating conditions.

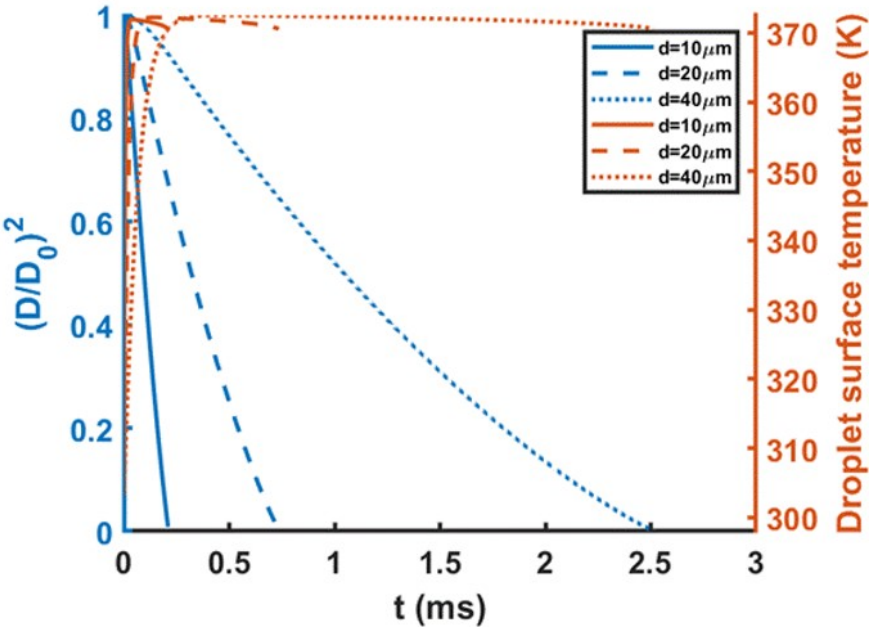


(a) Droplet lifetime and droplet surface temperature dependence on initial droplet size

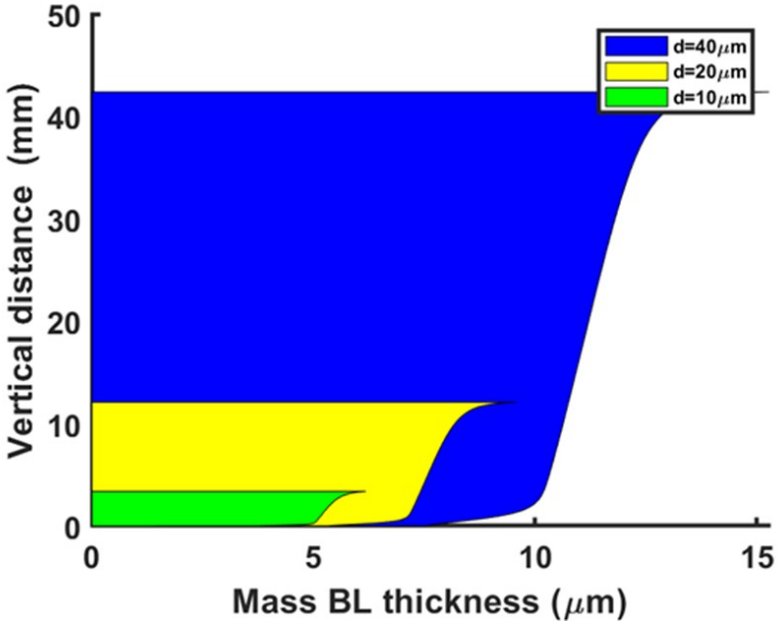


(b) The change in the mass boundary layer thickness dependence on initial droplet size

Figure 4.5: Effect of initial droplet size on precursor droplet vaporization

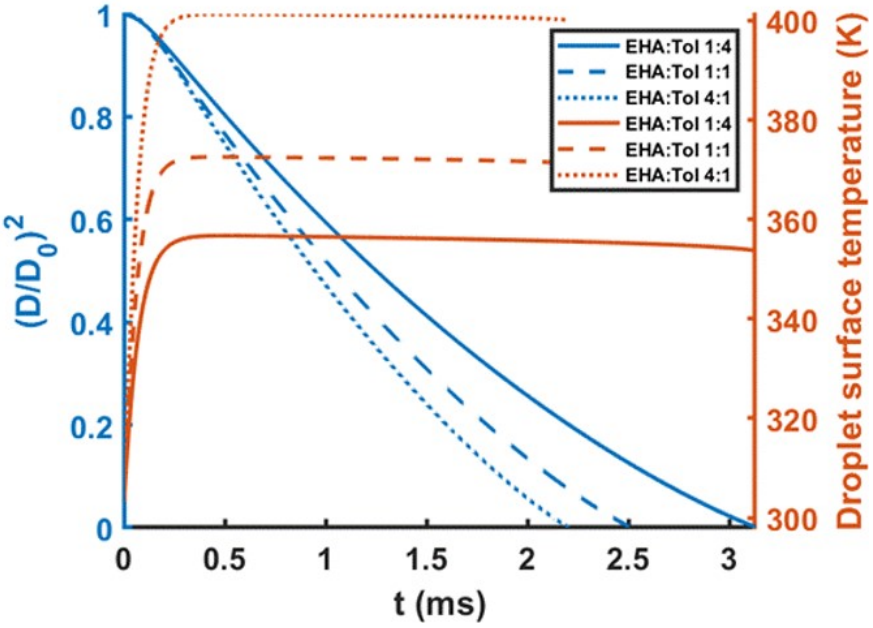


(a) Droplet lifetime and droplet surface temperature dependence on EHA/toluene solvent ratio

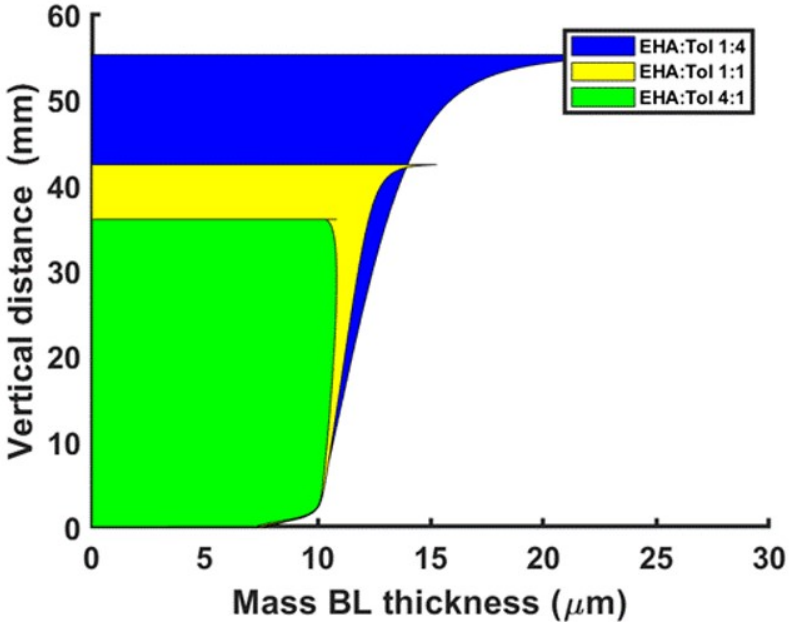


(b) The change in the mass boundary layer thickness dependence on EHA/toluene solvent ratio

Figure 4.6: Effect of EHA/toluene solvent ratio on precursor droplet vaporization

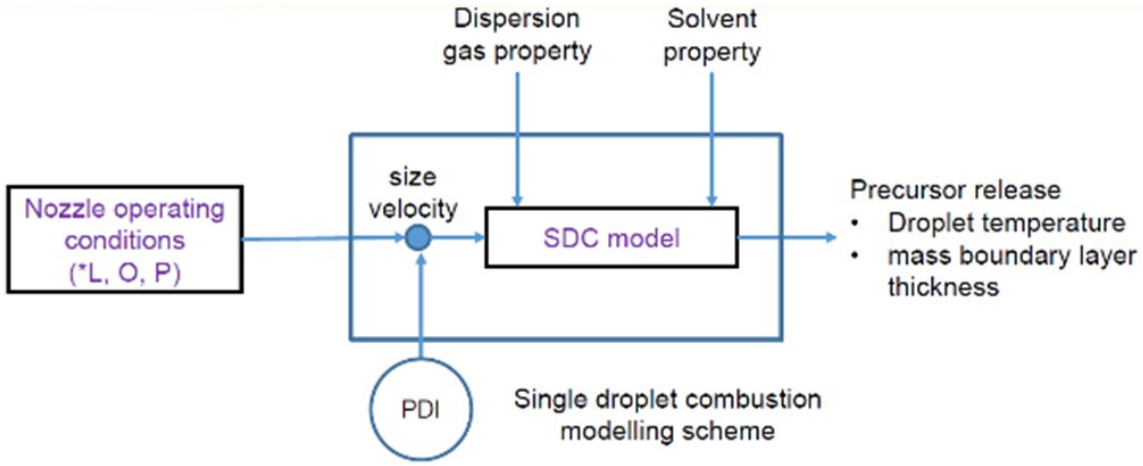


Figure 4.7: Scheme for practical application of SDC model for FSP synthesis

### 4.3.2 PDI Measurement

Six nozzle operating conditions (liquid flow rate (L) of 2-3 ml/min, gas flow rate (O) of 3.5-4.5 L/min, and gas pressure (P) of 1.5-2.5 bar) resulted in stable sprays for ethanol and heptane were investigated with the air-assisted nozzle. Heptane was chosen to represent a solvent mixture of EHA and toluene due to the similarities in their properties. Based on the PDI measurement, atomization by the external air-assisted nozzle progresses from the edge as indicated by the largest droplet size at the spray center, as shown for the L2O4.5P1.5 synthesis condition in figure 4.8a, due to the lower gas flow at the center. The droplet size distribution at +2 mm from the spray center in figure 4.8b and the droplet size distribution representative of the L2O4.5P1.5 synthesis condition (figure 4.9) are unimodal. The Sauter mean diameter (SMD) represents the characteristic mean diameter of the size distribution. This value also represents the mean value of the droplet surface area distribution, which is essentially relative to evaporation behavior. The PDI measurements at the six heptane conditions indicate that the droplets' SMD ranges between 22.5 - 33.2 miconm, the droplet velocity ranges between 9.99 -11.45 m/s, and the gas velocity ranges between 21.18 - 25.89 m/s, as shown in table 4.5.

Consistent with the high Weber numbers associated with this air-assisted nozzle, it is not

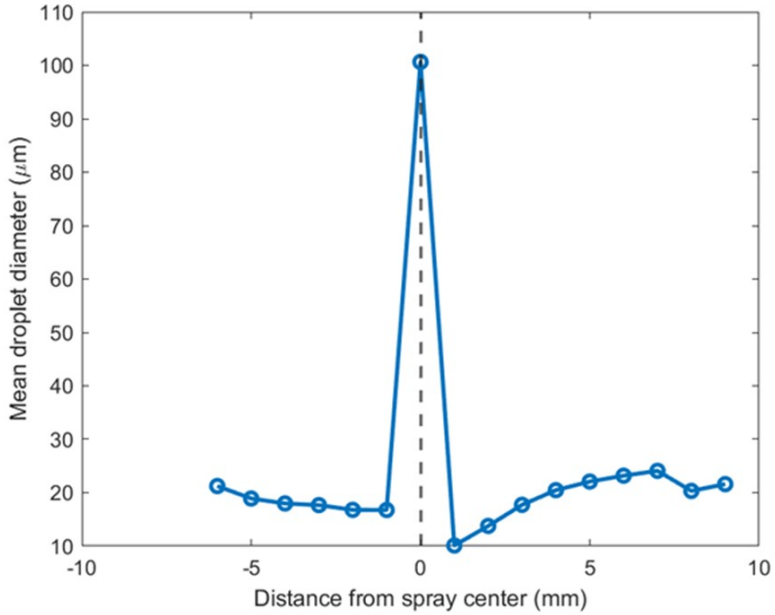


(a) Droplet size distribution for L2O4.5P1.5 (ethanol)

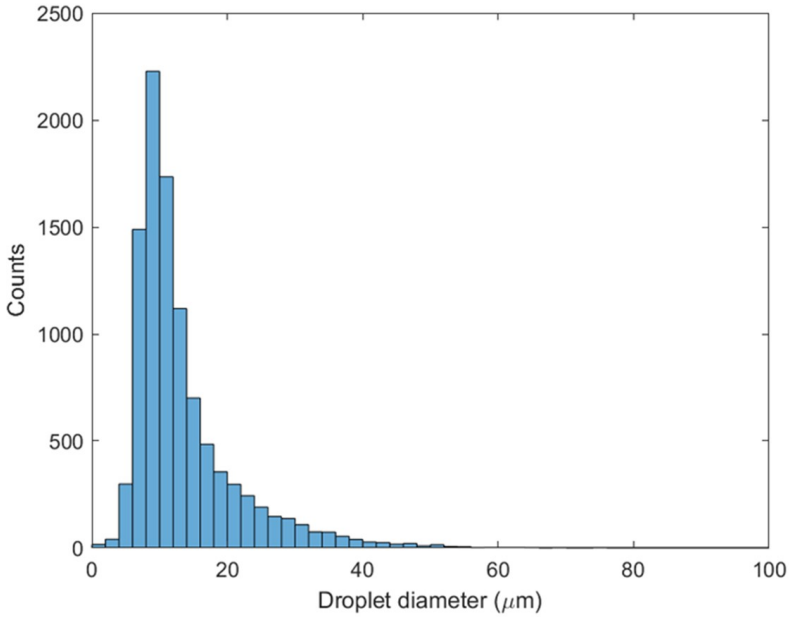


(b) Droplet size distribution at +2mm for L2O4.5P1.5 (ethanol)

Figure 4.8: PDI measurements

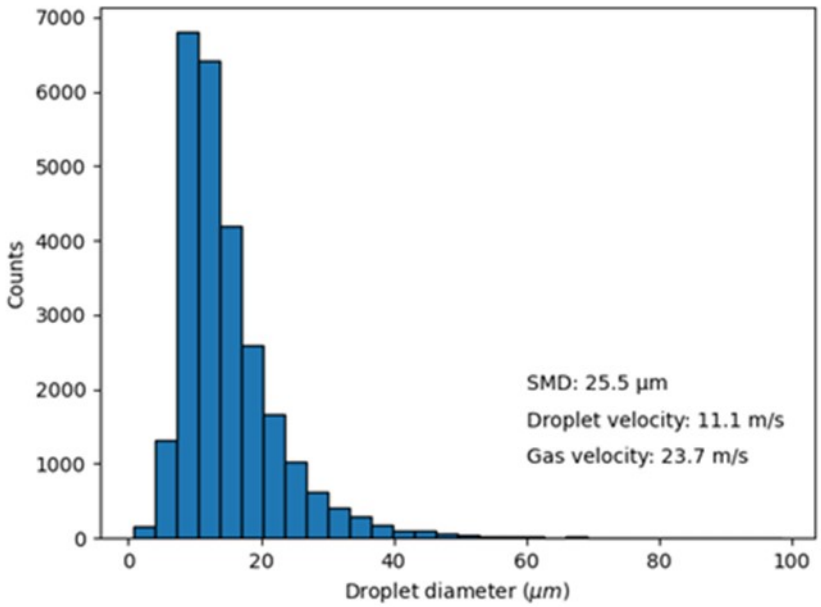


Figure 4.9: Overall droplet size distribution for L2O4.5P1.5 (heptane)

Table 4.5: Results of the PDI measurements at different synthesis conditions (L: liquid flow rate (ml/min), O: oxygen gas flow rate (L/min), and P: gas pressure of (bar))

| S/N | Synthesis Conditions | Droplet count | SMD | Avg droplet vel (m/s) | Gas vel (m/s) |
|---|---|---|---|---|---|
| 1 | L2O4.5P1.5 | 26058 | 25.55 | 11.07 | 23.74 |
| 2 | L3O4.5P1.5 | 35939 | 22.5 | 10.68 | 24.77 |
| 3 | L2O3.5P1.5 | 28008 | 31.84 | 9.99 | 22.52 |
| 4 | L3O3.5P1.5 | 34511 | 27.09 | 10.44 | 23.55 |
| 5 | L2O3.5P2.5 | 30763 | 33.2 | 10.64 | 21.18 |
| 6 | L3O3.5P2.5 | 40992 | 29.98 | 11.45 | 25.89 |

surprising that the dispersion gas flow predominantly controls the atomization process as increased dispersion gas causes an increased gas flow which better accelerates the droplets and enhances more droplet break-up [103].

### 4.3.3 Application of PDI measurements to the model

The PDI measurements of sprays generated with the synthesis conditions from the air-assisted nozzle are used as initial conditions in the model. Figure 4.10a through figure 4.11b show the droplet temperature and the MBLT for EHA/toluene mixtures at six different synthesis conditions using the developed model based on constant flame temperature. In all cases, the droplet temperature maximizes at about 373 K. In the first 15 mm in the flame (vertically), the rate of precursor release remains relatively the same for all the synthesis conditions (provided the precursor does not decompose) due to the same heating rate and MBLT. However, at above 15 mm, the release of precursors decreases with decreasing liquid flow rates (L3O4.5P1.5 vs. L2O4.5P1.5, L3O3.5P1.5 vs. L2O3.5P1.5) and lowering oxygen flow rates (L3O4.5P1.5 vs. L3O3.5P1.5 and L2O4.5P1.5 vs. L2O3.5P1.5) due to the increasing MBLT, despite that the temperatures continue to be roughly the same for all the synthesis conditions. Increasing the nozzle pressure drop from 1.5 bar to 2.5 bar also reduces the release rate due to the increased MBLT, while the suppression of precursor release rate at a reduced liquid flow rate is further confirmed at the pressure drop of 2.5 bar (L3O3.5P2.5 vs. L2O3.5P2.5). These imply that reducing liquid and oxygen flow rates and increasing pressure drop for the atomization will individually enhance the number of fine primary particles due to increased MBLT at 15 mm above the nozzle tip.

Furthermore, the precursor vaporization will be inherently slow since the 373 K maximum droplet temperature is less than the vaporization temperature of the precursor. Hence, a higher droplet lifetime will be required for the complete vaporization of the precursor. If

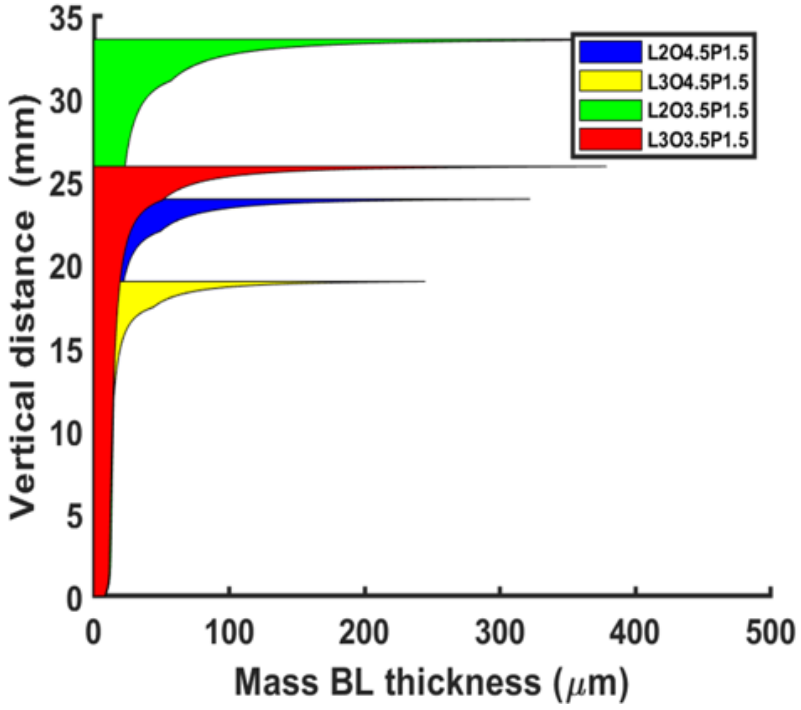


(a) The change in the mass boundary layer thickness as a function of vertical distance in the flame

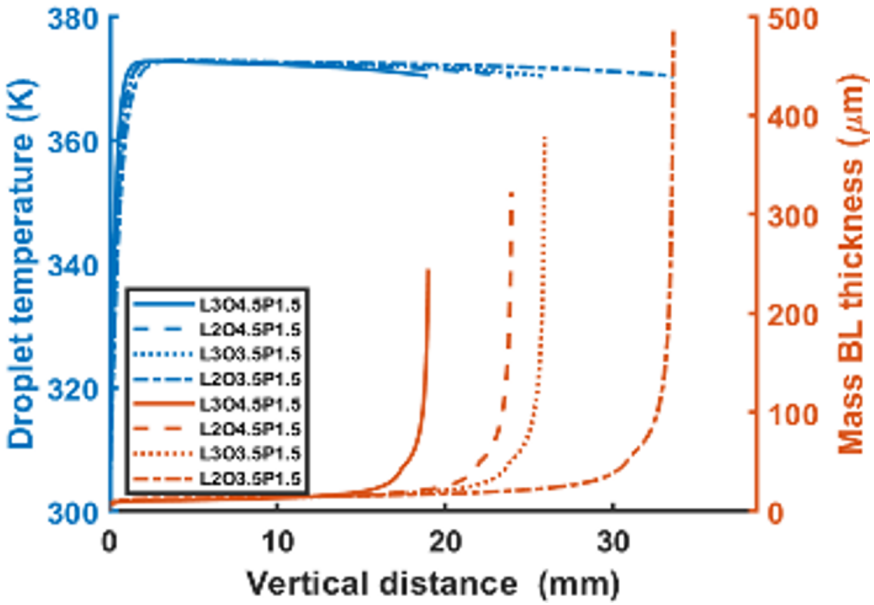


(b) Droplet temperature and mass boundary layer thickness as a function of vertical distance in the flame

Figure 4.10: Synthesis conditions at 1.5 bar

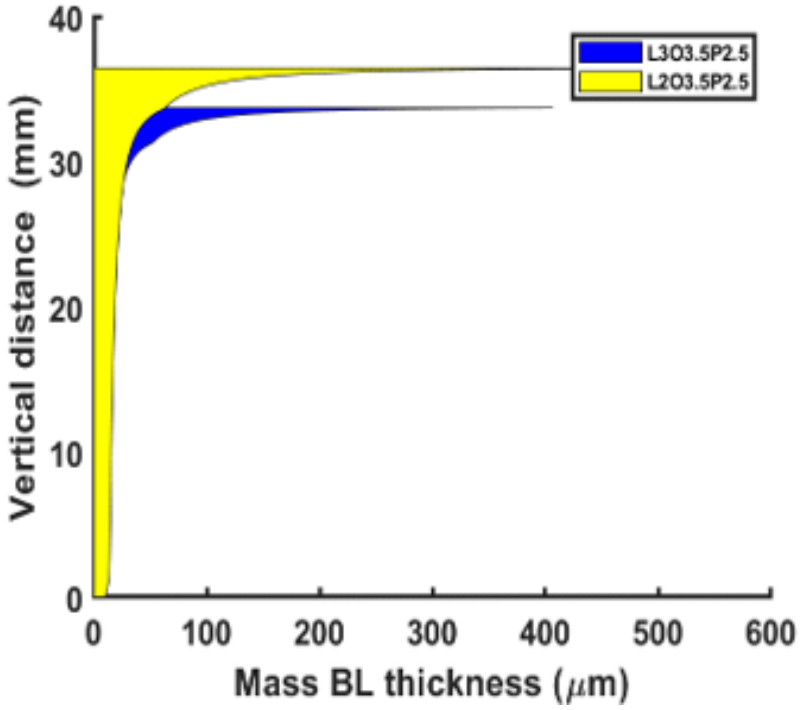


(a) The change in the mass boundary layer thickness as a function of vertical distance in the flame

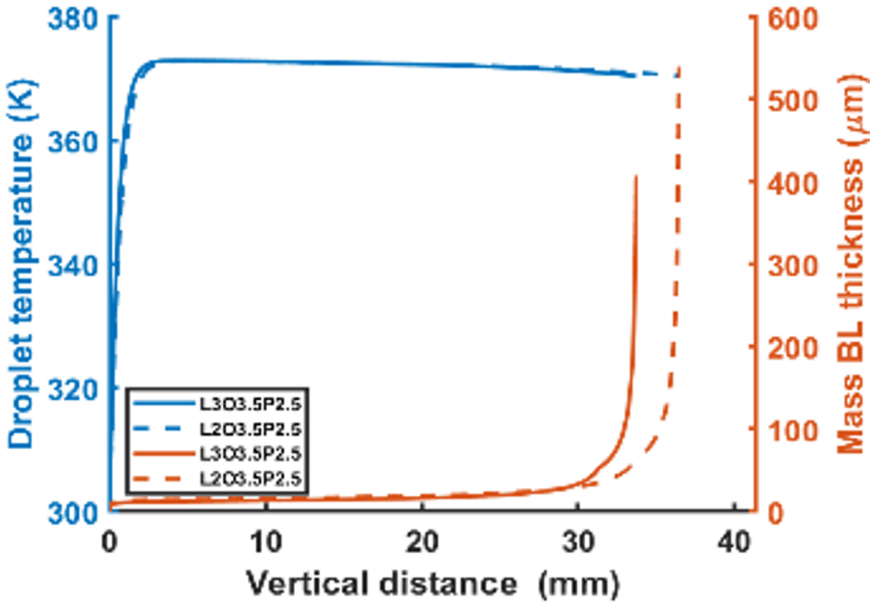


(b) Droplet temperature and mass boundary layer thickness as a function of vertical distance in the flame

Figure 4.11: Synthesis conditions at 2.5 bar

total precursor vaporization time is tuned to be the same for all the considered synthesis conditions and in between the lowest and highest droplet lifetimes, the L2O3.5P2.5 condition will most likely ensure complete vaporization of precursors due to its highest droplet lifetime ($\sim$ 2.3) ms, and the highest vertical distance traveled ($\sim$ 37 mm) before complete solvent vaporization. The complete precursor vaporization will ensure a gas-to-particle formation route rather than the droplet-to-particle formation route to produce homogeneous nanoparticles. On the other hand, the L3O4.5P1.5 condition is less likely to result in complete precursor vaporization due to its lowest droplet lifetime ( $\sim$ 1 ms and $\sim$ 19 mm), assuming the same total precursor vaporization time is remained the same ensured for all the cases. In such a case of complete solvent vaporization before complete precursor vaporization, the droplet-to-particle route is followed for particle formation; however, some precursor molecules are still vaporized, indicative of gas-to-particle formation, leading to a mixture of gas-to-particle and droplet-to-particle formation routes. By extension, particle formation at the other synthesis conditions is expected to proceed with different degrees of mixing of formation routes depending on their droplet vaporization time. In other words, the tendency for pure gas-to-particle mechanism increases in the order of L3O4.5P1.5 ($\sim$ 1.08 ms), L2O4.5P1.5 ($\sim$ 1.38 ms), L3O3.5P1.5 ($\sim$ 1.5 ms), L3O3.5P2.5 ($\sim$ 1.75 ms), L2O3.5P1.5 ($\sim$ 2.05 ms), and L2O3.5P2.5 ($\sim$ 2.3 ms) due to their increasing droplet lifetime. However, the extent of the mixture of the formation routes will generally be dictated by the droplet temperature, droplet lifetime, loading, and vaporization rate.

## 4.4 Conclusions and Proposed Work

The SDC model is scrutinized to quantitatively extract and apply the droplet heating rate and the MBLT around the droplet to understand precursor vaporization during flame spray pyrolysis. Based on the model, the heating rate drives precursor droplet vaporization while

the MBLT created around the droplet can additionally control the precursor droplet vaporization. Furthermore, the solvent with a low specific heat capacity will enhance droplet vaporization for solvents and precursors, as in the case of the solvent mixture containing EHA. Based on droplet characterization of sprays generated with six synthesis conditions tested with the PDI system, the model reveals that all the synthesis conditions have similar temperature history. Still, the MBLT deviates above 15 mm in the flame, indicating a potential difference in the precursor release and consequently homogeneity of the primary particles above this region. Specifically, increasing the pressure drop during atomization and decreasing the oxygen and liquid flow rates are found to reduce precursor release rate above the 15 mm region. Application of the droplet characterization to the model also suggests that the L2O3.5P2.5 condition tends to result in a pure gas-to-particle formation route while the L3O4.5P1.5 condition could result in a droplet-to-particle route. However, quantification of precursor release can be carried out in the future by including precursor properties in the developed SDC model for the rational design of uniform nanomaterial synthesis by FSP.

# Chapter 5

# Control of Homogeneity of Flame Synthesized Particle using Film Theory-Single Droplet Combustion Modeling

## 5.1 Introduction

Homogeneity of the particle is an important factor that can contribute to the performance of catalysts. Homogeneous particle size distribution of catalysts can enhance the selectivity of valuable products during chemical reaction. It is therefore pertinent to have control over the homogeneity of particles during synthesis.

Flame synthesis is one of the synthesis techniques that allows control of particle size and particle homogeneity of synthesized particles. The solvent composition can be tuned to enhance droplet microexplosion which facilitates enhanced droplet vaporization leading to

an improved homogeneity of synthesized particles. The particles in the agglomeration stage during particle formation can also be quenched to control the rate of particle sintering for the control of particle size. Beyond adopting additional solvents or quenching ring, developing strategies to maintain particle homogeneity of particles will be beneficial for using flame synthesis for synthesizing high performing catalysts.

Control over the instantaneous release rate of the precursor gradient translating to the precursor concentration gradient can be adopted to control the homogeneity of the particles formed during synthesis. This is possible because the vaporization of precursor from the precursor-solvent droplet during flame spray pyrolysis (FSP) via the gas-to-particle mechanism is not typically fast and can therefore lead to a gradient of precursor vapor concentration during the synthesis which consequently results in a gradient of reaction products concentration. The nucleation of reaction products gradient will result in the distribution of sizes of primary nucleated particles during synthesis, since the size of particles formed during the FSP depends on the concentration of the nucleating precursor.

Despite the importance of the precursor release rate for the control of homogeneity, there is lack of experimental technique for its direct measurement and the modeling approach is being adopted . It is quantified through the single droplet combustion model based on its immediate release from the droplet. However, our previous single droplet combustion modeling provides a qualitative accurate prediction of precursor release rate based on the coupling of quantified temporal droplet temperature and the mass boundary layer thickness surrounding the droplet during combustion, based on the assumption of constant precursor total amount inside droplet. Here, we further quantified the precursor release rate by adopting the precursor diffusion model with two moving boundary conditions, to directly correlate the precursor release rate with the synthesis parameters for a more precise prediction of particle homogeneity in flame synthesis. In addition, the quantification is important where the droplet temperature and mass boundary layer give different directions of predicting precursor

release.

## 5.2 Methodology

### 5.2.1 Model development

The release of the precursor is modeled as the diffusion of the precursor vapor species in the spherical diffusional film created around the droplet by the solvent vapor, as described by the diffusion equation (5.1). There is no reaction inside the diffusional film and steady state approximation is considered at any instantaneous time during the vaporization process.

$$\frac{d}{dr}\left(r_2 \frac{cD_{prec-film}}{1-x_{prec}} \frac{dx_{prec}}{dr}\right) = 0 \tag{5.1}$$

where c is the molar concentration of the gas film which is given by equation (5.2)

$$c = \frac{\rho_{gasfilm}}{MW_{gasfilm}} \tag{5.2}$$

During the vaporization, the droplet shrinks resulting in decreasing $r_1$ value while the mass boundary layer thickness increases which can lead to a change in $r_2$. This result in a diffusional problem with two moving boundary conditions as described in equation (5.3), in which $x_{1,prec}$ is the precursor concentration at the surface of the droplet while $x_{2,prec}$ is the precursor concentration at the other side of the film, which is zero due to fast reaction of the precursor in the combustion zone of FSP.

$$r_1 = \frac{d_d}{2}; x_{1,prec} = x_{s,prec} \tag{5.3}$$

$$r_2 = r_1 + \sigma_M; x_{2,prec} = 0 \tag{5.4}$$

Similar to the solvent, the molar concentration of precursor vapor at the droplet surface, $x_{s,prec}$, is obtained from its molar concentration in the liquid droplet, $x_{s,prec}$, and its pure component vapor pressure by Raoult's law (with the assumption of ideal mixing by ignoring the effect of the difference in components' molar volumes in the liquid phase and the assumption of ideal gas behavior of species in the vapor phase), as in equation (5.5), while the vapour pressure is also obtained by Clausius Claperyon relation, as in equation (5.6), based on the droplet temperature obtained from the solvent vaporization model.

$$x_{s,prec} = \frac{x_{l,prec} P_{vp,prec}}{P_{atm}} \tag{5.5}$$

$$\ln\left(\frac{P_{vp,prec}}{P_{atm}}\right) = -\frac{\triangle H_v}{R}\left(\frac{1}{T_d} - \frac{1}{T_{bp,prec}}\right) \tag{5.6}$$

The analytical solution to the diffusion equation is given by the molar flow rate $W_{prec}$ described by equation (5.7) [111],

$$W_{prec} = \frac{4\pi c D_{prec-film}}{\frac{1}{r_1} - \frac{1}{r_2}} \ln\left(\frac{1 - x_{2,prec}}{1 - x_{1,prec}}\right) \tag{5.7}$$

which, using the boundary conditions, simplifies to equation (5.8), .

$$W_{prec} = \frac{4\pi c D_{prec-film}}{\frac{1}{(d_d/2)} - \frac{1}{(d_d/2)+\sigma_M}} \ln\left(\frac{1}{1 - x_{s,prec}}\right) \tag{5.8}$$

Equation (5.8) gives the instantaneous quantified precursor vaporization rate during synthesis. The parameters in the derived equation are time-variant, as determined from the droplet vaporization model. The quantified precursor release rate equation is consistent with the basis of qualitative prediction. From the equation, as the mass boundary layer thickness $\sigma_M$ increases, the precursor release rate $W_{prec}$ is reduced, while increased droplet temperature

Table 5.1: Properties of cerium ethyl hexanoate precursor

| S/N | Properties | values |
|---|---|---|
| 1 | Mol fraction | 0.001 |
| 2 | Diffusivity in gas film ($m^2/s$) | 3.97e-6* |
| 3 | Boiling point (K) | 498* |
| 4 | Heat of vaporization | 4.6e5* |
| 5 | Molecular weight (Kg/mol) | 569.7e-3 |

$T_d$ enhances the surface concentration of precursor vapor $x_{s,prec}$ which consequently leads to enhanced precursor release rate.

## 5.3 Results

### 5.3.1 Ranking of synthesis conditions based on precursor release

The six synthesis conditions whose droplet information is detailed in table 4.5 as characterized by PDI techniques are studied for their precursor release rate. The properties of the cerium ethyl hexanoate precursor considered are highlighted in table 5.1. Based on the previous qualitative prediction, the decrease in the heating rate and increase in the boundary layer thickness suggest the decreasing precursor release rate for the first four synthesis conditions. However, there is a conflict between the indications of these quantified metrics on precursor release for the last two synthesis condition. There is an increase in the MBLT for synthesis conditions 5 and 6 in consistence with the other four synthesis conditions suggesting decreasing precursor release while the heating rates for conditions 5 and 6 increase concerning the fourth synthesis condition offering an increased precursor release. It is difficult to determine the resultant effect on precursor release due to the conflict between the two quantified metrics. Figure 5.1a shows the quantified instantaneous precursor release rate during the course of the droplet vaporization. Like solvent vaporization, precursor vaporization occurs in two stages: (1) a region of increasing precursor vaporization rate

corresponding to the increasing droplet temperature and (2) a region of decreasing precursor vaporization rate corresponding to the constant droplet temperature. However, there is a lag in the precursor vaporization, as shown in figure 5.1b, compared to solvent vaporization. For all six synthesis conditions, the second vaporization period is typically longer than the first, indicating the second region's dominance for precursor vaporization. In addition, the precursor completely vaporizes at the end of the droplet lifetime following the same ranking as the qualitative analysis, indicating the consistency of the quantitative analysis with the qualitative analysis. The instantaneous precursor release rate in the first region decreases in the order of L3O4.5P1.5, L2O4.5P1.5, L3O3.5P1.5, L3O3.5P2.5, L2O3.5P1.5, L2O3.5P2.5 which is also consistent with the decreasing droplet lifetime/solvent vaporization time while the precursor release rate in the second region increases in the same order. The second region has a direct opposite ordering predominantly due to the increasing maximum vaporization rate in the specified order. The qualitative ranking of the synthesis conditions based on droplet temperature and mass boundary layer prediction matches the prediction from the quantitative modeling when the first vaporization is considered.

The cumulative flow after a particular period, shown in figure 5.2a, is quantified by integrating the instantaneous precursor vaporization rate curve in figure 5.1a. The cumulative precursor flow decreases and increases in the order of L3O4.5P1.5, L2O4.5P1.5, L3O3.5P1.5, L3O3.5P2.5, L2O3.5P1.5, L2O3.5P2.5 in the first and second region respectively, in consistence with the ranking based on the instantaneous vaporization rate in both regions. With the cumulative precursor flow at the end of the vaporization reflecting the maximum vaporizable precursor that is offered by each of the synthesis conditions, the maximum vaporizable precursor increases in the order of L3O4.5P1.5, L2O4.5P1.5, L3O3.5P1.5, L3O3.5P2.5, L2O3.5P1.5, L2O3.5P2.5, similar to the maximum instantaneous precursor vaporization rate. This implies that the maximum vaporizable precursor amount at each synthesis condition controls the vaporization rate. For the same precursor concentration of 0.1 mol% in the precursor-solvent solution, the L3O4.5P1.5 has the highest maximum vaporizable precursor

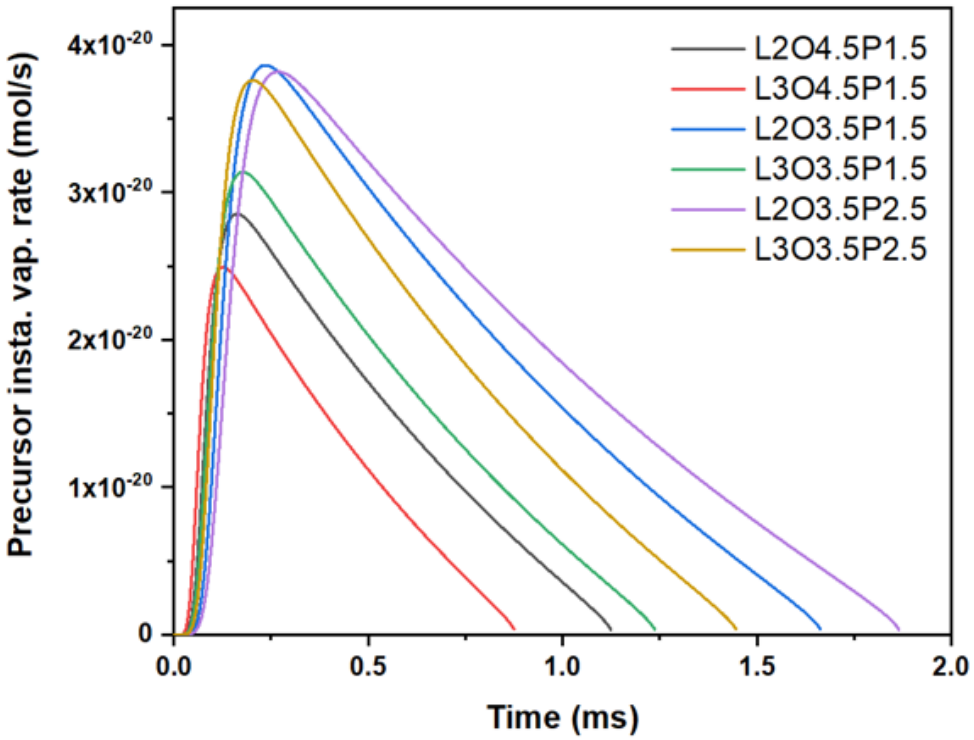


(a) Instantaneous precursor vaporization rates

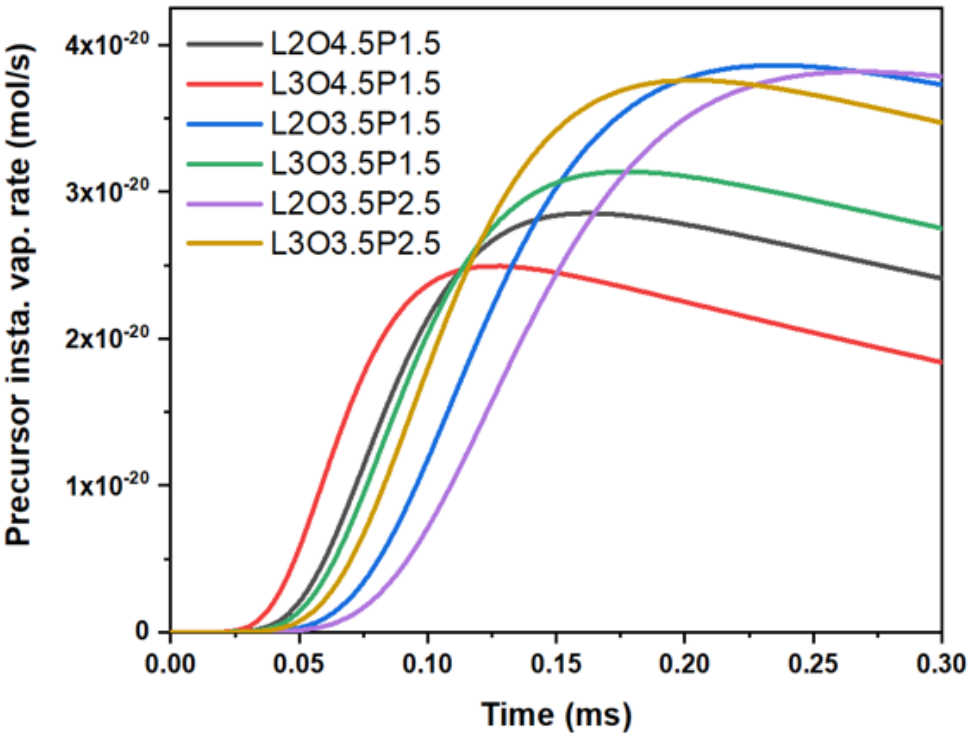


(b) Zoomed instantaneous precursor vaporization rates

Figure 5.1: Instantaneous precursor vaporization rates for solvent mixtures of EHA:Toluene of 1:1

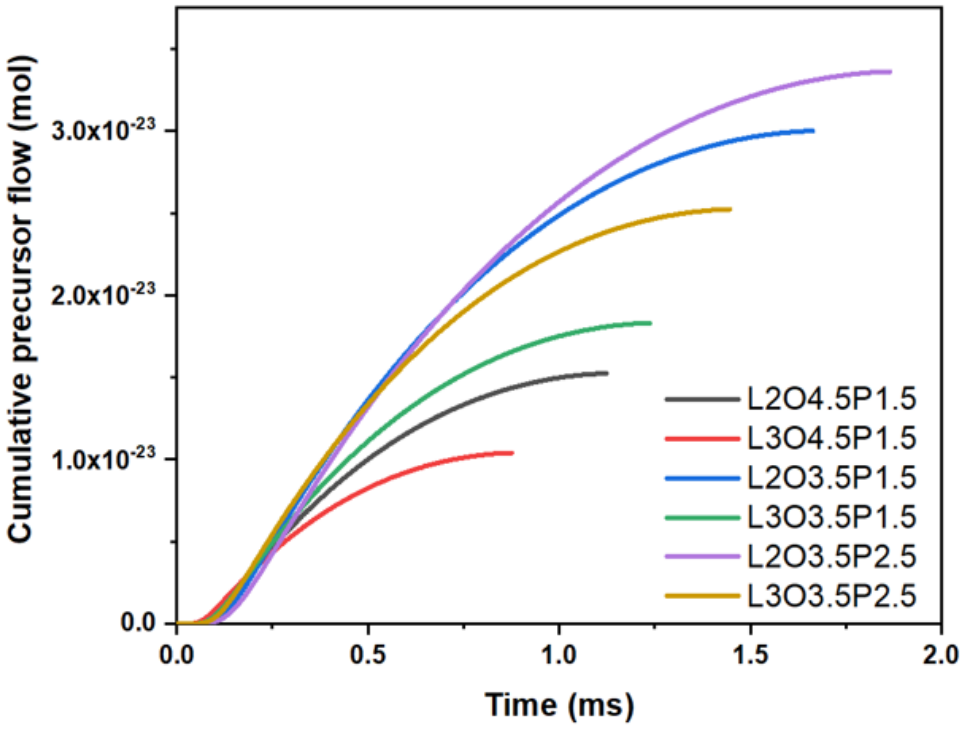


(a) Cumulative precursor vaporization

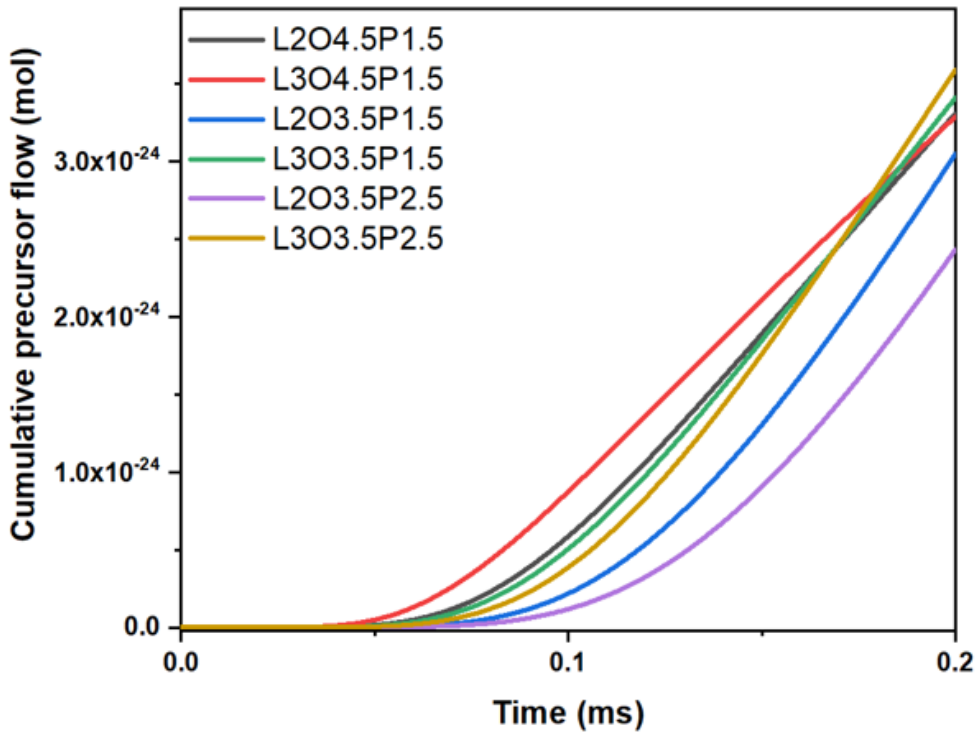


(b) Zoomed cumulative precursor vaporization

Figure 5.2: Cumulative precursor vaporizations for solvent mixtures of EHA:Toluene of 1:1

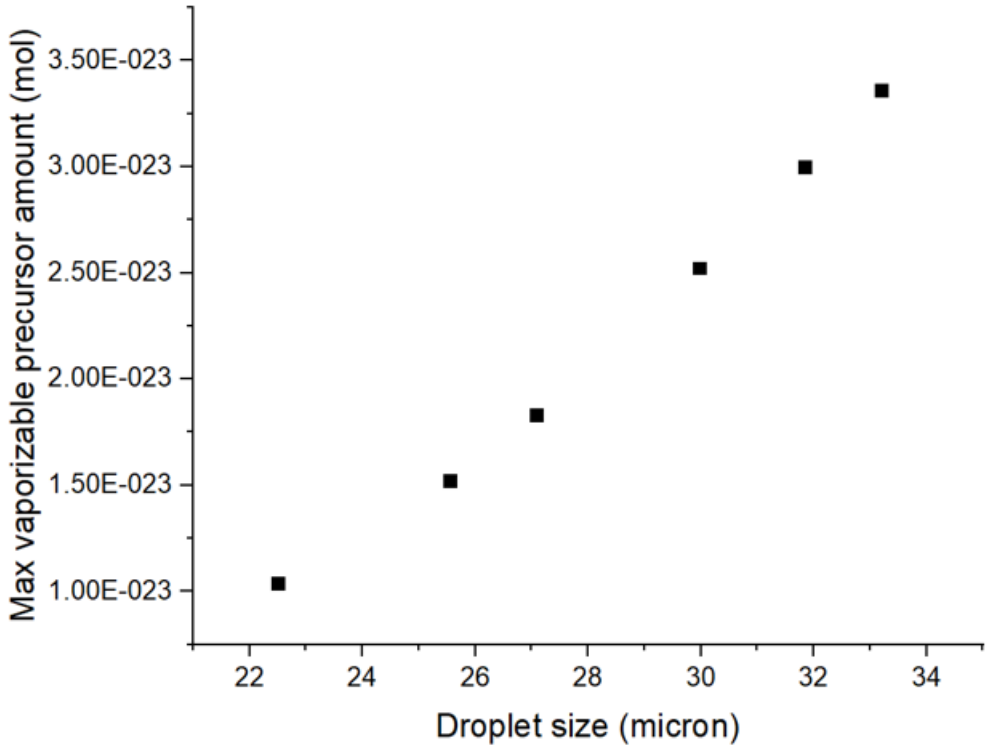


Figure 5.3: Maximum vaporizable precursor vs droplet size

of 3.5E-23 mol/droplet while L2O3.5P2.5 has the lowest amount at 1.0E-23 mol/droplet.

The order based on the instantaneous precursor vaporization rate in the first region is consistent with the previous order based on qualitative prediction, while the order based on the fast precursor vaporization rate in the second region suggests the direct opposite, indicating the heating rate and boundary layer thickness control the precursor vaporization rate in the first region while they do not exist in the second region. Figure 5.1 and figure 5.3 show that the instantaneous vaporization rate in the second region, the maximum vaporization rate and the maximum vaporizable precursor amount increase in the specified order due to the increasing droplet size associated with these synthesis conditions, indicating that the droplet size controls the second vaporization region. With the same precursor concentration of 0.1 %, increasing the droplet size increases both precursor vaporization rate and maximum vaporizable amounts due to the higher amount of the precursor in the droplet. In order words, the amount of precursor in each droplet controls the maximum precursor vaporization rate

during droplet combustion in FSP.

### 5.3.2 Prediction of particle homogeneity at different synthesis conditions

The uniformity of the particles formed by these synthesis conditions is investigated by considering the distribution of precursor release rates during the synthesis as shown in figure 5.4. All the synthesis conditions exhibit the same unique precursor release rate up to 2.5 E-23 mol/ms indicating similarity in the unique particle sizes. The number of particles having the unique sizes increases in the order of...., as the order of increasing amount of precursor, however their particle size distributions are similar in terms of their relative number. While the L3O4.5P1.5 condition has all of these unique sizes, other synthesis conditions have particles of larger sizes. The number of additional unique particle sizes increases in the order of L2O4.5P1.5 and L3O3.5P1.5 while the L3O3.5P2.5, L2O3.5P1.5 and L2O3.5P2.5 have roughly the same but the highest number of unique particle sizes. The number of particles for these unique cases increase in the order of L3O3.5P2.5, L2O3.5P1.5 and L2O3.5P2.5 due to the increasing precursor amount, yet they have similar particle size distribution.

**Homogeneity of synthesized catalysts (Proposed work)**

The synthesis conditions considered here can be applied to the synthesis of ceria-based catalysts, and the synthesized catalysts are characterized using microscopy techniques. The model-based predicted homogeneity of the particles can then be compared with the particle size distribution obtained experimentally.

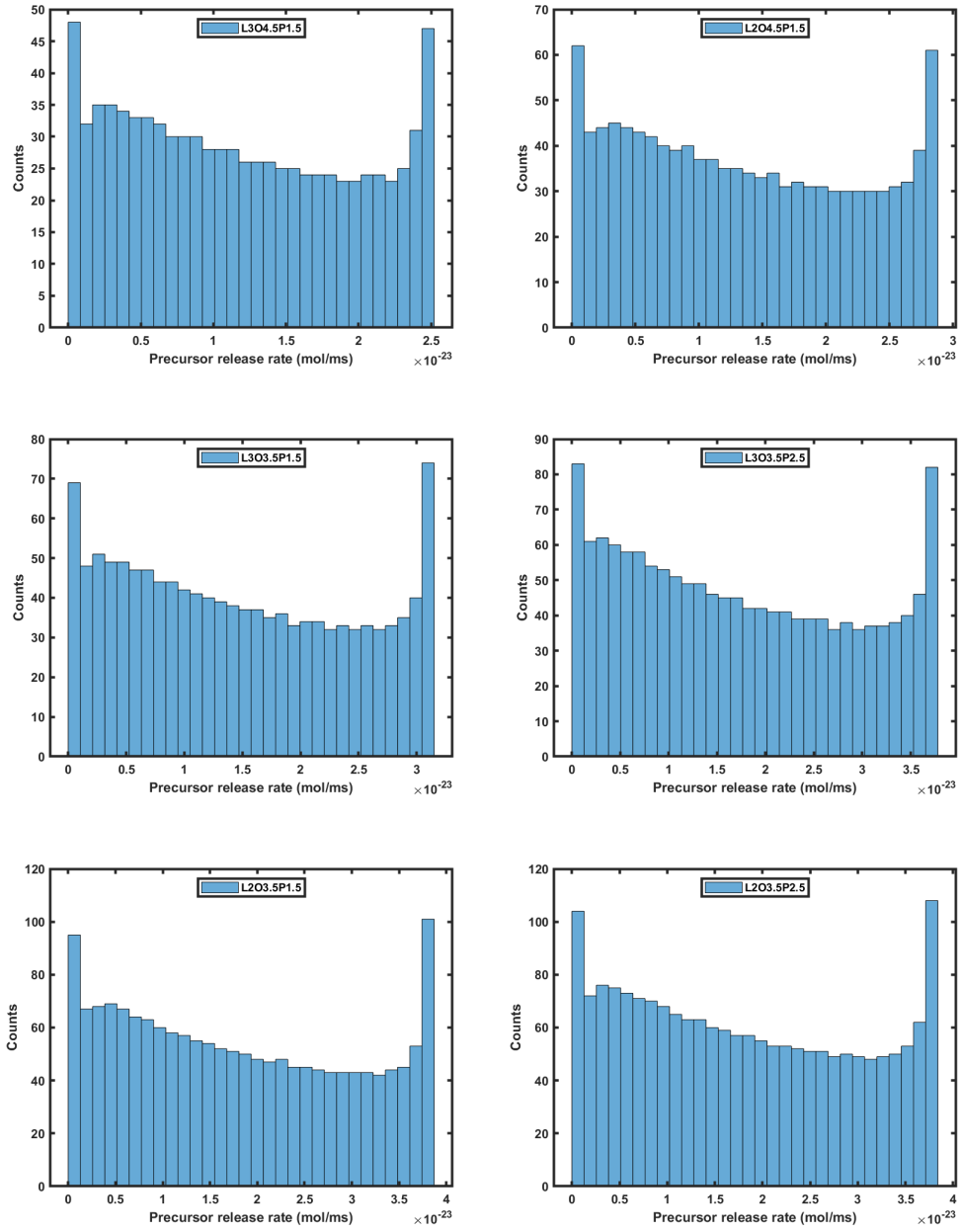


Figure 5.4: Distribution of precursor release rate at different synthesis conditions

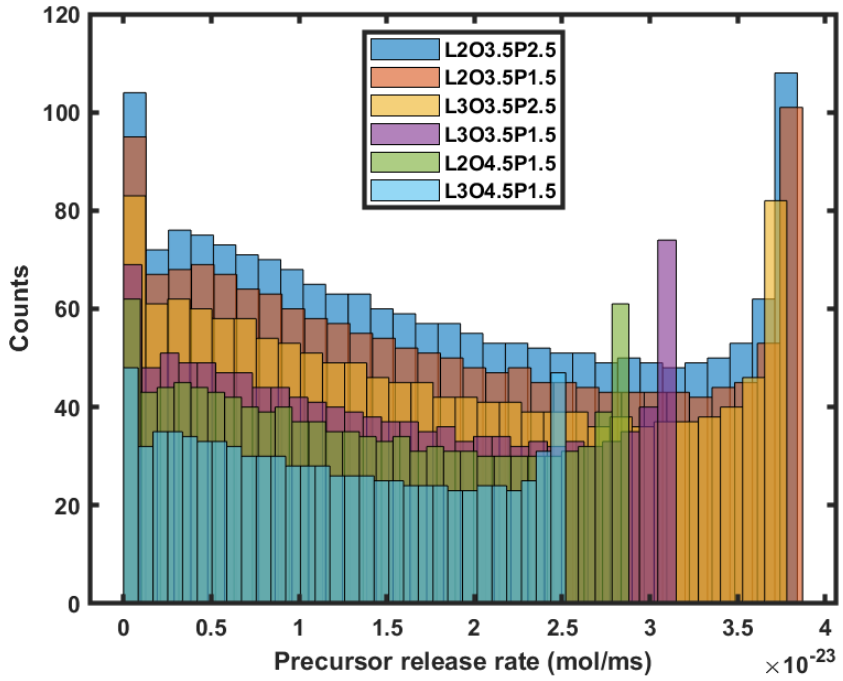


Figure 5.5: Combined count distribution of precursor release rates at the six different synthesis conditions

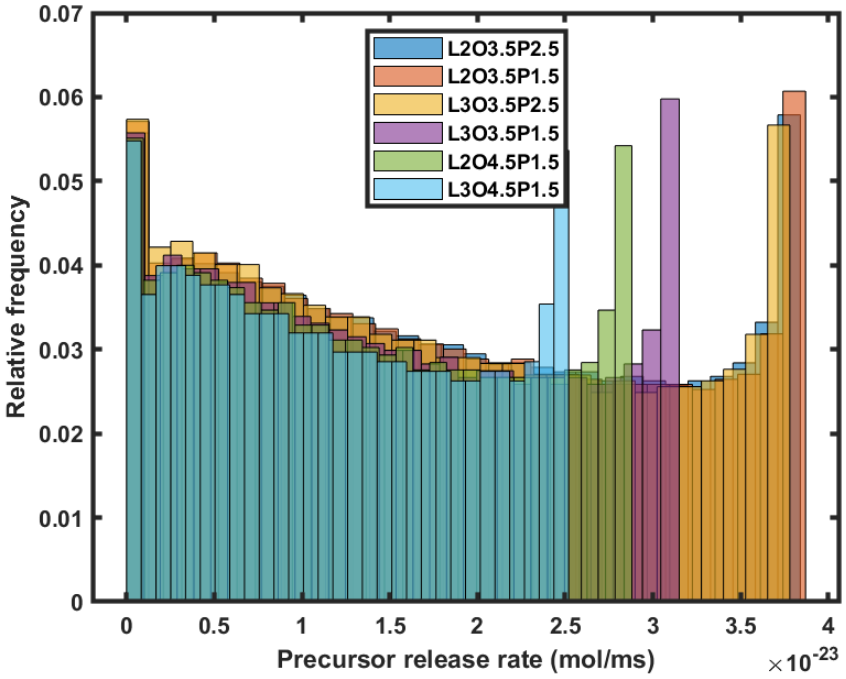


Figure 5.6: Combined frequency distribution of precursor release rates at the six synthesis conditions

## 5.4 Conclusions

Quantification of the release rate of the precursor is modeled as diffusion with moving boundaries in the mass boundary layer created by the solvent vapor around the droplet. The temporal droplet temperature and mass boundary layer profiles obtained from the droplet vaporization model are directly used in the precursor diffusion model to generate the instantaneous release rate of the precursor during the synthesis. The quantification of precursor release rate validates the qualitative prediction while it also applies to general cases, including situations when prediction by qualitative analysis seems complicated. It further identifies the amount of precursor inside the droplets as an important factor determining the maximum precursor vaporization rate during flame spray pyrolysis. Frequency analysis of the quantified precursor release rate was applied to predict particle size distribution. Based on frequency analysis of precursor release rates of 6 synthesis conditions, the L3O4.5P1.5 condition is predicted to have some unique particle sizes, while the other synthesis conditions share the same particle sizes but additionally contain larger particles. L2O4.5P1.5 has an increased number of particle sizes, followed by L3O3.5P1.5, while the L3O3.5P2.5, L2O3.5P1.5 and L2O3.5P2.5 have roughly the same but highest number of unique particle sizes. Size distribution of particles synthesized at these synthesis conditions can be obtained experimentally using microscopy techniques and computational model predictions.

# Chapter 6

# An Outlook on the Application of Machine Learning for Catalyst Discovery in Flame Spray Pyrolysis

## 6.1 Introduction

With the rise of the adoption of machine learning (ML) as a new and complementary paradigm of scientific research, scientific discovery has benefitted a great deal of unprecedented progress in recent years. Massive impact spans from those in basic and applied research in bioinformatics to chemoinformatics, and now to catalysis and material science creating opportunities for rapid discovery of materials and knowledge extraction. Catalysis and material science fields from both experimental and computational perspectives are being enhanced by ML. The high volume of data in computational catalysis and material informatics including those in several established databases has favored the significant extension of its capability and solution to its deficiency such as uncertainty through machine learning.

Now, the scrutiny of ubiquitous DFT and material data is done to extract better insight for more rapid and effective determination of active site structures and reaction mechanisms involved in catalytic reactions; and to create a library of materials of predicted properties [112]. For instance, rather than solely depending on the single crystal DFT calculations for the catalytic performance of RhAu alloy for NO decomposition, Jinnouchi and Ashai [113] explored a machine-learning scheme to capture the atomic-scale defects of the alloy for a more efficient prediction of active sites and activities of the alloy catalyst. Similarly, a machine learning surrogate model was explored to ratify the complexity of modeling bimetallic nanoparticle catalysts to better understand and predict for $CO_2$ electrochemical reduction [114]. In the field of computational material science, part of the most exciting ML application includes the use of LASSO-1D for the prediction of intrinsic dielectric breakdown field of insulators binary compounds with extension to 3 and 5 atoms systems with similar accuracy, based on the two most important properties of the materials [115, 116]. Also, Bialon et al [117, 118] explored the ML clustering approach based on three functional descriptors derived from three-primary material properties to create a 3-dimensional crystal structure map that allocates one of 64 different prototypical binary crystal structures to any binary sp-d-valent compounds. However most recently, experimental catalysis has also started gaining knowledge-based insight from experimental results through ML, starting from the deduction of heuristics of high performance catalysts such as seeking the most important reaction conditions and relative importance between catalyst preparation variables and reaction conditions, for instance for CO oxidation over copper-based catalysts [119], WGS reactions Pt and Au catalysts [120] and dry reforming of methane catalysts [121]; and catalysts composition-activity mapping [122]. In a somewhat related but independent application, advanced ML algorithms have been used for spectral data processing and analysis to extract quantitative and qualitative information from some characterization spectra such as for the identification of chemical species from Raman spectra [123], imaging of chemical properties of materials from Time of Flight Secondary Ion Mass Spectrometry [124], ele-

mental analysis from laser-induced breakdown spectroscopy [125, 126, 127] among others. Perhaps, due to the complexity of catalytic reactions, a developing idea in the application of machine learning in experimental catalysis is the inclusion of machine-learning spectra analyzed information from relevant catalyst bulk and surface characterization as part of the features for more accurate machine learning catalytic performance modeling, prediction and knowledge extraction [128]. This includes mapping the activity of catalysts to their structural properties to predict untested but characterized catalysts' activity, helping to guide the choice of active catalysts and therefore reducing the time for discovering catalysts. ML is also currently being explored in the design of the synthesis routes of catalyzed reactions such as the predictive identification of ligands for Pd-catalyzed C–N coupling reaction [129] and others [130], replacing the traditional trial-and-error synthesis conditions selection carried out by human scientists and providing guidance for better decision making.

FSP is a technique used to synthesize materials by combusting atomized spray of their precursor solutions. One of its key features is that its synthesis environment such as the thermal and chemical environment can be precisely controlled through its numerous synthesis parameters. Due to the numerosity of parameters, it could sometimes be challenging to optimize material property. However, much data can be generated from the synthesis process. Motivated by the power of data-driven methodology as proven in various fields including science and engineering, we are interested in developing a data-driven methodology that will enable automated synthesis for the accelerated discovery of high performing materials. In this work, machine learning methodology is developed for FSP to allow for the accelerated discovery of high performing catalysts. Developing AI-FSP methodology involves optimizing a target nanomaterial property such as structures or phases within FSP synthesis conditions parameter search space. This is achieved by searching a vast parameter space of solvent choice/solvent mixture ratio and flame synthesis conditions. Relevant descriptors which characterize the critical steps and processes involved in the particle formation in the flame are employed with the most suitable ML algorithm to generate the machine learning models

that will capture the underlying relationship within the synthesis condition parameters.

## 6.2 AI-FSP methodology development

Relevant features were engineered based on the fundamental understanding of the FSP process. The thermal and chemical environment of the synthesis conditions, such as the equivalence ratio and the adiabatic flame temperature were derived computationally from the synthesis conditions. One capability of the AI-FSP methodology is to be able to identify possible 'values' of a particular property of a material obtainable during FSP, such as the potential number of phases of mixed oxide and the possible structure of single atom catalysts. Unsupervised learning was adopted to identify the hidden patterns in the synthesis conditions that could result in different catalyst properties. K-means clustering is an unsupervised learning algorithm that aims to create a partition of instances into non-overlapping subsets such that instances within the same subsets are similar while those outside the subsets are dissimilar. It is a popular and fast method of clustering. It has been adopted as a multivariate chemometric method for solving structural problems of biomolecules such as allergenicity detection [131]. It has also been employed to identify the naturality of medicinal materials based on their microelement contents [132]. In this algorithm, the positions of cluster centroids are optimized at stabilized centroids from some initial randomly selected centroids through iterative calculations. It does this by minimizing the within-cluster sum-of-squares (also known as the initial) criterion which measures how internally coherent the clusters are, as illustrated in figure 6.1. The algorithm is composed in such a way that instances are assigned to the clusters having the shortest distance to them and the new centroids are determined based on the means of the distances of the newly assigned instances. Due to its high sensitivity to cluster center initialization, the algorithm sometimes does not guarantee convergence to the global optimum, but this problem was avoided by choosing the best result

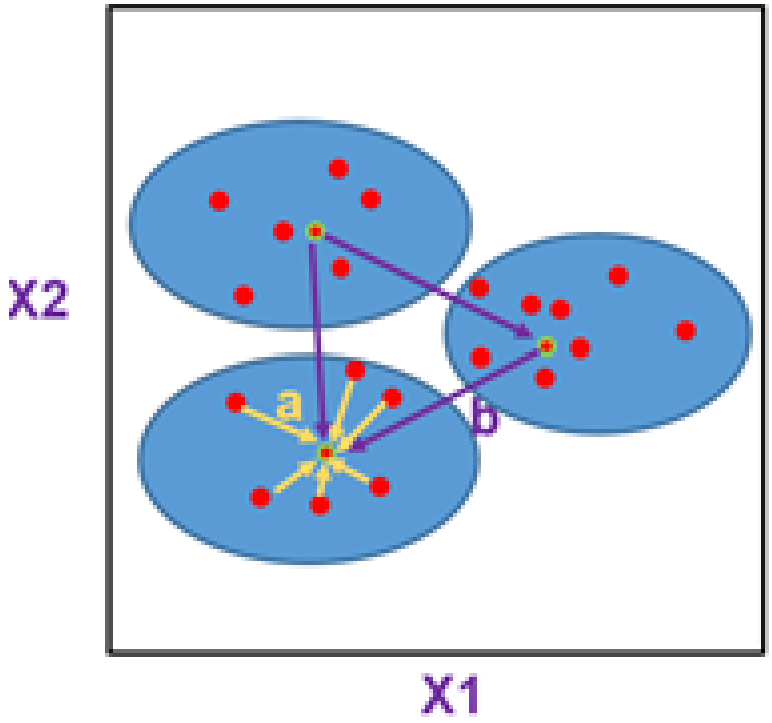


Figure 6.1: K-means algorithm working principle (X1 and X2 are features)

from multiple trainings of the algorithm with several different initial conditions riding on the fast convergence of this algorithm. To ensure the accuracy of the clustering algorithm, a careful choice of the similarity measure was considered based on the nature of the data set and the performance of different similarity measures. Based on 18 features and 14500 synthesis conditions generated within the parameter search space (liquid flow 2-4 ml/min, EHA solvent fraction 0-1, total gas flow 3-5 L/min, gas pressure 1.5 and 2.5, nitrogen flow content 0-90% total gas flow), the visualization of the clustering in the 2D space of liquid flow and oxygen flow shown in figure 6.2a indicate significant non-overlapping of clusters while in 2D space of solvent ratio and gas pressure shown in Figure 6.2b indicate some considerable overlapping. However, the optimal number of clusters is 2 based on the elbow method as shown in Figure 6.2c. This suggests that synthesizable materials will have one of 2 possible 'values' of a particular property.

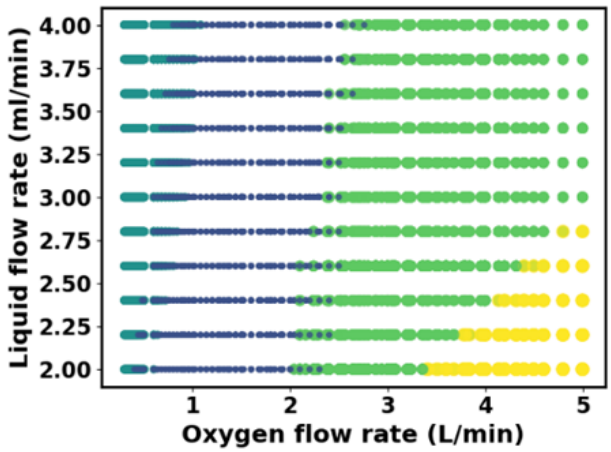


(a) Oxygen flow and liquid flow space

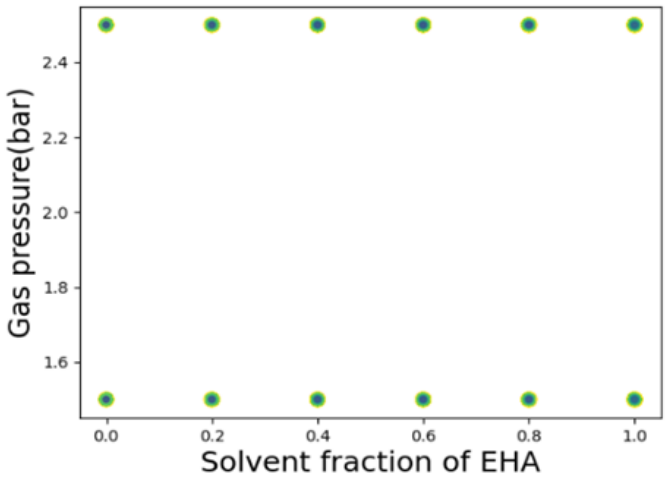


(b) gas pressure and EHA solvent fraction dimension

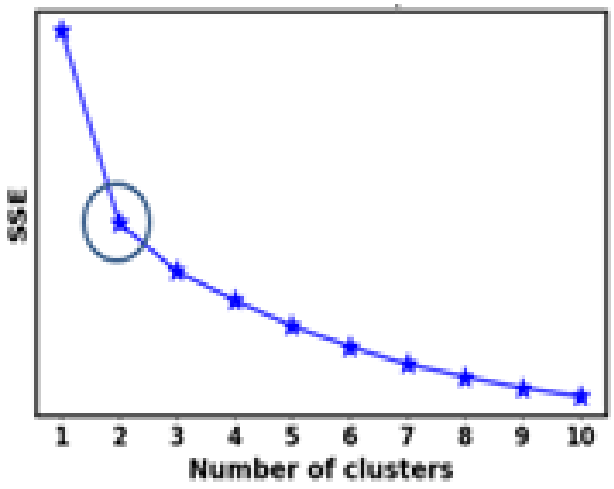


(c) Optimization of the number of clusters based on the elbow method

Figure 6.2: Visualization of clustering and optimization of clusters

## 6.3 Specific proposed work

For all the capabilities that will be developed, it is desired to improve the accuracy of our machine learning predictions. The accuracy can be generally improved by additional relevant features generated from a deeper understanding of the flame spray pyrolysis technique, as depicted by the general scheme in figure 6.3. Since the above clustering was carried out based on the synthesis environment features in the spray, features relating to how the precursor droplets respond to the synthesis environments will provide more relevant fundamental information that will characterize the synthesis conditions. Since this is related to the combustion of the droplet, a physics-based droplet combustion model could be utilized to generate relevant features such as the droplet heating rate and the boundary layer around the droplets. In addition, LIBS spectra that monitor the particle formation process can be added as well, as features. The built model will be applied to guide synthesis by suggesting significant nonidentical synthesis conditions which will produce catalysts of various chemical properties. Recommended synthesis conditions are used for the synthesis of catalysts.

As a case study and proof of concept, the methodology will be applied to optimize the ceria-zirconia-manganese mixed oxide system for its enhanced activity and stability as oxidation catalysts. More specifically, the phase of the Ce-Mn-Zr system will be optimized to achieve a synthesis of a single phase with large lattice parameter change. Existing experimental data consisting of analyzed XRD phase information of 81 synthesized catalysts and the LIBS spectra obtained during synthesis will be used to train the machine learning algorithms. Different ML algorithms will be evaluated for the choice of the best performing algorithm.

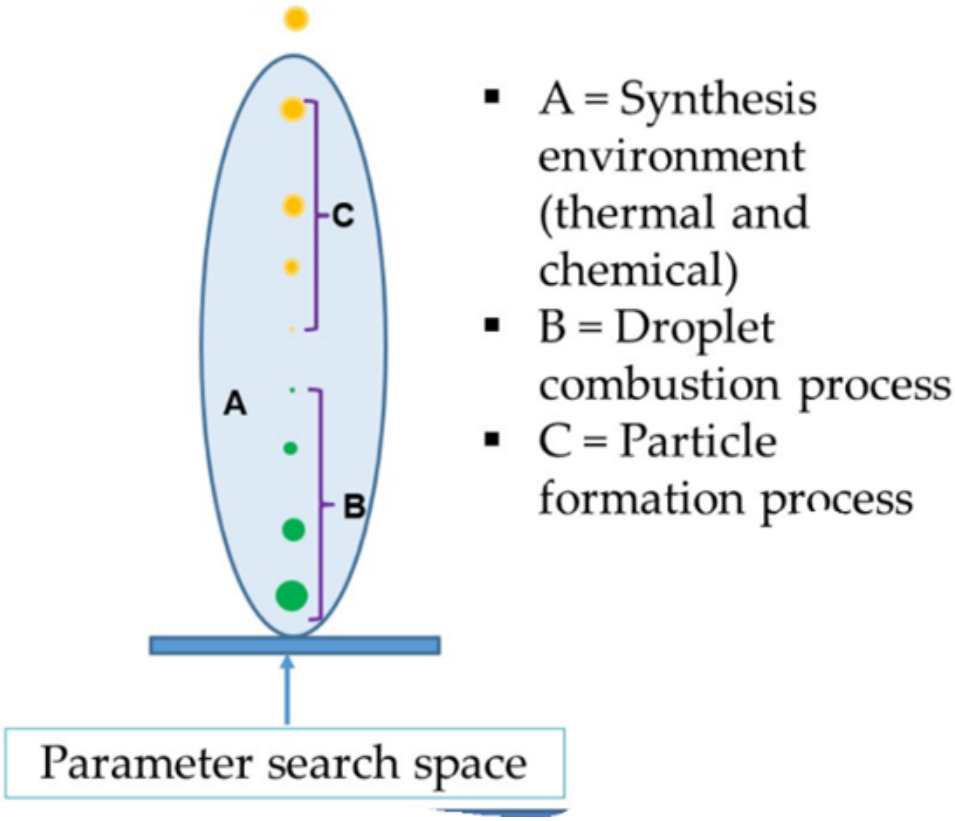


Figure 6.3: Overall scheme for feature generation in FSP

# Chapter 7

# Conclusions and Recommendations

## 7.1 Conclusions

The control of the physical and chemical properties of catalysts is important for the improvement of existing catalysts and development of new ones. Downsizing the nanoparticle and clusters to atomically dispersed level can enhance the activity of the metal while minimizing the utilization of precious metal. The size of the support and the size distribution can also influence the chemical property of the catalysts, consequently contributing to the catalytic performance. Both the downsizing of metal particles to atomically dispersed metal and the prediction of the homogeneity of catalysts particle can be achieved using flame spray pyrolysis.

The control of the speciation of Pd on $CeO_2$ support is dependent on the Pd loading and the chemical environment during FSP process. The Pd loading dictates the Pd vapor concentration inside the flame in which high loading facilitates the formation of nucleating clusters while low loading increases the tendency for isolation of nucleating species. Highly dispersed $Pd^{n+}$, $Pd^0$ and $Pd^0$ can therefore be synthesized on the $CeO_2$ support at high loading while

dispersion up to atomically dispersed Pd can be additional attained at low loading. In addition, the oxidizing environment can form the oxide of Pd which could have a higher tendency to nucleate as isolated species on the support. Consequently, exclusive stabilization of atomically dispersed Pd can be attained at a higher loading in an oxidizing environment than in a reducing environment. The stabilized atomically dispersed Pd demonstrates surface reconstruction under temperature ramping which can be responsible for its enhanced methane oxidation activity.

The mass boundary layer that limits the rate of precursor release should be considered together with the droplet temperature for a more accurate prediction of homogeneity of catalysts particle in flame spray pyrolysis. The mass boundary layer thickness is reduced when the initial size of the precursor droplet is reduced, but it may not be significantly influenced by the solvent ratio such as in the case of EHA/toluene solvent mixture. However, the nozzle operating conditions can predict similar droplet temperature on the basis of constant flame temperature, but the mass boundary layer thickness can be increased when the oxygen flow is reduced, liquid flow is reduced and atomizing pressure is increased. The enhanced accuracy of the prediction of precursor release can be useful for the prediction of homogeneity of various complexity.

## 7.2 Recommendation

This work has demonstrated the use of flame spray pyrolysis for the control of both the speciation of metal particles and the prediction of homogeneity of flame synthesized particles. Specifically, oxidizing environment can achieve exclusive stabilization of atomically dispersed Pd at a higher loading than reducing environment. Also, the mass boundary layer can enhance the accuracy of the prediction, allowing the prediction of complicated size distribution. Based on these, the following tasks are recommended as future work.

1. The interplay between the loading and the oxidizing environment can be further explored to increase the loading at which atomically dispersed Pd can be exclusively stabilized.

2. Insitu analysis reveals that the atomically dispersed Pd demonstrates surface construction while it also demonstrates higher methane activity. The direct investigation of the behavior of the atomically dispersed Pd under methane oxidation can be carried out.

3. Insitu methane oxidation over different structures has identified the $CH_2$ conversion as an important step to the enhancement of methane oxidation reaction over the atomically dispersed Pd. The detailed methane oxidation reaction mechansims can be established.

4. The effects of micro-explosion of precursor droplets on homogeneity can be investigated.

# Bibliography


[1] Xiao-Feng Yang, Aiqin Wang, Botao Qiao, Jun Li, Jingyue Liu, and Tao Zhang. Single-atom catalysts: a new frontier in heterogeneous catalysis. *Accounts of chemical research*, 46(8):1740–1748, 2013.

[2] Maria Flytzani-Stephanopoulos and Bruce C Gates. Atomically dispersed supported metal catalysts. *Annu. Rev. Chem. Biomol. Eng*, 3(1):545–574, 2012.

[3] Huabin Zhang, Guigao Liu, Li Shi, and Jinhua Ye. Single-atom catalysts: emerging multifunctional materials in heterogeneous catalysis. *Advanced Energy Materials*, 8(1):1701343, 2018.

[4] William E Kaden, William A Kunkel, Matt D Kane, F Sloan Roberts, and Scott L Anderson. Size-dependent oxygen activation efficiency over pd n/tio2 (110) for the co oxidation reaction. *Journal of the American Chemical Society*, 132(38):13097–13099, 2010.

[5] Mika Valden, Xiaofeng Lai, and DW9733505 Goodman. Onset of catalytic activity of gold clusters on titania with the appearance of nonmetallic properties. *science*, 281(5383):1647–1650, 1998.

[6] Xiaohui Huang, Huan Yan, Li Huang, Xiaohui Zhang, Yue Lin, Junjie Li, Yujia Xia, Yanfu Ma, Zhihu Sun, Shiqiang Wei, et al. Toward understanding of the support effect on pd1 single-atom-catalyzed hydrogenation reactions. *The Journal of Physical Chemistry C*, 123(13):7922–7930, 2018.

[7] Gregory M Mullen, Edward J Evans, Benjamin C Siegert, Nathan R Miller, Benjamin K Rosselet, Iliya Sabzevari, Adrianna Brush, Zhiyao Duan, and C Buddie Mullins. The interplay between ceria particle size, reducibility, and ethanol oxidation activity of ceria-supported gold catalysts. *Reaction Chemistry & Engineering*, 3(1):75–85, 2018.

[8] X-D Zhou and Wayne Huebner. Size-induced lattice relaxation in $ceo_2$ nanoparticles. *Applied Physics Letters*, 79(21):3512–3514, 2001.

[9] Sameer Deshpande, Swanand Patil, Satyanarayana VNT Kuchibhatla, and Sudipta Seal. Size dependency variation in lattice parameter and valency states in nanocrystalline cerium oxide. *Applied Physics Letters*, 87(13):133113, 2005.

[10] Georgios Giannakakis, Maria Flytzani-Stephanopoulos, and E Charles H Sykes. Single-atom alloys as a reductionist approach to the rational design of heterogeneous catalysts. *Accounts of chemical research*, 52(1):237–247, 2018.

[11] Judith Corker, Frédéric Lefebvre, Christine Lécuyer, Véronique Dufaud, Françoise Quignard, Agnès Choplin, John Evans, and Jean-Marie Basset. Catalytic cleavage of the ch and cc bonds of alkanes by surface organometallic chemistry: An exafs and ir characterization of a zr-h catalyst. *Science*, 271(5251):966–969, 1996.

[12] F Humblot, JP Candy, F Le Peltier, B Didillon, and JM Basset. Surface organometallic chemistry on metals: Selective dehydrogenation of isobutane into isobutene on bimetallic catalysts prepared by reaction of tetran-butyltin on silica-supported platinum catalyst. *Journal of Catalysis*, 179(2):459–468, 1998.

[13] Qi Fu, Howard Saltsburg, and Maria Flytzani-Stephanopoulos. Active nonmetallic au and pt species on ceria-based water-gas shift catalysts. *Science*, 301(5635):935–938, 2003.

[14] Botao Qiao, Aiqin Wang, Xiaofeng Yang, Lawrence F Allard, Zheng Jiang, Yitao Cui, Jingyue Liu, Jun Li, and Tao Zhang. Single-atom catalysis of co oxidation using pt1/feox. *Nature chemistry*, 3(8):634–641, 2011.

[15] Yuanjun Chen, Shufang Ji, Chen Chen, Qing Peng, Dingsheng Wang, and Yadong Li. Single-atom catalysts: synthetic strategies and electrochemical applications. *Joule*, 2(7):1242–1264, 2018.

[16] RA Sheldon and Herman van Bekkum. *Fine chemicals through heterogeneous catalysis*. LibreDigital, 2008.

[17] Shuhui Sun, Gaixia Zhang, Nicolas Gauquelin, Ning Chen, Jigang Zhou, Songlan Yang, Weifeng Chen, Xiangbo Meng, Dongsheng Geng, Mohammad N Banis, et al. Single-atom catalysis using pt/graphene achieved through atomic layer deposition. *Scientific reports*, 3(1):1–9, 2013.

[18] WC Cheong, Y Wang, LR Zheng, H Xiao, C Chen, DS Wang, Q Peng, L Gu, XD Han, J Li, et al. Direct observation of noble metal nanoparticles transforming to thermally stable single atoms. 2018.

[19] Yonggang Yao, Zhennan Huang, Pengfei Xie, Lianping Wu, Lu Ma, Tangyuan Li, Zhenqian Pang, Miaolun Jiao, Zhiqiang Liang, Jinlong Gao, et al. High temperature shockwave stabilized single atoms. *Nature nanotechnology*, 14(9):851–857, 2019.

[20] John Jones, Haifeng Xiong, Andrew T DeLaRiva, Eric J Peterson, Hien Pham, Sivakumar R Challa, Gongshin Qi, Se Oh, Michelle H Wiebenga, Xavier Isidro Pereira Hernández, et al. Thermally stable single-atom platinum-on-ceria catalysts via atom trapping. *Science*, 353(6295):150–154, 2016.

[21] Qi Fu, Svetlana Kudriavtseva, Howard Saltsburg, and Maria Flytzani-Stephanopoulos. Gold–ceria catalysts for low-temperature water-gas shift reaction. *Chemical Engineering Journal*, 93(1):41–53, 2003.

[22] Deepak Kunwar, Shulan Zhou, Andrew DeLaRiva, Eric J Peterson, Haifeng Xiong, Xavier Isidro Pereira-Hernandez, Stephen C Purdy, Rik ter Veen, Hidde H Brongersma, Jeffrey T Miller, et al. Stabilizing high metal loadings of thermally stable platinum single atoms on an industrial catalyst support. *ACS Catalysis*, 9(5):3978–3990, 2019.

[23] Filip Dvořák, Matteo Farnesi Camellone, Andrii Tovt, Nguyen-Dung Tran, Fabio R Negreiros, Mykhailo Vorokhta, Tomáš Skála, Iva Matolínová, Josef Mysliveček, Vladimír Matolín, et al. Creating single-atom pt-ceria catalysts by surface step decoration. *Nature communications*, 7(1):1–8, 2016.

[24] Rui Lang, Wei Xi, Jin-Cheng Liu, Yi-Tao Cui, Tianbo Li, Adam Fraser Lee, Fang Chen, Yang Chen, Lei Li, Lin Li, et al. Non defect-stabilized thermally stable single-atom catalyst. *Nature communications*, 10(1):1–10, 2019.

[25] P Wynblatt and NA Gjostein. Supported metal crystallites. *Progress in solid state chemistry*, 9:21–58, 1975.

[26] CG Granqvist and RA Buhrman. Statistical model for coalescence of islands in discontinuous films. *Applied Physics Letters*, 27(12):693–694, 1975.

[27] Xiao-Chun Huang, Yan-Yong Lin, Jie-Peng Zhang, and Xiao-Ming Chen. Ligand-directed strategy for zeolite-type metal–organic frameworks: zinc (ii) imidazolates with unusual zeolitic topologies. *Angewandte Chemie International Edition*, 45(10):1557–1559, 2006.

[28] Peiqun Yin, Tao Yao, Yuen Wu, Lirong Zheng, Yue Lin, Wei Liu, Huanxin Ju, Junfa Zhu, Xun Hong, Zhaoxiang Deng, et al. Single cobalt atoms with precise n-coordination as superior oxygen reduction reaction catalysts. *Angewandte Chemie*, 128(36):10958–10963, 2016.

[29] Bo Liu, Hiroshi Shioyama, Tomoki Akita, and Qiang Xu. Metal-organic framework as a template for porous carbon synthesis. *Journal of the American Chemical Society*, 130(16):5390–5391, 2008.

[30] Melike Babucci, F Eylul Sarac Oztuna, Louise M Debefve, Alexey Boubnov, Simon R Bare, Bruce C Gates, Ugur Unal, and Alper Uzun. Atomically dispersed reduced graphene aerogel-supported iridium catalyst with an iridium loading of 14.8 wt%. *ACS Catalysis*, 9(11):9905–9913, 2019.

[31] Konstantin Khivantsev, Nicholas R Jaegers, Libor Kovarik, Jonathan C Hanson, Franklin Tao, Yu Tang, Xiaoyan Zhang, Iskra Z Koleva, Hristiyan A Aleksandrov, Georgi N Vayssilov, et al. Rücktitelbild: Achieving atomic dispersion of highly loaded transition metals in small-pore zeolite ssz-13: High-capacity and high-efficiency low-temperature co and passive nox adsorbers (angew. chem. 51/2018). *Angewandte Chemie*, 130(51):17152–17152, 2018.

[32] Tatyana Yu Kardash, Andrey I Stadnichenko, Olga A Stonkus, Elena M Slavinskaya, Valerii A Svetlichnyi, Andrei I Boronin, Elizaveta A Derevyannikova, et al. Structural insight into strong pt-ceo 2 interaction: from single pt atoms to ptox clusters. 2019.

[33] Pengfei Xie, Tiancheng Pu, Anmin Nie, Sooyeon Hwang, Stephen C Purdy, Wenjian Yu, Dong Su, Jeffrey T Miller, and Chao Wang. Nanoceria-supported single-atom platinum catalysts for direct methane conversion. *Acs Catalysis*, 8(5):4044–4048, 2018.

[34] Kakeru Fujiwara and Sotiris E Pratsinis. Atomically dispersed pd on nanostructured tio2 for no removal by solar light. *AIChE Journal*, 63(1):139–146, 2017.

[35] Kakeru Fujiwara and Sotiris E Pratsinis. Single pd atoms on tio2 dominate photocatalytic nox removal. *Applied Catalysis B: Environmental*, 226:127–134, 2018.

[36] Kunlun Ding, Ahmet Gulec, Alexis M Johnson, Neil M Schweitzer, Galen D Stucky, Laurence D Marks, and Peter C Stair. Identification of active sites in co oxidation and water-gas shift over supported pt catalysts. *science*, 350(6257):189–192, 2015.

[37] Pengxin Liu, Yun Zhao, Ruixuan Qin, Shiguang Mo, Guangxu Chen, Lin Gu, Daniel M Chevrier, Peng Zhang, Qing Guo, Dandan Zang, et al. Photochemical route for synthesizing atomically dispersed palladium catalysts. *Science*, 352(6287):797–800, 2016.

[38] Haisheng Wei, Yujing Ren, Aiqin Wang, Xiaoyan Liu, Xin Liu, Leilei Zhang, Shu Miao, Lin Li, Jingyue Liu, Junhu Wang, et al. Remarkable effect of alkalis on the chemoselective hydrogenation of functionalized nitroarenes over high-loading pt/feo x catalysts. *Chemical science*, 8(7):5126–5131, 2017.

[39] Yiwei Liu, Zhi Li, Qiuying Yu, Yanfei Chen, Ziwei Chai, Guofeng Zhao, Shoujie Liu, Weng-Chon Cheong, Yuan Pan, Qinghua Zhang, et al. A general strategy for fabricating isolated single metal atomic site catalysts in y zeolite. *Journal of the American Chemical Society*, 141(23):9305–9311, 2019.

[40] Soran Shwan, Magnus Skoglundh, Lars F Lundegaard, Ramchandra R Tiruvalam, Ton VW Janssens, Anna Carlsson, and Peter NR Vennestrøm. Solid-state ion-exchange of copper into zeolites facilitated by ammonia at low temperature. *Acs Catalysis*, 5(1):16–19, 2015.

[41] Chang Hyuck Choi, Minho Kim, Han Chang Kwon, Sung June Cho, Seongho Yun, Hee-Tak Kim, Karl JJ Mayrhofer, Hyungjun Kim, and Minkee Choi. Tuning selectivity of electrochemical reactions by atomically dispersed platinum catalyst. *Nature communications*, 7(1):1–9, 2016.

[42] Youqi Zhu, Tai Cao, Chuanbao Cao, Jun Luo, Wenxing Chen, Lirong Zheng, Juncai Dong, Jian Zhang, Yunhu Han, Zhi Li, et al. One-pot pyrolysis to n-doped graphene with high-density pt single atomic sites as heterogeneous catalyst for alkene hydrosilylation. *Acs Catalysis*, 8(11):10004–10011, 2018.

[43] Rui Lang, Tianbo Li, Daiju Matsumura, Shu Miao, Yujing Ren, Yi-Tao Cui, Yuan Tan, Botao Qiao, Lin Li, Aiqin Wang, et al. Hydroformylation of olefins by a rhodium single-atom catalyst with activity comparable to rhcl (pph3) 3. *Angewandte Chemie International Edition*, 55(52):16054–16058, 2016.

[44] Liangbing Wang, Wenbo Zhang, Shenpeng Wang, Zehua Gao, Zhiheng Luo, Xu Wang, Rui Zeng, Aowen Li, Hongliang Li, Menglin Wang, et al. Atomic-level insights in optimizing reaction paths for hydroformylation reaction over $rh/coo$ single-atom catalyst. *Nature communications*, 7(1):1–8, 2016.

[45] Xinjiang Cui, Kathrin Junge, Xingchao Dai, Carsten Kreyenschulte, Marga-Martina Pohl, Sebastian Wohlrab, Feng Shi, Angelika Bruckner, and Matthias Beller. Synthesis of single atom based heterogeneous platinum catalysts: high selectivity and activity for hydrosilylation reactions. *ACS central science*, 3(6):580–585, 2017.

[46] Wengang Liu, Leilei Zhang, Xin Liu, Xiaoyan Liu, Xiaofeng Yang, Shu Miao, Wentao Wang, Aiqin Wang, and Tao Zhang. Discriminating catalytically active fen x species of atomically dispersed fe–n–c catalyst for selective oxidation of the c–h bond. *Journal of the American Chemical Society*, 139(31):10790–10798, 2017.

[47] Lili Lin, Wu Zhou, Rui Gao, Siyu Yao, Xiao Zhang, Wenqian Xu, Shijian Zheng, Zheng Jiang, Qiaolin Yu, Yong-Wang Li, et al. Low-temperature hydrogen production from water and methanol using pt/$\alpha$-moc catalysts. *Nature*, 544(7648):80–83, 2017.

[48] Leo DeRita, Sheng Dai, Kimberly Lopez-Zepeda, Nicholas Pham, George W Graham, Xiaoqing Pan, and Phillip Christopher. Catalyst architecture for stable single atom dispersion enables site-specific spectroscopic and reactivity measurements of co adsorbed to pt atoms, oxidized pt clusters, and metallic pt clusters on tio2. *Journal of the American Chemical Society*, 139(40):14150–14165, 2017.

[49] Adam S Hoffman, Chia-Yu Fang, and Bruce C Gates. Homogeneity of surface sites in supported single-site metal catalysts: assessment with band widths of metal carbonyl infrared spectra. *The journal of physical chemistry letters*, 7(19):3854–3860, 2016.

[50] Adam S Hoffman, Louise M Debefve, Shengjie Zhang, Jorge E Perez-Aguilar, Edward T Conley, Kimberly R Justl, Ilke Arslan, David A Dixon, and Bruce C Gates. Beating heterogeneity of single-site catalysts: Mgo-supported iridium complexes. *ACS Catalysis*, 8(4):3489–3498, 2018.

[51] Gareth S Parkinson. Single-atom catalysis: How structure influences catalytic performance. *Catalysis letters*, 149(5):1137–1146, 2019.

[52] Leo DeRita, Joaquin Resasco, Sheng Dai, Alexey Boubnov, Ho Viet Thang, Adam S Hoffman, Insoo Ro, George W Graham, Simon R Bare, Gianfranco Pacchioni, et al. Structural evolution of atomically dispersed pt catalysts dictates reactivity. *Nature materials*, 18(7):746–751, 2019.

[53] Zdenek Jakub, Jan Hulva, Matthias Meier, Roland Bliem, Florian Kraushofer, Martin Setvin, Michael Schmid, Ulrike Diebold, Cesare Franchini, and Gareth S Parkinson. Local structure and coordination define adsorption in a model ir1/fe3o4 single-atom catalyst. *Angewandte Chemie*, 131(39):14099–14106, 2019.

[54] Hojin Jeong, Dongjae Shin, Beom-Sik Kim, Junemin Bae, Sangyong Shin, Chanyeong Choe, Jeong Woo Han, and Hyunjoo Lee. Controlling the oxidation state of pt single atoms for maximizing catalytic activity. *Angewandte Chemie*, 132(46):20872–20877, 2020.

[55] Andrew J Therrien, Alyssa JR Hensley, Matthew D Marcinkowski, Renqin Zhang, Felicia R Lucci, Benjamin Coughlin, Alex C Schilling, Jean-Sabin McEwen, and E Charles H Sykes. An atomic-scale view of single-site pt catalysis for low-temperature co oxidation. *Nature Catalysis*, 1(3):192–198, 2018.

[56] Joaquin Resasco, Leo DeRita, Sheng Dai, Joseph P Chada, Mingjie Xu, Xingxu Yan, Jordan Finzel, Sergei Hanukovich, Adam S Hoffman, George W Graham, et al. Uniformity is key in defining structure–function relationships for atomically dispersed metal catalysts: The case of pt/ceo2. *Journal of the American Chemical Society*, 142(1):169–184, 2019.

[57] Jesse F Goellner, Bruce C Gates, Georgi N Vayssilov, and Notker Rösch. Structure and bonding of a site-isolated transition metal complex: Rhodium dicarbonyl in highly dealuminated zeolite y. *Journal of the American Chemical Society*, 122(33):8056–8066, 2000.

[58] Pedro Serna and Bruce C Gates. Molecular metal catalysts on supports: organometallic chemistry meets surface science. *Accounts of chemical research*, 47(8):2612–2620, 2014.

[59] Louise M Debefve, Adam S Hoffman, Alexander J Yeh, Ron C Runnebaum, Sarah Shulda, Ryan M Richards, Ilke Arslan, and Bruce C Gates. Iridium atoms bonded to crystalline powder mgo: Characterization by imaging and spectroscopy. *The Journal of Physical Chemistry C*, 124(1):459–468, 2019.

[60] Alper Uzun, Volkan Ortalan, Nigel D Browning, and Bruce C Gates. Site-isolated iridium complexes on mgo powder: individual ir atoms imaged by scanning transmission electron microscopy. *Chemical communications*, (31):4657–4659, 2009.

[61] Justin O Ehresmann, Philip W Kletnieks, Ann Liang, Vinesh A Bhirud, Olesya P Bagatchenko, Eric J Lee, Meghan Klaric, Bruce C Gates, and James F Haw. Titelbild: Evidence from nmr and exafs studies of a dynamically uniform mononuclear single-site zeolite-supported rhodium catalyst (angew. chem. 4/2006). *Angewandte Chemie*, 118(4):535–535, 2006.

[62] Jorge E Perez-Aguilar, Cong-Yan Chen, James T Hughes, Chia-Yu Fang, and Bruce C Gates. Isostructural atomically dispersed rhodium catalysts supported on sapo-37 and on hy zeolite. *Journal of the American Chemical Society*, 142(26):11474–11485, 2020.

[63] Dong Jiang, Gang Wan, Carlos E Garcia-Vargas, Linze Li, Xavier Isidro Pereira-Hernandez, Chongmin Wang, and Yong Wang. Elucidation of the active sites in single-atom pd1/ceo2 catalysts for low-temperature co oxidation. *ACS Catalysis*, 10(19):11356–11364, 2020.

[64] Ya-Qiong Su, Jin-Xun Liu, Ivo AW Filot, Long Zhang, and Emiel JM Hensen. Highly active and stable ch4 oxidation by substitution of ce4+ by two pd2+ ions in ceo2 (111). *ACS catalysis*, 8(7):6552–6559, 2018.

[65] Ya-Qiong Su, Ivo AW Filot, Jin-Xun Liu, and Emiel JM Hensen. Stable pd-doped ceria structures for ch4 activation and co oxidation. *ACS catalysis*, 8(1):75–80, 2018.

[66] Jingrui Ye, Dang-guo Cheng, Fengqiu Chen, and Xiaoli Zhan. Controlled synthesis of sintering-resistant pd@ ceo2 core–shell nanotube catalysts for co oxidation. *Industrial & Engineering Chemistry Research*, 58(48):21972–21982, 2019.

[67] Na Ta, Jingyue Liu, Santhosh Chenna, Peter A Crozier, Yong Li, Aling Chen, and Wenjie Shen. Stabilized gold nanoparticles on ceria nanorods by strong interfacial anchoring. *Journal of the American Chemical Society*, 134(51):20585–20588, 2012.

[68] M Cargnello, JJ Delgado Jaén, JC Hernández Garrido, K Bakhmutsky, T Montini, JJ Calvino Gámez, RJ Gorte, and P Fornasiero. Exceptional activity for methane combustion over modular pd@ ceo2 subunits on functionalized al2o3. 2012.

[69] Thomas P Senftle, Adri CT Van Duin, and Michael J Janik. Methane activation at the pd/ceo2 interface. *ACS Catalysis*, 7(1):327–332, 2017.

[70] Sara Colussi, Arup Gayen, Matteo Farnesi Camellone, Marta Boaro, Jordi Llorca, Stefano Fabris, and Alessandro Trovarelli. Nanofaceted pd-o sites in pd-ce surface superstructures: Enhanced activity in catalytic combustion of methane. *Angewandte Chemie International Edition*, 48(45):8481–8484, 2009.

[71] Giulia Spezzati, Yaqiong Su, Jan P Hofmann, Angelica D Benavidez, Andrew T DeLaRiva, Jay McCabe, Abhaya K Datye, and Emiel JM Hensen. Atomically dispersed pd–o species on ceo2 (111) as highly active sites for low-temperature co oxidation. *ACS catalysis*, 7(10):6887–6891, 2017.

[72] Xuefei Wan, Daniel Goberman, Leon L Shaw, Guangshun Yi, and Gan-Moog Chow. Valence states of nanocrystalline ceria under combined effects of hydrogen reduction and particle size. *Applied Physics Letters*, 96(12):123108, 2010.

[73] Rui You, Zhaorui Li, Tian Cao, Bing Nan, Rui Si, and Weixin Huang. Synthesis in a glovebox: utilizing surface oxygen vacancies to enhance the atomic dispersion of palladium on ceria for carbon monoxide oxidation and propane combustion. *ACS Applied Nano Materials*, 1(9):4988–4997, 2018.

[74] Myeong Gon Jang, Sinmyung Yoon, Dongjae Shin, Hyung Jun Kim, Rui Huang, Euiseob Yang, Jihun Kim, Kug-Seung Lee, Kwangjin An, and Jeong Woo Han. Boosting support reducibility and metal dispersion by exposed surface atom control for highly active supported metal catalysts. *ACS Catalysis*, 12(8):4402–4414, 2022.

[75] Wey Yang Teoh. A perspective on the flame spray synthesis of photocatalyst nanoparticles. *Materials*, 6(8):3194–3212, 2013.

[76] VN Morris, RA Farrell, AM Sexton, and MA Morris. Lattice constant dependence on particle size for ceria prepared from a citrate sol-gel. In *Journal of Physics: Conference Series*, volume 26, page 028. IOP Publishing, 2006.

[77] Chao Wang, Cun Wen, Jochen Lauterbach, and Erdem Sasmaz. Superior oxygen transfer ability of pd/mnox-ceo2 for enhanced low temperature co oxidation activity. *Applied Catalysis B: Environmental*, 206:1–8, 2017.

[78] Alexander J Hill, Chang Yup Seo, Xiaoyin Chen, Adarsh Bhat, Galen B Fisher, Andrej Lenert, and Johannes W Schwank. Thermally induced restructuring of pd@ ceo2 and pd@ sio2 nanoparticles as a strategy for enhancing low-temperature catalytic activity. *ACS Catalysis*, 10(3):1731–1741, 2019.

[79] Xiuxiu Shi, Xueguang Wang, Xingfu Shang, Xiujing Zou, Weizhong Ding, and Xionggang Lu. High performance and active sites of a ceria-supported palladium catalyst for solvent-free chemoselective hydrogenation of nitroarenes. *ChemCatChem*, 9(19):3743–3751, 2017.

[80] Gengnan Li, Liang Li, and Dong Jiang. Facile synthesis of highly active mesoporous pdceo x solid solution for low-temperature co oxidation. *The Journal of Physical Chemistry C*, 119(22):12502–12507, 2015.

[81] WB Carter, GW Book, TA Polley, DW Stollberg, and JM Hampikian. Combustion chemical vapor deposition of ceo2 film. *Thin Solid Films*, 347(1-2):25–30, 1999.

[82] PP Semyannikov, VM Grankin, IK Igumenov, and AF Bykov. Mechanism of thermal decomposition of palladium $\beta$-diketonates vapour on hot surface. *Le Journal de Physique IV*, 5(C5):C5–205, 1995.

[83] Shruthi Dasappa and Joaquin Camacho. Thermodynamic barrier to nucleation for manganese oxide nanoparticles synthesized by high-temperature gas-to-particle conversion. *Energy & Fuels*, 35(2):1874–1884, 2021.

[84] Erdem Sasmaz, Chao Wang, Michael J Lance, and Jochen Lauterbach. In situ spectroscopic investigation of a pd local structure over pd/ceo 2 and pd/mno x–ceo 2 during co oxidation. *Journal of Materials Chemistry A*, 5(25):12998–13008, 2017.

[85] Satoshi Hinokuma, Hiroaki Fujii, Madoka Okamoto, Keita Ikeue, and Masato Machida. Metallic pd nanoparticles formed by pd- o- ce interaction: A reason for sintering-induced activation for co oxidation. *Chemistry of Materials*, 22(22):6183–6190, 2010.

[86] Atsushi Satsuma, Ryota Sato, Kaoru Osaki, and Kenichi Shimizu. Unique effect of surface area of support on propene combustion over pd/ceria. *Catalysis today*, 185(1):61–65, 2012.

[87] Matteo Monai, Tiziano Montini, Raymond J Gorte, and Paolo Fornasiero. Catalytic oxidation of methane: Pd and beyond. *European Journal of Inorganic Chemistry*, 2018(25):2884–2893, 2018.

[88] Jon G McCarty. Kinetics of pdo combustion catalysis. *Catalysis Today*, 26(3-4):283–293, 1995.

[89] Abhaya K Datye, Jaime Bravo, Travis R Nelson, Paolina Atanasova, Maxim Lyubovsky, and Lisa Pfefferle. Catalyst microstructure and methane oxidation reactivity during the $pd \leftrightarrow pdo$ transformation on alumina supports. *Applied Catalysis A: General*, 198(1-2):179–196, 2000.

[90] Robert J Farrauto, MC Hobson, Teresa Kennelly, and EM Waterman. Catalytic chemistry of supported palladium for combustion of methane. *Applied Catalysis A: General*, 81(2):227–237, 1992.

[91] Sara Colussi, Alessandro Trovarelli, Cinzia Cristiani, Luca Lietti, and Gianpiero Groppi. The influence of ceria and other rare earth promoters on palladium-based methane combustion catalysts. *Catalysis Today*, 180(1):124–130, 2012.

[92] Sara Colussi, Alessandro Trovarelli, Erik Vesselli, Alessandro Baraldi, Giovanni Comelli, Gianpiero Groppi, and Jordi Llorca. Structure and morphology of pd/al2o3 and pd/ceo2/al2o3 combustion catalysts in pd–pdo transformation hysteresis. *Applied Catalysis A: General*, 390(1-2):1–10, 2010.

[93] Philippe O Thevenin, Ana Alcalde, Lars J Pettersson, Sven G Järås, and José Luis G Fierro. Catalytic combustion of methane over cerium-doped palladium catalysts. *Journal of Catalysis*, 215(1):78–86, 2003.

[94] Shuiqing Li, Yihua Ren, Pratim Biswas, and D Tse Stephen. Flame aerosol synthesis of nanostructured materials and functional devices: Processing, modeling, and diagnostics. *Progress in Energy and Combustion Science*, 55:1–59, 2016.

[95] Arthur H Lefebvre and Vincent G McDonell. *Atomization and sprays*. CRC press, 2017.

[96] Arto J Gröhn, Sotiris E Pratsinis, and Karsten Wegner. Fluid-particle dynamics during combustion spray aerosol synthesis of zro2. *Chemical Engineering Journal*, 191:491–502, 2012.

[97] Christopher Abram, Maksim Mezhericher, Frank Beyrau, Howard A Stone, and Yiguang Ju. Flame synthesis of nanophosphors using sub-micron aerosols. *Proceedings of the Combustion Institute*, 37(1):1231–1239, 2019.

[98] Jili Wei, Shuiqing Li, Yihua Ren, Yiyang Zhang, and D Tse Stephen. Investigating the role of solvent formulations in temperature-controlled liquid-fed aerosol flame synthesis of yag-based nanoparticles. *Proceedings of the Combustion Institute*, 37(1):1193–1201, 2019.

[99] Yihua Ren, Jinzhi Cai, and Heinz Pitsch. Theoretical single-droplet model for particle formation in flame spray pyrolysis. *Energy & Fuels*, 35(2):1750–1759, 2021.

[100] Florian Meierhofer, Haipeng Li, Michael Gockeln, Robert Kun, Tim Grieb, Andreas Rosenauer, Udo Fritsching, Johannes Kiefer, Johannes Birkenstock, Lutz Madler, et al. Screening precursor–solvent combinations for li4ti5o12 energy storage material using flame spray pyrolysis. *ACS applied materials & interfaces*, 9(43):37760–37777, 2017.

[101] Federico Dalla Barba, Jietuo Wang, and Francesco Picano. Revisiting d 2-law for the evaporation of dilute droplets. *Physics of Fluids*, 33(5):051701, 2021.

[102] C Chauveau, M Birouk, and I Gökalp. Why the d2-law does not hold during droplet vaporization in microgravity conditions. In *In21st Annual Conference on Liquid Atomization and Spray Systems,(ILASS Europe 2007), Mugla, Turkey*, 2007.

[103] Martin C Heine and Sotiris E Pratsinis. Droplet and particle dynamics during flame spray synthesis of nanoparticles. *Industrial & engineering chemistry research*, 44(16):6222–6232, 2005.

[104] B Abramzon and WA Sirignano. Droplet vaporization model for spray combustion calculations. *International journal of heat and mass transfer*, 32(9):1605–1618, 1989.

[105] Guangfa Yao. A film-theory-based model for a multicomponent droplet evaporation at both low-and high-pressure environments. 2006.

[106] Thamali R Jayawickrama, Nils Erland L Haugen, Matthaus U Babler, Muhammad Aqib Chishty, and Kentaro Umeki. The effect of stefan flow on the drag coefficient of spherical particles in a gas flow. *International Journal of Multiphase Flow*, 117:130–137, 2019.

[107] MC Yuen and La W CHEN. On drag of evaporating liquid droplets. 1976.

[108] Yuan Sheng, Maria L Botero, Manoel Y Manuputty, Markus Kraft, and Rong Xu. Co3o4 and fe x co3–x o4 nanoparticles/films synthesized in a vapor-fed flame aerosol reactor for oxygen evolution. *ACS Applied Energy Materials*, 1(2):655–665, 2018.

[109] Scott B Leask, Alice K Li, Vincent G McDonell, and Scott Samuelsen. Preliminary development of a measurement reference using a research simplex atomizer. *Journal of Fluids Engineering*, 141(12), 2019.

[110] Florian Meierhofer, Lutz Mädler, and Udo Fritsching. Nanoparticle evolution in flame spray pyrolysis—process design via experimental and computational analysis. *AIChE Journal*, 66(2):e16885, 2020.

[111] R Byron Bird. Transport phenomena. *Appl. Mech. Rev.*, 55(1):R1–R4, 2002.

[112] Changwon Suh and Krishna Rajan. Combinatorial design of semiconductor chemistry for bandgap engineering:"virtual" combinatorial experimentation. *Applied surface science*, 223(1-3):148–158, 2004.

[113] Ryosuke Jinnouchi and Ryoji Asahi. Predicting catalytic activity of nanoparticles by a dft-aided machine-learning algorithm. *The journal of physical chemistry letters*, 8(17):4279–4283, 2017.

[114] Zachary W Ulissi, Michael T Tang, Jianping Xiao, Xinyan Liu, Daniel A Torelli, Mohammadreza Karamad, Kyle Cummins, Christopher Hahn, Nathan S Lewis, Thomas F Jaramillo, et al. Machine-learning methods enable exhaustive searches for active bimetallic facets and reveal active site motifs for co2 reduction. *Acs Catalysis*, 7(10):6600–6608, 2017.

[115] Chiho Kim, Ghanshyam Pilania, and Rampi Ramprasad. Machine learning assisted predictions of intrinsic dielectric breakdown strength of abx3 perovskites. *The Journal of Physical Chemistry C*, 120(27):14575–14580, 2016.

[116] Chiho Kim, Ghanshyam Pilania, and Rampi Ramprasad. From organized high throughput data to phenomenological theory: The example of dielectric breakdown. In *APS March Meeting Abstracts*, volume 2016, pages K22–004, 2016.

[117] T Hammerschmidt, AF Bialon, and R Drautz. Structure map including off-stoichiometric and ternary sp-d-valent compounds. *Modelling and Simulation in Materials Science and Engineering*, 25(7):074002, 2017.

[118] Arthur F Bialon, Thomas Hammerschmidt, and Ralf Drautz. Three-parameter crystal-structure prediction for sp-d-valent compounds. *Chemistry of Materials*, 28(8):2550–2556, 2016.

[119] M Erdem Gunay and Ramazan Yildirim. Neural network analysis of selective co oxidation over copper-based catalysts for knowledge extraction from published data in the literature. *Industrial & engineering chemistry research*, 50(22):12488–12500, 2011.

[120] Çağla Odabaşı, M Erdem Günay, and Ramazan Yıldırım. Knowledge extraction for water gas shift reaction over noble metal catalysts from publications in the literature between 2002 and 2012. *International journal of hydrogen energy*, 39(11):5733–5746, 2014.

[121] Ayşe Neslihan Şener, M Erdem Günay, Aybüke Leba, and Ramazan Yıldırım. Statistical review of dry reforming of methane literature using decision tree and artificial neural network analysis. *Catalysis Today*, 299:289–302, 2018.

[122] Simone C Sieg, Changwon Suh, Timm Schmidt, Michael Stukowski, Krishna Rajan, and Wilhelm F Maier. Principal component analysis of catalytic functions in the composition space of heterogeneous catalysts. *QSAR & Combinatorial Science*, 26(4):528–535, 2007.

[123] Jinchao Liu, Margarita Osadchy, Lorna Ashton, Michael Foster, Christopher J Solomon, and Stuart J Gibson. Deep convolutional neural networks for raman spectrum recognition: a unified solution. *Analyst*, 142(21):4067–4074, 2017.

[124] Anton V Ievlev, Alexei Belianinov, Stephen Jesse, David P Allison, Mitchel J Doktycz, Scott T Retterer, Sergei V Kalinin, and Olga S Ovchinnikova. Automated interpretation and extraction of topographic information from time of flight secondary ion mass spectrometry data. *Scientific reports*, 7(1):1–7, 2017.

[125] Thomas F Boucher, Marie V Ozanne, Marco L Carmosino, M Darby Dyar, Sridhar Mahadevan, Elly A Breves, Kate H Lepore, and Samuel M Clegg. A study of machine learning regression methods for major elemental analysis of rocks using laser-induced breakdown spectroscopy. *Spectrochimica Acta Part B: Atomic Spectroscopy*, 107:1–10, 2015.

[126] I Gemp, I Durughar, M Parente, MD Dyar, and S Mahadevan. Deep learning models for spectroscopic data: Semi-supervised generative models applied to laser-induced breakdown spectroscopic data. In *48th Annual Lunar and Planetary Science Conference*, number 1964, page 1696, 2017.

[127] Tian-Long ZHANG, WU Shan, Tang Hong-Sheng, Wang Kang, Duan Yi-Xiang, and LI Hua. Progress of chemometrics in laser-induced breakdown spectroscopy analysis. *Chinese Journal of Analytical Chemistry*, 43(6):939–948, 2015.

[128] Andrew J Medford, M Ross Kunz, Sarah M Ewing, Tammie Borders, and Rebecca Fushimi. Extracting knowledge from data through catalysis informatics. *ACS Catalysis*, 8(8):7403–7429, 2018.

[129] Jun Li and Martin D Eastgate. Making better decisions during synthetic route design: leveraging prediction to achieve greenness-by-design. *Reaction Chemistry & Engineering*, 4(9):1595–1607, 2019.

[130] Marwin HS Segler, Mike Preuss, and Mark P Waller. Planning chemical syntheses with deep neural networks and symbolic ai. *Nature*, 555(7698):604–610, 2018.

[131] Miroslava Nedyalkova and Vasil Simeonov. Multivariate chemometrics as a strategy to predict the allergenic nature of food proteins. *Symmetry*, 12(10):1616, 2020.

[132] Li-Xian Sun, Fen Xu, Yi-Zeng Liang, Yu-Long Xie, and Ru-Qin Yu. Cluster analysis by the k-means algorithm and simulated annealing. *Chemometrics and intelligent laboratory systems*, 25(1):51–60, 1994.

[133] Kenneth G Rappé, Craig DiMaggio, Josh A Pihl, Joseph R Theis, Se H Oh, Galen B Fisher, Jim Parks, Vencon G Easterling, Ming Yang, Mark L Stewart, et al. Aftertreatment protocols for catalyst characterization and performance evaluation: low-temperature oxidation, storage, three-way, and nh3-scr catalyst test protocols. *Emission Control Science and Technology*, 5(2):183–214, 2019.

[134] Li He, Yilin Fan, Jérôme Bellettre, Jun Yue, and Lingai Luo. A review on catalytic methane combustion at low temperatures: Catalysts, mechanisms, reaction conditions and reactor designs. *Renewable and Sustainable Energy Reviews*, 119:109589, 2020.

# Appendix A

# Supplementary Information for Synthesis of Atomically Dispersed Pd

## A.1 Chemical environment during the synthesis

The flame ER is defined as the ratio of actual fuel to oxygen ratio to the stoichiometric fuel to oxygen ratio, which is used to control the combustion gases such as CO, $CO_2$ and $H_2O$ of the solvent mixtures. These gases dictate the chemical environment of the precursors in which the ER less than one indicates oxidizing environment predominantly containing oxygen while the equivalence ratio above one indicates the reducing environment. The theoretical combustion gas compositions provided by the combustion of the toluene and EHA solvents were determined from the equivalence ratio using an algorithm developed based on the following considerations. The thermal energy of the flame is sufficient to vaporize both EHA and toluene. There is conservation of matter during phase change of the solvents. Toluene which is more volatile vaporizes first and undergoes combustion first before the less volatile EHA solvent, whereas all the solvent molecules get vaporized by the thermal environment in

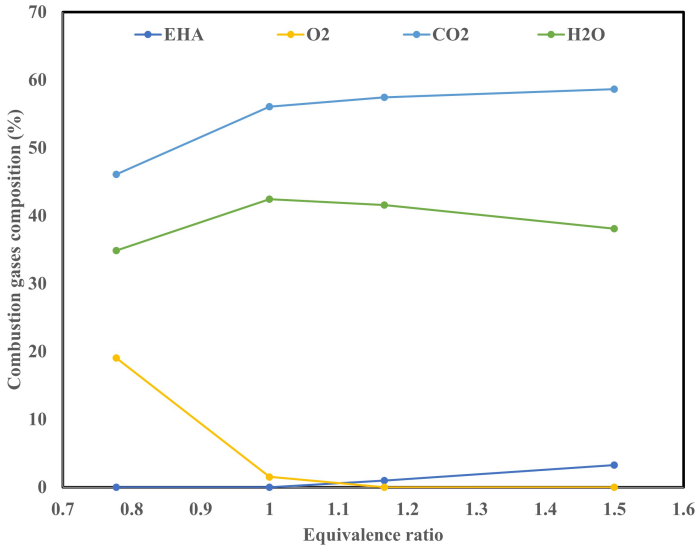


Figure A.1: Gas compositions as a function of Equivalence ratio

the flame. The excess solvent vapor in excess of that required for combustion with available oxygen is assumed not to be combusted by ambient air. Complete combustion of solvents into $H_2O$ and $CO_2$ is considered. Figure A.1 shows the gas composition as a function of the equivalence ratio of the spray flame.

The equivalence ratio (ER) 0.8 has a 20 % of $O_2$ in addition to $CO_2$ and $H_2O$ . As the ER increases to one, oxygen vanishes with only $CO_2$ and $H_2O$ as the combustion gas species. As the ER increases further, the percentage of $O_2$ remains zero, the $CO_2$ and $H_2O$ species percentage increase and the additional EHA can be oxidized through the ambient air into $CO_2$ and $H_2O$ . These combustion gas compositions constitute the chemical environment of the precursors during the synthesis.

When $Pd(acac)_2$ and CeEH in dissolved EHA and toluene solvents are injected into the flame, the precursors undergo reactions including thermal decompositions and direct oxidations. The cerium ethyl hexanoate undergoes decomposition into ceria. $Pd(acac)_2$ can undergo gaseous decomposition at 305 °C [82] to Pd. It can also decompose at 196 °C in inert environment and at 180 °C in an oxidizing environment. However, continuous heating up to

800 °C results in PdO which consequently decomposes back to Pd at temperature greater than 900 °C. Hence, possible reactions for the $Pd(acac)_2$ in the flame are:

$$CeEH \rightarrow CeO_2, CO_2, H_2O$$

$$Pd(acac)_2 \rightarrow Pd + L \rightarrow Pd, CO_2, H_2O$$

$$Pd + O_2 \rightarrow PdO$$

$$2PdO \rightarrow 2Pd + O_2$$

In the reducing environment, possible Pd species for nucleation on ceria are Pd and/or PdO, while in the oxidizing environment, only PdO and $PdO_2$ are more likely to be available for nucleation. These chemical environments are dictated by the combustion gases which have been controlled by the flame equivalence ratio.

## A.2 Supplementary data

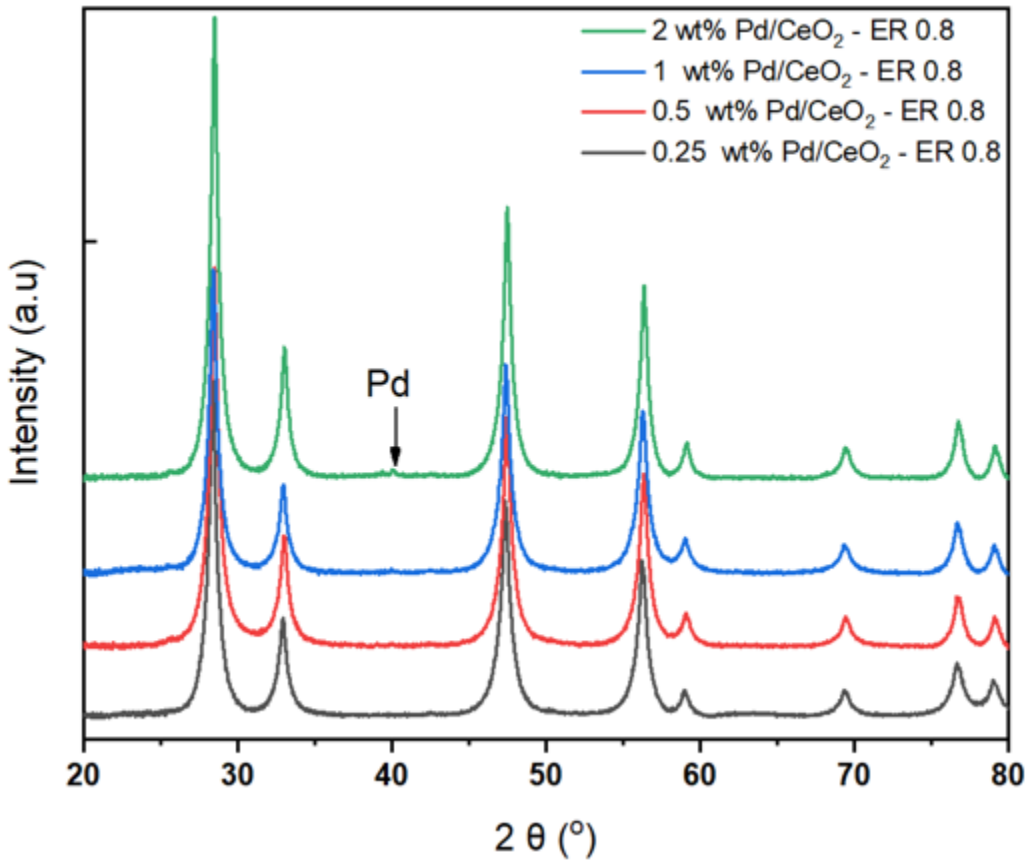


Figure A.2: XRD pattern for catalysts synthesized at different loading in the oxidizing environment

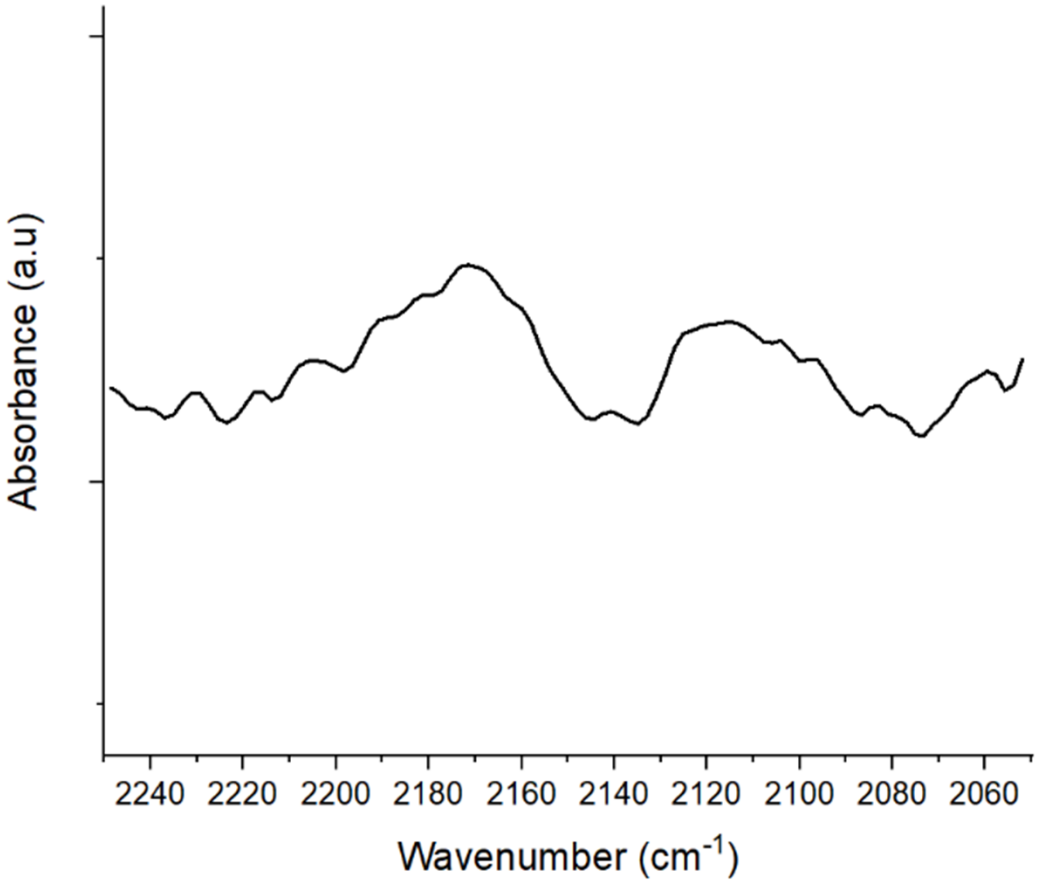


Figure A.3: CO DRIFT on fumed silica. CO is injected after $N_2$ flows over the inert silica sample for 30 mins at room temperature and stopped. Background is taken during $N_2$ purging. While the signal amplitude of 1500 is uniform for other experiments, the signal amplitude for silica sample experiment cannot be increased above 400 even at the maximum aperture size of 8 mm due to the whitish color of the sample. The low light signal reaching the detector is responsible for the low signal-to-noise ratio in the spectra

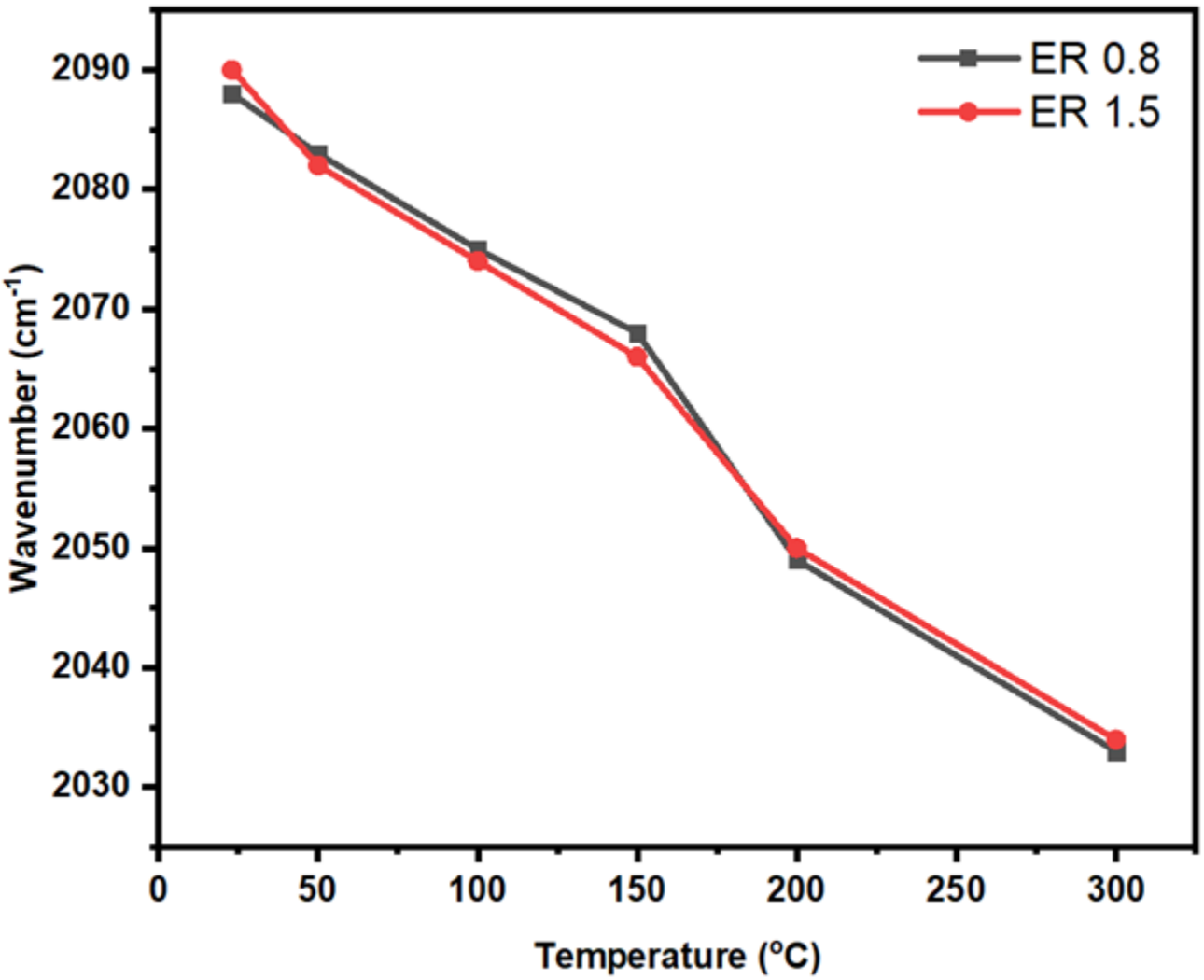


Figure A.4: The shifting of the grouped peaks under temperature ramping for both 1 wt.% $Pd/CeO_2$ catalysts synthesized at ER 0.8 and ER 1.5

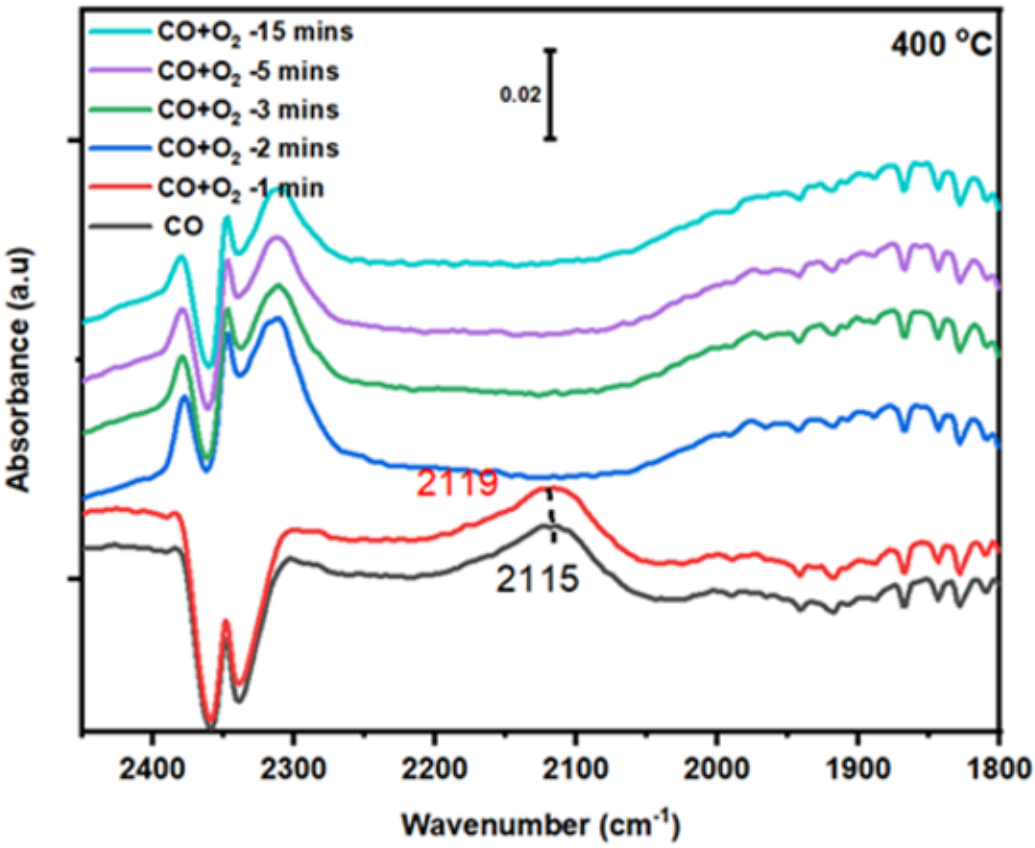


Figure A.5: CO oxidation with oxygen gas at 400 °C 1 wt% $Pd/CeO_2$ synthesized in the oxidizing environment condition (ER 0.8)

There is immediate disappearance of the adsorbed CO peak after introducing oxygen. The negative $CO_2$ peak also becomes positive indicative of $CO_2$ production. The adsorbed CO removal and $CO_2$ production is indicative of oxidation of the adsorbed CO.

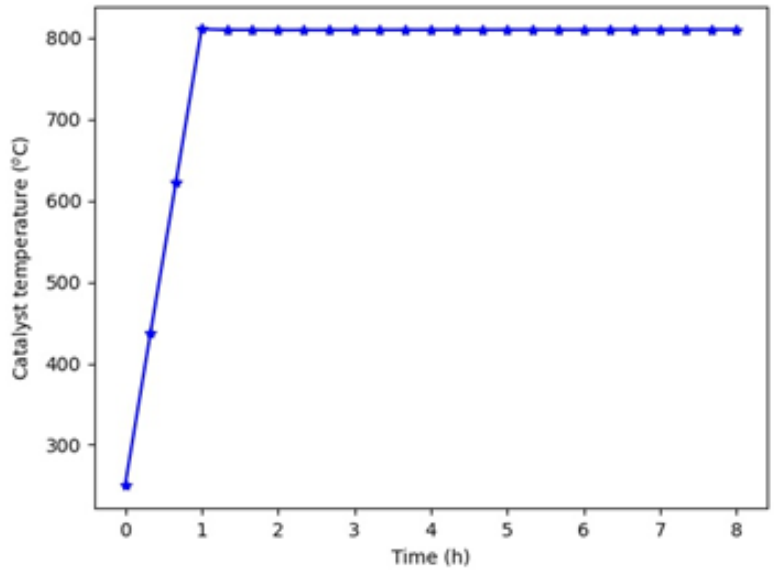


(a) Temperature profile for 8 h.

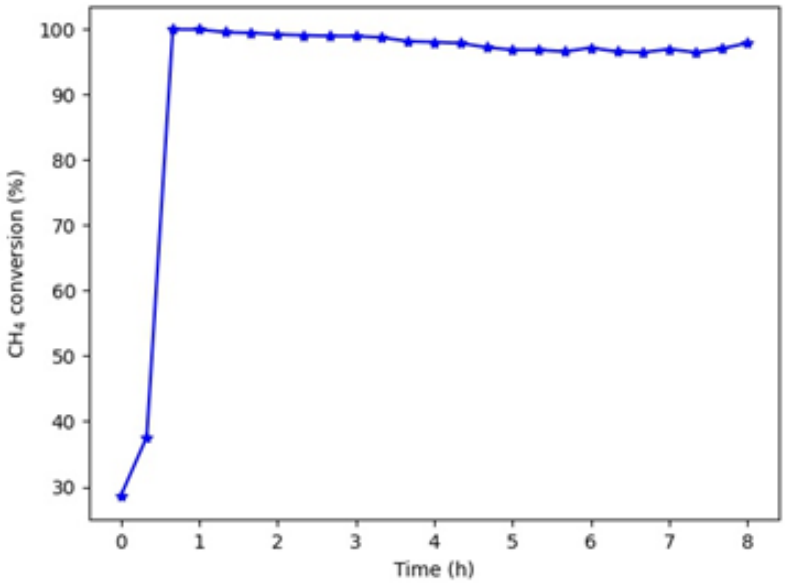


(b) Methane conversion for 8 hrs

Figure A.6: Stability test for 1 wt% $Pd/CeO_2$ catalyst synthesized at oxidizing environment

The catalyst temperature remains constant at 800 °C throughout the duration of the test. The catalyst reaches full conversion from about 620 °C and there is insignificant change in the full methane conversion throughout the duration of the test at 800 °C

# Appendix B

# Optimization of Catalytic Performance Through Reactor Design

This chapter discusses the details of the design of the fixed bed reactor used to evaluate the catalytic performance of the methane oxidation reaction conducted in chapter 2.

## B.1 Introduction

Advanced Combustion and Emission Control (ACEC) Technical Team of the U.S. DRIVE Partnership has specified requirements for instrumentation and testing conditions for oxidation catalysts for consistent metric reporting [133]. However, the technical know-how to achieve this is not presented. Adopting the same methodology of optimizing the reactor and flow systems may be necessary in order to further ensure consistency in metric reporting. Here, a methodology to maximize reactor performance within the several constraints recommended by the ACEC team has been developed to follow their protocol.

## B.2 Reactor system experimental set-up

The catalysts testing system consists of the reactor tube inserted through a furnace. The reactor temperature is adjusted by controlling the furnace temperature. The feed gas into the reactor is controlled by Brooks MFCs using the MFC control box and the exhaust gas from the reactor is analyzed using the GC equipped with FID and TCD detector.

## B.3 Result

### B.3.1 Reaction temperature

Methane oxidation reaction temperature ramping testing protocol is adopted and integrated into the reactor system. The temperature ramping of the furnace is appropriately synchronized with the GC data collection and waiting time. Both the GC data and the temperature data collected from the experiment run using this defined protocol are fed in a python code developed for direct calculation and generation of the light off curve, giving a higher order of magnitude analysis. The temperature of the catalyst bed measured by thermocouple is close to the furnace set point temperature, as shown in figure B.1, but the catalysts bed temperature positively deviates from the furnace temperature as the temperature increases. The ramping rate of the catalysts bed is close to the set-point temperature ramping rate at 2.5 $^{o}$C/min, except that the bed's temperature slightly decreases in ramping down region below 200 $^{o}$C, as shown in figure B.2a.

The catalytic testing with both rampings show similar performance as shown in the light off curve in the figure, indicating that the **furnace set point** ramping rate can be **reliably used** as an alternative for the catalyst bed thermocouple reading in cases where thermocouples are challenging to be inserted inside the catalyst bed.

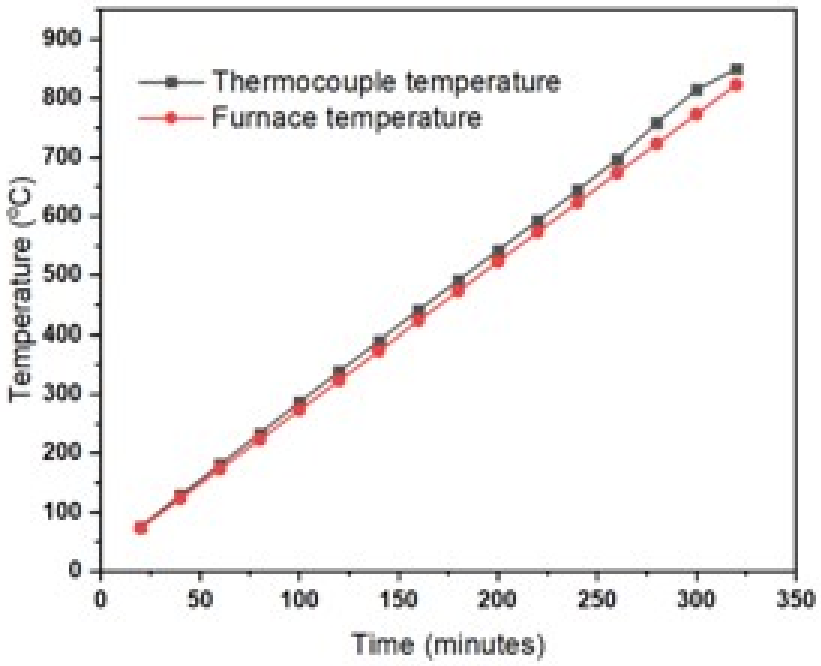


Figure B.1: Measured (Thermocouple) vs set-point temperature-GHSV: 96,000 ml/g/h, inlet gas feed: 4% $CH_4$, 16% $O_2$ and 80% $N_2$ 1 wt% $Pd/CeO_2$ ; 75 mg catalyst.

### B.3.2 Micro channeling

Optimization of the reactor system is carried out using 0.5 % (5000 pm) $CH_4$. Figure B.4a and figure B.4b show methane oxidation light off curve with and without catalysts respectively on 7 mm ID reactor. With an empty reactor tube containing nonreactive quartz wool (Without any catalyst), methane oxidation begins from 700 °C and reaches only 20 % conversion at 800 °C due to the gas phase reaction. With 1 wt% $Pd/CeO_2$ catalyst, methane oxidation begins from about 350 °C and has a $T_{50}$ of 554 °C while full methane conversion is achieved at 800 °C. The negligible methane conversion in the empty reactor with respect to the reactor loaded with catalyst indicates that the performance for the latter is solely due to the activity of the catalysts, further validating the reactor system. To investigate micro channeling at the reaction condition, the aspect ratio H/d of the bed is increased by 2 by mixing the 75 mg catalysts with 75 mg of silica. Figure B.4b, which directly compares the catalytic performance with and without the addition of silica shows almost the same

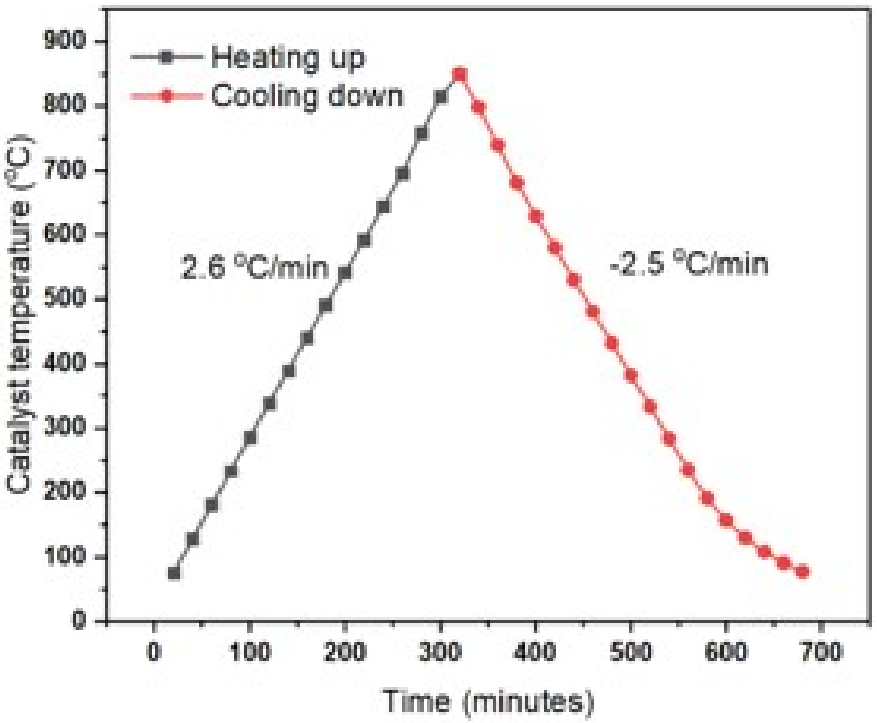


(a) Ramp up and ramp down temperature profile

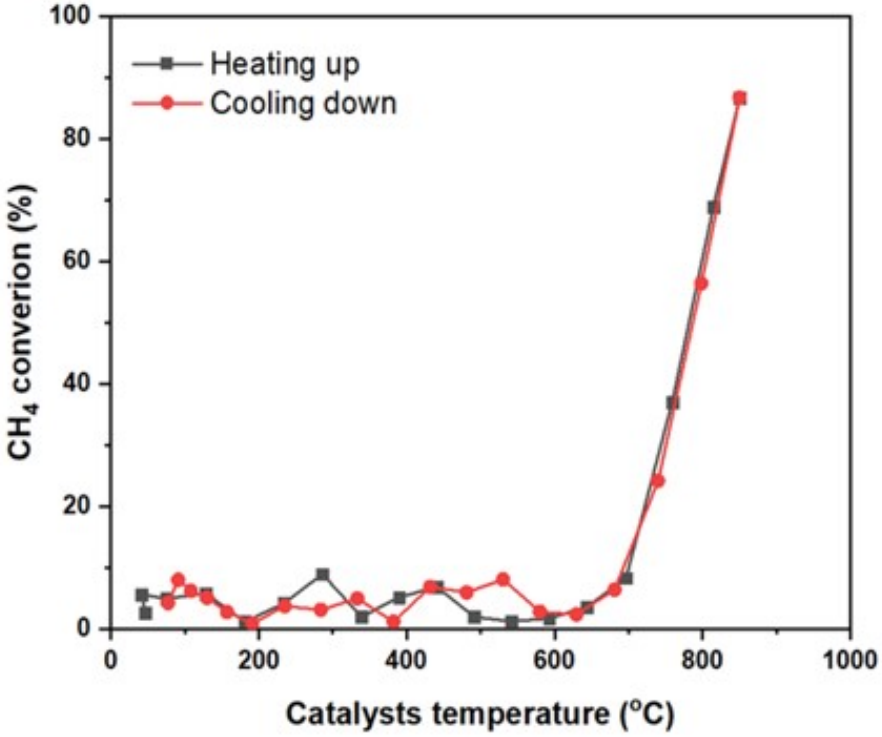


(b) Light off curve for ramp up and ramp down temperature

Figure B.2: Light off curve for ramp up and ramp down temerature method of 1 wt% $Pd/CeO_2$ ; 75 mg catalysts; GHSV: 96,000 ml/g/h, inlet gas feed: 4% $CH_4$, 16% $O_2$ and 80% $N_2$

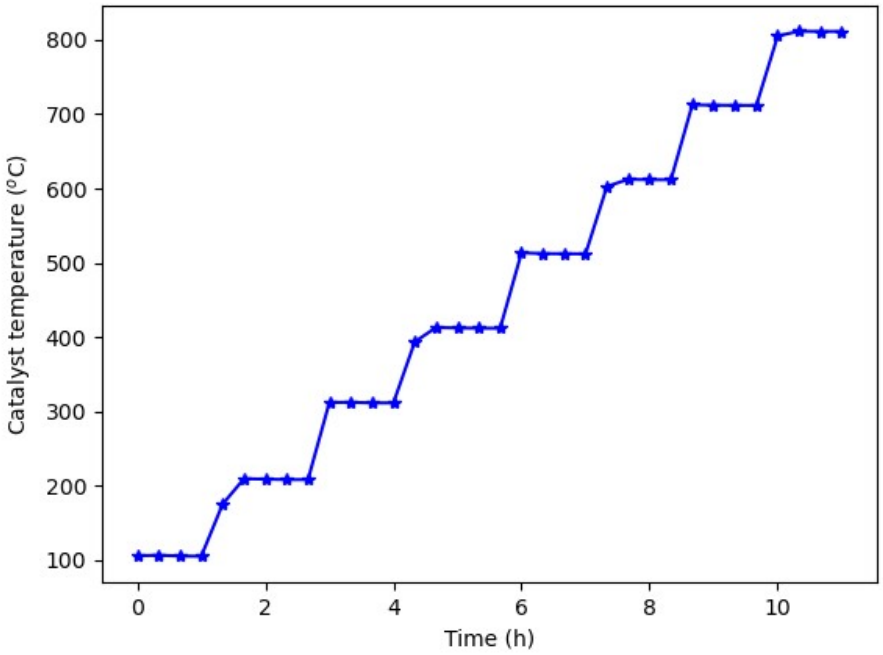


(a) Stagewise temperature ramping

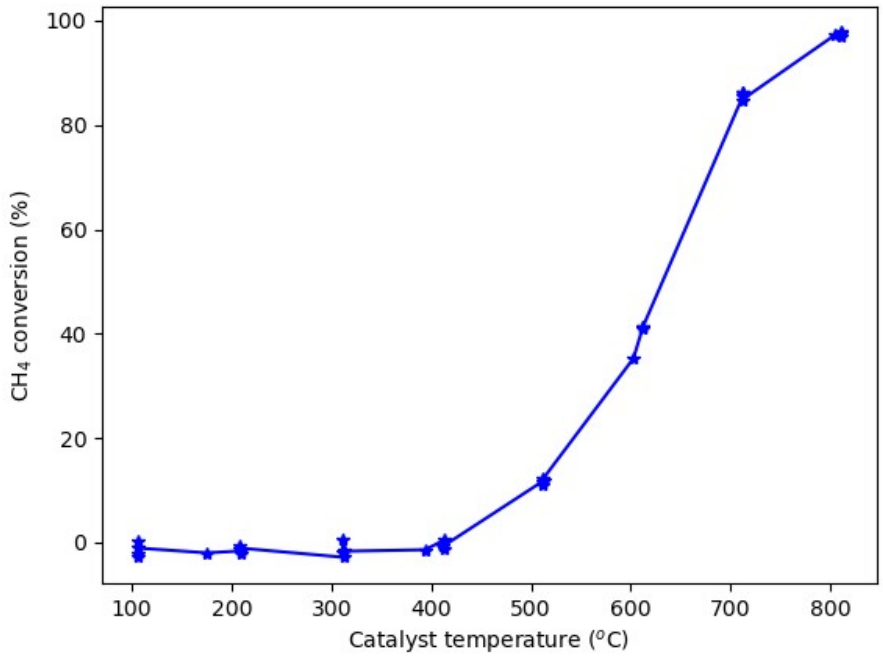


(b) Conversion at Stagewise temperature ramping

Figure B.3: Conversion from stagewise temperature ramping

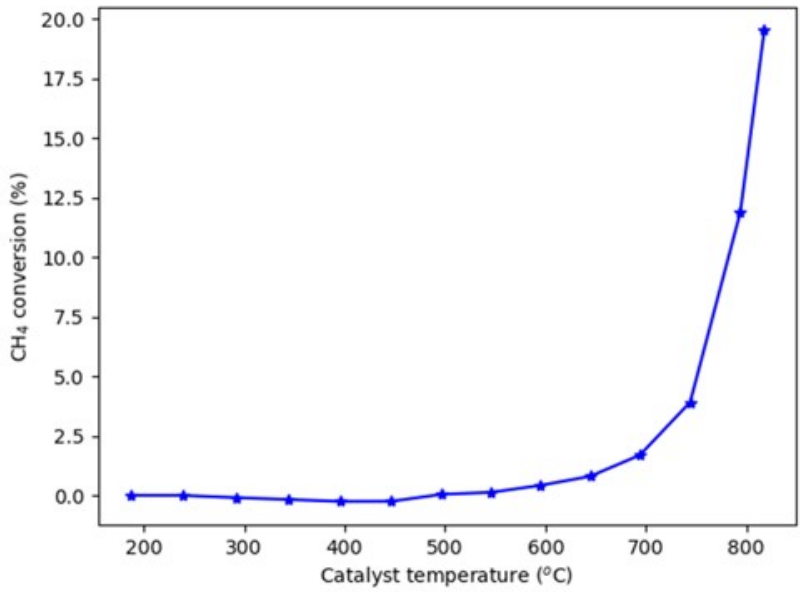


(a) Reactor performance without catalyst

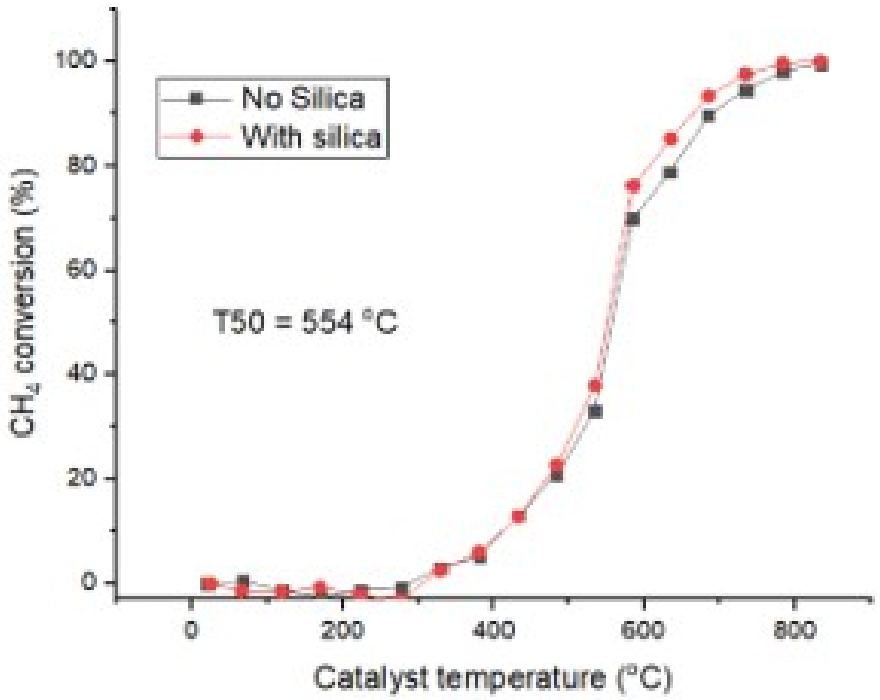


(b) Reactor performance over catalyst over 75 mg catalysts and 75 mg catalyst mixed with 75 mg silica

Figure B.4: The performance of the fixed bed reactor with and without catalyst using 7 mm ID reactor; GHSV: 48,000 ml/g/h, inlet gas feed: 0.5% $CH_4$, 4% $O_2$ and $N_2$ balance

performance for both catalysts. The slightly less conversion without silica at temperature above 600 °C can be due to gas expansion caused by the elevated temperature. This indicates a lack of micro channeling in general in both cases and that increasing the aspect ratio by silica addition, and mixing does not improve the catalytic performance. This shows that avoiding micro channeling by only enhancing the aspect ratio with silica does not enhance the catalytic performance.

### B.3.3 Residence time

Residence time is an important factor that influences catalytic performance. High residence time of reaction gases in fixed bed reactors allows prolonged contacting of the gases with the catalyst resulting in enhanced performance. The methane oxidation conversion increases with increasing residence time [134]. In order to further optimize the testing performance of catalysts in the fixed bed reactor, the residence time is enhanced by 9, and the corresponding reactor size and reaction conditions are obtained, using a theoretical approach developed as follows.

With the same catalysts amount (same in terms of volume and mass), the height of the new catalytic bed can be related to the height of the bed in the 7mm ID reactor according to the equation ((B.1))

$$h_2 = h_1 * \left(\frac{D_1}{D_2}\right)^2 \tag{B.1}$$

while their aspect ratios $AR$ are related by

$$\frac{AR_2}{AR_1} = \frac{h_2/D_2}{h_1/D_1} = \left(\frac{D_1}{D_2}\right)^3 \quad ; \quad AR_2 = AR_1 * \left(\frac{D_1}{D_2}\right)^3 \tag{B.2}$$

With the same packing structure and for the same GHSV, the superficial velocity $v$ of the

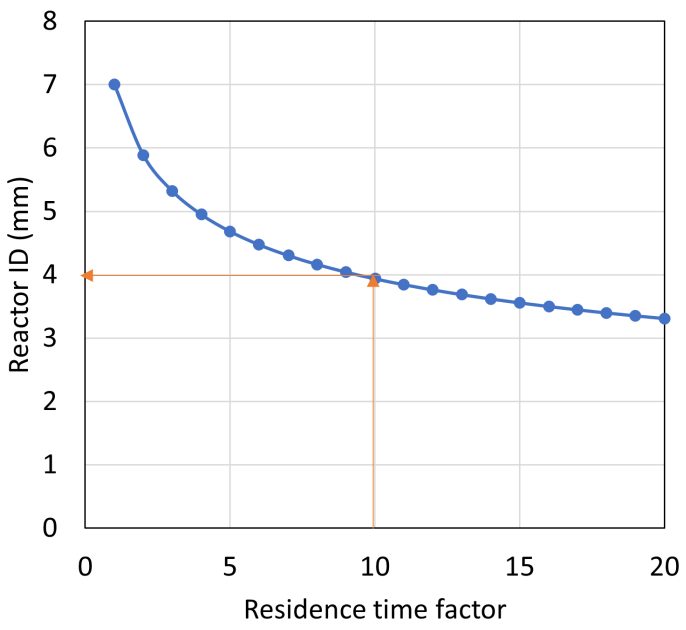


Figure B.5: Residence time factor with respect to the residence time of 7 mm ID reactor.

feed gas through the catalytic bed is, according to mass conservation, related to the velocity through the catalytic bed in the 7 mm ID reactor by equation ((B.3))

$$v_2 = \left(\frac{D_1}{D_2}\right)^2 * v_1 \tag{B.3}$$

Hence, the residence time of the reaction gas in the catalytic bed with respect to the residence time in the 7mm reactor is given by equation ((B.4)).

$$\frac{\tau_2}{\tau_1} = \frac{v_2 * h_2}{v_1 * h_1} = \left(\frac{D_1}{D_2}\right)^4 \tag{B.4}$$

Hence, the reactor size $D_2$ of the new reactor is given as

$$D_2 = D_1 * \left(\frac{\tau_1}{\tau_2}\right)^{\frac{1}{4}} \tag{B.5}$$

The consequent reactor ID-residence time factor chart is shown in figure B.5

Hence, with respect to the 7 mm ID reactor, a reactor of ID $\sim$ 4 mm is required to enhance the residence time by 9 for the same GHSV of 48,000 ml/g/h.

### B.3.4 Optimizing the GHSV for designed reactor

The GHSV that will be suitable for the new 4 mm ID reactor is further investigated experimentally to search for the maximum GHSV that avoids mass transfer limitation. Figure B.6 shows the catalytic performance of 0.25 wt % ER 1.5 $Pd/CeO_2$ catalyst at different GHSV on the 4 mm ID reactor using 0.5 % $CH_4$, 4 % $O_2$, with $N_2$ balance gas feed. Decreasing the GHSV further from 60000 ml/g/h to 48000 ml/g/h, the conversion is enhanced compared to that of the 60000 ml/g/h due to reduced residence time through the catalysts bed. When the GHSV is reduced further to 40000 ml/g/h, the conversion remains the same as that of the 48000 ml/g/h GHSV at the low conversion/temperature region (less than 30% conversion), indicating the absence of mass transfer limitation at the 48000 ml/g/h condition. The 48000 ml/g/h is therefore chosen as the optimal condition for the 4 mm ID reactor and this region is suitably considered for subsequent kinetic studies.

Figure B.7 directly compares the catalytic performance of the 4 mm ID reactor at the optimal GHSV with the 7 mm reactor at the same 48000 ml/g/h GHSV. The 4 mm ID reactor consistently produce a better catalytic performance (lower $T_{50}$ ) at all temperatures than the 7 mm ID reactor. This confirms the enhancement of catalytic performance by enhancing the residence time and avoiding mass transfer limitation. An increase in the loading of the active palladium metal - increases the catalytic performance of the catalysts, as shown in Figure B.8, further validating the reactor system and the optimized testing conditions.

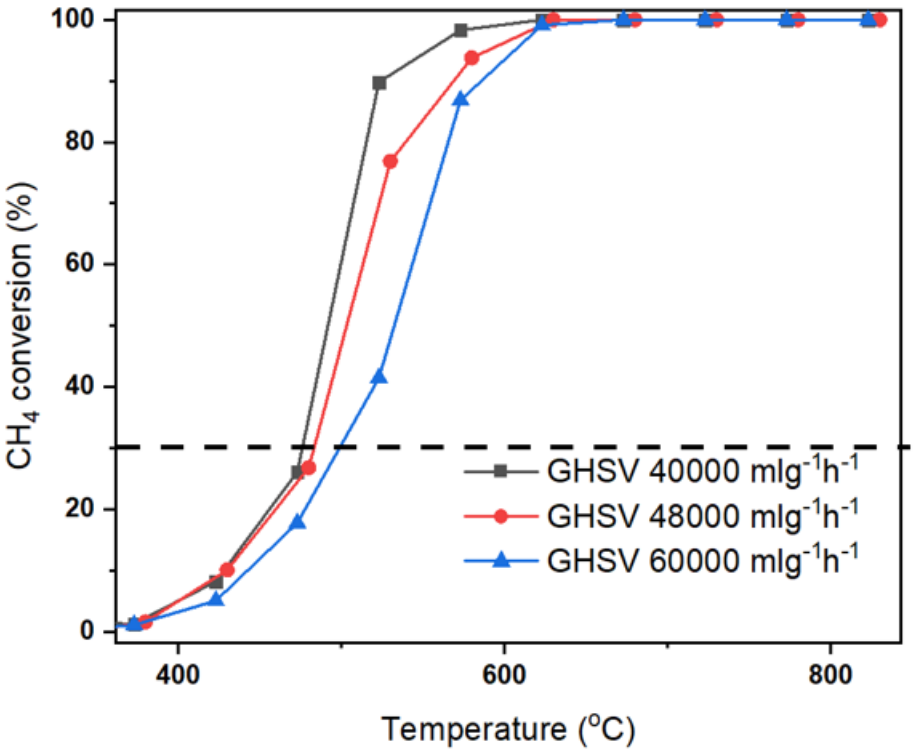


Figure B.6: Effect of gas hourly space velocity (GHSV) on methane oxidation conversion over 0.25 wt% ER 1.5 $Pd/CeO_2$ catalyst (GHSV from 96,000 to 40,000 ml/g/h); inlet gas feed: 0.5% $CH_4$, 4% $O_2$ and $N_2$ balance

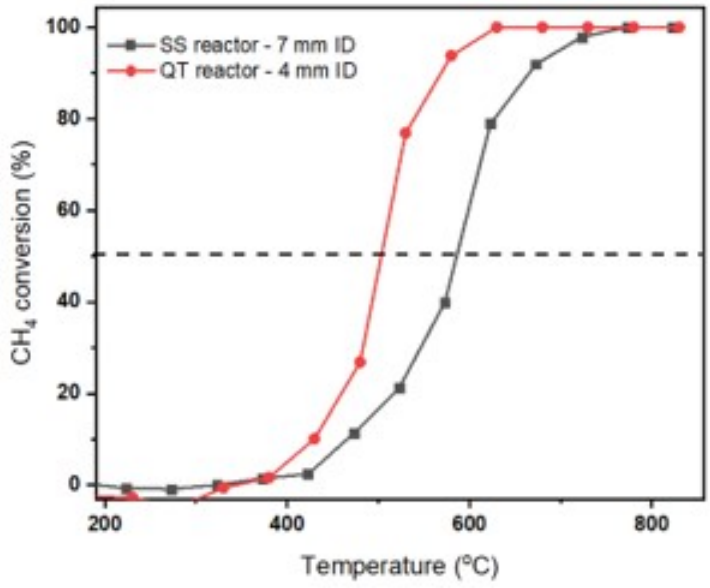


Figure B.7: Catalytic performance at Methane oxidation conversion over 0.25 wt% ER 1.5 $Pd/CeO_2$ catalyst using 4mm ID and 7 mm ID reactors; GHSV: 48,000 ml/g/h, inlet gas feed: 0.5% $CH_4$, 4% $O_2$ and $N_2$ balance

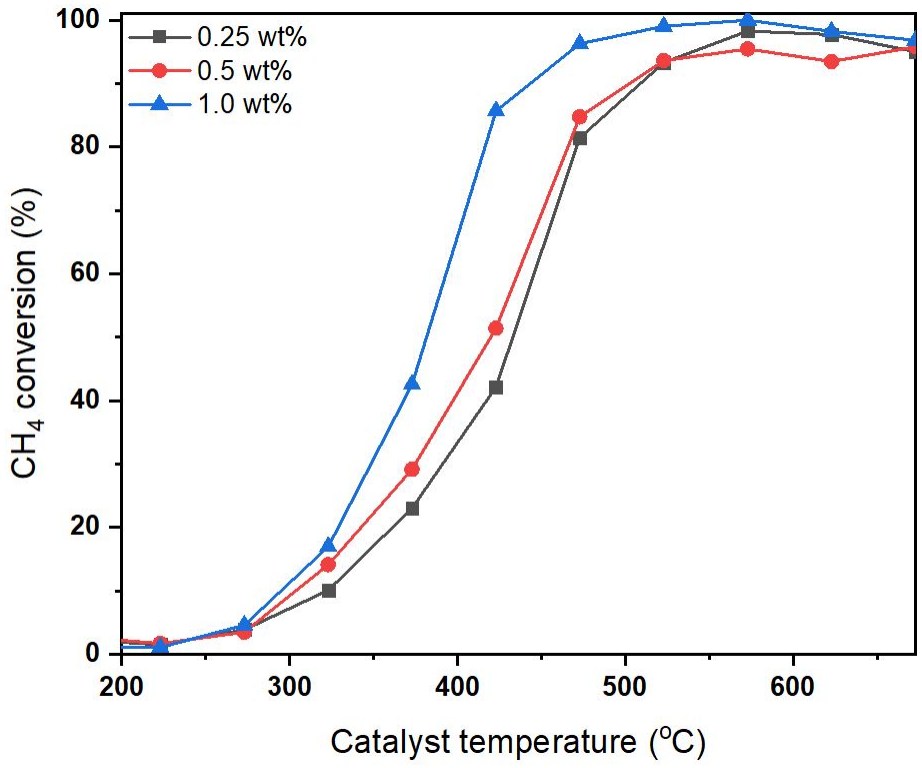


Figure B.8: Catalytic performance of $Pd/CeO_2$ at 0.25 wt.%, 0.5 wt.% and 1 wt.% Pd loading

## B.4 Conclusion and Recommendations

Here is the demonstration of the design of the reactor system based on the recommendation of the Advanced Combustion and Emission Control (ACEC) technical team. The design follows the constraint stipulated by the ACEC team with the aim of developing a procedure that can be used in lab for the optimization of reaction performance.

# Appendix C

# MATLAB Source Code for Single droplet Combustion Modelling

## C.1 MATLAB code for modelling of droplet combustion

Listing C.1: MATLAB code for droplet combustion modelling

```
1 %Code developed for droplet evaporation
2 %%
3 clc
4 clear
5 % close all
6
7 initial_droplet_size = 10e-6;%50e-6%*10^(-6); %m
8 volflow=3 %ml; of liquid precursor to calculate the droplet
    velocity at nozzle exit
```

```
x1=0.5; x2=1-x1;  %mass fraction in solvents in solution: x1=
   fuel1 is toluene
Nozd=0.5e-3;% m
initial_droplet_vel = 11%(volflow*1e-6/60)/(pi*(Nozd^2)/4)  %m/
   s
%initial_droplet_vel= 10 %m/s
ambient_gas_vel = 23; %m/s
Label ='d=10\mum ';% 'EHA:Tol 1:4';%
axislabelfontsize = 15;
xticklabelsize = 15;

areafillplotcolor='green'; % blue yellow green
plotlinewidth = 2;
axislinewidth =2;

dd0=initial_droplet_size;
%%iteration parameters
h = 1e-6;   %time step, 0.001 ms from Ref 19
maxitN = 50000;%200000;
ddter = 1e-6;
Tderr_value = 0.1;  % termination criteria
%mdoterr_value = 0.000001;  % termination criteria

%%
%Oxidant propoerties: Flame is considered stationary with model
    oxygen gas in our case.
Tinf = 2500; % in K
```

```
YFinf = 0;
uginf = ambient_gas_vel;  % ambient gas velocity='flame speed'
rhoinf = 1.429; %Kg/m3, density of O2 gas % density of gas far
   from droplet == density of model gas inside flame
MWoxd = 16*1e-3; %kg/mol  %mw oxy
CPair=29.378/MWoxd; %J/Kg/K  CP oxygen gas
koxd=0.02658;   %W/m/k     thermal conductivity of oxygen
mewoxd=0.0000447; %Pa.S  viscosity of air
Doxd=0.0000176; %m2/s   ...of oxygen???

rhooxd = rhoinf;  %
%%          First fuel
%fuel1 liquid property: fuel is toluene here; %properties
   should be at or around 0.5(To+Tboil)=341
Tbp_f1 = 110.6 + 273 ; % K
R = 8.314; % J/K/mol
MWf_1 = 92.14*1e-3;  %kg/mol toluene molecular weight
dheltaHvap_1 = 38000/MWf_1;     %J/mol divided by Kg/mol=J/Kg
%rho_liqfuel0 = 862; % kg/m3 at 298   Note: both densities are
   needed (298 and 325.55K
rholiq_1 = 821.5; % kg/m3 at 341.8K
CPfl_1 = 166.9/MWf_1;  % J/Kg/K at 324K

%fuel1 vapour property
rhofv_1 = 2.519;  %kg/m3 at 450K (value also available at 383K)
CPfv_1=139.9/MWf_1; %J/Kg/K  at 400K
kfv_1= 0.0132; % W/m/k at 400K
```

```
57 Dfv_1 = 1.04e-5; %m2/s at 332K
58 mewfv_1 = 9.45e-6;  %Pa.s at 400K
59
60 %%          Second fuel
61 %fuel2 liquid property: fuel is EHA here. %properties should be
       at or around 0.5(To+Tboil)=399
62 Tbp_f2 = 498; % K
63 R = 8.314; % J/K/mol
64 MWf_2 = 144.21*1e-3;  %kg/mol ethanol molecular weight
65 dheltaHvap_2 = 66600/MWf_2;     %J/mol divided by Kg/mol=J/Kg
66 %rho_liqfuel0 = 926; % kg/m3 at 298   Note: both densities are
      needed (298 and 325.55K
67 rholiq_2 = 843.5; % kg/m3 at 341.8K
68 CPfl_2 = 225.1/MWf_2;  % J/Kg/K at 324K
69
70 %fuel1 vapour property
71 rhofv_2 = 3.9;  %kg/m3 at 393K
72 CPfv_2= 223.6/MWf_2; %J/Kg/K  at 400K
73 kfv_2= 0.02756; % W/m/k at 450K
74 Dfv_2 = 3.97e-6; %m2/s at 300K octadecane
75 mewfv_2 = 7.5e-6;  %Pa.s at 450K decane
76
77 %%
78 %Fuel property combined
79 rhod0 = ((x1/rholiq_1) + (x2/rholiq_2))^(-1);
80 md0 = rhod0*(4/3)*pi*(dd0/2)^3;
81 dheltaHvap_d = x1*dheltaHvap_1 + x2*dheltaHvap_2;
```

```
82 CPfl_d = x1*CPfl_1 + x2*CPfl_2;
83
84 %mew
85 mewfbar_1 = mewfv_1;
86 mewfbar_2 = mewfv_2;
87 mewoxdbar = mewoxd;
88
89 MWoxd_f1= (MWoxd/MWf_1);
90 mewf1_oxd= (mewfbar_1/mewoxdbar);
91 MWf1_oxd= (MWf_1/MWoxd);
92 mewoxd_f1= (mewoxdbar/mewfbar_1);
93
94 MWoxd_f2= (MWoxd/MWf_2);
95 mewf2_oxd= (mewfbar_2/mewoxdbar);
96 MWf2_oxd= (MWf_2/MWoxd);
97 mewoxd_f2= (mewoxdbar/mewfbar_2);
98
99 mewf1_f2= (mewfbar_1/mewfbar_2);
100 MWf2_f1= (MWf_2/MWf_1);
101 MWf1_f2= (MWf_1/MWf_2);
102 mewf2_f1= (mewfbar_2/mewfbar_1);
103 %k
104 kfbar_1 = kfv_1;
105 kfbar_2 = kfv_2;
106 koxdbar = koxd;
107 %kgbar= (kfbar_avg/((1+(((1-YFbar)/YFbar)*phif_oxd))))+(koxdbar
      /((1+((YFbar/(1-YFbar))*phioxd_f))));
```

```
108
109 %%
110 %Initials
111 Td0 = 30+273;    % in K       % initial temperature
112 z0  = 0;
113 ud0 = initial_droplet_vel;    %m/s           % initial droplet
      velocity
114 m1_0 = x1*md0;
115 m2_0 = x2*md0;
116 dd0 = initial_droplet_size; % in m     % initial droplet
      diameter
117
118 % md0 = rhod0*(4/3)*pi*(dd0/2)^3;    % initial droplet mass =
      density *vol     ;
119 mdot0 = 1e-20;
120 Qd_dot0 = 1e-20;
121
122 %%
123 %variable initialization
124 Td(1)=Td0;
125 z(1)=z0;
126 ud(1)=ud0;
127 m1(1)= m1_0;
128 m2(1)=m2_0;
129 dd(1)=dd0;
130 mdott(1)=mdot0;
131 Qd_dott(1)=Qd_dot0;
```

```
132 md(1) = m1(1) + m2(1);
133
134 % XFs0 = exp((-dheltaHvap/R) * (1/Td(1)-1/Tbp));  %P/Patm,
      clausius clapeyron equation, mol frac
135 % YFs0 = XFs0*(MWf/(XFs0*MWf + (1-XFs0)*MWoxd)); %mass fraction
136 % YFss(1) = YFs0;
137 x1molfrac = (x1/MWf_1)/(x1/MWf_1 + x2/MWf_2);
138 x2molfrac = (x2/MWf_2)/(x1/MWf_1 + x2/MWf_2);
139
140 P=1; % 1bar
141 XFs1_0 = x1molfrac*exp((-dheltaHvap_1*MWf_1/R) * (1/Td(1)-1/
      Tbp_f1));  %P/Patm, clausius clapeyron equation, mol frac
142 XFs2_0 = x2molfrac*exp((-dheltaHvap_2*MWf_2/R) * (1/Td(1)-1/
      Tbp_f2));  %P/Patm, clausius clapeyron equation, mol frac
143 YFs1_0 = XFs1_0*MWf_1/((XFs1_0*MWf_1 + XFs2_0*MWf_2 + (1 -
      XFs1_0 - XFs2_0)*MWoxd));  % mass frac
144 YFs2_0 = XFs2_0*MWf_2/((XFs1_0*MWf_1 + XFs2_0*MWf_2 + (1 -
      XFs1_0 - XFs2_0)*MWoxd));  % mass frac
145 YFs_tott(1) = YFs1_0 + YFs2_0;
146 YFss1(1) = YFs1_0;
147 YFss2(1) = YFs2_0;
148 Re0 = rhoinf*abs(ud0-uginf)*dd0/mewoxd;   %mewoxy
149 CD0 = (24/Re0)*(1+Re0^(2/3)/6);
150
151 themalthickness(1)=1e-20;
152 massthicknesss(1)=1e-20;
153 CD(1)=CD0;
```

```
154 %%
155 Ar=1/3;
156 t(1) = 0;
157 for ii = 1:maxitN
158     XFs1 = x1molfrac*exp((-dheltaHvap_1*MWf_1/R) * (1/Td(ii)-1/
        Tbp_f1));  %P/Patm, clausius clapeyron equation, mol
        frac
159     XFs2 = x2molfrac*exp((-dheltaHvap_2*MWf_2/R) * (1/Td(ii)-1/
        Tbp_f2));  %P/Patm, clausius clapeyron equation, mol
        frac
160     YFs1 = XFs1*MWf_1/((XFs1*MWf_1 + XFs2*MWf_2 + (1-XFs1-XFs2)
        *MWoxd));  % mass frac
161     YFs2 = XFs2*MWf_2/((XFs1*MWf_1 + XFs2*MWf_2 + (1-XFs1-XFs2)
        *MWoxd));  % mass frac
162     YFs_tot=YFs1+YFs2;
163 %     y_v1s = YFs1/YFs_tot;
164 %     y_v2s = YFs2/YFs_tot;
165     y_v1s = YFs1*mdott(ii)/(YFs1*mdott(ii) + YFs2*mdott(ii));
166     y_v2s = YFs2*mdott(ii)/(YFs1*mdott(ii) + YFs2*mdott(ii));
167
168     CPfv = y_v1s*CPfv_1 + y_v2s*CPfv_2;
169     YFbar = YFs_tot + Ar*(YFinf-YFs_tot);
170 %     YFbar=0.5;
171     YF1bar = YFs1 + Ar*(YFinf-YFs1);
172     YF2bar = YFs2 + Ar*(YFinf-YFs2);
173     Tbar = Td(ii) + (1/3)*(Tinf-Td(ii));
```

```
174     %rhofv = rhod0 / (1 + beta*(Tbar(ii) - T0)) % assuming
            works for both vap and liqd
175     rhofv = ((y_v1s/rhofv_1) + (y_v2s/rhofv_2))^(-1);
176     rhofvbar=rhofv;  %for now
177     rhoairbar=rhooxd;  % should be correct
178     rhogbar =((YF1bar/rhofv_1) + (YF2bar/rhofv_2) + ((1-YF1bar-
            YF2bar)/rhoairbar))^(-1);
179 %     rhogbar=2.0005;
180
181     CPfvbar = CPfv;     % A CPfvbar function on T can be used.
            Will be evaluated at Tbar
182     CPairbar = CPair;
183     CPgbar=CPfv_1*YF1bar+CPfv_2*YF2bar+(1-YF1bar-YF2bar)*
            CPairbar;
184 %     CPgbar= 1.8094e+03;
185     %mewfbar = mewfv;
186     %mewoxdbar = mewoxd;
187     %MWoxd_f= (MWoxd/MWavg);
188     %mewf_oxd= (mewfbar/mewoxdbar);
189     %MWf_oxd= (MWavg/MWoxd);
190     %mewoxd_f= (mewoxdbar/mewfbar);
191     phif1_oxd=((1+((mewf1_oxd)^(1/2))*(MWoxd_f1)^(1/4))^2)/((4/
            sqrt(2))*(1+MWf1_oxd)^(1/2));%eqn14 wilke
192     phioxd_f1=((1+((mewoxd_f1)^(1/2))*(MWf1_oxd)^(1/4))^2)/((4/
            sqrt(2))*(1+MWoxd_f1)^(1/2));
193     phif2_oxd=((1+((mewf2_oxd)^(1/2))*(MWoxd_f2)^(1/4))^2)/((4/
            sqrt(2))*(1+MWf2_oxd)^(1/2));%eqn14 wilke
```

```
194       phioxd_f2=((1+((mewoxd_f2)^(1/2))*(MWf2_oxd)^(1/4))^2)/((4/
              sqrt(2))*(1+MWoxd_f2)^(1/2));
195       phif1_f2=((1+((mewf1_f2)^(1/2))*(MWf2_f1)^(1/4))^2)/((4/
              sqrt(2))*(1+MWf1_f2)^(1/2));%eqn14 wilke
196       phif2_f1=((1+((mewf2_f1)^(1/2))*(MWf1_f2)^(1/4))^2)/((4/
              sqrt(2))*(1+MWf2_f1)^(1/2));
197       mewgbar= (mewfbar_1/((1+(((x2/x1)*phif1_f2)+((1-x1-x2)/x1)*
              phif1_oxd))))+(mewfbar_2/((1+((x1/x2)*phif2_f1)+((1-x1-
              x2/x2)*phif2_oxd))))+(mewoxdbar/((1+((x1/(1-x1-x2))*
              phioxd_f1)+((x2/(1-x1-x2))*phioxd_f2)))); %eqn 12 wilke
198         % mewgbar = 3.2722e-05;
199       %kfbar = kfv; %
200       %koxdbar = koxd;
201       kgbar= (kfbar_1/((1+((x2/x1)*phif1_f2)+((1-x1-x2)/x1)*
              phif1_oxd)))+(kfbar_2/((1+((x1/x2)*phif2_f1)+((1-x1-x2)/
              x2)*phif2_oxd)))+(koxdbar/(1+((x1/(1-x1-x2))*phioxd_f1)
              +(x2/(1-x1-x2))*phioxd_f2));
202         % kgbar= 0.0258;
203
204       Dgbar=y_v1s*Dfv_1 + y_v2s*Dfv_2; %m2/s
205   %     Dgbar= 1.4500e-05;
206       Lebar= kgbar/(rhogbar*Dgbar*CPgbar);
207       Prbar=  CPgbar* mewgbar/kgbar; % 0.7;
208       Scbar=   mewgbar/( rhogbar* Dgbar);   %0.8;
209       Re = rhoinf*abs(ud(ii)-uginf)*dd(ii)/mewgbar;
210       %if Re<=1
211         %  f=1;
```

```
212     %elseif Re>1 %&& Re<=400
213     %    f = Re^0.077;
214     %end
215     %Nu0 = 1+(1+Re*Prbar)^(1/3)*f;
216     %Sh0 = 1+(1+Re*Scbar)^(1/3)*f;
217
218     Nu0 = 2+(0.552*(Re))^(1/2)*Prbar^(1/3);
219     Sh0 = 2+(0.552*(Re))^(1/2)*Scbar^(1/3);
220     themalthickness0 = dd(ii)/(Nu0 - 2);
221     massthicknesss0 = dd(ii)/(Sh0 - 2);
222     BT(1) = 2;
223     for i=1:3000
224         FT = (1+BT(i))^0.7*log(1+BT(i))/BT(i);
225         BM = (YFs_tot - YFinf)/(1-YFs_tot);
226         FM = (1+BM)^0.7*log(1+BM)/BM;
227
228         Shstar = 2+(Sh0 - 2)/FM;
229         mdot_tot = pi*rhogbar*Dgbar*dd(ii)*Shstar*log(1+BM);
230         Nustar = 2+(Nu0 - 2)/FT;
231
232         phi = (CPfvbar/CPgbar)*(Shstar/Nustar)*(1/Lebar);
233         BT(i+1) = (1+BM)^phi - 1;
234         eps = abs(BT(i+1)-BT(i));
235         if  eps <0.01
236             break
237         end
238     end
```

```
239
240       BT=BT(end);
241       themalthickness(ii+1) = FT*themalthickness0;
242       massthickness(ii+1) = FM*massthicknesss0;
243
244       Qd_dot = mdot_tot*((CPfvbar*(Tinf - Td(ii))/BT) -
             dheltaHvap_d);
245       CD = (24/Re)*(1+Re^(2/3)/6); %0.8;
246       rhod=rhod0;  % if density of droplet is assumed constant
247
248       y(1) = Qd_dot/(CPfl_d*md(ii));  %Td
249       y(2) = ud(ii);  %z
250       y(3) = (3/4)*(CD/dd(ii))*(rhoinf/rhod)*abs((uginf - ud(ii))
             )*(uginf - ud(ii));  %ud
251       y(4) = -y_v1s*mdot_tot;    %m1  y_v1s
252       y(5) = -y_v2s*mdot_tot;     %m2
253       y(6) = (2/(pi*dd(ii)^2))*(y(4)/rholiq_1 + y(5)/rholiq_2);
               %dd
254       %y(3) = -2*(mdot/(pi*rhod*(dd(ii))^2)); %- (dd(ii)/(3*rhod)
             )*drhodTd*y(1);
255 %       y(4) = ud(ii);
256 %       y(5) = -mdot;
257       y;
258       Td(ii+1) = Td(ii) +h*y(1);
259       z(ii+1) = z(ii) +h*y(2);
260       ud(ii+1) = ud(ii) +h*y(3);
261       m1(ii+1) = m1(ii) + h*y(4);
```

```
262     m2(ii+1) = m2(ii) + h*y(5);
263     dd(ii+1) = dd(ii) +h*y(6);
264     t(ii+1) = t(1) + h*ii;
265
266     md(ii+1) = m1(ii+1) + m2(ii+1);
267     mdott(ii+1) = -(y(4) + y(5));  %total
268     YFss1(ii+1) = YFs1;
269     YFss2(ii+1) = YFs2;
270     YFs_tott(ii+1) = YFs_tot;
271     Qd_dott(ii+1) = Qd_dot;
272     CD(ii+1)=CD;
273
274     Tderr = abs(Td(ii+1)-Td(ii));
275     mdoterr = abs((mdott(ii+1) - mdott(ii))/mdott(ii));
276
277     if dd(ii+1)<ddter && Tderr < Tderr_value %&& mdoterr<
        mdoterr_value %&& t(ii+1)==100 %||  %
278         break
279     end
280 %     ii
281 end
282 NIter=ii
283 Qd_dot
284
285 %plotting
286
287 figure(1)
```

```
% ah = get(gca,'XTickLabel');
% set(gca,'FontWeight','bold','XTickLabel',ah,'fontsize',
   xticklabelsize)
set(gca,'FontWeight','bold', 'linewidth', axislinewidth)
xAX = get(gca,'XAxis');
set(xAX,'FontSize', xticklabelsize)
yAX = get(gca,'YAxis');
set(yAX,'FontSize', xticklabelsize)

hold on
% ylim([0 inf]);
yyaxis left
%plot(z,Td)
plot(t*1000,dd*1e6, 'DisplayName', Label, 'linewidth',
   plotlinewidth);
xlabel('t (ms)'); ylabel('Droplet size (\mum)'); ylim([0 inf]);
      % 'DisplayName', Label
legend
yyaxis right
yAX = get(gca,'YAxis');
set(yAX,'FontSize', xticklabelsize)
plot(t*1000,Td, 'DisplayName', Label, 'linewidth',
   plotlinewidth); ylabel('Droplet surface temperature (K)');
   ylim([Td0-5 inf]);
saveas(figure(1),'size and temp.tif')

figure(2)
```

```
set(gca,'FontWeight','bold', 'linewidth', axislinewidth)
xAX = get(gca,'XAxis');
set(xAX,'FontSize', xticklabelsize)
yAX = get(gca,'YAxis');
set(yAX,'FontSize', xticklabelsize)
hold on
yyaxis left
plot(t*1000,ud, 'DisplayName', Label, 'linewidth',
   plotlinewidth); xlabel('t (ms)'); ylabel('Droplet velocity (
   m/s)');ylim([0 inf])
legend
yyaxis right
yAX = get(gca,'YAxis');
set(yAX,'FontSize', xticklabelsize)
plot(t*1000,z*1000, 'DisplayName', Label, 'linewidth',
   plotlinewidth);
xlabel('t (ms)'); ylabel('Distance (mm)','interpreter','latex')
   ;ylim([0 inf])   %'Vaporization rate $\dot{m}$ /md0 (/s)'
%legend
saveas(figure(2),'vel and distance.tif')

figure(3)
set(gca,'FontWeight','bold', 'linewidth', axislinewidth)
xAX = get(gca,'XAxis');
set(xAX,'FontSize', xticklabelsize)
yAX = get(gca,'YAxis');
set(yAX,'FontSize', xticklabelsize)
```

```
hold on
yyaxis left
plot(t*1000,YFs_tott, 'DisplayName', Label, 'linewidth',
   plotlinewidth);
xlabel('t (ms)'); ylabel('Droplet surface concentration');ylim
   ([0 inf])
yyaxis right
yAX = get(gca,'YAxis');
set(yAX,'FontSize', xticklabelsize)
legend
plot(t*1000,mdott/md0, 'DisplayName', Label, 'linewidth',
   plotlinewidth);
xlabel('t (ms)'); ylabel('Vaporization rate $\dot{m}$/m  (1/s)'
   ,'interpreter','latex');ylim([0 inf])   %'Vaporization rate
   $\dot{m}$ /md0 (/s)'
saveas(figure(3),'surface conc and vap rate.tif')

figure(4)
set(gca,'FontWeight','bold', 'linewidth', axislinewidth)
xAX = get(gca,'XAxis');
set(xAX,'FontSize', xticklabelsize)
yAX = get(gca,'YAxis');
set(yAX,'FontSize', xticklabelsize)
hold on
yyaxis left
plot(t*1000,Qd_dott, 'DisplayName', Label, 'linewidth',
   plotlinewidth);
```

```
354 xlabel('t (ms)'); ylabel('Heat transfer rate (J/s)');ylim([0
      inf])
355 yyaxis right
356 yAX = get(gca,'YAxis');
357 set(yAX,'FontSize', xticklabelsize)
358 legend
359 plot(t*1000,mdott/md0, 'DisplayName', Label, 'linewidth',
      plotlinewidth);
360 xlabel('t (ms)'); ylabel('Vaporization rate $\dot{m}$/m  (/s)',
      'interpreter','latex');ylim([0 inf])   %'Vaporization rate
      $\dot{m}$ /md0 (/s)'
361 saveas(figure(4),'Heat transfer rate and vap rate.tif')
362
363 figure(5)
364 set(gca,'FontWeight','bold', 'linewidth', axislinewidth)
365 xAX = get(gca,'XAxis');
366 set(xAX,'FontSize', xticklabelsize)
367 yAX = get(gca,'YAxis');
368 set(yAX,'FontSize', xticklabelsize)
369 hold on
370 % plot(Td,Qd_dott, 'DisplayName', Label); xlabel('Td (K)');
      ylabel('Heat transfer rate (J/s)');ylim([0 inf])
371 xx=themalthickness*1e6;   %to micron
372 yyt=t*1000;
373 yy=z*1000;
374 % plot(themalthickness*1e3, z*1000)
```

```
% fill([0 0 themalthickness*1e3], [max(z*1000) 0 z*1000], [0 0
    z*1000])
% fill(themalthickness*1e3, z*1000, z*1000)
% fill( t*1000, themalthickness*1e3, t*1000)
aa=area(yyt,xx, 'DisplayName','Boundary layer');%,  max(t*1000)
    )
% aa=area(themalthickness*1e3,t*1000)%,  max(t*1000))
xlabel('t (ms)'); ylabel('Thermal BL thickness (\mum)');
max(xx)

%%plot
plot(yyt,xx, 'DisplayName',Label);
% legend off
% patch([xx fliplr(xx)], [yy max(yy)*ones(size(yy))], 'red', '
    DisplayName','Boundary layer')  %[xx max(xx)*ones(size(xx))]
     %colorbar
% xlabel('Boundary layer thickness (mm)'); ylabel('Vertical
    distance  (mm)');
legend
% colorbar
% patch(xx,yy,'red')
% colormap(t*1000)
% colormap winter
% aa.FaceColor =t*1000
saveas(figure(5),'Thermal boundary layer.tif')

figure(6)
```

```
set(gca,'FontWeight','bold', 'linewidth', axislinewidth)
xAX = get(gca,'XAxis');
set(xAX,'FontSize', xticklabelsize)
yAX = get(gca,'YAxis');
set(yAX,'FontSize', xticklabelsize)
hold on

%%plot
xx=themalthickness*1e6;
yyt=t*1000;
yy=z*1000;

max(xx)
% plot(xx,yy)%, 'DisplayName',Label);
legend off
patch([xx fliplr(xx)], [yy max(yy)*ones(size(yy))],
   areafillplotcolor, 'DisplayName',Label)  %[xx max(xx)*ones(
   size(xx))] %colorbar   % 'DisplayName','Boundary layer'
xlabel('Thermal BL thickness (\mum)'); ylabel('Vertical
   distance  (mm)');
legend
% colorbar
saveas(figure(6),'Thermal boundary layer vertical.tif')

figure(7)
set(gca,'FontWeight','bold', 'linewidth', axislinewidth)
xAX = get(gca,'XAxis');
```

```
421 set(xAX,'FontSize', xticklabelsize)
422 yAX = get(gca,'YAxis');
423 set(yAX,'FontSize', xticklabelsize)
424 hold on
425
426 % plot(Td,Qd_dott, 'DisplayName', Label); xlabel('Td (K)');
      ylabel('Heat transfer rate (J/s)');ylim([0 inf])
427 vv=massthickness*1e6;
428 yyt=t*1000;
429 yy=z*1000;
430 % plot(themalthickness*1e3, z*1000)
431 % fill([0 0 themalthickness*1e3], [max(z*1000) 0 z*1000], [0 0
      z*1000])
432 % fill(themalthickness*1e3, z*1000, z*1000)
433 % fill( t*1000, themalthickness*1e3, t*1000)
434 bb=area(yyt,vv, 'DisplayName','Mass Boundary layer');%,  max(t
      *1000))
435 % aa=area(themalthickness*1e3,t*1000)%,  max(t*1000))
436 xlabel('t (ms)'); ylabel('Mass BL thickness (\mum)');
437 max(vv)
438
439 %%plot
440 plot(yyt,vv, 'DisplayName',Label);
441 legend
442 saveas(figure(7),'Mass Boundary layer.tif')
443
444 figure(8)
```

```
445 set(gca,'FontWeight','bold', 'linewidth', axislinewidth)
446 xAX = get(gca,'XAxis');
447 set(xAX,'FontSize', xticklabelsize)
448 yAX = get(gca,'YAxis');
449 set(yAX,'FontSize', xticklabelsize)
450 hold on
451
452 %%plot
453 vv=massthickness*1e6;
454 yyt=t*1000;
455 yy=z*1000;
456
457 max(vv)
458 % plot(xx,yy)%, 'DisplayName',Label);
459 legend off
460 patch([vv fliplr(vv)], [yy max(yy)*ones(size(yy))],
      areafillplotcolor, 'DisplayName',Label)  %[xx max(xx)*ones(
      size(xx))] %colorbar   % 'DisplayName','Boundary layer'
461 xlabel('Mass BL thickness (\mum)'); ylabel('Vertical distance
      (mm)');
462 legend
463 % colorbar
464 saveas(figure(8),'Mass boundary layer vertical.tif')
465
466 figure(9)
467 vv=massthickness*1e6;
468 set(gca,'FontWeight','bold', 'linewidth', axislinewidth)
```

```
xAX = get(gca,'XAxis');
set(xAX,'FontSize', xticklabelsize)
yAX = get(gca,'YAxis');
set(yAX,'FontSize', xticklabelsize)
hold on
yyaxis left
plot(t*1000,dd*1e6, 'DisplayName', Label, 'linewidth',
   plotlinewidth); xlabel('t (ms)'); ylabel('Droplet size (\mum
   )');ylim([0 inf])
legend
yyaxis right
yAX = get(gca,'YAxis');
set(yAX,'FontSize', xticklabelsize)
plot(t*1000,vv, 'DisplayName', Label, 'linewidth',
   plotlinewidth);
xlabel('t (ms)'); ylabel('Mass BL thickness (\mum)');ylim([0
   inf])   %'Vaporization rate $\dot{m}$ /md0 (/s)'
legend
saveas(figure(9),'mass BL vs size.tif')
```

## C.2 MATLAB Source code for 2D motion of droplet during combustion

Listing C.2: MATLAB code for droplet combustion modelling

```
clf
flame_height = 55e-3;%microm
```

```
3  zz=z;
4  zz;
5  zs=zz*1e3;
6  colorbar
7  format bank
8
9  for i=1:length(Td)
10     clf
11 %      [XX,YY,ZZ] = ellipsoid(zz(end)/2,zz(end)/2,zz(end)/2,dd
       (1)*8,dd(1)*8,zz(end)/2);
12     [XX,YY,ZZ] = ellipsoid(0,0,flame_height/2,flame_height/8,
          flame_height/8,-dd(1)+flame_height/2);
13     flam=surf(XX,YY,ZZ,'facecolor', 'red', 'edgealpha', 0);  %
          #0072BD
14     alpha(flam,0.2)
15 %      alpha 0.3
16     hold on
17     [X,Y,Z] = sphere;
18     r=50*dd(i)/2;
19     constmag=5;
20     X1=X*r*constmag;
21     Y1=Y*r*constmag;
22     Z1=Z*r*constmag;
23     xypos=0;
24     zpos=zz(i)+60*dd(1);
25     surf(X1+xypos,Y1+xypos,Z1+zpos, 'facecolor', 'green', '
          edgealpha', 0);
```

```
26 %      alpha 1
27       axis equal
28       set(gca, 'box', 'on' ,'XLim', [-flame_height/2,
            flame_height/2],'YLim', [-flame_height/2, flame_height
            /2], 'ZLim', [0, flame_height], 'XTick',[], 'YTick', [],
             'ZTick', []); %, 'XTick',[], 'YTick', [], 'ZTick', []
            'box','off','visible', 'off',
29 %      set(gca,  'box','off','XLim', [-dd(1)-2e-4, zz(end)+2e
    -4],'YLim', [-dd(1)-2e-4, zz(end)+2e-4], 'ZLim', [-2*dd(1),
    flame_height], 'XTick',[], 'YTick', []);%, 'ZTick', []); %,
    'XTick',[], 'YTick', [], 'ZTick', []
30
31       %      set(gca, 'XLim', [-dd(1), zz(end)], 'YLim', [-dd(1),
            zz(end)], 'ZLim', [-zz(end)/5, zz(end)], 'XTick',[], '
            YTick', [], 'ZTick', []); %, 'XTick',[], 'YTick', [], '
            ZTick', []
32
33 %      title(['t = ', sprintf('%0.3f',t(i)*1e3), ' ms, ','d = ',
    sprintf('%0.3f',dd(i)*1e6), ' \mum', ', T = ', sprintf('%0.2
    f',Td(i)), ' K, z = ', sprintf('%0.3f',zz(i)*1e3), ' mm' ]);
34       %text(0,0, -zz(end)/4, '10 \mum ethanol droplet in 2500 K
            ambient oxygen')
35 %      ylabel('10 \mum ethanol droplet in 2500 K ambient oxygen
    ')
36 %      title('10 \mum ethanol droplet in 2500 K ambient oxygen')
    ;
37       title('Droplet vaporization');
```

```
38 %      myTextt = sprintf('t = %.3f ms', t(i)*1e3);
39 %      myTextd = sprintf('d = %.3f m', dd(i)*1e6);
40       dleft=flame_height/2.4; dright=flame_height/6;
41 %
42 %      text(xypos-dleft,xypos-dleft, flame_height*0.9, ['t = ',
     sprintf('%0.3f',t(i)*1e3), ' ms, '], 'FontWeight', 'Bold');
43 %      text(xypos-dleft,xypos-dleft, flame_height*0.8, ['d = ',
     sprintf('%0.3f',dd(i)*1e6), ' \mum'], 'FontWeight', 'Bold');
44 %      text(xypos+dright,xypos+dright, flame_height*0.9, ['T =
     ', sprintf('%0.2f',Td(i)), ' K'], 'FontWeight', 'Bold');
45 %      text(xypos+dright,xypos+dright, flame_height*0.8, ['z =
     ', sprintf('%0.3f',zz(i)*1e3), ' mm' ], 'FontWeight', 'Bold
     ');
46       dleft=flame_height/2.4; dright=flame_height/6;
47       text(xypos-dleft,xypos-dleft, flame_height*0.9, 'EHA:Tol
            1:1', 'FontWeight', 'Bold');
48       text(xypos-dleft,xypos-dleft, flame_height*0.85, ['d_0 = ',
            sprintf('%0.1f',dd(1)*1e6), ' \mum'], 'FontWeight', '
            Bold');
49       text(xypos-dleft,xypos-dleft, flame_height*0.8, ['T_f = ',
            sprintf('%0.0f',Tinf), ' K'], 'FontWeight', 'Bold');
50       text(xypos-dleft,xypos-dleft, flame_height*0.75, ['H_f = ',
             sprintf('%0.1f',flame_height*1e3), ' mm' ], 'FontWeight
            ', 'Bold');
51       text(xypos+dright,xypos+dright, flame_height*0.9, ['t = ',
            sprintf('%0.3f',t(i)*1e3), ' ms, '], 'FontWeight', 'Bold
            ');
```

```
52      text(xypos+dright,xypos+dright, flame_height*0.85, ['d = ',
           sprintf('%0.2f',dd(i)*1e6), ' \mum'], 'FontWeight', '
           Bold');
53      text(xypos+dright,xypos+dright, flame_height*0.8, ['T = ',
           sprintf('%0.1f',Td(i)), ' K'], 'FontWeight', 'Bold');
54      text(xypos+dright,xypos+dright, flame_height*0.75, ['z = ',
            sprintf('%0.3f',zz(i)*1e3), ' mm' ], 'FontWeight', '
           Bold');
55      %      text(0,0, flame_height*0.75,  myTextd)
56      colormap;
57      view(90,0); %2D
58  %     colorbar
59  %     h = colorbar;
60  %     ylabel(h, 'droplet temp');
61      grid off
62      drawnow
63  %     pause(1)
64  %     hold on
65      videovector(i)=getframe(gcf);
66  end
67  % colorbar
68  % rectangle('Position',[-dd(1),-zz(end)/5,zz(end),zz(end)],'
       Curvature',[1,1],...
69  %           'FaceColor','r')
70  % daspect([1,1,1])
71  % xlim([-dd(1), zz(end)])
72  % ylim([-zz(end)/5, zz(end)])
```

```
73 video=VideoWriter('Droplet evaporation5-new.avi', 'Uncompressed
       AVI');
74 open(video)
75 writeVideo(video, videovector)
```

# Appendix D

# Python Source Code on Machine Learning Application in Flame Spray Pyrolysis

## D.1 Python class for chemical environment

```
"""
Created on Thu Apr  9 08:21:49 2020
@author: musanajimu
"""
import os
import numpy as np
import pandas as pd
import matplotlib.pyplot as plt
import glob
import scipy as sc
```

```
11 from scipy.signal import find_peaks
12 import sympy as sp
13 from itertools import product
14
15 class Feature:
16     def __init__(self, volflow_O2, Volflow_N2,
          volflow_fuel_total, vol_frac1, pressure):
17         self.volflow_O2=volflow_O2
18         self.Volflow_N2=Volflow_N2
19         self.volflow_fuel_total=volflow_fuel_total
20         self.vol_frac1=vol_frac1
21         self.vol_frac2=1-self.vol_frac1
22         self.pressure = pressure
23
24         self.volgasflow = self.volflow_O2+self.Volflow_N2
25         # self.vol_ratio1 = (1/self.vol_frac1) - 1
26         # self.vol_ratio2 = 1/self.vol_ratio1
27         # self.vol_frac1 = self.vol_ratio1/(self.vol_ratio1+
              self.vol_ratio2)
28         # self.vol_frac2 = self.vol_ratio2/(self.vol_ratio1+
              self.vol_ratio2)
29
30     def rawsyncon(self):
31         oxy_flow = self.volflow_O2
32         nitro_flow = self.Volflow_N2
33         fuel_flow = self.volflow_fuel_total
34         gas_pressure = self.pressure
```

```
35          solv_frac1EHA = self.vol_frac1
36          self.raw_cond = [oxy_flow, nitro_flow, fuel_flow,
               solv_frac1EHA, gas_pressure]
37          return self.raw_cond
38
39      def rawsynconlabel(self):
40          self.rawsyncon()
41          dic_rawsyncondlabel = {"oxy_flow":"Oxygen flow rate(L/
               min)",
42                "nitro_flow":"Nitrogen flow rate(L/min)",
43                "fuel_flow":"Liquid flow rate(ml/min)",
44                "solv_frac1EHA":"Solvent fraction of EHA",
45                "gas_pressure":"Gas pressure(bar)"
46                }
47          self.rawsyncon_label = list(dic_rawsyncondlabel.values
               ())
48          # self.rawsyncon_label = ['oxy_flow', 'nitro_flow', '
               fuel_flow', 'solv_frac1EHA', 'gas_pressure']
49          return self.rawsyncon_label
50
51      def sprayatom(self):
52          Liq_gas_volratio = self.volflow_fuel_total/self.
               volgasflow
53          #liq_gas_massratio
54          #Re; Weber no, estimated droplet size, estimated
               droplet velocity
55          self.spray_atom = [Liq_gas_volratio]
```

```
56          return self.spray_atom
57
58      def sprayatomlabel(self):
59          dic_sprayatomlabel = {"Liq_gas_volratio":"Liquid to gas
                volume ratio(ml/min:L/min)"}
60          #liq_gas_massratio
61          #Re; Weber no, estimated droplet size, estimated
               droplet velocity
62          self.sprayatom_label = list(dic_sprayatomlabel.values()
               )
63          # self.sprayatom_label = ['Liq_gas_volratio']
64          return self.sprayatom_label
65
66      def combustion_chemicalEnv_param(self):
67          'combustion parameters'
68          density_EHA = 0.9031
69          density_Tol = 0.8623
70          Molarmass_EHA = 144.214
71          Molarmass_tol = 92.14
72
73          density_fuel1 = density_EHA
74          density_fuel2 = density_Tol
75          Molarmass_fuel1 = Molarmass_EHA
76          Molarmass_fuel2 = Molarmass_tol
77
78          stoicEHA = [1, 11,  8,  8]
79          n_stoic_coef_fuel_1 = stoicEHA[0]
```

```
80          n_stoic_coeff_O2_1 = stoicEHA[1]
81          n_stoic_coeff_CO2_1 = stoicEHA[2]
82          n_stoic_coeff_H2O_1 = stoicEHA[3]
83
84          stoicTol = [1, 9,  7,  4]
85          n_stoic_coef_fuel_2 = stoicTol[0]
86          n_stoic_coeff_O2_2 = stoicTol[1]
87          n_stoic_coeff_CO2_2 = stoicTol[2]
88          n_stoic_coeff_H2O_2 = stoicTol[3]
89
90          #n_CH4_actual = volflow_CH4/22.4
91          n_fuel_1_actual = self.vol_frac1*self.
               volflow_fuel_total*density_fuel1/Molarmass_fuel1   #
               conservation of mass during phase change
92          n_fuel_2_actual = self.vol_frac2*self.
               volflow_fuel_total*density_fuel2/Molarmass_fuel2
93          n_O2_actual = self.volflow_O2/22.4
94          n_N2_actual = self.Volflow_N2/22.4
95
96          self.F_to_Ox_stoic = (n_stoic_coef_fuel_1 +
               n_stoic_coef_fuel_2)/(n_stoic_coeff_O2_1 +
               n_stoic_coeff_O2_2)
97          self.F_to_Ox_actual  = (n_fuel_1_actual +
               n_fuel_2_actual)/n_O2_actual
98          self.F2_to_Ox2_stoic =  n_stoic_coef_fuel_2/
               n_stoic_coeff_O2_2
99
```

```
100         self.equiv_ratio  =  self.F_to_Ox_actual/self.
               F_to_Ox_stoic
101
102         if self.equiv_ratio < 1:   #oxygen in excess, oxygen
               actual is more than the oxygen required to combust
               both fuel, fuel 2 combust first
103             n_fuel_1_combusted = n_fuel_1_actual
104             n_fuel_2_combusted = n_fuel_2_actual
105             n_O2_1_combusted = n_fuel_1_combusted *
                   n_stoic_coeff_O2_1/n_stoic_coef_fuel_1
106             n_O2_2_combusted = n_fuel_2_combusted *
                   n_stoic_coeff_O2_2/n_stoic_coef_fuel_2
107             n_CO2_produced = (n_fuel_1_combusted *
                   n_stoic_coeff_CO2_1/n_stoic_coef_fuel_1) + (
                   n_fuel_2_combusted * n_stoic_coeff_CO2_2/
                   n_stoic_coef_fuel_2)
108             n_H2O_produced = (n_fuel_1_combusted *
                   n_stoic_coeff_H2O_1/n_stoic_coef_fuel_1) + (
                   n_fuel_2_combusted * n_stoic_coeff_H2O_2/
                   n_stoic_coef_fuel_2)
109
110         else: #fuel in excess
111             if  self.F2_to_Ox2_stoic > (n_fuel_2_actual/
                   n_O2_actual):  #oxygen is in excess of oxygen
                   reqd to combust fuel 2 only,
112                 n_fuel_2_combusted = n_fuel_2_actual
113                 n_O2_2_combusted = n_fuel_2_combusted *
```

```
                n_stoic_coeff_O2_2/n_stoic_coef_fuel_2
114             n_O2_1_combusted = n_O2_actual -
                n_O2_2_combusted
115             n_fuel_1_combusted = n_O2_1_combusted *
                n_stoic_coef_fuel_1/n_stoic_coeff_O2_1
116
117             n_CO2_produced = (n_O2_1_combusted *
                n_stoic_coeff_CO2_1/n_stoic_coeff_O2_1) + (
                n_O2_2_combusted * n_stoic_coeff_CO2_2/
                n_stoic_coeff_O2_2)
118             n_H2O_produced = (n_O2_1_combusted *
                n_stoic_coeff_H2O_1/n_stoic_coeff_O2_1) + (
                n_O2_2_combusted * n_stoic_coeff_H2O_2/
                n_stoic_coeff_O2_2)
119
120         else: # oxygen is not in excess of fuel 2, and
              hence not in excess of both fuel - i.e all
              oxygen combust
121             n_O2_2_combusted = n_O2_actual
122             n_fuel_2_combusted = n_O2_2_combusted *
                n_stoic_coef_fuel_2/n_stoic_coeff_O2_2
123             n_O2_1_combusted = 0
124             n_fuel_1_combusted = 0
125
126             n_CO2_produced = (n_O2_1_combusted *
                n_stoic_coeff_CO2_1/n_stoic_coeff_O2_1) + (
                n_O2_2_combusted * n_stoic_coeff_CO2_2/
```

```
                n_stoic_coeff_O2_2)
127             n_H2O_produced = (n_O2_1_combusted *
                n_stoic_coeff_H2O_1/n_stoic_coeff_O2_1) + (
                n_O2_2_combusted * n_stoic_coeff_H2O_2/
                n_stoic_coeff_O2_2)
128
129         self.n_O2_actual = n_O2_actual
130         self.n_N2_actual = n_N2_actual
131         self.n_fuel_1_actual = n_fuel_1_actual
132         self.n_fuel_2_actual = n_fuel_2_actual
133         self.n_fuel_1_combusted = n_fuel_1_combusted
134         self.n_fuel_2_combusted = n_fuel_2_combusted
135         self.n_O2_1_combusted = n_O2_1_combusted
136         self.n_O2_2_combusted =n_O2_2_combusted
137
138         self.n_CO2_produced = n_CO2_produced
139         self.n_H2O_produced = n_H2O_produced
140         self.n_fuel_1_in_excess = n_fuel_1_actual -
              n_fuel_1_combusted
141         self.n_fuel_2_in_excess = n_fuel_2_actual -
              n_fuel_2_combusted
142         self.n_fuel_total_in_excess = self.n_fuel_1_in_excess +
               self.n_fuel_2_in_excess
143         self.n_O2_in_excess = n_O2_actual -  n_O2_1_combusted -
               n_O2_2_combusted
144         self.n_N2_actual = n_N2_actual
145
```

```
146         self.total_mol_after_reaction = self.
              n_fuel_total_in_excess + self.n_O2_in_excess + self.
              n_CO2_produced + self.n_H2O_produced + self.
              n_N2_actual
147         percentage_n_fuel_1_in_excess = 100*(self.
              n_fuel_1_in_excess/self.total_mol_after_reaction)
148         percentage_n_fuel_2_in_excess = 100*(self.
              n_fuel_2_in_excess/self.total_mol_after_reaction)
149         percentage_n_fuel_total_in_excess = 100*(self.
              n_fuel_total_in_excess/self.total_mol_after_reaction
              )
150         percentage_n_O2_in_excess = 100*(self.n_O2_in_excess/
              self.total_mol_after_reaction)
151         percentage_n_CO2_produced = 100*(self.n_CO2_produced/
              self.total_mol_after_reaction)
152         percentage_n_H2O_produced = 100*(self.n_H2O_produced/
              self.total_mol_after_reaction)
153         percentage_n_N2_actual = 100*(self.n_N2_actual/self.
              total_mol_after_reaction)
154
155         total_mol_after_reaction = self.
              total_mol_after_reaction
156         self.combustion_chemicalEnv = [
              percentage_n_fuel_1_in_excess,
157                                        percentage_n_fuel_2_in_excess
                                             ,
158                                        percentage_n_fuel_total_in_excess
```

```
                                        ,
159                                     percentage_n_O2_in_excess
                                        ,
160                                     percentage_n_CO2_produced
                                        ,
161                                     percentage_n_H2O_produced
                                        ,
162                                     percentage_n_N2_actual,
163                                     total_mol_after_reaction
                                        ]
164         return self.combustion_chemicalEnv
165
166     def combustion_chemicalEnv_paramlabel(self):
167         self.combustion_chemicalEnv_param()
168         dic_combustion_chemicalEnvlabel = {"
              percentage_n_fuel_1_in_excess":"Percentage of fuel1-
              EHA in excess (%)",
169                 "percentage_n_fuel_2_in_excess":"Percentage of
                    fuel2-Tol in excess (%)",
170                 "percentage_n_fuel_total_in_excess":"Percentage
                    of total fuel in excess (%)",
171                 "percentage_n_O2_in_excess":"Percentage of O2 in
                     excess (%)",
172                 "percentage_n_CO2_produced":"Percentage of CO2
                    produced (%)",
173                 "percentage_n_H2O_produced":"Percentage of H2O
                    produced (%)",
```

```
174                 "percentage_n_N2_actual":"Percentage of N2  (%)"
175                 }
176         self.combustion_chemicalEnvlabel = list(
              dic_combustion_chemicalEnvlabel.values())
177         return self.combustion_chemicalEnvlabel
178
179     def combustion_tempEnv_param(self):
180         # combustion_chemicalEnv_param()
181         Equiv_ratio = self.equiv_ratio
182         T = sp.Symbol('T')
183         #Cp_CH4 =
184         #Cp_Etol =  29.071
185         Cp_CO2 = 56.21#*T**2     #(kJ / kmol-K) @298K
186         Cp_H2O = 43.87     #(kJ / kmol-K) @298K
187         Cp_N2 = 33.71     #(kJ / kmol-K) @298K
188         Cp_CH4 = 33.71
189         #Cp_fuel = Cp_CH4
190         Cp_O2 = 22#*T
191
192         Hf_fuel_EHA = -559500     #(kJ / kmol) @298K
193         Hf_fuel_tol = 50000    #(kJ / kmol) @298K
194
195         Hf_fuel_1 = Hf_fuel_EHA
196         Hf_fuel_2= Hf_fuel_tol
197
198         Cp_fuel_EHA = 309.75     #(J/mol-K) @528K, gas
199         Cp_fuel_tol = 103.7     #(J/mol-K) @298K, gas   NIST
```

```
200         Cp_fuel_1 = Cp_fuel_EHA
201         Cp_fuel_2 = Cp_fuel_tol
202
203         #Hf_CH4 = -74831
204         #Hf_fuel = Hf_CH4
205         Hf_CO2 = -393546        #(kJ / kmol) @298K
206         Hf_H2O = -241845        #(kJ / kmol) @298K
207         Hf_O2 = 0
208         Hf_N2 = 0
209
210         DheltaH_rxn = self.n_CO2_produced*Hf_CO2 + self.
               n_H2O_produced*Hf_H2O - self.n_fuel_1_combusted*
               Hf_fuel_1 - self.n_fuel_2_combusted*Hf_fuel_2
211         Liq_oxid_ratio = self.volflow_fuel_total/self.
               volflow_O2
212
213         def adiabatic_temperature(Cp_fuel_1, Cp_fuel_2, Cp_O2,
               Cp_CO2, Cp_H2O):
214             "calculate the adiabatic temperature of solvents
                   mixtures given the amount of the fuel and
                   oxidant"
215             h_f_bef_rxn = self.n_fuel_1_actual*Hf_fuel_1   +
                   self.n_fuel_2_actual*Hf_fuel_2  +  self.
                   n_O2_actual*Hf_O2   +   self.n_N2_actual*Hf_N2
216
217             h_f_after_rxn = (self.n_CO2_produced*(Hf_CO2 + sp.
                   integrate(Cp_CO2, (T, 298, T)))
```

```
218             + self.n_H2O_produced*(Hf_H2O + sp.integrate(
                   Cp_H2O, (T, 298, T)))
219             + self.n_fuel_1_in_excess*(Hf_fuel_1 + sp.
                   integrate(Cp_fuel_1, (T, 298, T)))
220             + self.n_fuel_2_in_excess*(Hf_fuel_2 + sp.
                   integrate(Cp_fuel_2, (T, 298, T)))
221             + self.n_O2_in_excess*(Hf_O2 + sp.integrate(Cp_O2,
                    (T, 298, T)))
222             + self.n_N2_actual*(Hf_N2 + sp.integrate(Cp_N2, (T
                   , 298, T)))
223             )
224
225             self.adiabatictemp = sp.solve(h_f_after_rxn  -
                   h_f_bef_rxn,  T)
226             return self.adiabatictemp
227
228         Tadiabatic = adiabatic_temperature(Cp_fuel_1, Cp_fuel_2
                , Cp_O2, Cp_CO2, Cp_H2O)
229         Tadiabatic = Tadiabatic[0]
230         ##Temp = 0.5*(298 + Tadd[0])
231         self.combustion_tempEnv = [Equiv_ratio, Tadiabatic,
                DheltaH_rxn, Liq_oxid_ratio]
232         return self.combustion_tempEnv
233
234     def combustion_tempEnv_paramlabel(self):
235         self.combustion_tempEnv_param()
236         dic_combustion_chemicalEnvlabel = {"Equiv_ratio":"
```

```
            Equivalence ratio",
237                     "Tadiabatic":"Adiabatic temperature (K)",
238                     "DheltaH_rxn":"Heat of solvents combustion (
                          KJ/Kmol)",
239                     "Liq_oxid_ratio":"Liquid to oxygen volume
                          ratio (ml/min:L/min)",
240                     }
241         self.combustion_chemicalEnvlabel = list(
               dic_combustion_chemicalEnvlabel.values())
242         return self.combustion_chemicalEnvlabel
243
244 volflow_fuel_total=3;
245 volflow_O2=7.5;
246 Volflow_N2=0;
247 vol_frac1=0.5;
248 pressure=1.5;
249
250 featuree=Feature(volflow_O2, Volflow_N2, volflow_fuel_total,
       vol_frac1, pressure)
251 # featuree = Feature(2, 0, 3.5, 1, 1, 1.5)
252 rawsynconditionf  = featuree.rawsyncon()
253 sprayatomizationf  = featuree.sprayatom()
254 combustion_paraf = featuree.combustion_chemicalEnv_param()
255
256 print(featuree.combustion_tempEnv_param())
257 # combinedfeature = rawsynconditionf+sprayatomizationf+
       combustion_paraf
```

```
# fff = np.array(combinedfeature)
# # print(fff)
# fff_df = pd.DataFrame(fff)
# fff_df.to_csv('fff.csv')
```

## D.2 Calling the chemical environment python class

Here is an illustration of how to use the method for determining the chemical environment

```
"""
Created on Thu Mar 24 18:49:36 2022
@author: MusaN
"""
import  pandas as pd
import numpy as np
import matplotlib
import matplotlib.pyplot as plt
import os

volflow_fuel_total=2;
volflow_O2=4.5;
Volflow_N2=0;
vol_frac1=0.5;
pressure=1.5;
featuree=Feature(volflow_O2, Volflow_N2, volflow_fuel_total,
   vol_frac1, pressure)
# featuree = Feature(2, 0, 3.5, 1, 1, 1.5)
rawsynconditionf  = featuree.rawsyncon()
```

```
sprayatomizationf  = featuree.sprayatom()
combustion_paraf = featuree.combustion_chemicalEnv_param()
print(featuree.combustion_tempEnv_param())
```

## D.3 Python code for data generation

```
"""
Created on Thu Dec  3 16:04:26 2020
@author: musan
This code generates data
"""
import random
import os
import numpy as np
import pandas as pd
import matplotlib.pyplot as plt
import glob
import scipy as sc
from scipy.signal import find_peaks
import sympy as sp
from itertools import product

liq = [2,4]
gas=[3,5]
#
    ================================================================================
```

```
# #  Synthesis conditions data generation
#
    ============================================================================


# (random.normalvariate(6,2))
##Generate synthetic synthesis conditions
# liquidflow_mlpmin = [random.uniform(min(liq),max(liq)) for i
    in range(20)]
# gasflow_lpm = [random.uniform(3,5) for i in range(20)]
# pressure_bar = [random.uniform(1.5,3) for i in range(5)]
# solv_volfracEHA = [random.uniform(0,1) for i in range(4)]

liquidflow_mlpmin = [2+i/50 for i in range(0,101,5)]
gasflow_lpm = [gas[0]+i/(100/(gas[1]-gas[0])) for i in range
    (0,101,5)]
nitrogen_content_percentage = [i for i in range(0,99,5)]
pressure_bar = [i+0.5 for i in range(1,3,1)]
solv_volfracEHA = [i/10 for i in range(0,11,1)]

# liquidflow_mlpmin = [2,3]
# gasflow_lpm = [3.5,4.5]
# nitrogen_content_percentage = [0]
# pressure_bar = [1.5]
# solv_volfracEHA = [0.5]

```

```
42 syncon = list(product(liquidflow_mlpmin, solv_volfracEHA,
      gasflow_lpm, nitrogen_content_percentage, pressure_bar))
43 features_label = ['liquidflow_mlpmin', 'solv_volfracEHA', '
      gasflow_lpm','nitrogen_content_percentage','pressure_bar']
44 features_df = pd.DataFrame(syncon, columns=features_label)
45 features_df['oxyflow'] = features_df['gasflow_lpm']*(1-
      features_df['nitrogen_content_percentage']/100)
46 features_df['nitrogenflow'] = features_df['gasflow_lpm']*(
      features_df['nitrogen_content_percentage']/100)
47 features_df.to_csv('PSynCondition.csv')
48
49 # print(len(features_df.T))
50 # plot features
51 # plt.plot(features_df, 'o--')
52 # plt.legend()
53 # plt.show()
54 #
      ================================================================================

55 # # Synthesis cocnditions and features generation
56 #
      ================================================================================

57 ##Data generation
58 from Tadd_solvents_Class import Feature
59 # Feature(volflow_O2, Volflow_N2, volflow_fuel_total, vol_frac1
      , pressure)
```

```
compd_list_attribute=[]
for i in range(len(features_df)):     #range(len(features_df))
    compdf = Feature(features_df.oxyflow[i],
                     features_df.nitrogenflow[i],
                     # features_df.nitrogen_content_percentage[
                        i]*features_df.gasflow_lpm[i],
                     features_df.liquidflow_mlpmin[i],
                     features_df.solv_volfracEHA[i],
                     features_df.pressure_bar[i]
                     )

    rawsynconditionf  = compdf.rawsyncon()     #[oxy_flow,
       nitro_flow, fuel_flow, solv_frac1EHA, gas_pressure]
    sprayatomizationf  = compdf.sprayatom()    #[self.
       Liq_gas_volratio]
    combustion_chemEnvf = compdf.combustion_chemicalEnv_param()
    combustion_tempEnvf = compdf.combustion_tempEnv_param()
    combinedfeature = rawsynconditionf + sprayatomizationf +
       combustion_chemEnvf + combustion_tempEnvf
    compd_list_attribute.append(combinedfeature)

rawsyn_label = compdf.rawsynconlabel()
sprayatom_label = compdf.sprayatomlabel()
combustion_chemicalEnv_param_label = compdf.
   combustion_chemicalEnv_paramlabel()
combustion_tempEnv_param_label = compdf.
   combustion_tempEnv_paramlabel()
```

```
81
82 featurelistlabel = rawsyn_label + sprayatom_label +
      combustion_chemicalEnv_param_label +
      combustion_tempEnv_param_label
83 print(featurelistlabel)
84 # label = featurelistlabel
85 compd_list_attribute = np.array(compd_list_attribute)
86 label=['oxy_flow', 'nitro_flow','fuel_flow', 'solv_frac1EHA', '
      gas_pressure',
87         'Liq_gas_volratio',
88         'percentage_n_fuel_1_in_excess', '
             percentage_n_fuel_2_in_excess',
89        'percentage_n_fuel_total_in_excess', '
           percentage_n_O2_in_excess', 'percentage_n_CO2_produced
           ',
90        'percentage_n_H2O_produced', 'percentage_n_N2_actual', '
           total_mol_after_reaction',
91        'Equiv_ratio', 'Tadiabatic', 'DheltaH_rxn', '
           Liq_oxid_ratio'
92        ]
93 compd_list_attribute_df = pd.DataFrame(compd_list_attribute,
      columns=label)
94 compd_list_attribute_df.to_csv('ddSynConditionCalcequic.csv')
```

## D.4 Python code for label dictionary

```
1 """
```

```
Created on Sun Dec  6 14:12:28 2020
@author: musan
"""

label=['oxy_flow', 'nitro_flow','fuel_flow', 'solv_frac1EHA', 'gas_pressure',
       'Liq_gas_volratio',
       'percentage_n_fuel_1_in_excess', 'percentage_n_fuel_2_in_excess',
      'percentage_n_fuel_total_in_excess', 'percentage_n_O2_in_excess', 'percentage_n_CO2_produced',
      'percentage_n_H2O_produced', 'percentage_n_N2_actual', 'total_mol_after_reaction',
      'Equiv_ratio', 'Tadiabatic', 'DheltaH_rxn', 'Liq_oxid_ratio'
      ]

label_dic = {"oxy_flow":"Oxygen flow rate (L/min)",
             "nitro_flow":"Nitrogen flow rate (L/min)",
             "fuel_flow":"Liquid flow rate (ml/min)",
             "solv_frac1EHA":"Solvent fraction of EHA",
             "gas_pressure":"Gas pressure(bar)",
             "Liq_gas_volratio":"Liquid to gas vol ratio (ml/min:L/min)",
             "percentage_n_fuel_1_in_excess":"Percentage of fuel1-EHA in excess (%)",
```

```
21              "percentage_n_fuel_2_in_excess":"Percentage of
                  fuel2-Tol in excess (%)",
22              "percentage_n_fuel_total_in_excess":"Percentage of
                   total fuel in excess (%)",
23              "percentage_n_O2_in_excess":"Percentage of O2 in
                  excess (%)",
24              "percentage_n_CO2_produced":"Percentage of CO2
                  produced (%)",
25              "percentage_n_H2O_produced":"Percentage of H2O
                  produced (%)",
26              "percentage_n_N2_actual":"Percentage of N2 (%)",
27              "total_mol_after_reaction":"Total mole after
                  reaction",
28              "Equiv_ratio":"Equivalence ratio",
29               "Tadiabatic":"Adiabatic temperature (K)",
30               "DheltaH_rxn":"Heat of solvents combustion(KJ/
                    Kmol)",
31               "Liq_oxid_ratio":"Liq to O2 ratio(ml/min:L/min)"
32
33                    }
```

## D.5 Python code for machine learning class

```
1  """
2  Created on Sat Dec  5 01:50:46 2020
3  @author: musan
4  """
```

```
5  import os
6  import glob
7  import numpy as np
8  import pandas as pd
9  import matplotlib.pyplot as plt
10 from sklearn.metrics import mean_squared_error
11 from sklearn.model_selection import cross_val_score
12 from sklearn.metrics import mean_absolute_error
13 from sklearn.preprocessing import StandardScaler
14
15 from itertools import product
16 from sklearn.preprocessing import StandardScaler
17 import pandas as pd
18 import numpy as np
19 import matplotlib.pyplot as plt
20 from sklearn.cluster import KMeans
21 from mpl_toolkits.mplot3d import Axes3D
22
23 from sklearn.kernel_ridge import KernelRidge
24 from sklearn.linear_model import Ridge
25 from sklearn.ensemble import RandomForestRegressor
26 from sklearn import linear_model
27 from sklearn.neighbors import KNeighborsRegressor
28 from sklearn.cross_decomposition import PLSRegression
29 from sklearn import svm
30
31 import FSP_dict
```

```
32 class Kmeansclustering:
33     def __init__(self, data_df):
34         self.data_df=data_df
35         self.data = StandardScaler().fit_transform(self.data_df
               )
36 
37     def kmeansclusteringtrain(self, clusterNum):
38         self.clusterNum = clusterNum
39         k_means = KMeans(init="k-means++", n_clusters=self.
               clusterNum, n_init=12, random_state=1)
40         k_means.fit(self.data)
41         self.k_means_labels = k_means.labels_  # cluster label
               for the normalized but still same for the original
               data
42         self.k_means_cluster_centers = k_means.cluster_centers_
                 # cluster center but it will be normalized centers
43         # self.data["Clus_km"] = self.k_means_labels
44         # self.Xdata.to_csv('rSynCon_n_cluster.csv')
45 
46     def kmeansclusteringgenerate(self):
47         self.data_df["Clus_km"] = self.k_means_labels
48         self.data_df.to_csv('rSynCon_n_cluster.csv')
49 
50     def KM_gen_clusteredcentroid(self):
51         print(self.data_df.groupby('Clus_km').mean())
52         clustered_centroid = self.data_df.groupby('Clus_km').
               mean()
```

```
53          clustered_centroid.to_csv('rSynCon_cluster_centroid.csv
                ')
54
55      def plotclusters(self, Xdatalabel, ydatalabel):
56          area = np.pi * ( self.data_df["Clus_km"]+1)**2
57          plt.figure()
58          plt.scatter(self.data_df[Xdatalabel], self.data_df[
                ydatalabel], s=area, c=self.k_means_labels.astype(np
                .float), alpha=0.5)
59          # plt.scatter(self.data_df[Xdatalabel], self.data_df[
                ydatalabel])#, s=area)
60          # plt.xlabel(Xdatalabel, fontsize=18)
61          # plt.ylabel(ydatalabel, fontsize=16)
62          plt.xlabel(FSP_dict.label_dic[Xdatalabel], fontsize=18)
63          plt.ylabel(FSP_dict.label_dic[ydatalabel], fontsize=18)
64          plt.xticks(fontsize=16)
65          plt.yticks(fontsize=16)
66          plt.tight_layout()
67          plt.show()
68          # plt.savefig('plot2')
69
70      def generate_sse_plot(self, no_cluster_trial):
71          '''Generate sse plot for different cluster size to find
                the optimal clusters'''
72          no_cluster_trial = no_cluster_trial
73          sse = []
74          possiblecluster_size = list(range(1, no_cluster_trial
```

```
            +1))
75          for k in possiblecluster_size:
76              kmeans = KMeans(n_clusters=k)
77              kmeans.fit(self.data)
78              # kmeans.fit(self.data)
79              sse.append(kmeans.inertia_)    #Sum of squared
                    distances of samples to their closest cluster
                    center
80          plt.figure()
81          # plt.style.use("fivethirtyeight")
82          plt.rcParams["font.weight"] = "bold"
83          plt.rcParams["axes.labelweight"] = "bold"
84          plt.rcParams['axes.linewidth'] = 2
85          plt.plot(possiblecluster_size, sse, 'b*-', linewidth=2,
                markersize=14)
86          plt.xticks(possiblecluster_size)
87          plt.xlabel("Number of clusters", fontsize=18)
88          plt.ylabel("SSE", fontsize=18)
89          plt.xticks(fontsize=16)
90          plt.yticks([])
91          plt.title('Elbow Method For Optimal k', fontsize=18)
92          plt.tight_layout()
93          plt.show()
```

## D.6 Python code - main

```
1   """
```

```
Created on Fri Dec  4 20:27:15 2020
@author: musan
"""
import os
import glob
import numpy as np
import pandas as pd
import matplotlib.pyplot as plt
from sklearn.metrics import mean_squared_error
from sklearn.model_selection import cross_val_score
from sklearn.metrics import mean_absolute_error
from sklearn.preprocessing import StandardScaler

import itertools
from itertools import product
from sklearn.preprocessing import StandardScaler
import pandas as pd
import numpy as np
import matplotlib.pyplot as plt
from sklearn.cluster import KMeans
from mpl_toolkits.mplot3d import Axes3D

from sklearn.kernel_ridge import KernelRidge
from sklearn.linear_model import Ridge
from sklearn.ensemble import RandomForestRegressor
from sklearn import linear_model
from sklearn.neighbors import KNeighborsRegressor
```

```
29 from sklearn.cross_decomposition import PLSRegression
30 from sklearn import svm
31
32 plt.close()
33 data = pd.read_csv("ddSynConditionCalc.csv", index_col=0)
34 label=['oxy_flow', 'nitro_flow','fuel_flow', 'solv_frac1EHA', '
     gas_pressure',
35         'Liq_gas_volratio',
36         'percentage_n_fuel_1_in_excess', '
             percentage_n_fuel_2_in_excess',
37        'percentage_n_fuel_total_in_excess', '
           percentage_n_O2_in_excess', 'percentage_n_CO2_produced
           ',
38        'percentage_n_H2O_produced', 'percentage_n_N2_actual', '
           total_mol_after_reaction',
39        'Equiv_ratio', 'Tadiabatic', 'DheltaH_rxn', '
           Liq_oxid_ratio'
40        ]
41 no_of_clusters=5
42 clustersizeforssetrial=10
43 print(len(data))
44
45 from Class_ML import Kmeansclustering
46 KM = Kmeansclustering(data)
47 KM.kmeansclusteringtrain(no_of_clusters)
48 KM.kmeansclusteringgenerate()
49 KM.KM_gen_clusteredcentroid()
```

```
'''
plotting
'''
plt.rcParams["font.weight"] = "bold"
plt.rcParams["axes.labelweight"] = "bold"
plt.rcParams['axes.linewidth'] = 2

plotvari1raw = ['oxy_flow', 'nitro_flow','fuel_flow', '
   solv_frac1EHA', 'gas_pressure']
plotvarlist1 = list(itertools.combinations(plotvari1raw,2))

ii=1
for plotval in plotvarlist1:
    plotvariab = list(plotval)
    KM.plotclusters(plotvariab[0], plotvariab[1])
    # plt.savefig("Image "+ plotvariab[0] +" vs "+ plotvariab
       [1] + ".png",format="PNG")
    plt.savefig("plot rawsyn "+str(ii)+".png",format="PNG")
    ii+=1

plotvari2chemE = [
            # 'percentage_n_fuel_1_in_excess', '
               percentage_n_fuel_2_in_excess',
      'percentage_n_fuel_total_in_excess', '
        percentage_n_O2_in_excess', 'percentage_n_CO2_produced
        ',
      'percentage_n_H2O_produced', 'percentage_n_N2_actual']
```

```
72 plotvarlist2 = list(itertools.combinations(plotvari2chemE,2))
73
74 ii=1
75 for plotval in plotvarlist2:
76     plotvariab = list(plotval)
77     KM.plotclusters(plotvariab[0], plotvariab[1])
78     # plt.savefig("Image "+ plotvariab[0] +" vs "+ plotvariab
       [1] + ".png",format="PNG")
79     plt.savefig("plot chemE "+str(ii)+".png",format="PNG")
80     ii+=1
81
82 plotvari3tempE = ['nitro_flow', 'solv_frac1EHA', 'Equiv_ratio',
    'Tadiabatic', 'DheltaH_rxn', 'Liq_oxid_ratio', '
   total_mol_after_reaction']
83 plotvarlist3 = list(itertools.combinations(plotvari3tempE,2))
84
85 ii=1
86 for plotval in plotvarlist3:
87     plotvariab = list(plotval)
88     KM.plotclusters(plotvariab[0], plotvariab[1])
89     # plt.savefig("Image "+ plotvariab[0] +" vs "+ plotvariab
       [1] + ".png",format="PNG")
90     plt.savefig("plot tempE "+str(ii)+".png",format="PNG")
91     ii+=1
92
93 # KM.plotclusters('Tadiabatic[0]', 'n_N2_actual')
94 #
```

```
# KM.generate_sse_plot(clustersizeforssetrial)
plt.close('all')
KM.generate_sse_plot(10)
plt.savefig("K optimization plot.png")
#
    ================================================================================


# Training
#
    ================================================================================
```

# Appendix E

# List of dimensionless numbers

## E.1 List of non-dimensional numbers

Prandtl number: $Pr = \frac{\nu}{\alpha} = \frac{\hat{C}_p \mu}{k}$

Schmidt number: $Sc = \frac{\nu}{D_{AB}} = \frac{\mu}{\rho D_{AB}}$

Lewis number: $Le = \frac{\alpha}{D_{AB}} = \frac{k}{\rho \hat{C}_p D_{AB}}$